Electronics and Computer Science

Smart Electronic Materials and Systems Research Group

University of Southampton

Temperature monitoring of nozzle guide vanes using ultrasonic guided waves

by

Lawrence Martyn Yule

ORCiD: 0000-0002-0324-6642

A thesis for the degree of

Doctor of Philosophy

December 2022

University of Southampton

Abstract

Electronics and Computer Science
Smart Electronic Materials and Systems Research Group

Doctor of Philosophy

Temperature monitoring of nozzle guide vanes using ultrasonic guided waves

by Lawrence Yule

This thesis explores the use of ultrasonic guided waves for the online temperature monitoring of nozzle guide vanes (NGVs). These components are found within the turbine section of jet engines, operated at up to 1800°C. A literature review covering the currently used methods of temperature monitoring for NGVs has identified the potential of a new online sensor. Ultrasonic guided waves can propagate through thin structures such as NGVs, where different modes of propagation exhibit differing properties in respect to their sensitivity to temperature, amplitude, and dispersiveness. The complex geometry of NGVs represents a challenge to the implementation of such a system. Cooling hole arrays and multi-layered thermal barrier coatings are likely to have a considerable impact on wave propagation. In this study the effect of temperature, cooling hole structures, and thermal barrier coatings on wave propagation has been investigated through dispersion curve prediction, experimental measurement, and finite element simulation.

An experimental test system has been developed to target modes of interest, and analyse the effect of temperature on wave propagation. The temperature sensitivities of individual modes have been measured successfully. Results are in good agreement with predicted values extracted from dispersion curves, despite the range of errors identified. A finite element model mimicking the experimental setup has been developed and validated against experimental results. The temperature range was extended up to 1000°C for an Inconel 718 plate, which is a Nickel-based super alloy typically used for jet engine components. Results continue to align with predictions at 1000°C.

The effect of cooling hole structures on wave propagation are investigated through experimentation and COMSOL simulation. In general, dense hole arrays at the leading edge of a vane limit pulse-echo operation, however pitch-catch operation is still viable with careful mode and wavelength selection. In less dense areas away from the leading edge, temperature hotspot detection is possible in both configurations, although pulse-echo operation is likely to be more applicable. Sensors may need to be operated from both sides of the vane to effectively cover the whole array. Even under the favourable conditions of these models (with limited additional reflections, environmental noise, etc.) identifying changes in temperature at multiple locations is challenging, and the extent to which reflections from cooling holes can be used for this application is highly dependant on the specific geometry of the vane.

The effect of thermal barrier coatings on wave propagation has been investigated through the generation of dispersion curves and the use of COMSOL simulations. The range of materials, make up of the layered structure, and the types of application methods typically used have been considered, and the effect of temperature on the system has been evaluated. Dispersion curves generated for the multi-layered composite show how the higher order modes increase in complexity in comparison with the response in a single material. Through-thickness displacement varies across the thickness as material properties vary, with the top coat often exhibiting considerably larger displacement than then other layers. Although the work carried out on a single material (Aluminium or Inconel 718) looked to have promising advantages to working at higher order modes, the application of TBCs complicates signal propagation, causing a greater number of modes to propagate with similar wave velocities, which limits the ability to target a single mode. Operating at a lower frequency where there only the two fundamental modes are present is likely to be the most effective method of targeting/identifying single modes.

Contents

List of Figures

List of Tables

Accompanying material

All data supporting this study are openly available from the University of Southampton repository at DOI: 10.5258/SOTON/D2343.

This includes the following:

- Raw data from experimental measurements undertaken in Chapters 4 and 5.
- MATLAB scripts used to measure time of flight, and to calculate FFT/2D-FFT. Used throughout Chapters 4 to 6.
- COMSOL (v6.0) models used throughout Chapters 4 to 6.
- Temperature dependant material properties used in the generation of dispersion curves, and for COMSOL simulations (Chapters 3 to 6).

Declaration of Authorship

I declare that this thesis and the work presented in it is my own and has been generated by me as the result of my own original research.

I confirm that:

1. This work was done wholly or mainly while in candidature for a research degree at this University;
2. Where any part of this thesis has previously been submitted for a degree or any other qualification at this University or any other institution, this has been clearly stated;
3. Where I have consulted the published work of others, this is always clearly attributed;
4. Where I have quoted from the work of others, the source is always given. With the exception of such quotations, this thesis is entirely my own work;
5. I have acknowledged all main sources of help;
6. Where the thesis is based on work done by myself jointly with others, I have made clear exactly what was done by others and what I have contributed myself;
7. Parts of this work have been published as:
    - Student poster "Temperature monitoring of nozzle guide vanes (NGVs) using ultrasonic guided waves" [1] presented at ASME Turbo Expo 2020. Virtual conference 21–25 September 2020.
    - Journal paper "Surface temperature condition monitoring methods for aerospace turbomachinery: exploring the use of ultrasonic guided waves" [2] published to IOP Measurement, Science, and Technology.
    - Conference paper "Towards in-flight temperature monitoring for nozzle guide vanes using ultrasonic guided waves" [3] published to AIAA Propulsion Energy, 9–11 August 2021.
    - Journal paper "Modelling and Validation of a Guided Acoustic Wave Temperature Monitoring System" [4] published to MDPI Sensors Special Issue "Sensors for Severe Environments".

Signed:.. Date:..................

Acknowledgements

First and foremost I would like to acknowledge the support and guidance of my supervisors, Nick Harris, Bahareh Zaghari, and Martyn Hill, without which this project would not have been a success. Throughout my candidature they have provided me with their instruction, wisdom, and encouragement, that I am sincerely grateful for. I have thoroughly enjoyed working with them over the last three years, and I am looking forward to continuing our work in the future.

I would also like to express a special thanks to my parents, Neil and Maxine, who have always instilled in me the belief that anything is possible if I put my mind to it, and have supported me wholeheartedly in everything that I have done. I am incredibly grateful to the both of you. To my wonderful partner, Gem, thank you for encouraging and supporting me throughout this journey, I truly could not have done it without you. I had my doubts over my ability to achieve this, but I am so glad I persevered with it, and it is thanks to the three of you. I hope I have made you proud!

Definitions and Abbreviations

Acronyms

2D-FFT	two-dimensional fast fourier transform
AlN	aluminium nitride
APS	air plasma spraying
BSS	baseline signal stretch
CFD	computational fluid dynamic
CFL	Courant Friedrichs Lewy number
CFRP	carbon fibre reinforced plastics
EB-PVD	electron-beam physical vapor deposition
EMAT	electromagnetic acoustic transducer
FEM	finite element modelling
FFT	fast fourier transform
IDT	interdigital transducer
IR	infrared
LGS	langasite
NDE	non-destructive evaluation
NGV	nozzle guide vane
NO_x	nitrogen oxide
OBS	optimal baseline selection
PCB	printed circuit board
PLD	pulse laser deposition
PMMA	polymethyl methacrylate
PWAS	piezoelectric wafer active sensor
ReCOB	rare earth calcium oxyborate single crystals
RTD	resistance temperature detector
SAW	surface acoustic wave
SHM	structural health monitoring
TBC	thermal barrier coating

TFTC	thin film thermocouple
TGO	thermally grown oxide
THP	thermal history paint
UOTSes	ultrasonic oscillating temperature sensors
UV	ultraviolet
YCOB	yttrium calcium oxoborate single crystals
YSZ	yttrium-stabilised-zirconia (Y_2O_3–ZrO_2)
ZnO	zinc oxide

Symbols

α	coefficient of thermal expansion ($^{\circ}C^{-1}$)
λ	wavelength (m)
ν	Poisson ratio
ω	angular frequency ($\mathrm{rad\,s^{-1}}$)
A	antisymmetric mode
B	modes in multi-layered media
c	wave velocity ($\mathrm{m\,s^{-1}}$)
c_L	bulk longitudinal velocity ($\mathrm{m\,s^{-1}}$)
c_p	phase velocity ($\mathrm{m\,s^{-1}}$)
c_T	bulk shear velocity ($\mathrm{m\,s^{-1}}$)
d	propagation distance (m)
d_{aligned}	propagation distance between wedges (m)
d_{offset}	wedge foot offset distance (m)
$d_{\mathrm{reflected}}$	reflected propagation distance (m)
E	Young's modulus (GPa)
f	frequency (Hz)
fd	frequency-thickness product ($\mathrm{MHz\,mm^{-1}}$)
h	thickness (m)
k	angular wavenumber ($\mathrm{rad\,m^{-1}}$)
K	rate of change of wave velocity with temperature ($\mathrm{m\,s^{-1}\,^{\circ}C^{-1}}$)
np	number of cycles
S	symmetric mode
t	time (s)
T	temperature (°C)
t_F	time of flight (s)
t_{aligned}	total time of flight through plate and wedges (s)

$t_{\mathrm{reflected}}$	reflected time of flight (s)
t_{wedge}	time of flight through wedges only (s)
u	heat transfer coefficient ($\mathrm{W/(m^2 \cdot K)}$)
v_{group}	group velocity ($\mathrm{m\,s^{-1}}$)

CHAPTER 1

Introduction

Nozzle guide vanes (NGVs) are static components found in the turbine section of jet engines (Figure 1.1) that are used to direct airflow towards rotating turbine blades. During engine operation they are exposed to extremely high temperatures from the gas of the combustion chamber, and often require thermal barrier coatings and active cooling systems to protect the superalloy substrate. Temperature monitoring of these components is important for a number of reasons: identifying potential failures before they occur, evaluating the need for maintenance, investigating ways of improving engine efficiency, and reducing fuel consumption. Although there are a number of well established offline monitoring methods, online temperature monitoring of NGVs is difficult to achieve with the currently available technologies (see Chapter 2), due to the harsh conditions of the turbine, in addition to space, access, and power constraints. Ultrasonic guided waves are used for a wide range of structural health monitoring applications, and can often offer a number of benefits over traditional alternatives. In many implementations of guided wave based sensors the effect of temperature on their operation and response is compensated for, however the relationship between wave velocity and temperature has the potential to be used for temperature monitoring applications. This thesis investigates a number of aspects of guided wave based temperature monitoring that need to be considered for implementing a system on a nozzle guide vane. The complex wave propagation of guided waves is investigated, and the suitability of a range of wave modes are considered for temperature monitoring. The signal processing requirements for accurately monitoring changes in time of flight are explored, taking into account the dispersive nature of guided waves. Elements such as temperature sensitivity, temperature range, and response time are considered, in addition to the potential error associated with such a system. The geometry of nozzle guide vanes is also considered, as features such as cooling hole arrays and thermal barrier coatings will have substantial effects on wave propagation, and therefore the ability to monitor changes in temperature.

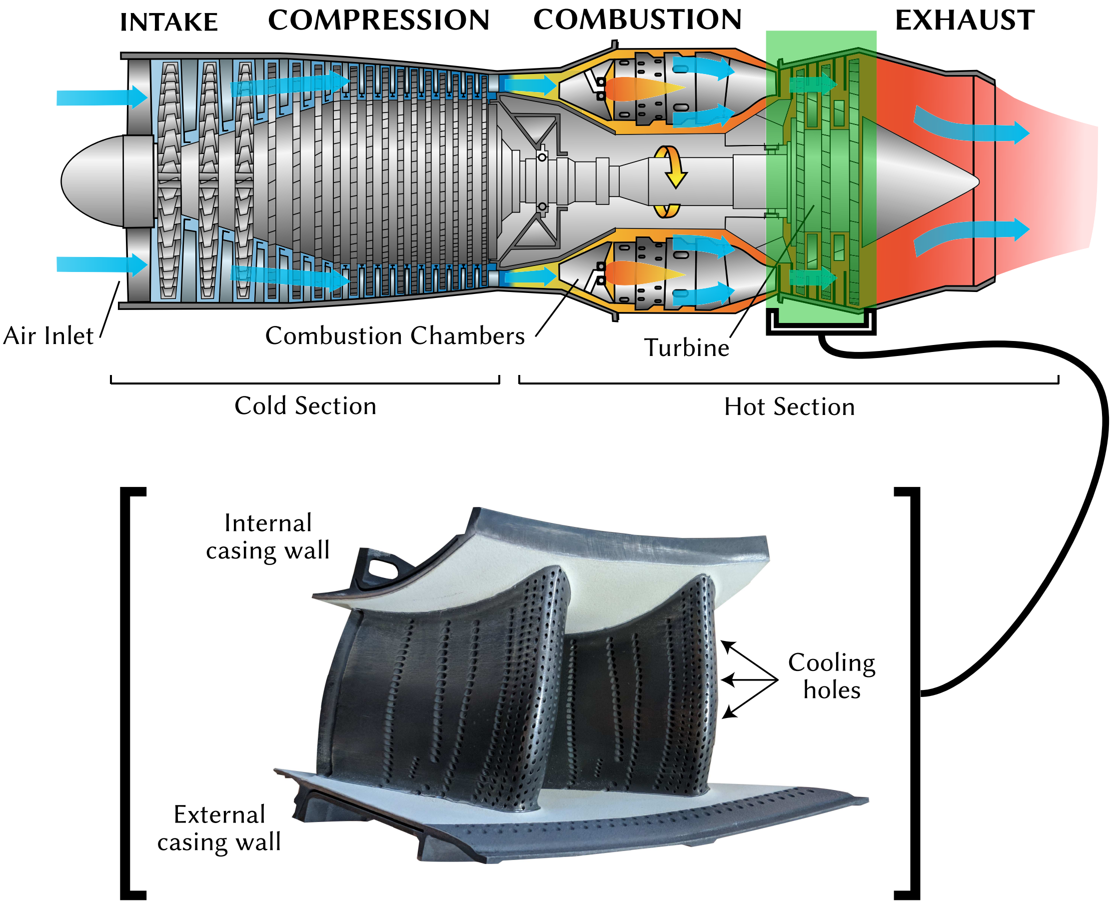

Figure 1.1 – Jet engine cross-section with highlighted nozzle guide vane [5]. Used under CC BY-SA 4.0 license.

1.1 Research objectives & questions

The overarching research objective is to determine if a guided wave based temperature monitoring system is suitable for use on gas turbine nozzle guide vanes. Such a system should be capable of temperature a resolution that provides accurate determination of the operating conditions, which allows the operating temperature of the turbine to be increased closer to the thermal limits of components. Response times should be fast enough to detect potentially dangerous high temperatures and feed data into active control systems. Spatial temperature monitoring is important for detecting the location of hotspots, where failure is mostly likely to occur. With this in mind there are a number of points to be considered, including sensor configuration, wave propagation, environmental impact, and a signal processing.

One key objective is to understand the effects of the physical environment on wave propagation in an NGV-like structure. This includes evaluating the effects of the propagation medium (material properties, cooling hole arrays, and surface coatings), and environmental conditions (temperature, acoustic noise, and gas flow) on wave propagation. The conditions listed previously will have differing effects on different Lamb wave modes, which leads to an additional objective of identifying the most appropriate mode (or mode group) for temperature monitoring in this environment. In order to evaluate these factors a test system will be developed that can transmit/receive Lamb waves in an NGV-like structure, which will also allow investigation into the signal processing requirements of a real system. Another objective is to identify a suitable sensor configuration that can survive in high temperatures, and operate under the restrictions of the environment. This includes low power operation, strict space constraints, and the ability to last for the lifetime of turbine with minimal servicing. Additionally, the type of sensor and the interface between the sensor and the NGV structure will impact the types of waves that can be generated, which further complicates the selection of suitable sensor configurations. A requirement for the monitoring of NGVs is the ability to monitor temperature spatially, in order to identify likely points of failure. An objective of this study is to determine if the monitoring of temperature at multiple locations is possible, through the acoustic reflections created by wave interaction with cooling holes. The ability to identify temperature hotspots will also be explored.

These objectives raise the following research questions:

1.1.1 Research questions

1. How can the temperature dependence of Lamb waves be utilised for temperature monitoring?
   - This question is considered in Section 3.3.2, where dispersion curves are used to show how temperature affects guided wave propagation. The varying sensitivities of different modes are shown. The effect of temperature on material properties is explored in Section 4.1, and the following sections investigate time of flight based measurement methods for temperature monitoring, both experimentally and through simulation.
2. How can the theoretical temperature sensitivity of individual Lamb wave modes be verified experimentally?
   - In Section 4.3 the wave velocity and temperature sensitivity of the S_0, A_1, and S_1 modes are measured experimentally using a wedge transducer based measurement system. Aluminium is used a test material.
3. What is the effect of the physical environment on Lamb wave propagation?

  - High temperatures (Chapter 4)
  - Cooling hole arrays (Chapter 5)
  - Thermal barrier coatings (Chapter 6)

4. Which of the Lamb wave modes (or group of modes) is most appropriate for temperature monitoring of NGVs?
    - This is considered throughout the thesis, based on the effect of temperature on wave propagation in Chapter 4, the effect of cooling hole arrays in Chapter 5, and the effect of thermal barrier coatings in Chapter 6. Overall conclusions are made in Chapter 7.
5. To what extent can acoustic reflections from cooling holes be used to monitor temperature at a number of locations or detect hotspots across the structure of an NGV?
    - This is explored in Chapter 5 through three-dimensional finite element simulations, where typical cooling hole arrays at both the leading and trailing edge of a vane are considered.
6. What is the most suitable transducer configuration for exciting Lamb waves in NGVs?
    - The range of sensors available for the generation and acquisition of guided waves is explored in Section 3.1.2, along with the selection of piezoelectric materials suitable for use at high temperatures. Based on the conclusions of Chapter 7, the most suitable transducer configuration for use on NGVs is discussed in Section 7.2.

The answers to these research questions will lead to a conclusion on how a guided wave based temperature monitoring system can be implemented on a nozzle guide vane. The effect of the physical environment on wave propagation will be known, and the most suitable modal region of temperature monitoring will have been identified. The extent to which the wave interaction with cooling holes can be used to monitor temperature at a number of locations will be known. A measurement system that can theoretically operate at high temperatures will have been identified. The outcome of these studies can form the basis of future investigations into the design of a measurement system suitable for use at high temperatures, and the testing of a system on an installed NGV.

1.2 Thesis summary

The thesis is organised into six main chapters:

- Chapter 2 – A literature review of the currently available temperature monitoring methods for nozzle guide vanes, both offline and online.
- Chapter 3 – An investigation into the potential for guided wave based temperature monitoring systems.
- Chapter 4 – The temperature sensitivity of guided waves.
- Chapter 5 – The effect of cooling holes on wave propagation.
- Chapter 6 – The effect of thermal barrier coatings on wave propagation
- Chapter 7 – Overall conclusions.

The literature review in Chapter 2 considers the currently available options for the temperature monitoring of nozzle guide vanes, including both offline and online systems. The outcome of the review is in identifying the benefits of online monitoring systems, in terms how they can impact reliability, safety, and costs. The need for a new sensor has been identified, one that can monitor the temperature of a vane in real time with minimum interference to operating conditions. The sensor should not reduce the lifetime of the vane, cause damage to its structure, require large amounts of power, or require regular maintenance, ideally surviving for the lifetime of the engine. Response time should be fast in order to accurately record the changes in temperature during start-up, shut-down, and overshoot events, while resolution and accuracy should be comparable to traditional monitoring methods.

The potential of an ultrasonic based temperature monitoring system is considered in Chapter 3, based on the usage of ultrasound for other structural health monitoring applications, and the limited usage of ultrasound for temperature sensing. The range of prospective sensor options are considered, and their suitability for operation at high temperatures is evaluated. Guided waves are a subset of ultrasonic sensing that are considered for this application, due to the geometry of the structure. An introduction to the topic is provided, where Lamb wave propagation is discussed. This includes the use of dispersion curves for predicting the modal response of a material, the varying effect of temperature on different modes, and the signal analysis of multi-modal wave packets. The choice of excitation signal is discussed, as differing numbers of cycles and the use of windowing can have a large effect on frequency response as well as the ability to measure time-of-flight. Two-sided excitation methods are discussed as a way to reduce the number of propagating modes and simplify signal analysis. The chapter is concluded by considering how the use of guided waves could be applied to nozzle guide vanes for temperature sensing, as well potential other applications.

Chapter 4 considers the temperature sensitivity of guided waves through prediction, experimentation, and simulation. Theoretical evaluation of the temperature sensitivity of Lamb wave modes highlights the potential of the method. The sensitivities of the S_0, A_1, and S_1 modes for a 1 mm thick Aluminium plate have been extracted from dispersion curves generated from material properties. The prediction indicates that group velocity will reduce with increasing temperature. An experimental test system has been developed to validate the theoretical predictions. Two variable angle wedge transducers have been used to target the modes of interest, and a measurement of time of flight between transducers has been used to calculate the group velocity. Results are in good agreement with theoretical predictions, showing that a time of flight based measurement system is capable of monitoring a change in temperature effectively. A two-dimensional finite element model (COMSOL) has been developed and validated against experimental results, to investigate the effect of other factors on wave propagation. The effect of extending the temperature range of a monitoring system up to that of a gas turbine (~1000°C) in a Nickel-based super alloy (Inconel 718) is investigated through theoretical prediction and 2D-FE simulation.

In Chapter 5, the effect of cooling holes on wave propagation and the extent to which the reflections from these holes can be used to monitor temperature at different locations is investigated both experimentally and through 3D-FE simulation. The geometry at the leading edge of a vane as well as towards the trailing edge is considered, and the extent to which either pulse-echo or pitch-catch sensor configurations can be used is evaluated. At the leading edge of a vane a dense array of cooling holes are often used, as this area is exposed to the highest gas temperatures. This region is likely to have a large impact on wave propagation, which is shown by the limited propagation distance in a pulse-echo configuration. When operated in a pitch-catch configuration, careful mode and wavelength selection is required to transmit a wave packet suitable for time-of flight measurement. Hotspot detection will be difficult to achieve in this region, although the use of machine learning models should be explored in the future to detect small changes in wave propagation due to temperature. Towards the trailing edge of the vane, where there are usually less holes and a greater spacing between them, pulse-echo operation has been shown to be more viable. Reflections from cooling holes are detectable, and a temperature hotspot can be identified. It should be noted however, that even under the favourable conditions of these models (with limited additional reflections, environmental noise, etc.) identifying changes in temperature a multiple locations is challenging, and the extent to which reflections from cooling holes can be used for this application is highly dependant on the specific geometry of the vane.

In Chapter 6, the effect of thermal barrier coatings (TBCs) on wave propagation is investigated through theoretical prediction and 2D-FE simulation, considering variances in material properties, layer thicknesses, and application techniques. Dispersion curves generated for the multi-layered composite show how the higher order modes increase in complexity in comparison with the response in a single material. Through-thickness displacement varies across the thickness as material properties vary, with the top coat often exhibiting considerably larger displacement than then other layers. The application of TBCs has been shown to complicate signal propagation, and the number of modes suitable for use in temperature monitoring applications is reduced. Operating with the use of lower order modes is likely to be the most effective method of exciting single identifiable modes.

The results of these studies are summarised in Chapter 7, and the most suitable method of implementing a guided wave based temperature monitoring system is discussed. A number of general recommendations have been made in regards to selecting an appropriate wave mode and operating frequency, as well as considering the response time and temperature resolution that can be expected from such a system. The range of further research necessary in this field is also discussed, which includes the effect of curved geometry on wave propagation, and determining the most suitable transducer configuration that can operate in the harsh conditions of a turbine.

1.3 Research contributions

Novel contributions from this research are summarised below:

- In Chapter 4, a wedge transducer based temperature monitoring system is introduced that shows excellent accuracy when compared to dispersion curve based prediction. A novel finite element model of the experimental setup was validated against experimental results. The model was used to analyse the effect of temperature up to 1000°C in an Inconel 718 plate. It is shown that temperature can be accurately determined through the calculation of wave velocity, and comparison with dispersion curves.
- In Chapter 5 the effect of typical NGV cooling hole structures on ultrasonic guided wave propagation is investigated, at both the leading and trailing edges of the vane. The effect of temperature is considered, and methods of detecting temperature hotspots are discussed. It is shown that the introduction of holes reduces material stiffness, slowing wave propagation. In areas with dense arrays of holes, pitch-catch operation is more viable than pulse-echo operation. When less holes are present the use of reflected signals may allow hotspots to be detected.
- In Chapter 6 the addition of thermal barrier coatings to a superalloy substrate is considered. The effect on wave propagation for this multi-layered composite is evaluated through analysis of dispersion curves, through-thickness displacement profiles, 2D-FFT, and COMSOL simulation.
- In Chapter 7 the findings of the previous chapters are summarised, and a number of general recommendations are made. The most suitable wave modes and transducer configurations are discussed, and the expected temperature resolution and accuracy for such a system is evaluated.

CHAPTER 2

Nozzle guide vane (NGV) temperature monitoring

This literature review considers surface temperature monitoring methods for turbomachinery applications, focusing on jet engine turbine blades and nozzle guide vanes (NGVs).

Carbon dioxide emission is the largest contributor from aviation to global warming, comprising 70% of aircraft engine emissions [6]. A small improvement in the design of a jet engine will result in a sizeable reduction in pollution, as well as in fuel and engine costs [7, 8]. The results of temperature monitoring can inform the research and development process to improve the operation and efficiency of components [9]. More accurate monitoring in terms of absolute temperature, spatial resolution, and time history allows for further development, maximising the effectiveness of components. Current and past methods focus on testing parts in controlled environments before installation in an engine, with the majority of methods requiring the blade or vane to be removed from the engine for analysis after a test has taken place. This can be improved with online methods that allow for monitoring during normal engine operation. Online methods provide considerably more data for analysis during start-up and cool down of the engine rather than only providing a peak result. The currently available online methods can only provide point measurements (in the form of thermocouples) or require optical access (pyrometry & thermographic phosphors) which is difficult to achieve in the cramped conditions of a turbine. These online systems have been utilised in test rigs and gas turbines but have not been adapted for use on in-service jet engines because of space, weight, and power constraints. An improvement to these sensors would greatly benefit gas turbine manufacturers, allowing for further development in turbine blade and NGV design by better understanding their limits. If the uncertainty of temperature measurements can be reduced then engine efficiency can be improved by operating components closer to their ideal conditions [10].

Nozzle guide vanes are constructed using nickel-based superalloys to allow them to operate at high temperatures. An increase in turbine inlet temperature elevates the risk of failure from blade creep or oxidation, the extent to which is determined by the exposure time at raised temperatures [11]. To protect the vanes and increase their temperature limits, film cooling techniques [12] are used in combination with thermal barrier coatings. The development history of superalloys, film cooling techniques, and thermal barrier coatings, is shown in Figure 2.2. Film cooling has allowed gas temperatures to be increased from around 1000°C using uncooled blades to around 1800°C with cooled blades [13]. The air used for film cooling is drawn from the main gas path, reducing efficiency while increasing NO_x emissions [14]. As emission limits become stricter the use of film cooling may have to be reduced, emphasising the importance of temperature monitoring to allow components to be operated closer to their thermal limits. Thermal barrier coatings (TBCs) are used in combination with film cooling techniques to allow gas stream temperatures to be further increased. These coatings are normally multi-layered, utilising yttrium-stabilised-zirconia (YSZ; Y_2O_3–ZrO_2) as the insulating material, a thermally grown oxide layer (TGO), and a bonding layer [15]. The materials used for the ceramic insulating layer are chosen based on low thermal conductivity, high thermal stability, and a thermal expansion coefficient that closely matches that of the substrate. Depending on the materials used this layer reduces the substrate surface temperature by ~300°C. The TGO forms during operation of the component from high temperature oxidation. The bond coat is used to improve adhesion between the topcoat and the substrate, as well as to protect the substrate from oxidation [16]. The bonding layer is considered to be the most likely point of failure from exposure to excessively high temperatures [17], monitoring of this area is therefore vital for maintaining blade health. The total thickness of TBCs ranges from 120–400 μ m thick (Figure 2.1).

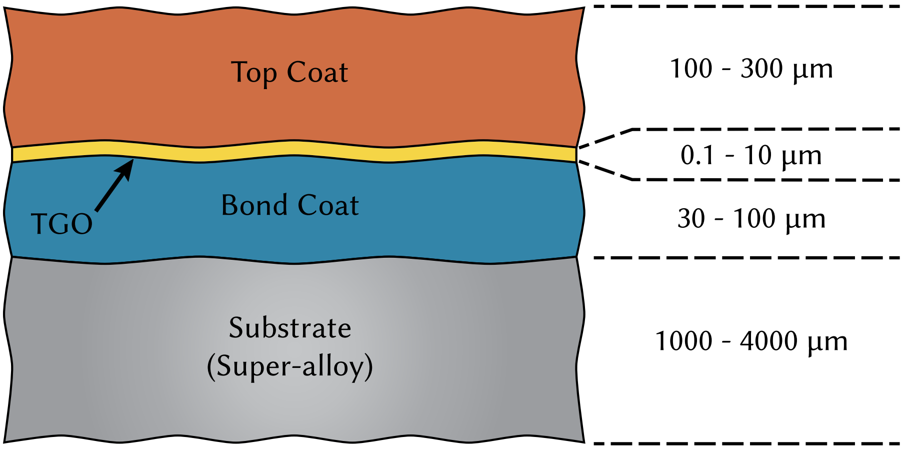

Figure 2.1 – Cross section of a typical turbine blade with TBC applied [18]. Reprinted with permission from Elsevier.

Reviews of condition monitoring/non-destructive evaluation (NDE)/structural health monitoring (SHM) for all aspects of gas turbines are provided by Abdelrhman [19] and Mevissen [20], however there are a limited number of studies that focus on developments in online surface temperature monitoring for jet engines. In the next section the methods currently used for temperature monitoring of turbine blades and NGVs are discussed. Starting with numerical simulations used in the design stage, followed by offline systems used for validation, and finally online systems used in monitoring engines during normal operation. Summaries of the methods can be found in tables 2.1 and 2.2.

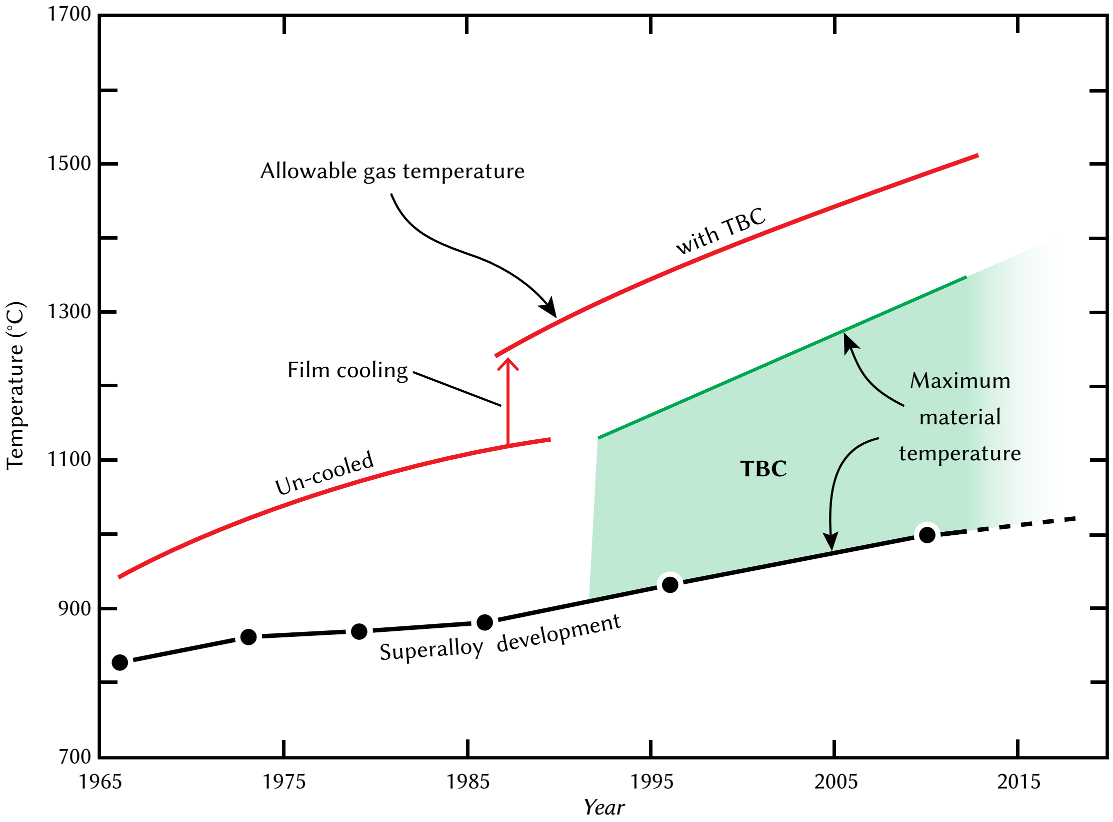

Figure 2.2 – The development history of superalloys, film cooling techniques, and thermal barrier coatings [21]. Reprinted with permission from Elsevier.

2.1 Current surface temperature monitoring strategies

Numerical simulations are used in the design stage of blades and vanes to predict the efficiency of cooling techniques before parts are put into production. Experimental data from offline or online monitoring can then be compared to numerical simulations for validation. Offline systems record the peak temperatures of the blade for later analysis at room temperature while online measurements are carried out in real time. The majority of the offline systems are well established having been used for many years, with online systems being more difficult to implement and operate reliably as sensors need to be installed inside of the engine. The implementation of online systems is further complicated when applied to jet engines, as there are severe restrictions on space, weight, and power. The systems can be further categorised into either point measurement methods or mapping methods, where point-based systems only record the temperature at a single location, but can be installed in arrays to provide more spatial information. Mapping methods allow for continuous measurement across the surface of the blade, allowing for analysis of temperature gradients. Figure 2.3 shows the range of temperature monitoring systems currently available for use on NGVs.

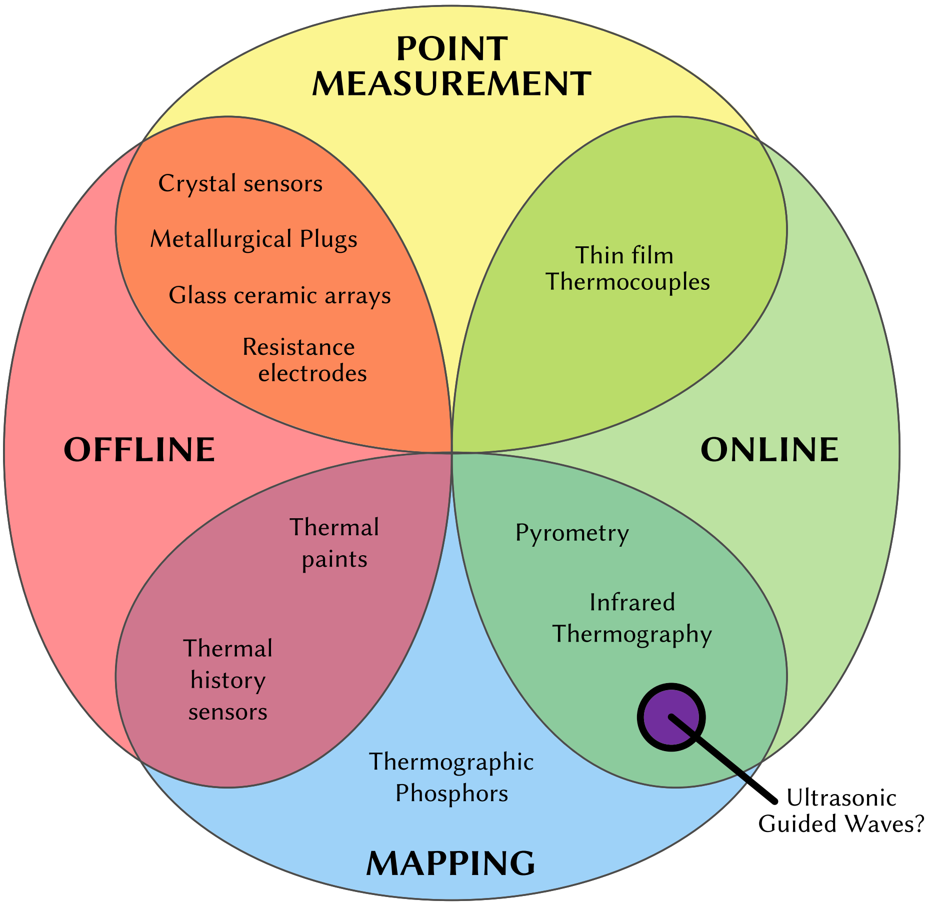

Figure 2.3 – Temperature monitoring systems for nozzle guide vanes.

2.2 Numerical methods for temperature estimation

Numerical simulations are used to find the cooling effectiveness of turbine blades and NGVs. Results of the simulations are validated against experimental results, such as those from temperature-sensitive paints [22]. Finite element modelling (FEM) can be used to predict the thermal load on a blade and analyse the effectiveness of blade cooling methods. There are two methods of calculations, uncoupled or coupled. Uncoupled methods are less computational intensive as the heat transfer coefficients used in the calculations are only computed at key engine operating conditions. Coupled methods use computational fluid dynamic (CFD) calculations to iterate the heat transfer coefficients, which improves accuracy over uncoupled methods. Findeisen *et al.* [23] compared two coupled methods, FEM1D and FEM2D. The FEM1D method uses simplified models of the cooling system making it suitable for initial designs, while the FEM2D method uses three dimensional CFD simulations that are more realistic but nearly a hundred times slower than FEM1D. This makes FEM2D models more suitable for comparison with experimental data. In order to validate complex thermal models over 80% of the surface should be measured, which is not possible with point measurement systems such as thermocouples [24]. Thermal maps allow manufacturers to better understand the effects of air flow on specific areas of components, which can help to improve the life cycle of a part. Areas of increased thermal stress can be identified, which may require additional cooling or design adjustment, while also highlighting less critical areas that could be reduced in weight or cooling.

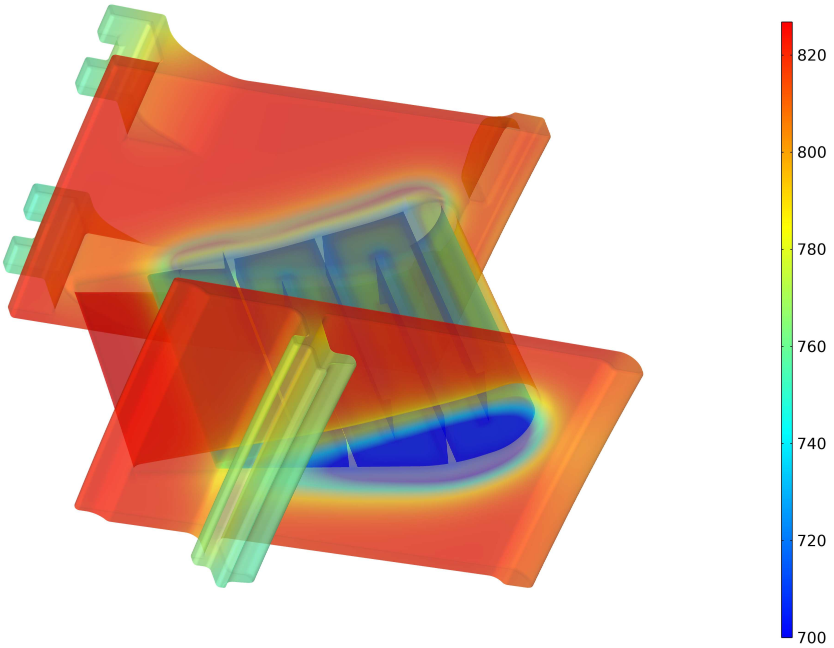

Figure 2.4 – Simplified COMSOL model of an internally cooled NGV showing surface temperature in degrees Celsius (°C), where the external gas temperature is 830°C [25].

Models are often used to predict heat transfer coefficients, which are strongly linked to the aerodynamic performance of the component. For example, Figure 2.4 shows a simplified COMSOL model of an internally cooled NGV showing surface temperature in degrees Celsius (°C), where the external gas temperature is 830°C. A small error in prediction of aerodynamic performance leads to a large error in the prediction of heat transfer coefficient [26]. The accuracy of heat transfer models is dependant on the turbulence model, the approach to three-dimensional modelling, and the density of geometric grid. An example of comparison between experimental measurements and the modelling of turbine blade heat transfer shows that there can be discrepancies of up to 40°C on the surface of a blade when the upstream gas temperature is 614°C [27]. Guan *et al.* [28] compared the results of a coupled model to experimental measurements from temperature sensitive paints, which provided comparable results when film cooling was taken into account. A comprehensive review of conjugate heat transfer models has been carried out by Samarasinghe [29].

2.3 Offline Monitoring Methods

Offline monitoring methods rely on an irreversible physical change to occur in order to accurately record the peak temperature of a surface. A summary of the available offline methods is shown in table 2.1. Thermal paints and thermal history sensors are the most commonly used methods as they allow temperature to be mapped across the surface of the blade or vane while being less intrusive than other methods.

2.3.1 Thermal paint or Temperature indicating paint

Specially formulated paints can be applied to the surface of a blade or vane that irreversibly change colour after exposure to high temperatures, recording the peak temperature at which they were exposed. Irreversible thermochromism takes place because of decomposition, i.e. changes to the crystal structure because of chemical reactions that produce new compounds. The change in colour is both a function of temperature and time, requiring careful control of exposure time for accurate analysis. Yang *et al.* [30] describe the development of temperature indicating paints including their formulation, application, and test methodology.

Paints can be categorised as single-change or multi-change, whereby single-change paints change colour once after exceeding a particular temperature threshold, and multi-change paints undergo multiple colour changes as temperature increases past a number of thresholds. Multi-change paints are more suitable for use on parts with large temperature gradients, such as turbine blades or NGVs. Examples of commercially available thermal paints produced by Thermographic Measurements Ltd, UK, can be seen in figures 2.5 and 2.6 [31].

Results can be visually interpreted by an operator drawing isothermal lines, or analysed with automated image processing techniques. When analysis is carried out by an operator only a small number of temperature changes can be identified, where colour changes are obvious. In order to measure a greater range of temperature changes other blades can be monitored with different paints during the same test. Results from the different blades can then be combined to provide a more detailed map. When analysis is carried out using image processing techniques accuracy can be improved to identify colour changes representing ±10°C changes, however inconsistent lighting conditions can cause significant sources of error. A large range of different paints can be used, covering the temperature range 150°C–1300°C. This range can be further extended to 1500°C with the use of fluorescent paint that is analysed under UV rather than visible light [32], which reduces the chance of operator error and the effect of variable lighting conditions [33].

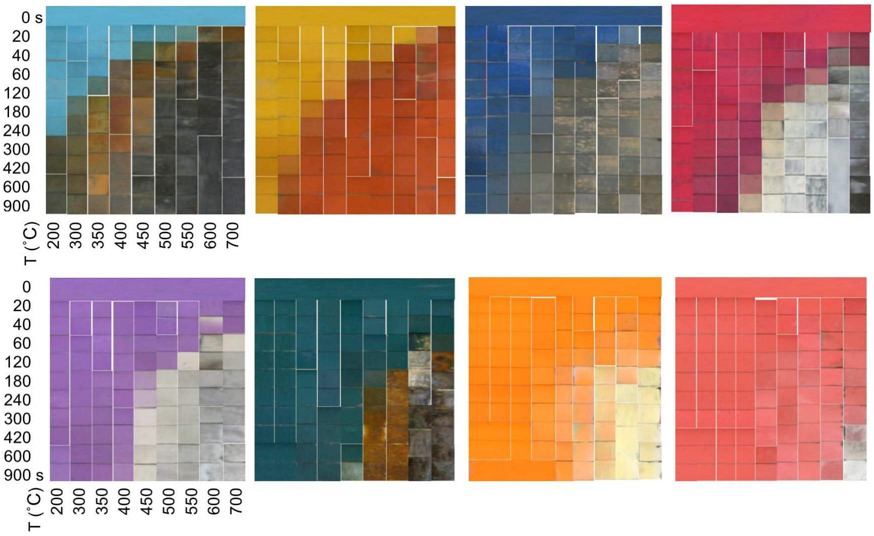

Figure 2.5 – Calibration colour maps for single-change paints: SC155, SC240, SC275, SC367, SC400, SC458, SC550, SC630 [31]. Reprinted with permission from the author.

Engine test data is often used to validate numerical models. In order to produce quantitative results from the use of thermal paints, the engine test data must be compared with calibration data, without which the paints only provide qualitative spatial information. Laboratory-based tests can be carried out to replicate engine conditions while the temperature is monitored using other methods (e.g. thermocouples, IR cameras) for validation of the real engine data. Another option is to validate the real data using predictions based on the paint's chemistry [34].

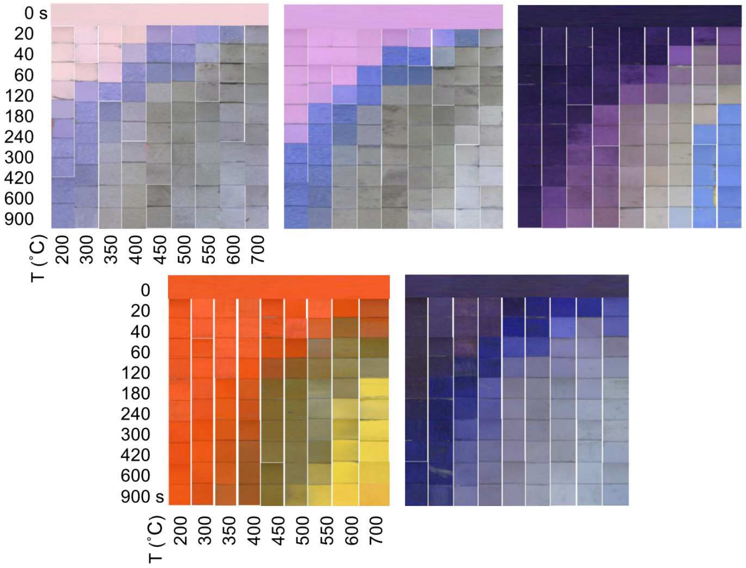

Figure 2.6 – Calibration colour maps for multi-change paints: MC135–2, MC165–2, MC395–3, MC490–10, MC520–7 [31]. Reprinted with permission from the author.

Colour changes are cross sensitive to environmental gases which must be accounted for when comparing results to calibration charts. Low paint durability means that testing time should be limited to between 3 and 5 minutes at peak temperatures for best results. [35]. Longer exposure time makes it difficult to determine if a colour change has occurred due to peak temperatures over a short period or lower temperatures over a longer period. Dismantling the engine for analysis can be time consuming and additional tests require the paint to be removed and reapplied before the engine is reconstructed. Many thermal paints contain cobalt, nickel, or lead compounds that are restricted for use by EU legislation (REACH [36]) because of their toxicity.

2.3.2 Thermal history sensors

Thermal history sensors are based on ceramic materials doped with luminescent transition or rare-earth ions. They are similar in principle to thermal paints in that exposure to high temperatures causes irreversible changes to their optical properties. The method was originally proposed by Feist in 2007 [37]. Resolution and accuracy is improved in comparison to thermal paints as the optical change is continuous across the surface of the part and can be analysed with an emission detector, as with online thermographic phosphors. Parts do not have to be fully dismantled for analysis, and the phosphors do not contain restricted chemicals (EU REACH regulation [36]). Biswas and Feist [38] discuss the theoretical background of thermal history sensors, their analysis methods, and carry out an experimental comparison against thermal paints and thermocouples. Results show good agreement between thermal paints and thermal history coating from 400°C to 900°C. Standard deviation of the thermal history coating measurement is typically below 5°C. Peral *et al.* [24] has developed an uncertainty model for the use of thermal history sensors from 400°C to 750°C, indicating that the maximum estimated uncertainty was ±6.3°C or ±13°C for 67% or 95% confidence levels respectively. This is believed to be well within the uncertainty of thermal models and the requirements for temperature measurements in harsh environments on gas turbines.

Araguás Rodriguez *et al.* [39] have carried out temperature measurements between 350°C and 900°C on three types of NGVs (without cooling, internally cooled, externally cooled) and compared the results to an embedded thermocouple. The THP was made up of an oxide ceramic pigment mixed into a water-based binder doped with lanthanide ions. Measurements are carried out using a handheld probe, each taking approximately five seconds. Precision of the measurement was ±5°C, and results were within the min-max range of the thermocouple results. An extended test (around 50 hours) using THPs was carried out by Pilgrim [40]. No damage to the THP was observed, and results are in agreement with temperature sensitive paints and CFD models (10°C difference between them). This shows an improvement over temperature sensitive paints, which can only be used for short term (~5 minutes) engine tests. The processes behind the optical changes that are caused by temperature are explained by Rabhiou *et al.* [41], followed by experimental results that show a Y_2SiO_5:Tb phosphor suitable for use up to 1000°C, with potential for further development to extend the upper temperature limit to 1400°C. A resolution comparison between temperature sensitive paints, pyrometry, and thermal history sensors is given by Amiel [42] in Table 2. Pyrometry methods provide the highest resolution (0.3°C), followed by thermal history sensors (1–5°C), and finally temperature sensitive paints (10–100°C). Heyes [43] carried out tests using a Y_2SiO_5:Tb phosphor suspended in IP 600 binder that could be used for temperature measurement from 400°C to 900°C. Results showed that the use of the binder caused some signal degradation, inhibiting the crystallisation process of the phosphor. This indicated the potential benefits of integrating the phosphors into thermal barrier coatings (TBCs), which negates the need for a binder.

A preliminary investigation was carried out utilising air plasma spraying (APS) of YAG:YSZ:Dy which showed promising results.

Although accuracy and resolution are improved in comparison to thermal paints, optical access to the parts is still required for analysis, which requires dismantling of the engine but not the parts themselves. Paints need to be removed and reapplied to carry out additional tests. The application of the paints requires sophisticated coating technologies which limits their uses. Careful phosphor selection is required as emission intensity decreases with increasing temperatures [17].

2.3.3 Other offline sensors

A number of other offline sensors have been developed for use on turbine blades or vanes that are described below. The use of these sensors is limited in comparison to temperature sensitive paints or thermal history sensors as they only provide point measurements while being more intrusive to blade operation.

Crystal temperature sensors have been developed to more accurately measure temperature gradients across blades in comparison with thermal paint methods. An array of crystal structures are installed on the surface of the blade using thermo-cement and exposed to neutron radiation (“illumination”), causing the atomic lattice to expand. When exposed to heat the lattice relaxes, which can be analysed with an X-ray diffraction microscope. If exposure time is also measured the temperature can be deduced from comparison with a calibration diagram. Accuracy of the method is ±10°C, up to at least 1400°C [44].

Glass ceramic arrays rely on using materials that all undergo different allotropic phase transformations when exposed to temperature changes. Using a single material will result in the same phase change whether the material is exposed to a high temperature for a short time, or a low temperature for a long time, which can be accounted for when using a number of materials. As temperature and exposure time increases optical transmittance is reduced, which can be measured using a UV light spectrophotometer. A disadvantage of this method is that it is strongly influenced by moisture in the environment (as found in aircraft engine exhausts), which causes large changes in the crystallisation structure of the glass. It also suffers from an inability to account for overheat events unless they are of sufficient magnitude (>50°C) [45].

Metallurgical temperature sensors are a family of offline sensors that can be machined into almost any shape. They are best suited to applications where wire connections are not possible, especially those where the sensor is immersed in a corrosive medium. Their accuracy is poor in comparison to thermocouples (around 10°C) and they can only be used to give rough estimates of temperature. Stainless steel “Feroplugs” reduce in ferromagnetism with increasing temperature exposure, which can be measured using a ferritscope or magnetic suspectometer. The reduction in ferromagnetism fully diminishes above 600°C, the upper limit of temperature measurement. Sigmaplugs have been developed to extend the measurement range, introducing a new phase that can be measured up to 900°C. Templugs are made of steel alloys that reduce in hardness with increasing temperature. The change in hardness can be measured and compared with calibration charts to determine the temperature if exposure time is known. Accuracy is around 15°C up to 600°C, reducing to 25°C up to 650°C [46]. Madison *et al.* [47] compared metallurgical temperature sensors with thermocouples when measuring piston temperatures in a running engine. Results were comparable however the metallurgical sensors were heavily influenced by areas with large thermal gradients.

2.4 Online Monitoring Methods

Online methods are used to measure temperature in real-time. This is particularly useful in comparison to offline methods as the monitoring can take place at start-up and cool down of the engine, rather than only providing a peak result. Another benefit over offline methods is the reduction in research and development time as the engine does not need to be dismantled between each test, which in turn reduces cost. This enables in-service data collection as opposed to short-term engine test data gathered from offline monitoring. Additional data helps to further validate numerical models when online systems are installed in test rigs, but they can also be used for condition monitoring applications on in-service engines. More comprehensive monitoring is beneficial in reducing maintenance schedules as these can be based on component health rather than a fixed number of operational hours. This has the benefits of reducing maintenance costs whilst minimising downtime. A reduction in the frequency of blade replacement is also beneficial to the environment. Table 2.2 shows the currently available online monitoring methods. Thermographic phosphors are the most commonly used method as they are less intrusive than point-based thermocouple or RTD arrays, while being more reliable than pyrometry methods.

2.4.1 Thermocouples

Conventional thermocouples are not suitable for use on turbine blades or NGVs, as their large size disrupts airflow, and reliably attaching them to the surface of a blade is difficult. Thin film thermocouples (TFTC) on the other hand can be directly fabricated on to the surface of a turbine blade or NGV (as shown in Figure 2.7), greatly improving long term durability in comparison to conventional thermocouples. COMSOL simulations carried out by Duan *et al.* [48] show a ~170°C difference between conventional thermocouples and their thin-film counterparts due to the distance between the thermocouple joint and the blade surface. The placement of a conventional thermocouple in its insulation filling adds an additional uncertainty of around 500 × 500 µm, which has a temperature difference from top to bottom of ~300°C. The uncertainty associated with the use of conventional thermocouples shows the motivation for the development of thin film equivalents.

The small footprint of TFTCs does not affect airflow, leading to more accurate measurements of fast temperature fluctuations. TFTCs have an extremely fast response time (<1 µs), are low cost, and have very fine spatial resolution at a single point. S-type platinum plus platinum 10% rhodium thermocouples have been shown to be stable up to 1100°C. However, oxidation of rhodium (which would occur in the gas path of a turbine) causes the thermoelectric potential to decrease, which in turn limits the upper working temperature of these types of thermocouple [49]. The main challenges to overcome with TFTCs are: developing an electrical insulation film that can withstand the harsh conditions of the turbine (high temperatures, shock, and vibration), and applying the sensor to curved surfaces.

Yang *et al.* [50] have shown that an S-type thermocouple can be fabricated using pulsed laser deposition (PLD) techniques that functions up to 700°C. To improve thermal stability at high temperatures composite ceramic oxides can be used, which have good anti-oxidation properties and have been shown to maintain high thermal outputs up to 1200°C [51]. Direct-Write Thermal Spray (DWTS) is a process by which powder, wire, or rods can be adhered to a complex substrate such as a blade or vane. A thermocouple can be embedded into the thermal barrier coating (TBC) on the surface

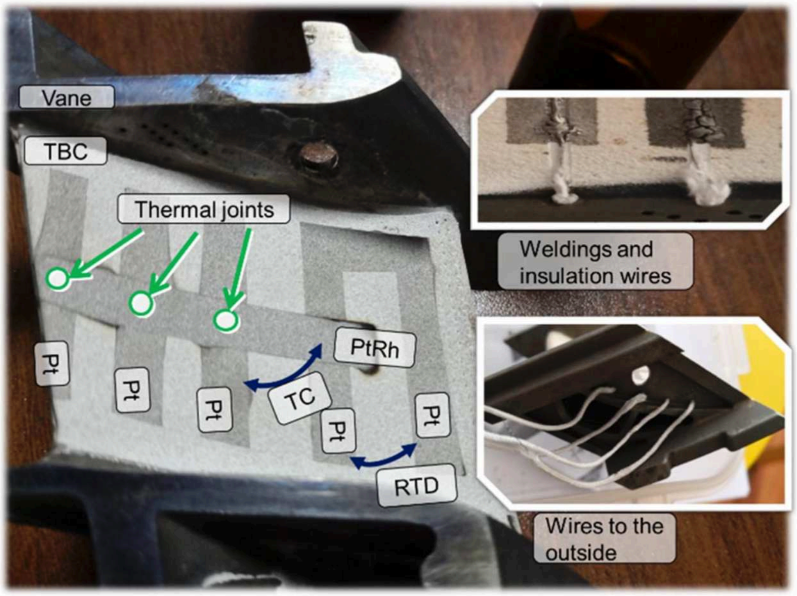

Figure 2.7 – TFTC array installed on a NGV. Used with the permission of Duan *et al.* [48], permission conveyed through Copyright Clearance Center, Inc.

of an NGV in this way and has been shown to perform well up to 450°C [52]. The addition of Al_2O_3 to YSZ(yttria-stabilized zirconia)-based TBCs improves their electrical insulation above 400°C which allows TFTCs to be used effectively [53]. A summary of TFTC systems is given by Satish *et al.* [54] along with the implementation of a K-type TFTC on an NGV deposited using an E-beam evaporation technique. Two methods of measuring temperature distribution on a TBC coating are given by Z. Ji *et al.* [55] whereby Pt soldering dots are placed along a PtRH thin film. Measurements are possible up to 1200°C with this method.

Despite the improvement of thin film thermocouples over conventional thermocouples they are still an invasive monitoring method. Only point measurements are possible unless installed in dense arrays which can have an impact on blade operation, requiring complex wiring systems. The connection between thin-film and lead wires is the primary failure point when installed on turbine blades [56]. Oxidation has a significant impact on the operation of TFTCs at high temperatures, causing drift and delamination [57], which makes the use of an insulation material vital.

2.4.2 Pyrometry

Optical pyrometry is a non-contact method of measuring thermal radiation emitted from the surface of a material. There is no upper temperature limit as thermal radiation increases with temperature, but there is a lower limit of around 500°C [58]. Measurement response is fast in comparison to conventional thermocouples as there is no thermal inertia to overcome. In order to implement a pyrometry system in a turbine optical access is required, which can be achieved by routing a probe through the wall of the turbine casing and connecting it to a detector via fibre optic cable, away from the high temperature environment of the turbine [58]. The system can be considered a point measurement system as the probe is focused on an area 1–10 mm in diameter however the point can be scanned across the surface to produce temperature maps [59]. A review of fibre optic thermometry methods is given by Yu *et al.* [60], covering blackbody, infrared, and fluorescence optical thermometers. For accurate results the emittance of the blades must be measured prior to installation to later be used in correcting the output of the pyrometer, however the emittance is also affected by factors such as surface roughness, oxidation state, and chemical composition, which will affect the overall accuracy of the system. A number of solutions have been proposed to improve the accuracy of emittance measurement, namely dual and triple spectral pyrometry [10, 61]. A review of multi-spectral pyrometry systems is given by Araújo *et al.* [62]. Accuracy is also affected by reflected radiation from other surfaces within the turbine, absorption of radiation in the gas path, interference from hot particles, and deposits forming on the surface of the probe lens. The effectiveness of pyrometry is negatively affected by the application of thermal barrier coatings (TBCs), which reduces emittance while increasing reflectivity of the blades. The thermal gradient of TBCs (~0.5°C/µm) means that careful wavelength selection is required to ensure that measurement is taking place at the required depth [63]. A number of authors have tested pyrometers on turbine engine test rigs [11, 64, 65]. Taniguchi *et al.* [66] have carried out temperature measurements using a pyrometer on a turbine blade rotating at 14,000 RPM. The system has a measurement range of 700–1150°C with an accuracy of ±3°C, over a 2 mm diameter area. The measurement probe is only inserted into the hot section of the engine for a short time (10s) before being removed to avoid damage, which limits the long term use of this method. Infrared thermography has also been used on gas turbines for crack and defect detection rather than absolute temperature measurement [67]. An IR camera in use on an NGV is shown in Figure 2.8. Although pyrometry can provide high accuracy (in favourable conditions) and fast response times, the need for optical access and their large size restricts their uses to dedicated test rigs and large gas turbines. It is unlikely that a pyrometry system could be installed inside of a jet engine for SHM applications without considerable reductions in size and weight. During long term use the build up of deposits on the surface of the probe lens will reduce accuracy and require regular maintenance. In order to produce temperature maps the probe must be scanned across the surface which would require mechanical movement of the probe, a potential point of failure.

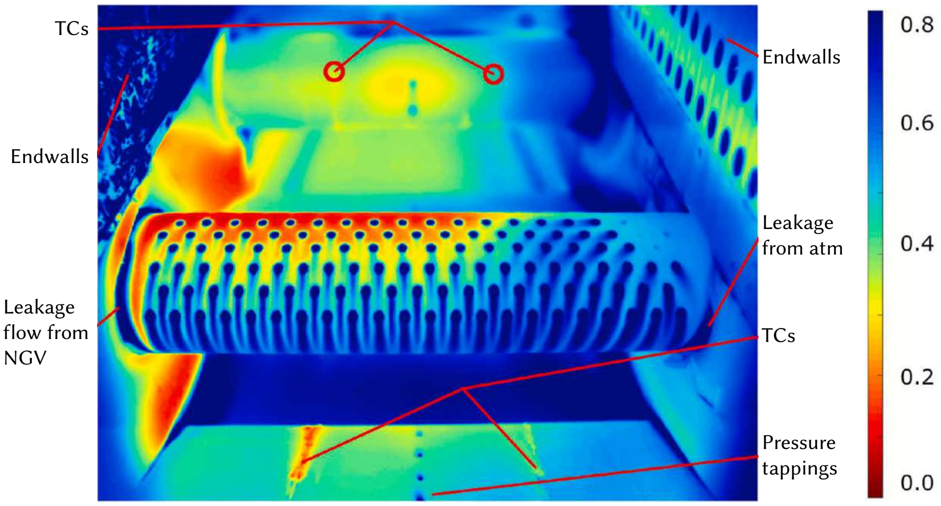

Figure 2.8 – IR camera in use on a nozzle guide vane [68]. Film cooling is only active on the right side, where effectiveness is higher (blue areas). Reprinted with permission from Elsevier.

2.4.3 Temperature sensitive paints

Temperature sensitive paints (TSPs) differ from thermal paints or temperature indicating paints in that they do not undergo permanent changes to their structure after exposure to high temperatures. The temperature dependence of luminescent molecules can be measured after application to the surface of a material using a polymer binder. The luminophore is excited by a light source, causing thermal quenching to take place. The intensity or decay lifetime of the luminescence can be measured using a camera, both of which are temperature dependent [69]. A selection of TSPs are described by Patel *et al.* [70], showing their useful temperature ranges. At low temperatures (<200°C) metal-ligand complexes (MLCs) are used as luminophores, whereas at high temperature thermographic phosphors are used.

2.4.4 Thermographic phosphors

Thermographic phosphors can be used in a very similar way to the metal-ligand complexes (MLCs) used in temperature sensitive paints however they are suitable for use up to much higher temperatures (~1600°C). They can be excited and analysed in the same way as TSPs using laser excitation and fluorescence detectors. A number of authors have carried out reviews of thermographic phosphor systems, covering the principles and theory of fluorescence [71], instrumentation [72], implementation [73], and discussion of phosphor materials and error analysis [74]. Phosphors can be applied to a blade or vane in a number of ways, the simplest of which is to mix the phosphor with a binder and apply it to the surface of the TBC, which provides a surface temperature measurement. A phosphor layer can also be applied beneath the TBC, which allows for monitoring of the temperature critical bonding layer. This is difficult to achieve as YSZ is mostly opaque to UV radiation, making excitation of the phosphor a challenge [18]. Phosphors can also be directly integrated into thermal barrier coatings (TBCs), acting as thermal insulation and as a sensor simultaneously. The first investigation into using phosphors embedded into thermal barrier coatings (TBCs), called ‘smart coating’ or ‘thermal barrier sensor coating’ was carried out by Feist [17]. Further development has shown that the addition of phosphors to produce sensor coatings does not affect the structure of TBCs and they can be applied using the same air plasma spray (APS) process as non-doped TBCs [75]. The system has been applied to an NGV in a Rolls-Royce Viper 201 engine with optical access provided through a dedicated window [76]. Yañez Gonzalez *et al.* compared temperature measurements from a TBC doped sensor, pyrometer, and thermocouple. A large temperature gradient between the surface of the TBC and the surface of the substrate is shown, with the phosphor sensing taking place close to the bond coat interface [77].

Online temperature measurements from 513°C to 767°C have been carried out on an operating engine by Jenkins *et al.* [78]. Measurements were carried out at rotational speeds up to 32,750 RPM. A laser was used for excitation of two phosphors applied to the TBC of the turbine blades, while a fibre optic probe was used for detection. Results were found to be within 25°C of of those estimated by the engine manufacturer. It is suggested that measurement range (from engine off to maximum engine power) can be improved by utilising Y_2O_3:Er phosphors [79]. Nau *et al.* [80] have presented results from the use of five different phosphors that allow measurements from room temperature up to 1500°C. Comparison of the phosphors show that their individual temperature ranges are limited (400°C). Measurements were carried out on two model combustor systems, and at high pressure, to demonstrate the potential application in real turbines. The main limitation of using thermographic phosphors is the need for optical access, both for excitation and detection, which is normally achieved with fibre optic probes. Careful selection of phosphor material is required to cover the entire temperature range of interest and to ensure that emission intensity is high enough for accurate detection at elevated temperatures [17]. In the case of turbine blades the excitation and detection needs to be synchronised with blade rotation which requires extremely fast response times [63], and is limited by the decay rate of the phosphor.

2.4.5 Other methods

Duan *et al.* [81] have found that the electrically conductive nature of TBCs at elevated temperatures (above 600°C) can be utilised as a form of smart sensor, by measuring a change in resistance with temperature. Experimental data shows good repeatability up to 950°C, measurement error of less than 3%, fast response time (~1s), and stability comparable to conventional thermocouples and TFTCs.

2.5 Concluding remarks

A review of the current methods of temperature sensing for turbine blades and NGVs in jet engines has been carried out. The range of monitoring systems available for both offline and online monitoring are summarised in Tables 2.1 and 2.2 respectively, where their working temperature ranges, temperature resolutions, spatial resolutions, and interrogation methods are compared.

Offline systems such as thermal paints and thermal history sensors are well established, but provide limited data in comparison to online systems. When used for the validation of thermal models online systems can provide considerably more information, covering temperature changes through start-up to shut-down of an engine, as well as recording over shoot events. There are a number of online systems available including thin film thermocouples (TFTCs), thermographic phosphors, and pyrometers. Thermocouples need to be embedded into the structure of a component and require a wire connection which is a significant point of failure, while only providing point measurements unless installed in dense arrays. Pyrometers can provide temperature maps without installing sensors onto the surface of a component, but optical access is required, and environmental factors have a significant impact on their accuracy. Thermographic phosphors require optical access to components for both excitation and analysis, as well as direct application of a phosphor to the surface. This makes sensors difficult to implement for condition monitoring applications because of space constraints, especially in jet engines.

The following chapter considers the use of ultrasonic guided waves as an alternate temperature monitoring method. A background on the use of ultrasound for structural health monitoring is provided, specifically looking at the use of guided waves. This is followed by an overview of the potential measurement devices for the generation and acquisition of guided waves, where the most suitable sensor for use on NGVs is evaluated. An introduction to the theory of Lamb waves is provided, which includes the use of dispersion curves, and considers the effect of temperature on wave propagation.

Method	Temperature range (°C)	Temperature resolution (°C)	Spatial resolution	Sensor type	Interrogation method
Crystal temperature sensors	up to 1400	± 10	Low	Surface mounted	Illumination + observation
Templugs	650	15–25	Low (single points)	Embedded in substrate	Analysis of ferromagnetism/hardness/phase
Glass ceramic arrays	1100	Not given	Low	Surface mounted	Observation only
Thermal paints (TIP)	Up to 1500	10–100	Moderate	Surface layer	Observation only
Thermal history sensors	150–1400	± 5	High	Surface layer or embedded in TBC	Illumination + observation

Table 2.1 – Summary of offline temperature monitoring methods.

Method	Temperature range (°C)	Temperature resolution (°C)	Spatial resolution	Sensor type	Interrogation method
Thin film thermocouples (TFTCs)	Up to 1200	± 2	Low (can be installed in arrays)	Surface mounted	Electrical connection
Infrared Thermography/Pyrometry	500->2000	0.3	Low (can be scanned)	Optical probe	Observation only
Temperature sensitive paints (MLCs)	<200	1–5	High	Surface layer	Illumination + observation
Thermographic phosphors	Up to 1600	1–5	High	Surface layer or embedded in TBC	Illumination + observation

Table 2.2 – Summary of online temperature monitoring methods.

CHAPTER 3

The potential of ultrasonic guided waves for the temperature monitoring of NGVs

The ideal sensor for nozzle guide vane temperature monitoring should be capable of mapping the temperature of a vane in real time with minimum interference to operating conditions. The use of a sensor should not reduce the lifetime of the component, cause damage to its structure, require large amounts of power, or require regular maintenance, ideally surviving for the lifetime of the engine. Response time should be fast in order to accurately record the changes in temperature during start-up, shut-down, and overshoot events, while resolution and accuracy should be comparable to traditional monitoring methods.

Ultrasonic guided wave technology may be suitable for this application as it can provide real-time sensing, fast response times, and the ability to re-use the sensor indefinitely. There is the potential for transducers to be kept away from the harsh conditions of the turbine by transmitting a wave through the structure of a vane and analysing the received signal. Measuring temperature in this way reduces the influence of the sensor on the operating condition of the component. The small footprint of the sensors would not affect the operation of the vane or disrupt airflow. Advancements in sensor materials for use at high temperatures as well as the associated signal processing may allow for sensors to be installed in harsh environments. The difficulties of this method are in managing the impact of high temperatures on electronic components [82] and sensor operation, which requires appropriate material selection and signal processing techniques.

The following section considers the use of ultrasound for structural health monitoring applications, and the methods used to compensate for the effect of temperature. This is followed by an overview of the range of measurement devices available for the generation and acquisition of guided waves, and the piezoelectric materials suitable for use at high temperatures. Section 3.2 considers the current implementations of acoustic sensors for temperature monitoring applications, for both bulk acoustic waves and guided waves. The following sections discuss in detail the propagation of guided (Lamb) waves, which includes: dispersion curve generation and analysis, the effect of temperature on their propagation, mode selection considerations, and the importance of selecting an appropriate excitation signal. The chapter is concluded by discussing the suitability of acoustic methods for the temperature monitoring of nozzle guide vanes.

3.1 Ultrasonic structural health monitoring

Ultrasound is of particular interest for SHM applications as it allows for small sensors, high precision, fast data rates, and can be utilised at frequencies much higher than inherent background vibration and noise [83]. Traditional ultrasonic NDE utilises A-scans, a measurement of signal amplitude against time, to detect cracks, defects etc. This can be extended to B [84], C [85, 86], or phased-array [87] scans to build an image of damage in an area by moving the transducers around and carrying out multiple measurements. This form of evaluation is not particularly suited to turbomachinery applications as the transducers would ideally be permanently installed on the structure. Guided wave SHM is of more interest as constructive interference with surfaces/boundaries allows waves to travel large distances with limited attenuation, which is already utilised for pipe [88] and rail inspection methods [89]. Guided waves have been proposed as a method of defect detection NDE for aircraft [90], installing transducers in large arrays to allow for guided wave tomography.

When using acoustic waves for SHM and NDE applications either a standalone sensor can be placed in an area of interest, or the structure of interest can directly be used as the sensing medium. In the context of high temperature turbomachinery it would be advantageous to avoid placing sensors into the gas path as they are difficult to interrogate and have the potential to affect operation of the engine components. The structure of turbine blades and NGVs can be used as the sensing medium assuming that an appropriate system of transducers can be implemented. When considering using a structure as a sensing medium its geometry has an impact on wave propagation. The geometry of a typical turbine blade or NGV is that of a thin plate like structure through which ultrasonic guided waves will propagate. Rayleigh waves (otherwise known as "Surface Acoustic Waves" (SAWs)) can be excited at high frequencies (at wavelengths much smaller than material thickness) and are confined to the surface of a material, while Lamb waves (otherwise known as "Guided Waves") will propagate if excited at frequencies with wavelengths in the order of material thickness, as they interact with both the upper and lower boundaries of a material. Although Rayleigh waves are non-dispersive they produce large surface motions that are highly sensitive to any discontinuities or defects and are highly affected by surface coatings such as TBCs [91]. Lamb waves will propagate through the multi-layered structure of substrate-bonding layer-TBC, where the through-thickness temperature gradient will affect wave propagation, rather than only the temperature at the surface of the TBC. The interaction between both boundaries of a material means that Lamb waves can be excited from the internal surface of an NGV, outside of the gas path. This reduces the influence of the sensor on turbine operation, and reduces the effect of temperature on sensor operation.

3.1.1 Temperature compensation techniques

In many applications of Lamb wave SHM/NDE the effect of temperature on wave propagation is an undesirable factor that is compensated for using various signal processing techniques. These methods attempt to eliminate the influence of temperature in order to isolate the variable of interest i.e. defects. Temperature compensation or calibration can be carried out by using thermocouples [92], but this is not ideal for the cases where the external use of a sensor is prohibited. Temperature compensation techniques, such as baseline signal stretch (BSS) [93, 94], optimal baseline selection (OBS) [95], hybrid combination of BSS and OBS [96, 97], combination of OBS and adaptive filter algorithm [98], Time of flight (t_F) calibration based on a linear relationship between t_F and temperature [99], Hilbert transform and the orthogonal matching pursuit algorithm [100], and temperature compensation for both velocity and phase changes [101, 102] have been proposed to reduce residuals between the baseline signal and the current signal. The BSS method only targets the wave velocity change, neglecting the change in phase and amplitude of the signal. The BSS method is restricted for small temperature variations. The OBS method can accommodate larger temperature variations, however it requires many baseline signals that have sufficiently low post-subtraction noise levels at different temperatures. Therefore, a combination of BSS and OBS can achieve temperature compensation with a low number of baselines. A new method introduced by Mariani *et al.* [101] considers amplitude and phase changes as well as wave speed changes. It is shown that the residual between the baseline signal and current signals roughly halved when the two signals were acquired at temperatures 15°C apart. Since this method has not been used for measuring temperature, the sensitivity of the technique has not been analysed. Joel Harley *et al.* have demonstrated the use of Mellin transform techniques for identifying damage under variable environmental conditions, with detection accuracy higher than that of Fourier analysis methods [103].

The following sections focus on the use of Lamb/guided waves for temperature monitoring.

3.1.2 Measurement devices for the generation and acquisition of guided waves

The choice of transducer for the generation and acquisition of guided waves is limited by a number of factors including: elevated temperatures, space, and power consumption. When transmitting a wave through the structure of a material transducers can either be operated in pulse-echo mode or in a pitch-catch configuration. Pulse-echo mode operates with a single transducer acting as both transmitter and receiver, where the signal reflected from features such as defects or boundaries are analysed. Pitch-catch configurations operate with multiple transducers, some acting as transmitters and some as receivers. Response times are faster in pitch-catch configurations as waves travel directly between transducers rather than requiring a reflection to operate. Systems designed to map defects or damage (tomography) operate in pitch-catch configurations, usually with multiple pairs of transmitters/receivers to allow for higher spatial accuracy. For rotating turbine blades a transducer could be implemented in a pulse-echo configuration, if a transducer could not be housed at the rotating tip of the blade. Transducers could be operated in a pitch-catch configuration on NGVs as transducers could be placed on either side of the static vane.

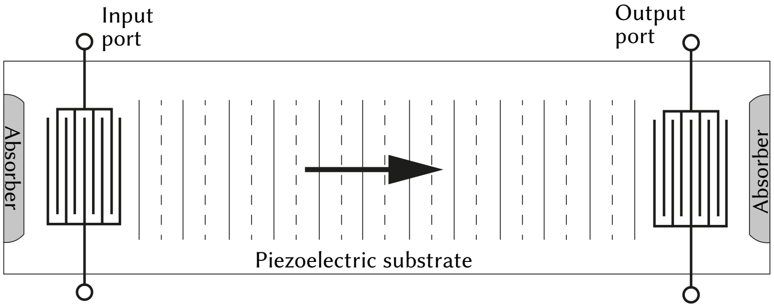

Figure 3.1 – A SAW delay line. Used with the permission of Ida [104], permission conveyed through Copyright Clearance Center, Inc.

Piezoelectric transducers are amongst the most common methods of generating and acquiring acoustic waves. They can be utilised in a number of different ways for either dedicated sensors or for transmitting a wave through a particular structure of interest. Many dedicated sensors are based on the use of interdigital transducers (IDTs) operated as either delay lines or resonators, and are often referred to as surface acoustic wave (SAW) devices. These sensors can be used for high temperature sensing and can be interrogated wirelessly [105, 106], however they would be difficult to implement on the structure of a turbine blade or NGV, while only providing a single point measurement.

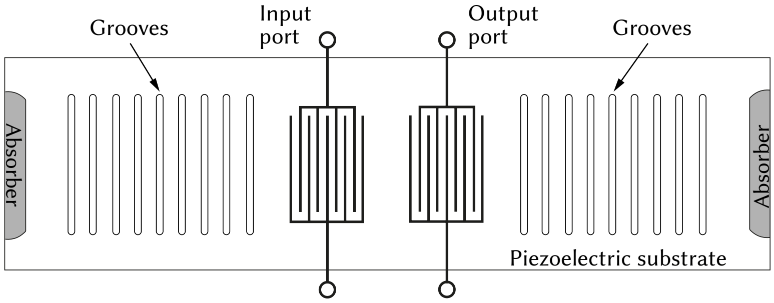

Figure 3.2 – A SAW resonator. Used with the permission of Ida [104], permission conveyed through Copyright Clearance Center, Inc.

In order to transmit a wave through a structure using piezoelectric materials there are a number of sensor options. All of these sensors are reliant on an effective bond between transducer and substrate, which is often difficult to a achieve at high temperatures.

Wedges (Figure 3.3) can be used to generate guided waves based on Snell's law [107], where a longitudinal wave produced by a piezoelectric transducer is transmitted through an angled wedge (typically made from a material with a slow longitudinal wave speed relative to the substrate, such as acrylic) into a substrate material where wave refraction takes place. Transmission of shear or surface acoustic waves are dependent on the material properties of the wedge and the substrate, and the wedge angle. A large benefit of this method is the ability to excite single Lamb wave modes in one direction [108]. Unfortunately a liquid couplant is required to form an effective bond between wedge and substrate, and there are a very limited number of materials with a longitudinal wave velocity slower than that of the superalloys used for NGVs, which makes the permanent installation of these sensors at high temperatures unlikely.

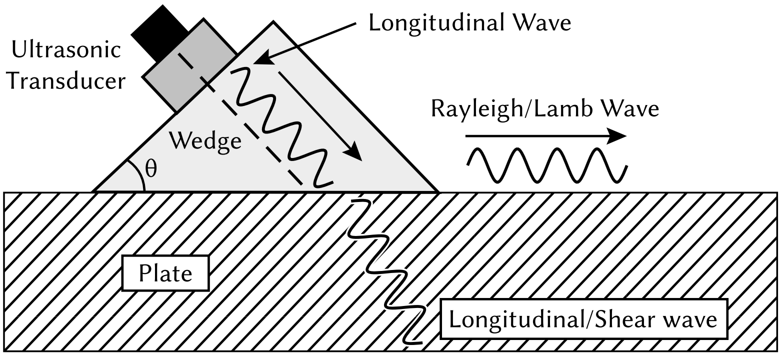

Figure 3.3 – A typical wedge transducer. Used with the permission of Ida [104], permission conveyed through Copyright Clearance Center, Inc.

Piezoelectric Wafer Active Sensors (PWAS) are being used extensively for SHM applications and have been shown to withstand exposure to extreme environments [109]. They are non-resonant wide-band devices [110] however they can be used for generation of single Lamb wave modes with careful geometry selection [111]. PWAS are small, inexpensive, and minimally invasive [110], making them potentially suitable for installation on turbine blades and NGVs if a suitable bonding method and piezoelectric material can be found.

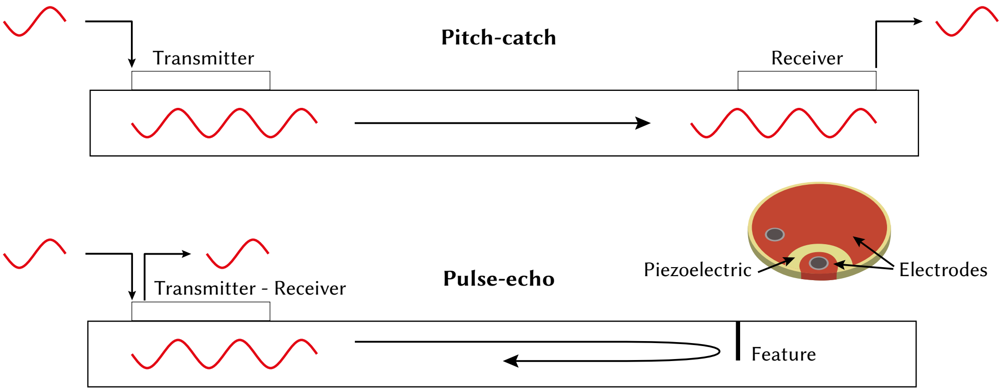

Figure 3.4 – PWAS sensors in pitch-catch and pulse-echo configurations.

One promising solution to the bonding problem is to use a waveguide to separate the transducer from the extreme environment of the turbine. This method is especially suited to guided waves as they are known to travel large distances with little attenuation, however the strong reflections from the boundaries of the material can cause scattering and mode conversion. Material discontinuities should also be considered [112]. One of the main challenges of this method is how to couple the waveguide to the structure of interest, as liquid couplants (as used for wedge coupling) are not suitable for use in high temperature environments, and simple welding is likely to introduce defects causing additional reflections and discontinuities to occur. It has been shown that clamping a waveguide to a structure can be effective even at relatively high temperatures (700°C) [113], although this method may not be suitable for installation on a turbine blade or NGV. A system of Hertzian contact points (Figure 3.5) may be more appropriate as only a small point would need to be in contact with the surface of interest. The contact size of the point determines the aperture size of the source, which can be considered as a point source up to very high frequencies, allowing for accurate measurement of absolute velocity [114]. This method of coupling has been used to measure the mechanical properties of carbon fibre reinforced plastics (CFRP) using measured phase velocities of the A_0 and S_0 Lamb wave modes [115]. Application force of the rods can be controlled with springs. An example of a welded waveguide system installed on a turbine vane is given by Willsch [116].

Other options for excitation/acquisition of acoustic waves include electromagnetic acoustic transducers (EMATs) [117] or lasers. Both of these methods could allow for contactless operation, however EMATs are quite inefficient, requiring large amounts of power to produce a signal of adequate amplitude. The use of lasers would require optical access to the surface of interest as well as the installation of a patch to protect the surface of the substrate from laser ablation [118].

Although the use of piezoelectric transducers is likely to be the most appropriate method of exciting acoustic waves for this application, temperature has an effect on their operation [119, 120]. The resonant frequency of a piezoelectric transducer reduces as temperature elevates [119] and if the

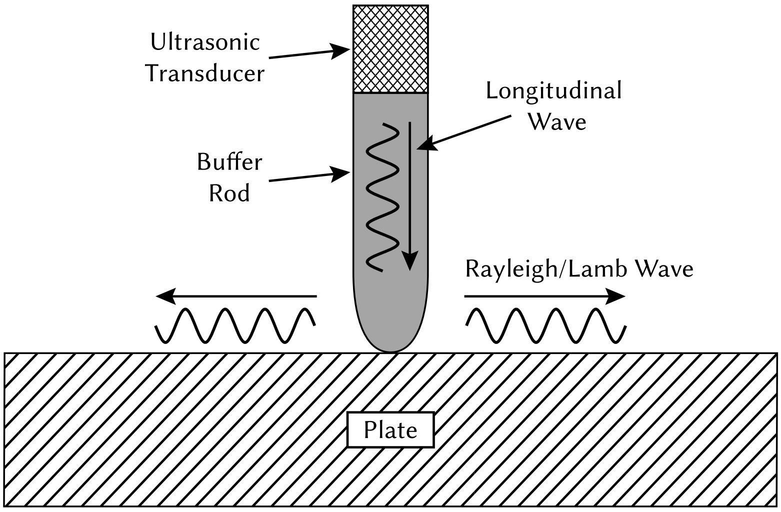

Figure 3.5 – An example Hertzian contact transducer.

transducer operates at the resonance ringing may be seen at some temperatures [101]. Filtering methods have been proposed to compensate for the transducer transfer function at different frequencies [121]. Temperature variations affect the bonding stiffness at the interface between the transducer and the structure. This results in frequency response changes which can affect both amplitude and the phase of the signal [122]. A common problem with all methods of excitation using piezoelectric materials is their reduction in sensitivity with increasing temperature, which makes the choice of piezoelectric material vitally important.

Figure 3.6 – Willsch's welded waveguide. Used with the permission of Willsch *et al.* [116], permission conveyed through Copyright Clearance Center, Inc.

3.1.3 Piezoelectric selection for high temperature sensing

Piezoelectric materials for high temperature sensors have been compared by a number of authors [123, 124, 125, 112, 119, 126, 127, 128]. Aluminium Nitride (AlN), Langasite (LGS), and Rare Earth Calcium Oxyborate Single Crystals (ReCOB), specifically Yttrium Calcium Oxyborate Single Crystals (YCOB), can be used for high temperature sensing with piezoelectrics [129]. YCOB has the highest operating temperature besides having a high resistivity at high temperatures. This signifies that YCOB will be able to operate at higher temperature as less heat is dissipated with a lower current. YCOB has relative small degradation in sensitivity with increasing temperatures of up to 1000°C, together with no significant phase change up to temperatures of 1500°C, which makes it ideal for high accuracy temperature measurements [130]. YCOB also has a linearly decreasing resistance with temperature, and a close to linearly decreasing resonance frequency with temperature, which can both be used for temperature measurement [131]. Aluminium Nitride (AlN) also exhibits a number of very promising properties necessary for high temperature sensing such as high electrical resistivity, temperature independence of electromechanical properties, and high thermal resistivity of the elastic, dielectric, and piezoelectric properties [132]. The use of an AlN sensor up to 800°C has been demonstrated for detection of laser generated Lamb waves in thin steel plates by Kim [133]. Unfortunately high-quality AlN single crystals are difficult to grow, showing a wide range of resistivity that greatly affects their suitability as ultrasound transducers [125].

3.2 Acoustic temperature sensing

Bulk acoustic waves such as longitudinal and shear waves have been used for temperature sensing for a number of years. Figure 3.7 shows displacement with respect to wave propagation direction for the three types of bulk acoustic waves in solids.

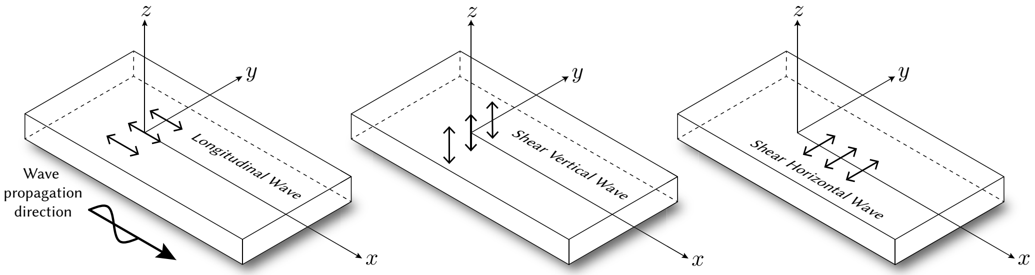

Figure 3.7 – Bulk acoustic waves in solids.

An overview of temperature sensing using acoustic waves is given by Lynnworth [134]. Davis *et al.* [135] experimented with an acoustic temperature sensor during variable frequency microwave curing of a polymer-coated silicon wafer. A sapphire buffer rod was used to separate the wafer from a Zinc Oxide (ZnO) transducer centred at approximately 600 MHz. Time of flight (t_F) was measured from the wafer/air interface reflection. Results were comparable to thermocouple measurements from 20°C to 300°C ± 2°C. Takahashi *et al.* [136] carried out 1D measurements of temperature distribution through a 30 mm thick steel plate in contact with molten aluminium (700°C). They noted that the system had a faster response time than the thermocouples used for validation of the method. Jia & Skliar [137, 138] have demonstrated a method for "UltraSound Measurements of Segmental Temperature Distribution" (US-MSTD) in solids, utilising reflections along the signal path to estimate temperature distribution. Three different methods of parametrizing the segmental temperature distribution are discussed. The system has been tested in an oxy-fuel combustor at temperatures up to 1100 degrees, with results comparable to thermocouple measurements [139]. Zhang and Cegla [140] have demonstrated a number of methods of 1D temperature monitoring through pipe walls, as well as a dual-wave (shear and longitudinal) system that is capable of simultaneously monitoring changes in thickness (from corrosion) and through-thickness temperature, which shows substantial improvements over single-wave systems [141]. Jeffrey *et al.* [142] demonstrates 2D spatial ultrasonic temperature measurement through a container of wax using 8 0.5 MHz transducers (4 transmitters, 4 receivers), with results comparable to thermocouple measurements. Balasubramaniam *et al.* [143] developed a temperature measurement system in which an externally cooled buffer rod was used to separate an ultrasound transducer from the hot material under test (molten glass). Changes in time of flight (t_F) with temperature were measured from reflections from a notch placed close to the solid-liquid boundary. A calibration procedure carried out from 25°C to 1200°C was used to compensate for the thermal gradients of the delay line, and results were compared against a thermocouple showing a greater than 2% precision. It was noted that the change in t_F due to temperature was greater than the change due to thermal expansion, leading to a non-linear relationship between temperature and time difference. Measurements were then carried out on molten glass with a resolution of 5°C (1 ns precision) using a 10 MHz transducer, however the author suggests resolution could be improved to 0.5°C with faster sampling. Ultrasonic oscillating temperature sensors (UOTSes) are another way to utilise ultrasound for temperature sensing whereby two transducers are setup to transmit through the material of interest in a feedback loop. A number of architectures are described by Hashmi *et al.* [144, 145], with sensitivities up to 280 Hz/K [146].

The uses of guided waves for temperature sensing purposes are limited. However, the fundamental antisymmetric Lamb wave mode, A_0, has been used for temperature monitoring of silicon wafers during rapid thermal processing [147]. Quartz pins are used as waveguides, connecting to the wafer through Hertzian contact points. Time of flight (t_F) was measured at a rate of 20 Hz from 100°C to 1000°C with an accuracy of ±5°C with this method. A laser excitation system has also been used to measure the temperature of silicon wafers during rapid thermal processing [148]. A broadband excitation pulse is used, and two different methods of signal processing are compared. A cross correlation method between a room temperature baseline signal and those at elevated temperatures, plus a matrix comparison method whereby an unknown signal is compared to a database of signals taken over the whole temperature range of interest. The matrix method was shown to require less signal averaging than the cross-correlation method, with an accuracy in the order of 1°C. The current implementations of acoustic temperature sensors demonstrate the potential of this method, but adapting these systems for use on turbine blades and NGVs will be challenging.

3.3 Lamb wave propagation

The geometry of turbine blades and nozzle guide vanes allows Lamb waves to propagate through their structure at ultrasound frequencies. Lamb waves are a type of elastic wave present in thin plates when wavelength is in the order of thickness. They are guided by the upper and lower boundaries of a material through a combination of longitudinal and shear vertical waves (see Figure 3.7) allowing for continuous wave propagation (Figure 3.8) [149]. The bulk acoustic waves discussed previously are non-dispersive, i.e their wave velocities are constant with frequency, whereas Lamb waves are dispersive and multi-modal which makes their analysis complex, especially when their are other factors such as changing temperatures are involved. The lowest order modes, the fundamental antisymmetric mode A_0, and the fundamental symmetric mode S_0 (Figure 3.9), are the most commonly used modes as they are relatively non-dispersive and comparatively easy to generate in comparison to the higher order modes (A_1, S_1, etc.). The anti-symmetric modes exhibit large out-of-plane motions that are more sensitive to surface features than the symmetric modes, which exhibit larger in-plane motion. When measured at the surface the A_0 mode normally propagates with a considerably higher amplitude than that of S_0, because of the comparatively larger out-of-plane motion.

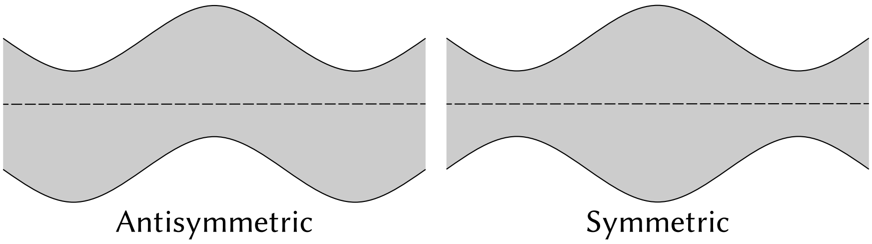

Figure 3.8 – Particle displacement of symmetric and antisymmetric Lamb wave modes in a plate.

Lower order Lamb waves are used extensively for NDE and SHM applications and an overview of their uses for damage identification is provided by Su [150]. Lamb waves have both phase and group velocities, the phase velocity relating to the speed at which the phase of any one frequency component of the wave travels, and the group velocity which describes the overall speed of energy transport through the propagating wave[1]. Phase velocity is generally higher than the group velocity. Time of flight (t_F) measurements of Lamb waves give the group velocity, while special phase comparison techniques are needed to measure the phase velocity [151].

To better understand the uses of Lamb waves their frequency spectrum can be split into three areas:

- Low frequency region – Contains the lowest two Lamb wave modes (A_0 & S_0). It is possible to selectively excite either mode as they have very different wave velocities, leading to large differences in excitation angle when using a wedge transducer for example.
- Mid-frequency region – Contains many dispersive modes with similar wave speeds making it difficult to excite specific modes without exciting others, leading the production of complex waveforms that are difficult to analyse.
- High frequency region – The modes become less dispersive and converge to similar wave speeds, leading to them travelling as a single packet. Group velocity can be measured for the packet. The A_0 & S_0 modes begin to act like a Rayleigh wave as their velocities converge.

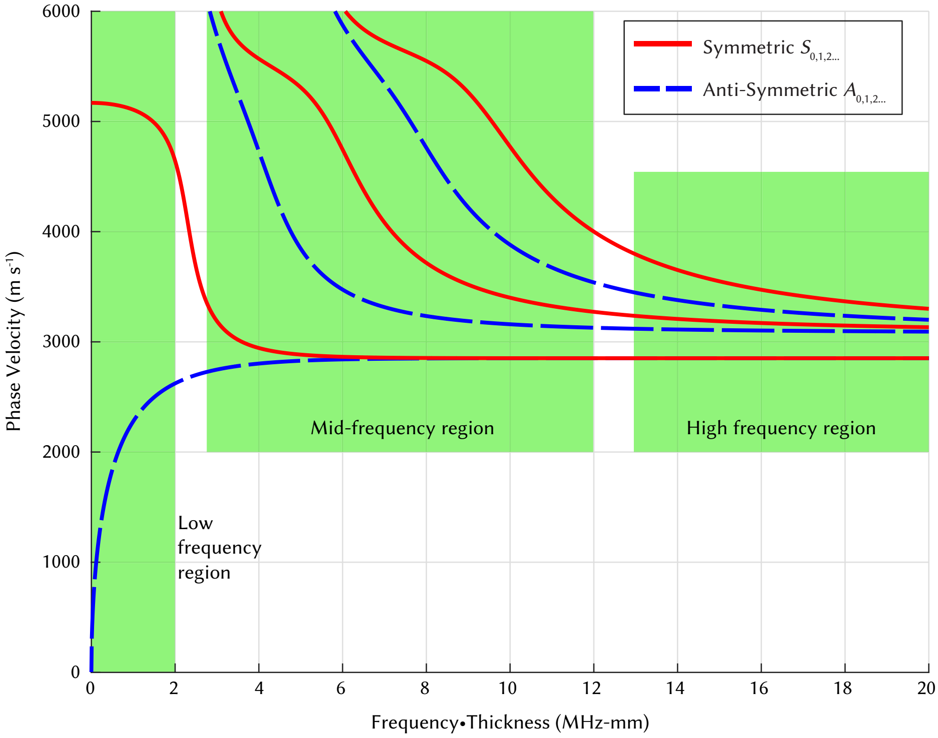

Figure 3.9 – Lamb wave phase velocity dispersion curves for Inconel 718.

Figure 3.9 shows phase velocity curves for the symmetric and anti-symmetric Lamb wave modes generated by The Dispersion Calculator [152] for the superalloy Inconel 718. Dispersion curves such as these can be be generated based on material properties allowing areas of interest to be identified.

---

[1] Group velocity is valid for isotropic, non-dissipative systems. Energy velocity applies when attenuation is present, otherwise it is equivalent to group velocity.

3.3.1 Generation of dispersion curves

The dispersion curves generated throughout this work have been produced using The Dispersion Calculator [152]. For isotropic media Rayleigh-Lamb equations are solved numerically to generate dispersion curves, based on the book by Rose [149]. The Rayleigh-Lamb frequency equations can be written as:

$$\frac{\tan(qh)}{\tan(ph)} = -\frac{4k^2pq}{(q^2-k^2)^2}, \tag{3.1}$$

for symmetric modes, and:

$$\frac{\tan(qh)}{\tan(ph)} = -\frac{q^2-k^2}{(4k^2pq)^2}, \tag{3.2}$$

for antisymmetric modes. Where p is given by:

$$p^2 = (\frac{\omega}{c_L}) - k^2, \tag{3.3}$$

and q is given by:

$$q^2 = (\frac{\omega}{c_T}) - k^2, \tag{3.4}$$

where c_L is bulk longitudinal velocity, c_T is bulk shear velocity, c_p is phase velocity, h is thickness, and ω is angular frequency. The angular wavenumber k is numerically equal to ω/c_p. The phase velocity is related to the wavelength by the simple relation $c_p = (\omega/2\pi)\lambda$. Once phase velocity is calculated stress, displacement, and group velocity can also be calculated. Group velocity is given by:

$$c_g = c_p^2\left[c_p - (fd)\frac{dc_p}{d(fd)}\right]^{-1}, \tag{3.5}$$

where fd denotes frequency thickness product. Note that, when the derivative of c_p with respect to fd becomes zero, $c_g = c_p$. Note also that, as the derivative of c_p with respect to fd approaches infinity (i.e., at cut-off), c_g approaches zero.

3.3.2 The effect of temperature on wave propagation

Changes in temperature affect material properties, namely Young's modulus, Poisson's ratio, and density. Changes in density are normally expressed as thermal expansion. The predicted changes in these properties with temperature with respect to wave velocity for aluminium are discussed at the beginning of Chapter 4. These changes result in shifts in dispersion curves, which can be used to predict the change in wave velocity with temperature. As an example of Lamb wave temperature dependence, Figure 3.10 shows the shift in group velocity dispersion curves for the superalloy Inconel 718 from 27°C to 1027°C. An increase in temperature causes a reduction in wave velocity (shifting down) and a reduction in frequency (shifting left). The temperature dependence at a particular frequency can also be calculated, which is useful when determining a suitable excitation frequency. Careful selection of excitation frequency can allow for high temperature sensitivity depending on the mode excited and the dispersiveness of the region. As an example Figure 3.11 shows the temperature dependence of the A_0 & S_0 modes at a frequency-thickness product of 1 MHz-mm. It should be noted that the anisotropy of Inconel based superalloys [153] is likely to have an impact on wave propagation, but for this study the material is considered to be isotropic.

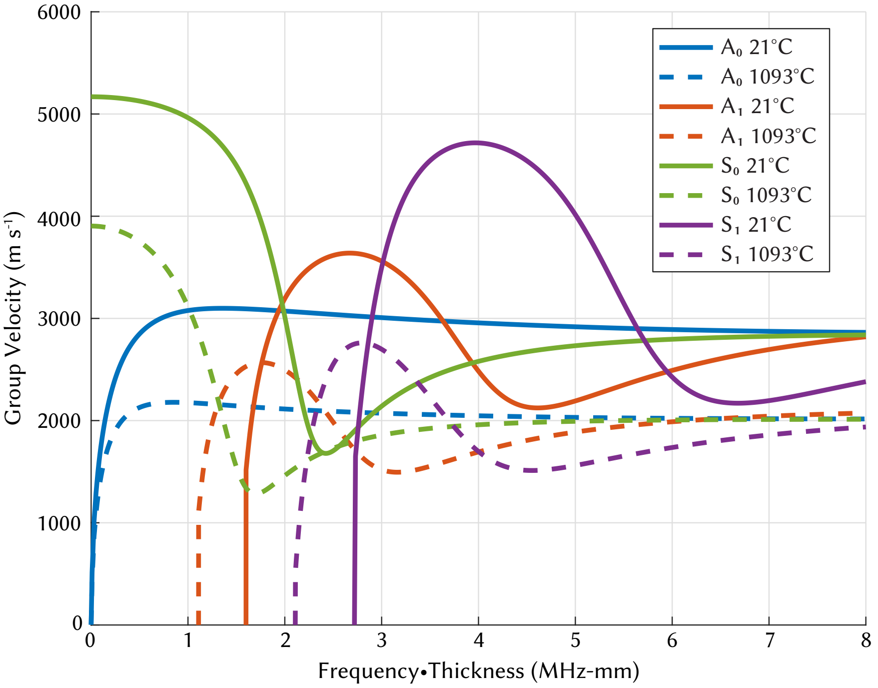

Figure 3.10 – A_0, S_0, A_1, and S_1 group velocity dispersion curve shift with temperature from 21°C to 1093°C for Inconel 718.

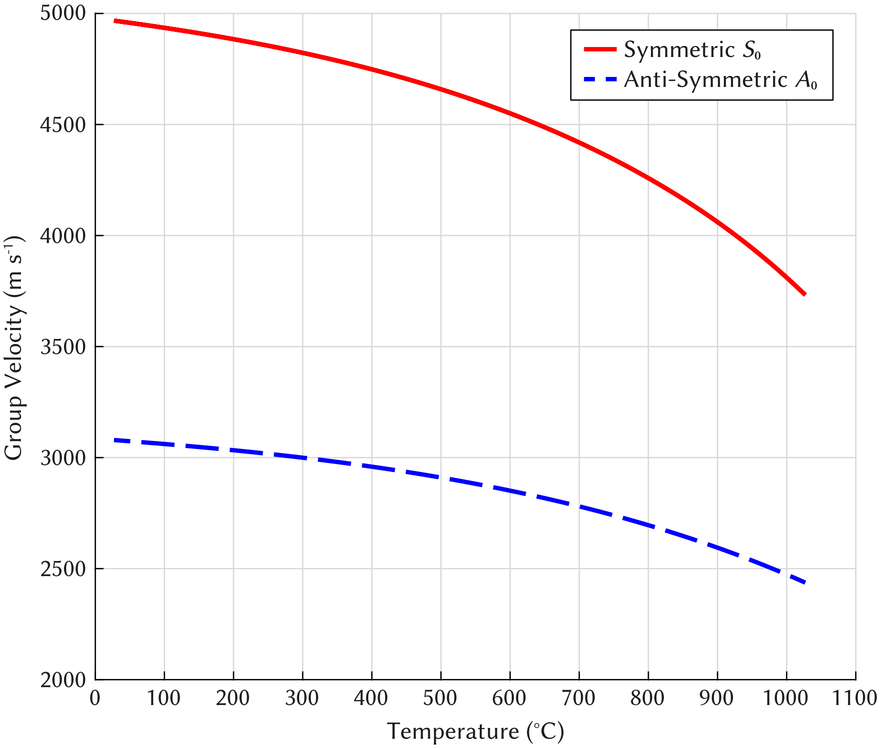

Figure 3.11 – A_0 & S_0 group velocity change with temperature from 27°C to 1027°C at 1 MHz for Inconel 718.

The change in wave velocity at this frequency-thickness product is non-linear because of two factors, a non-linear change in Young's modulus with increasing temperature, and the chosen frequency of 1 MHz falling into a more dispersive region as temperature increases, particularly for the S_0 mode. Average temperature sensitivity for the A_0 mode is $-0.898\ \mathrm{m\,s^{-1}\,°C^{-1}}$ and $-1.868\ \mathrm{m\,s^{-1}\,°C^{-1}}$ for the S_0 mode. It can be seen from Figure 3.10 that the A_0 mode has a relatively linear reduction in wave velocity with increasing temperature regardless of frequency, whereas the other modes have highly dispersive regions (steep slopes) that reduce in frequency (shift to the left) with increasing temperature. The high sensitivity to changes in temperature in these regions have great potential for temperature monitoring applications. Resolution is determined by the choice of time of flight (t_F) measurement method [154, 155]. If a sampling rate of 2.5 GHz is used on the example given above over a distance of 10 mm (rough distance to first line of cooling holes) a theoretical velocity resolution of $0.4\ \mathrm{m\,s^{-1}}$ for the S_0 mode and $0.2\ \mathrm{m\,s^{-1}}$ for the A_0 mode can be achieved at 1093°C, which would allow for a temperature resolution of <1°C at 1 MHz. This would require measurements of t_F at sub-wavelength resolution which, although challenging, can be achieved with cross-correlation methods [156, 157]. Linear interpolation of cross-correlation methods can be used to increase resolution without increasing sampling rate [158].

3.3.3 Mode selection considerations

The multi-modal nature of Lamb waves makes their analysis complex, however this can be simplified by targeting specific modes using careful selection of excitation frequency, to target a particular frequency-thickness product. This difficulty can be seen in Figure 3.12 where a large number of different modes combine to create a multi-modal wave packet. The varying wave speeds of each mode with frequency causes dispersion, which has an increasing effect the longer the waves propagate.

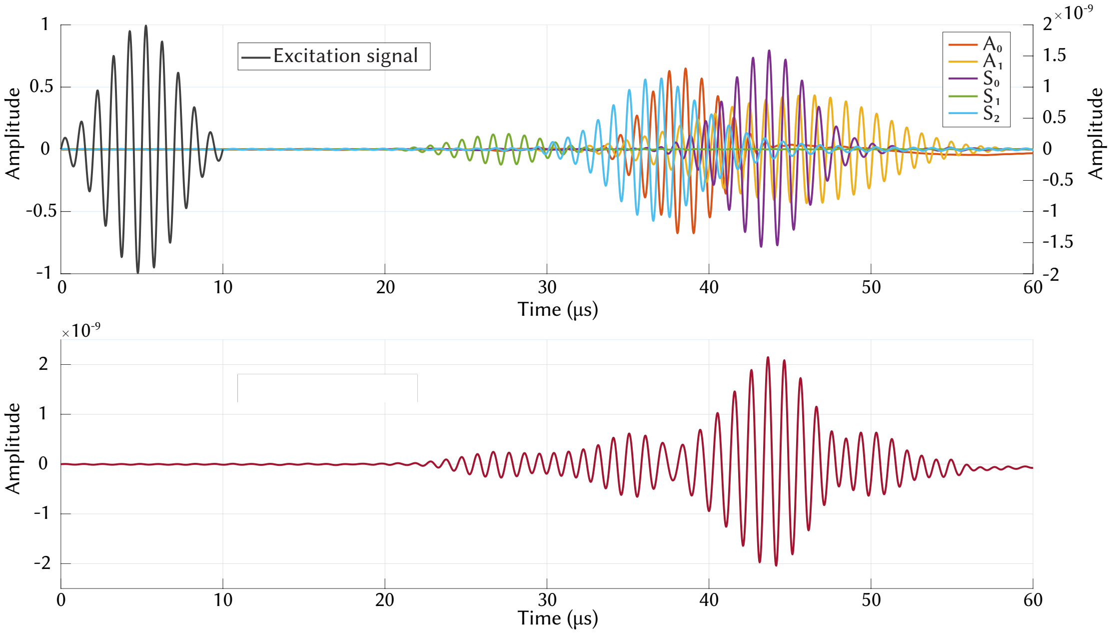

Figure 3.12 – An example of multi-modal wave packets. Simulated 100 mm wave propagation of 10–cycle Hamming windowed 1 MHz sine pulse in a 4 mm thick aluminium plate.

Below the cut-off frequency of the A_1 mode only the two fundamental modes (A_0 & S_0) are present. Their phase/group velocities are sufficiently different from one another that the modes can be distinguished between in the time domain, assuming a long enough propagation distance. The use of wedge transducers can further separate the modes, as the wedge angle required to excite them are largely different.

Although the non-dispersive nature of lower order modes (A_0 & S_0) makes them relatively easy to analyse, it would be advantageous to operate at higher frequencies as phase shifts are easier to detect when wavelengths are shorter, which leads to improved sensing resolution and accuracy. Above the cut-off frequency of the A_1 mode there are an increasing number of modes present. The relatively small difference in phase velocity between the higher order pairs (A_1 & S_1, A_2 & S_2, etc.) means that even with the use of wedge transducers it is not possible to selectively excite only one mode. The ability to differentiate between the modes is improved by targeting points of group velocity minima/maxima, where the modes are travelling with the largest differences in velocity, which helps to separate them in the time domain. As the wave speeds of the A_0 & S_0 modes converge (around 10 MHz-mm for Inconel 718) they behave as a Rayleigh wave, where the majority of particle motion takes place at the surface of the material.

Higher order modes such as A_1 & S_1 are more difficult to selectively excite as their phase/group velocities are similar, which leads to the formation of complex waveforms that are highly dispersive. However, as frequency-thickness product is increased further the excitability of higher order modes reduces significantly, which can allow less dispersive regions of lower order modes to be excited [159] (see high frequency region of figure 3.9). Wilcox [160] has presented a method of reducing the effect of dispersion on a transmitted signal if prior knowledge of dispersion curves are known. This relaxes the need to excite only a single mode and simplifies the analysis process. In the case of turbine blades and NGVs, the propagation distance is relatively short so the effect of dispersion is likely to be low, however a change in temperature will cause different regions of dispersion curves to be excited which will change the shape of a transmitted wave packet.

Jayaraman *et al.* [161] have presented the existence of “Higher Order Mode Cluster Guided Waves” (HOMC-GW), a non-dispersive region found at high frequency-thickness products in which the various modes all have similar group velocities. This causes them to move as a single envelope, which can be treated like a single non-dispersive mode. A number of aspects of HOMCs have been investigated including: their use for pipe inspections [162, 163, 164], their interaction with weld pads [165], and their interaction with notch-like defects in plates [166]. Khalili & Cawley [108] carried out an investigation into exciting singular higher order modes which found that the HOMC described by Jayaraman was likely to be single mode dominating a cluster (A_1 around 20 MHz-mm). The use of higher order modes for temperature sensing applications is explored in the following chapters.

3.4 Excitation signal

The choice of excitation signal is an important aspect of ultrasonic sensing. Figure 3.13 shows a comparison between 1 MHz pulse excitation signals with-and-without a Hamming window applied, as well as using a varying number of cycles. Applying a Hamming window to the excitation signal dramatically reduces the amplitude of sidelobes, while also producing a central peak to the pulse that can be identified in time-of-flight measurement. Varying the number of cycles in the pulse changes both amplitude and bandwidth. Using a three cycle pulse produces a signal with a comparatively wide bandwidth (0.4–1.6 MHz) and low amplitude, however the shorter signal helps in identifying the pulse in the time domain. Increasing the number of cycles to five produces a pulse with a bandwidth of 0.6–1.4 MHz, and adequate signal amplitude. Further increasing the number of cycles results in bandwidths comparable with the original signal, and nine cycles produces almost the same amplitude, however the length of the signals in the time domain begins to complicate time-of-flight measurement. In regions where reflections are expected (from cooling holes, for example) longer wave packets inhibit the ability to differentiate between them, and more interference occurs.

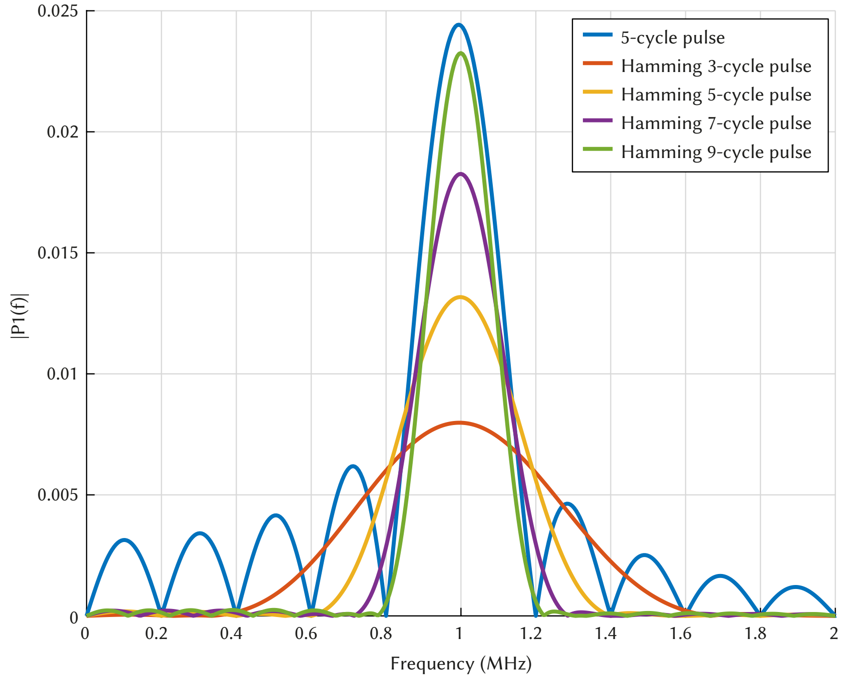

Figure 3.13 – FFT comparison of excitation signal with varying number of cycles.

Figure 3.14 shows the five cycle Hamming windowed pulse used throughout the majority of both the experimental and simulated studies in this thesis, while Equation (3.6) shows the function used to generate it. The number of cycles can easily be adjusted for different scenarios.

$$\begin{aligned}\text{Hamming windowed 5-cycle pulse} &= 0.54t\sin(2\pi f_0 t) - 0.46\cos\left(\frac{2\pi t}{t_0 np}\right) \text{ for } 0 \le t \le \left(\frac{np}{f_0}\right) \\ &= 0 \quad t > \left(\frac{np}{f_0}\right)\end{aligned} \tag{3.6}$$

where f_0 is 1 MHz, the number of cycles (np) is 5, t_0 is equal to $1/f_0$, and t is equal to zero to $np \times t_0$ in increments of $1/fs$.

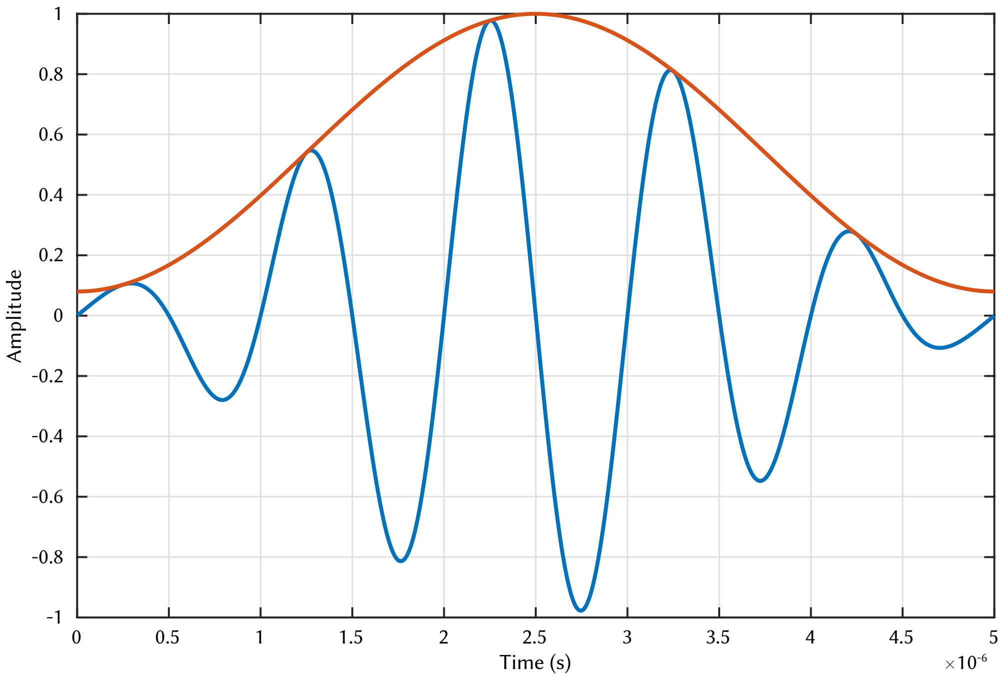

Figure 3.14 – Hamming windowed 5–cycle pulse.

3.4.1 Two-sided excitation

Two-sided excitation can be used to preferentially excite either the symmetric or anti-symmetric modes, by controlling the phase of the excitation signals. Figure 3.16 shows a comparison between preferential excitation of either the A_0 or S_0 mode using a COMSOL simulation. A 5-cycle 1 MHz Hamming windowed pulse is used to excite a 1 mm thick Aluminium plate. Two PZT discs, one placed on either side of the plate, are used for excitation, while another is used as a receiver at a distance of 100 mm. In-phase excitation preferentially excites the anti-symmetric modes, whereas applying one signal 180° out of phase excites the symmetric modes. Below the cut-off frequency of A_1 this results in single-mode excitation.

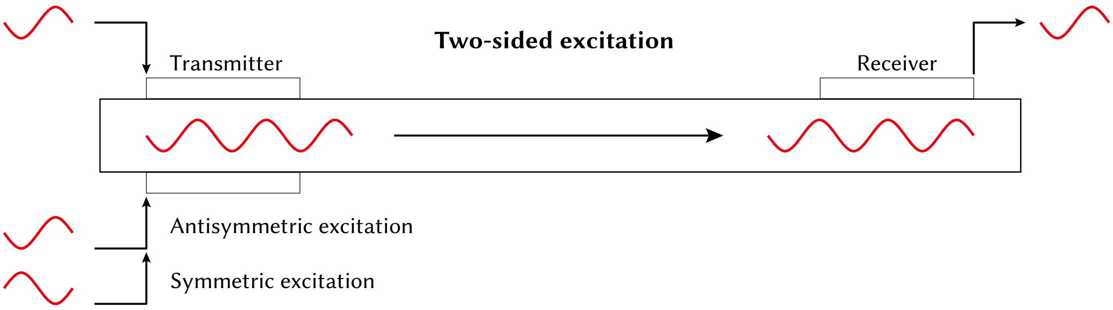

Figure 3.15 – Diagram of two-sided excitation COMSOL model.

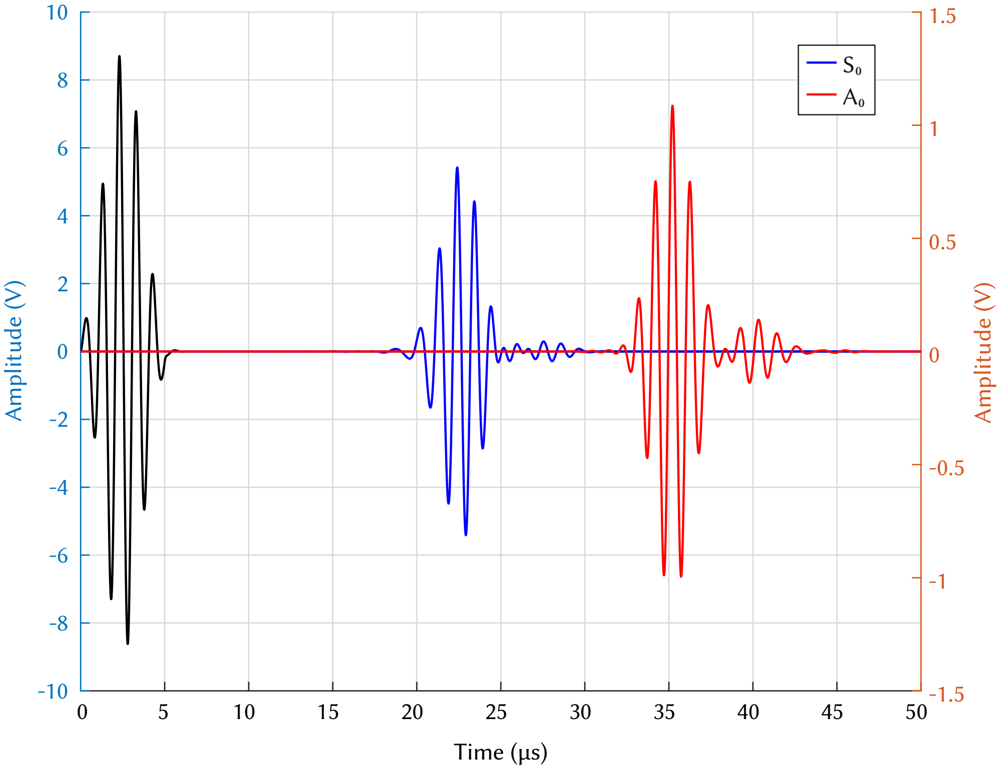

Figure 3.16 – Comparison of wave propagation for two-sided excitation methods. The symmetric modes (blue) are excited through in-phase operation, or the antisymmetric modes (red) are excited through out-of-phase operation.

3.5 Concluding remarks

A guided wave based temperature monitoring system offers a number of potential advantages over the currently available temperature monitoring methods for NGVs, such as low power operation, a small footprint, and limited need for maintenance. There are a number of options available for the generation and acquisition of guided waves, however the options become more limited when high temperatures and limited space/power constraints are considered. Wedge transducers can be used to target single wave modes and investigate their properties, but cannot be used in permanent installations. Piezoelectric transducers coupled into the structure through waveguides has been identified as a potential option, which would allow sensors to be distanced from the gas path. There are a range of piezoelectric materials suitable for operation at high temperatures, most notably YCOB and AlN. Two-sided excitation would be an effective method of reducing the number of propagating modes, reducing the complexity of signal processing required to track changes in time of flight for a single mode.

Bulk acoustic waves are used for a wide range of SHM applications, including temperature sensing, however because of the geometry of nozzle guide vanes, guided waves will propagate at ultrasound frequencies. Guided waves are also utilised for SHM applications because of their ability to travel large distances with limited attenuation, however their complex multi-modal propagation makes signal analysis difficult without careful consideration of excitation frequency and prior knowledge of dispersion curves. A number of authors have investigated the temperature dependence of Lamb waves [167, 168, 93, 169, 170] however their studies are limited to relatively low temperatures and the lowest order fundamental Lamb wave modes (A_0 & S_0). The following studies will consider the effect of higher temperatures on wave propagation, as well as the use of higher order modes. To achieve temperature resolutions and response times comparable with traditional sensors, the wavelength should be short to produce wave packets with clearly defined envelope peaks, which aides in time of flight measurement. This highlights the potential of operating at higher frequencies using higher order modes.

The following chapters will consider the impact of temperature, cooling holes, and surface coatings on wave propagation through a combination of prediction, experimentation and simulation. The results of these studies will show how the geometry of NGVs affects wave propagation, and be used to determine the most suitable mode/frequency range for temperature sensing. Future research will be necessary to develop a suitable sensor configuration, which can be informed by the outcome of this research.

3.6 Other applications

A guided wave based temperature monitoring system has potential for other applications. Batteries and battery packs are often arranged as thin cells, where the temperature of the cell gives an indication of cell health. A guided wave based system could allow the monitoring of the cross-sectional temperature of a cell with the use of small piezoelectric sensors, giving an advantage over point-based systems such as thermocouples. Ultrasonic methods are already used for the condition monitoring of batteries, such as in the monitoring of dendrite formation in aqueous zinc ion batteries [171], or for characterising the thickness and state of charge of the layers within lithium-ion batteries [172].

Printed circuit boards (PCBs) are another interesting application, where the current monitoring methods rely on introducing additional components to the board [173, 174], which takes up limited space, and generally only measures ambient temperature rather than that of the components themselves. Thermal cameras are often used in the design stage [175, 176], but aren't suitable for this application due to the z-axis space required to cover the whole board, and they aren't applicable when multiple boards are stacked together. A guided wave based system could allow small unobtrusive sensors to be placed at the edges of PCBs, and track temperature changes of individual components with fast response times and high temperature resolution. Active monitoring can be used to identify abnormalities that are indicative of a developing fault, which is particularly important for safety critical applications [177]. The electrification of the automotive and aerospace industries will require technology such as this in the future, as the data can be fed into integrated health management systems which will improve the reliability of the vehicle, reduce the number of inspections, and in turn reduce costs [178]. The technology can also have an impact on sustainability, as individual components can be replaced rather than whole board, and the lifetime of boards can be extended [179].

CHAPTER 4

Temperature sensitivity of guided waves

In this chapter the temperature sensitivity of guided waves is investigated through prediction, experimentation, and simulation. Aluminium was chosen as a test material, as it is readily available for experimentation purposes, and temperature dependant material properties for the particular grade of Aluminium (H14 1050) can be found in literature. Individual modes were isolated through the use of variable angle wedges, to allow each mode to be investigated separately.

The changes in material properties of aluminium with respect to temperature are discussed in the next section. The change in density, thermal expansion, and Poisson's ratio is negligible over the temperature of interest in this study (20°C–100°C) in comparison to the change in Young's modulus.

4.1 The effect of temperature on material properties

4.1.1 Density

The density, ρ, of a material decreases with increasing temperature. For Aluminium 1050, density decreases from 2700.10 $\mathrm{kg\,m^{-3}}$ at 20°C to 2680.86 $\mathrm{kg\,m^{-3}}$ at 100°C, as described by the equation:

$$\begin{aligned}\rho(T) = 2736.893 - 0.006011681{\times}T^1 - 0.0007012444{\times}T^2 + 0.0000013582{\times}T^3\\ -0.000000001367828{\times}T^4 + 0.0000000000005177991{\times}T^5,\end{aligned} \tag{4.1}$$

where T is temperature in Kelvin, the equation is valid from 130 K to 933 K [180, 181, 182].

Considering only a change in density, the increase in temperature from 20°C to 100°C will cause an increase in group velocity of 21.57 $\mathrm{m\,s^{-1}}$ for the S_0 mode (1 MHz-mm), 11.63 $\mathrm{m\,s^{-1}}$ for the A_1 mode (2.5 MHz-mm), and 17.52 $\mathrm{m\,s^{-1}}$ for the S_1 mode (4 MHz-mm).

4.1.2 Thermal expansion

Thermal expansion, the change in density for a change in temperature, causes a change in material dimensions which will affects wave speed, although the effect is small. The coefficient of thermal expansion, α, for Aluminium 1050 at 20°C is 2.3×10^{-5}, rising to 2.5×10^{-5} at 100°C, as described by the equation:

$$\alpha(T) = 1.243109\times10^{-5} + 5.050772\times10^{-8} \times T^1 - 5.806556\times10^{-11} \times T^2 + 3.014305\times10^{-14} \times T^3, \tag{4.2}$$

where T is temperature in Kelvin, the equation is valid from 230 K to 900 K [180, 181, 182].

The change in time of flight due to thermal expansion can be expressed using the equation [93]:

$$\delta t = \frac{d}{v}\left(\alpha - \frac{k}{v}\right)\delta T, \tag{4.3}$$

where d is the propagation distance (0.1 m), v is the group velocity, and k is the temperature sensitivity of group velocity, $\delta v/\delta T = k$. The group velocity can then be recalculated with the effect of thermal expansion included. The average change in velocity due to thermal expansion over the temperature range of interest (20°C–100°C) is -1.59 $\mathrm{m\,s^{-1}}$ for the S_0 mode (1 MHz-mm), -0.89 $\mathrm{m\,s^{-1}}$ for the A_1 mode (2.5 MHz-mm), and -1.47 $\mathrm{m\,s^{-1}}$ for the S_1 mode (4 MHz-mm). The change is sufficiently small that thermal expansion can be excluded from the COMSOL models used in the following chapters.

4.1.3 Poisson's ratio

The Poisson's ratio, ν, for Aluminium 1050 at 20°C is 0.3310, rising to 0.3325 at 100°C, as described by the equation [183]:

$$\begin{aligned}\nu(T) = 0.3238668 + 3.754548\times10^{-6} \times T^1 + 2.213647\times10^{-7} \times T^2 - 6.565023\times10^{-10} \\ \times T^3 + 4.21277\times10^{-13} \times T^4 + 3.170505\times10^{-16} \times T^5,\end{aligned} \tag{4.4}$$

where T is temperature in Kelvin, the equation is valid from 0 K to 773 K.

This is equivalent to a velocity change of 0.33 $\mathrm{m\,s^{-1}}$ for the S_0 mode at 100°C assuming no change to density or Young's modulus.

4.1.4 Young's modulus

The change in Young's modulus with temperature in Aluminium is represented by the Equation [184, 185, 186, 187]:

$$E(T) = 7.770329\times10^{10} + 2036488.0 \times T^1 - 189160.7 \times T^2 + 425.2931 \times T^3 - 0.3545736 \times T^4, \tag{4.5}$$

where T is temperature in Kelvin, and E is Young's modulus in Pascals.

This represents the largest change in wave velocity with respect to the other material properties. The S_0 mode at 1 MHz reduces in velocity by ~150 $\mathrm{m\,s^{-1}}$ over the temperature range 20°C–100°C.

4.2 Prediction study (Aluminium)

The temperature dependant dispersion curves and through thickness displacement profiles in this section were generated using The Dispersion Calculator [152]. The change in density (thermal expansion) and Poisson's ratio is ignored for this study, as the temperature range (20–100 °C) is small. The change in Young's modulus with temperature is described by Equation (4.5).

Temperature dependant dispersion curves for aluminium 1050 H14 are shown in Figure 4.1a. The angles of excitation required to excite the S_0, A_1, and S_1 modes are shown based on targeting the frequency-thickness products of 1 MHz-mm (28°), 2.5 MHz-mm (21°), and 4 MHz-mm (25°) respectively. These frequency-thickness products correspond closely to group velocity maxima for each of the targeted modes, which is advantageous for separating the modes in the time domain [188].

The group velocity of the S_0, A_1, and S_1 modes was extracted from the curves at frequency-thickness products of 1 MHz-mm, 2.5 MHz-mm, and 4 MHz-mm respectively. The extracted group velocities are shown in Figure 4.1b. The temperature sensitivities of the modes were calculated at 1°C increments over the temperature range 10–110°C. The sensitivity of the S_0 mode is 1.45–1.52 $\mathrm{m\,s^{-1}\,°C^{-1}}$, 0.77–0.87 $\mathrm{m\,s^{-1}\,°C^{-1}}$ for the A_1 mode, and 1.37–1.45 $\mathrm{m\,s^{-1}\,°C^{-1}}$ for the S_1 mode (see Equation 4.11). These values are frequency and mode dependent. The temperature sensitivities increase with temperature, as the modes reduces in frequency (shift left), and reduces in wave velocity (shift down). For reference, the sensitivity of the bulk longitudinal velocity is 1.40 $\mathrm{m\,s^{-1}\,°C^{-1}}$, while the sensitivity of the bulk shear velocity is 0.67 $\mathrm{m\,s^{-1}\,°C^{-1}}$.

Through thickness displacement profiles at 20°C for each of the modes targeted are shown in Figure 4.2. Over the small temperature range of this study the shape of the modes do not change dramatically with temperature. The S_0 mode (Figure 4.2a) shows comparatively larger in-plane motion than the other modes. Although the antisymmetric modes are associated with out-of-plane motion, the area of the spectrum targeted in this study exhibits larger in-plane motion (Figure 4.2b). The S_1 mode shows a similar amount of displacement to the A_1 mode (Figure 4.2c).

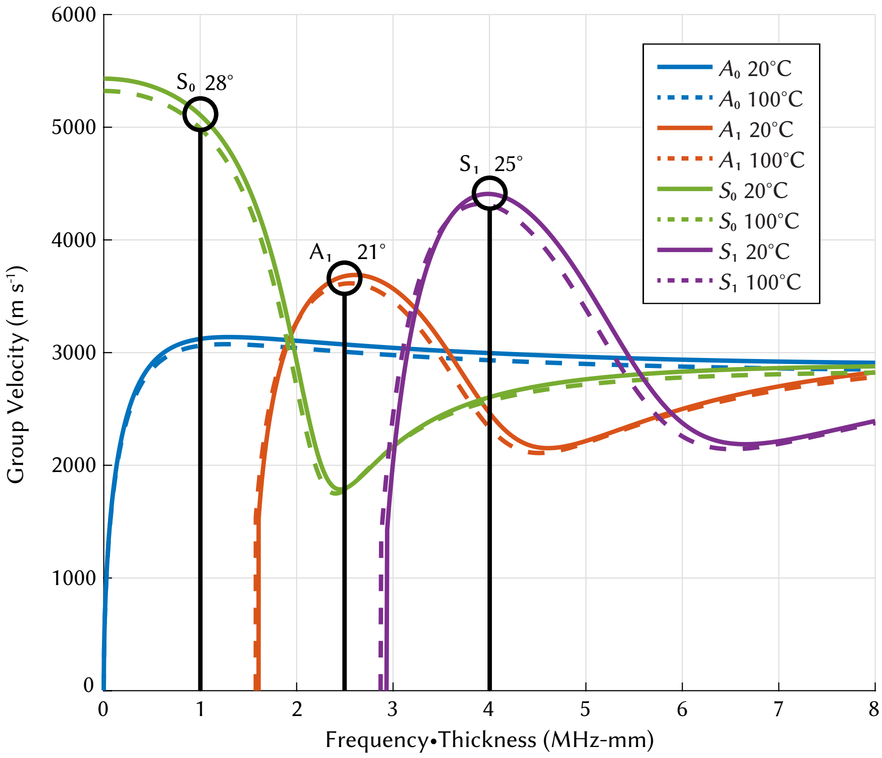

(a) A_0, S_0, A_1, and S_1 group velocity dispersion curve shift with temperature from 20°C to 100°C for Aluminium 1050 H14.

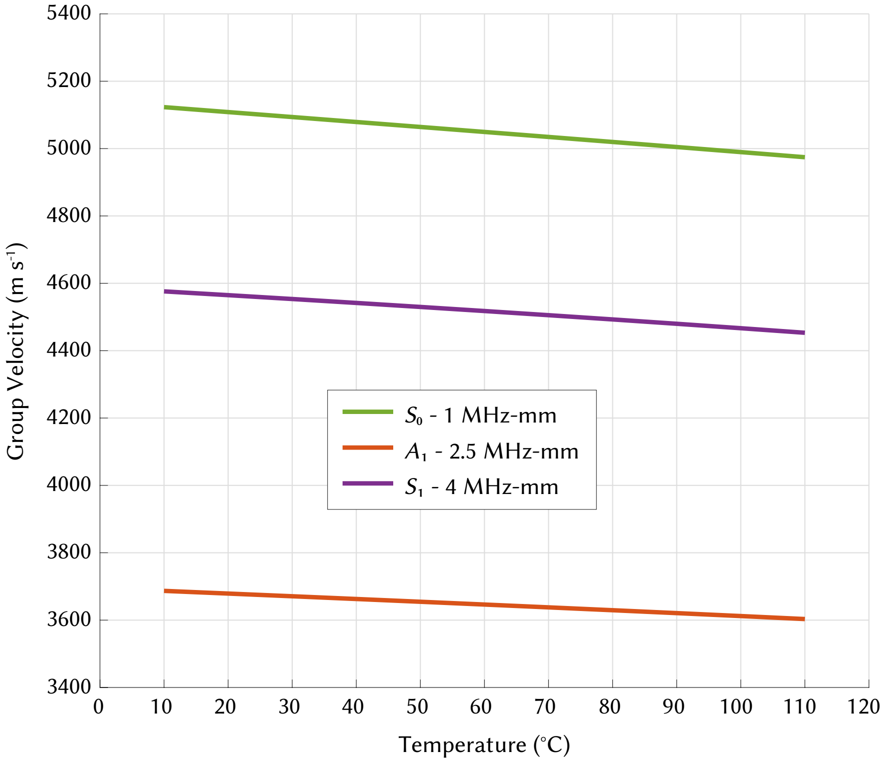

(b) S_0, A_1, and S_1 group velocity change with temperature from 10°C to 110°C for Aluminium 1050 H14. Calculated in 1°C increments.

Figure 4.1 – The effect of temperature on Lamb wave propagation for Aluminium 1050 H14.

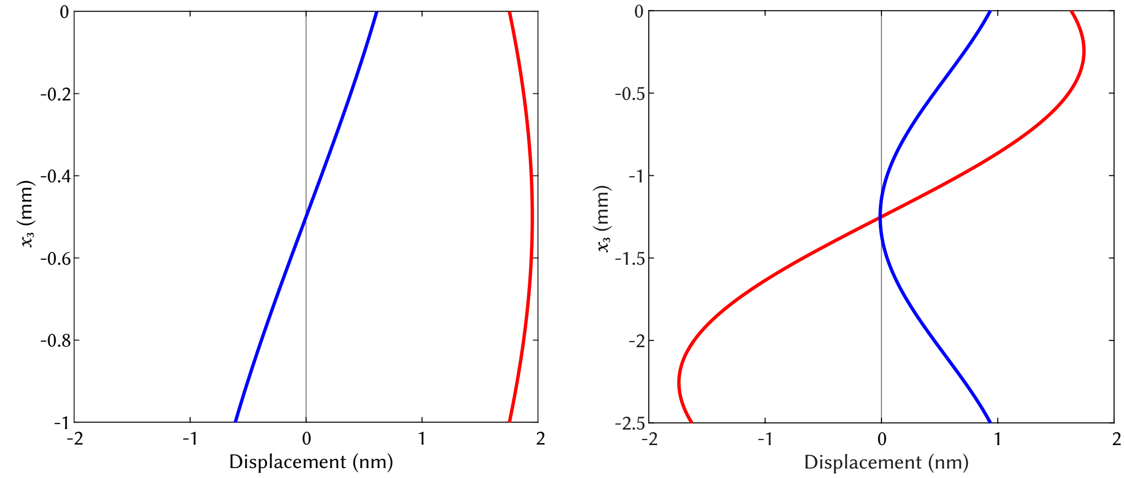

(a) S_0 Displacement.

(b) A_1 Displacement.

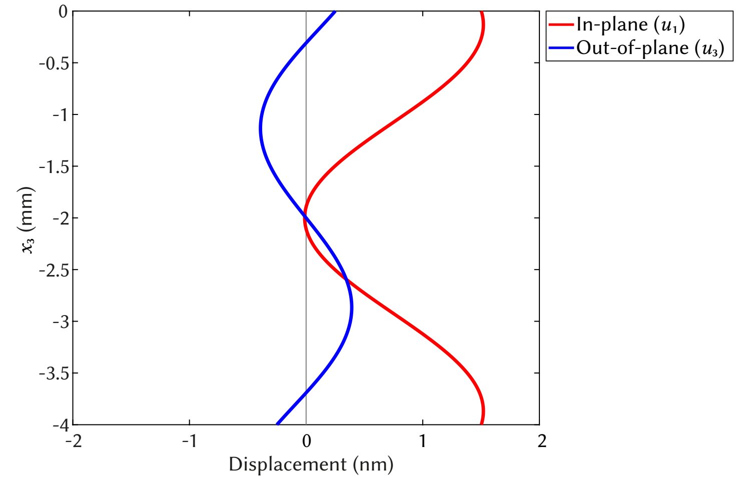

(c) S_1 Displacement.

Figure 4.2 – Through thickness displacement profiles for Aluminium 1050 H14 at 20°C.

4.3 Experimental study (Aluminium)

The group velocity temperature sensitivity of the S_0, A_1, and S_1 Lamb wave modes were experimentally measured, and validated against values extracted from dispersion curves.

Time of flight through a plate is has been measured, and group velocity calculated from the propagation distance. Variable angle acrylic wedges were used to preferentially excite the modes of interest, acting as both transmitters and receivers, in a pitch-catch configuration. Two piezoelectric transducers (Olympus A539S-SM) centred at 1 MHz were used for excitation/detection. A liquid couplant is used to couple the wedges to the plate. The thickness of the aluminium plate is varied to target different areas of the frequency-thickness spectrum. A 1 mm thick plate is used to target the S_0 mode at 1 MHz, a 2.5 mm plate to target the A_1 mode, and a 4 mm thick plate to target the S_1 mode.

A signal generator (GW Instek MFG-2230M) was used to generate a 5-cycle Hamming windowed pulse at 1 MHz. Signals are digitised using a Picoscope 3406DMSO USB Oscilloscope. Based on a sampling rate of $5{\times}10^8$ Hz the theoretical maximum temporal resolution is 2 ns. Signal processing is carried out in MATLAB. A zero-phase bandpass filter is applied to the signals to remove unwanted noise. The bandwidth of the filter matches the bandwidth of the excitation pulse, 0.6−1.4 MHz. Time of flight is measured through generating envelopes of the transmitted/received wave packets, finding the peaks of those envelopes, and calculating the time between them. The calculation of group velocity is dependant on removing the propagation time through the wedges, leaving only the time through the plate. This method of time of flight measurement can also be applied to more dispersive signals, which cannot be achieved using cross correlation methods. It should be noted, however, that more dispersive signals (e.g. A_1 & S_1 Vs. S_0) have a less defined central peak in their wave packets, which introduces a larger degree of error to the calculation of time of flight. Various signal processing techniques for time of flight measurement are discussed in detail by Guers [189].

The temperature of the aluminium plate is controlled using a hot plate, and is increased from room temperature up to 100°C, in ~10°C increments. As this method of heating does not produce a consistent temperature across the whole plate or in the wedges, an average temperature is calculated after measuring temperature using multiple thermocouples placed along the transmission path.

Measurement Hardware
2x Olympus ABWX-2001 Variable angle wedges
2x Olympus A539S-SM 1 MHz transducers
Olympus ultrasonic couplant B
GW Instek MFG-2203M Signal generator
Picoscope 3406DMSO USB Oscilloscope
Thermadata T-type temperature loggers
VWR Hot plate

Table 4.1 – Experimental measurement hardware.

The study is made up of three steps. Step one is the measurement of time of flight through the plate, at a distance of 100 mm between wedges, repeated at each temperature step, as shown in Figure 4.3.

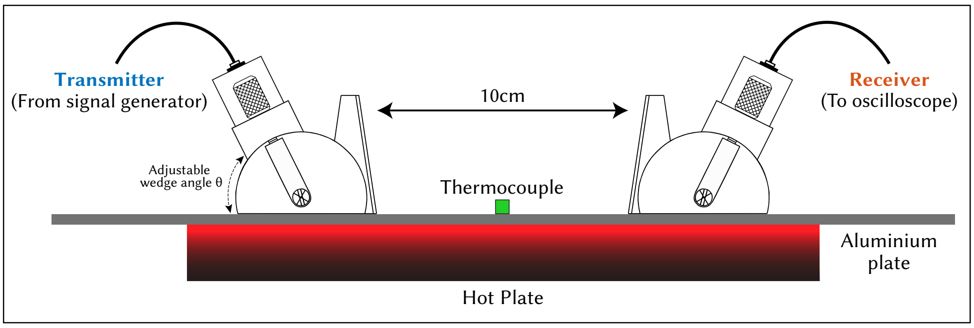

Figure 4.3 – Cross-sectional diagram of total time-of-flight measurement setup.

The second step is the measurement of wedge-to-wedge time of flight. This is repeated at each temperature step, immediately after total time of flight measurement, as shown in Figure 4.4.

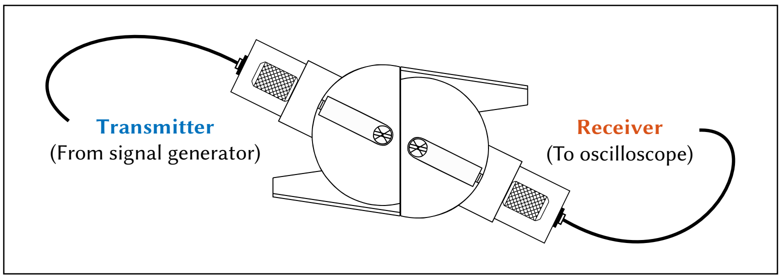

Figure 4.4 – Cross-sectional diagram of wedge-to-wedge time-of-flight measurement setup.

The third step is the measurement of time of flight through the plate at varying distances, for calculation of wedge foot offset. This is only carried out at room temperature.

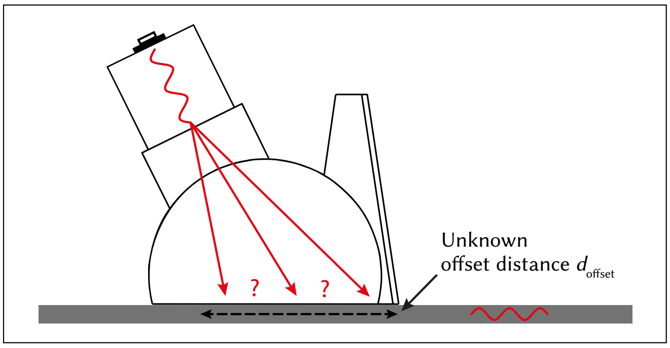

Figure 4.5 – Cross-sectional diagram showing unknown wedge foot offset distance.

Group velocity is calculated using Equation 4.6/4.7. The propagation time through the wedges (t_{wedge}) as measured using the configuration shown in Figure 4.4, has been subtracted from the time of flight t_{aligned} to ensure that only the propagation time through the plate is measured.

$$v = \frac{d}{t_F} \qquad [\mathrm{m\,s^{-1}}] \tag{4.6}$$

$$v = \left(\frac{d_{\text{aligned}} + d_{\text{offset}}}{t_{\text{aligned}} - t_{\text{wedge}}} \right) \qquad [\mathrm{m\,s^{-1}}] \tag{4.7}$$

The wedge foot offset (d_{offset}) is an unknown distance from the front edge of the wedge to where the wave enters the plate from the wedge (see Figure 4.5). This distance must be accounted for in order to accurately calculate group velocity. This distance has been calculated by measuring wave velocity at room temperature for the mode of interest at multiple wedge spacings (0.08 m to 0.14 m in 0.01 m increments) and looping through a range of plausible offset distances (0.02 m to 0.06 m in 0.00001 m increments) until the standard deviation across the range of wedge spacings is at a minimum. This ensures that the variation in measurement results is due to measurement error (e.g. small variances in setting the distance between wedges) rather than an incorrect estimation of wedge foot offset. This value varies with wedge angle and is recalculated for each wave mode measured.

The wedges allow for careful selection of excitation angle (see Figure 4.3) so that modes of interest can be targeted. The angle is determined based on Snell's law:

$$\text{Angle } \theta = \sin^{-1} \left(\frac{\text{Longitudinal wedge velocity}}{\text{Lamb wave phase velocity}} \right) \tag{4.8}$$

The specific angle required to excite each mode is detailed in Section 4.3.2 for S_0, Section 4.3.3 for A_1, and Section 4.3.4 for S_1.

Measurement of wave velocity depends on measurement of time of flight (t_F), which can be described by the Equation [93]:

$$t_F = \frac{d}{c}, \tag{4.9}$$

where d is the distance travelled at wave speed c, both of which are functions of temperature, T. The sensitivity of the time of flight to temperature can then be expressed as:

$$\delta t_F = \frac{d}{c} \left(\alpha - \frac{K}{c} \right) \delta \mathrm{T}, \tag{4.10}$$

where α is the coefficient of thermal expansion of the medium and K is the rate of change of wave velocity with temperature:

$$K = \frac{\delta \mathrm{c}}{\delta \mathrm{T}} \tag{4.11}$$

4.3.1 Test Method

An aluminium test plate is placed on top of a temperature controlled hot plate. Double sided tape is used to centre the plate and ensure that it does not move during the tests. Couplant is applied to the base of the wedges and they are placed onto the plate, aligned with a 3D printed spacer. The temperature of the aluminium plate is monitored using a thermocouple placed in the centre of the plate at the hottest point. The transmission path is set to pass under the thermocouple location, with the wedges equidistant from this position. Time of flight through the plate (t_{aligned}) is measured until it stabilises using the test setup shown in Figure 4.3. This ensures that the temperature gradient in the wedges has stabilised. Time of flight is now measured for the set temperature. Thirty measurements are taken after adjusting both wedge positions. The wedges are removed from the surface and placed together to measure the wedge-to-wedge time (t_{wedge}) as shown in Figure 4.4. Multiple measurements are taken after adjusting wedge-to-wedge position. The measurement process is repeated after allowing the time of flight to re-stabilise. Velocity is calculated using Equation 4.7. A mean average is calculated from the results of the repeated time of flight measurements, and velocity is calculated for every wedge-to-wedge result. An average velocity is calculated along with standard deviation.

The temperature gradient across the plate has been measured by placing four equally spaced thermocouples along the transmission path, from the centre of the plate to the furthest edge of a wedge transducer in 30 mm increments. The wedges are removed from the plate to place the thermocouples, and the temperature of the hot plate is raised to match the temperature recorded by the thermocouple placed in the centre of the plate during measurement of time of flight. Measurements are repeated after moving the thermocouples to the other half of the transmission path. A mean average temperature has been calculated for the total transmission path at each hot plate temperature setting.

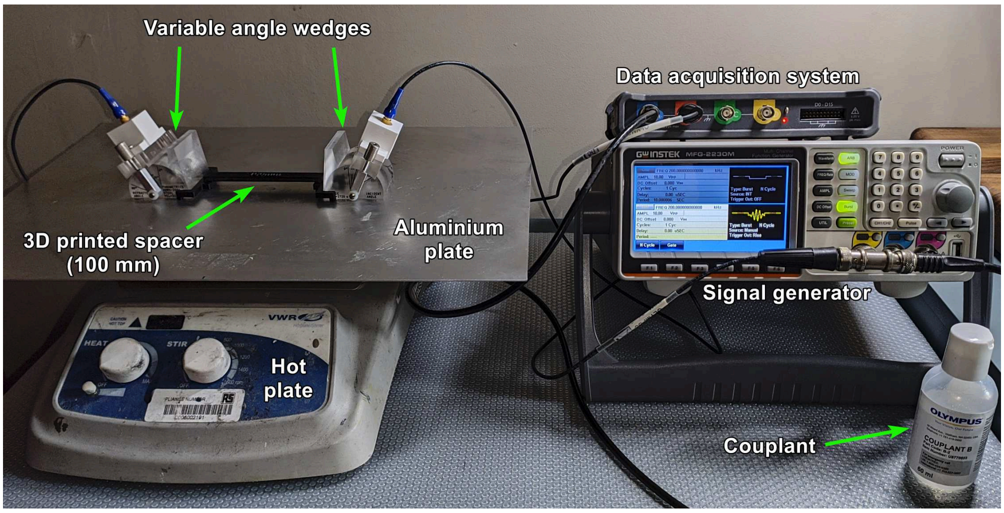

Figure 4.6 – Photograph of the experimental measurement equipment described in Table 4.1.

4.3.2 S_0 mode (1 MHz-mm)

The wedge angle required to excite the S_0 mode is:

$$27.9^\circ = \sin^{-1}\left(\frac{2477}{5298}\right) \tag{4.12}$$

The A_0 mode cannot be excited using this method as the phase velocity at this frequency (2312 $\mathrm{m\,s^{-1}}$) is slower than the longitudinal velocity of the wedge. If the A_0 mode is present in the signal it will not affect measurement of the S_0 mode as the group velocity is significantly different than that of the S_0 mode, which will cause a distinct second wave packet.

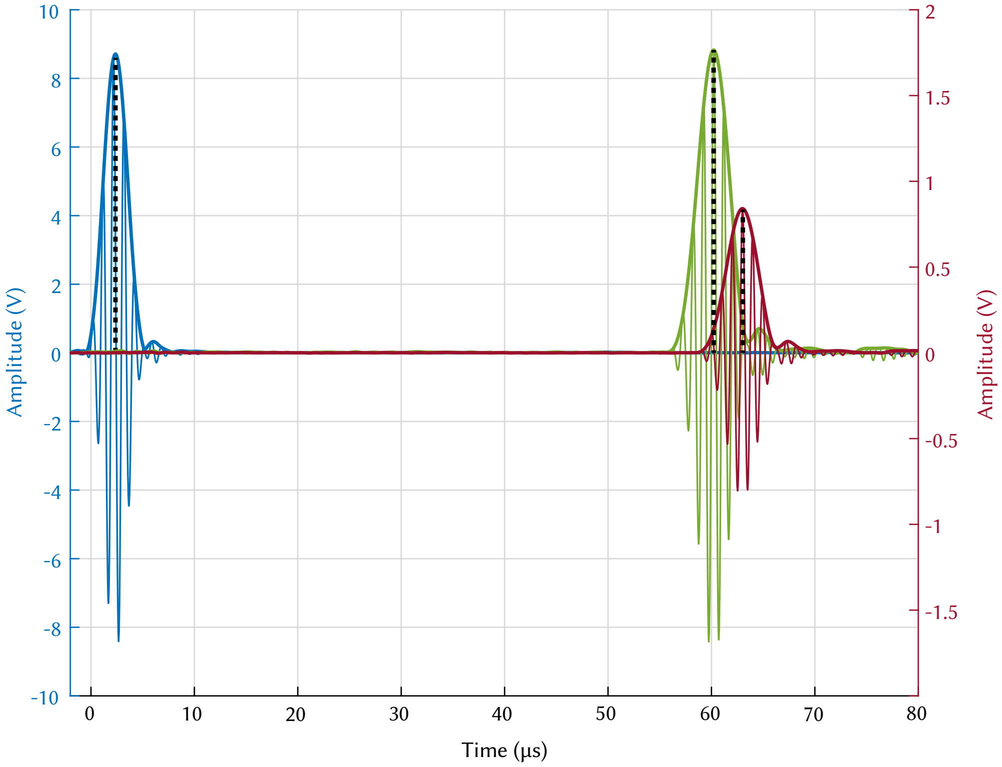

Figure 4.7 – Time of flight (t_F) measurement of S_0 mode using envelope peak method at 20°C (green) and 100°C (red).

4.3.2.1 S_0 mode results

Figure 4.8 shows the experimentally measured wave velocity of the S_0 mode plotted against theoretical wave velocity extracted from the dispersion curves. Error bars show the standard deviation from the mean. After accounting for the temperature gradient across the transmission path by calculating a temperature average the change in velocity is comparable with predicted velocity extracted from dispersion curves, within 4.89 ± 2.27 $\mathrm{m\,s^{-1}}$ on average. The temperature sensitivity of the system is 1.26–1.78 $\mathrm{m\,s^{-1}\,°C^{-1}}$ over the range 24°C–94°C. The sensitivity is extracted from a second-order polynomial fit of the data (r^2 = 0.9992). The slope away from predicted results (increasing with temperature) can be attributed to the increasing temperature gradient, both in the plate and in the wedges. The gradient is shown to be almost linear (r^2=0.9967) across the measurement distance. Increasing temperature is also likely to have an effect on the operation of the piezoelectric transducer (amplitude and centre frequency), however this effect is likely to be negligible over the tested temperature range. The wedge angle required to excite the S_0 mode will also vary with temperature, however the change is only around 1° between 20°C and 100°C.

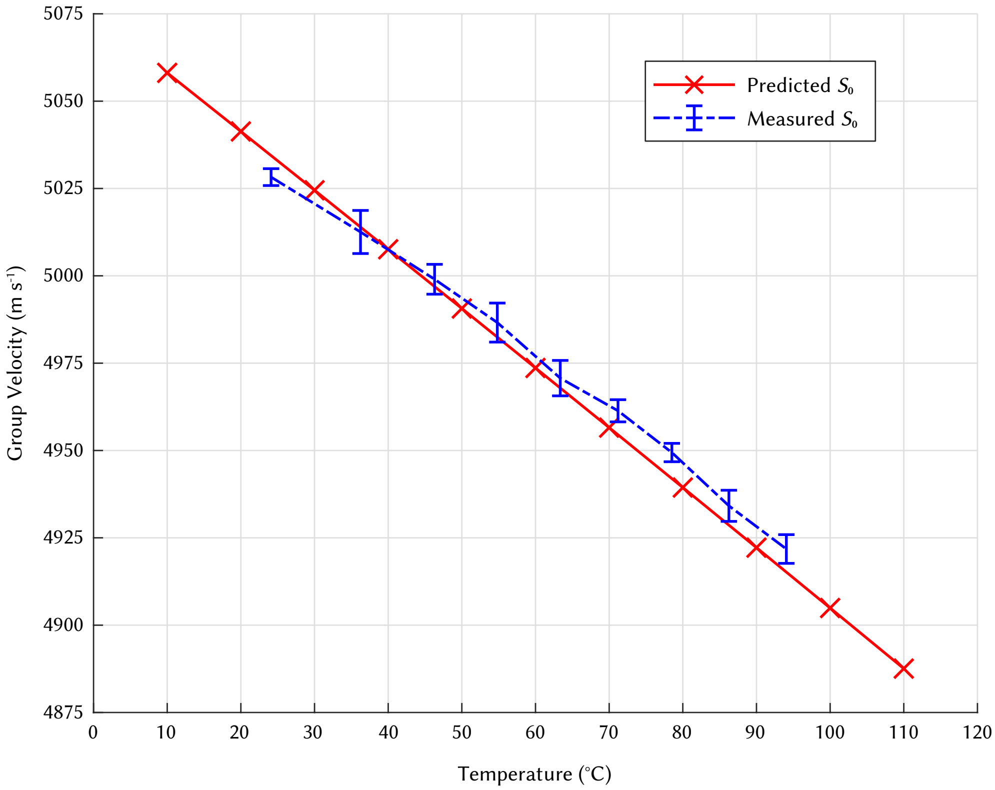

Figure 4.8 – Group velocity change with temperature for the S_0 mode in Aluminium 1050 H14.

4.3.3 A_1 mode (2.5 MHz-mm)

The wedge angle required to excite the A_1 mode is:

$$21.3^\circ = \sin^{-1}\left(\frac{2477}{6808}\right) \tag{4.13}$$

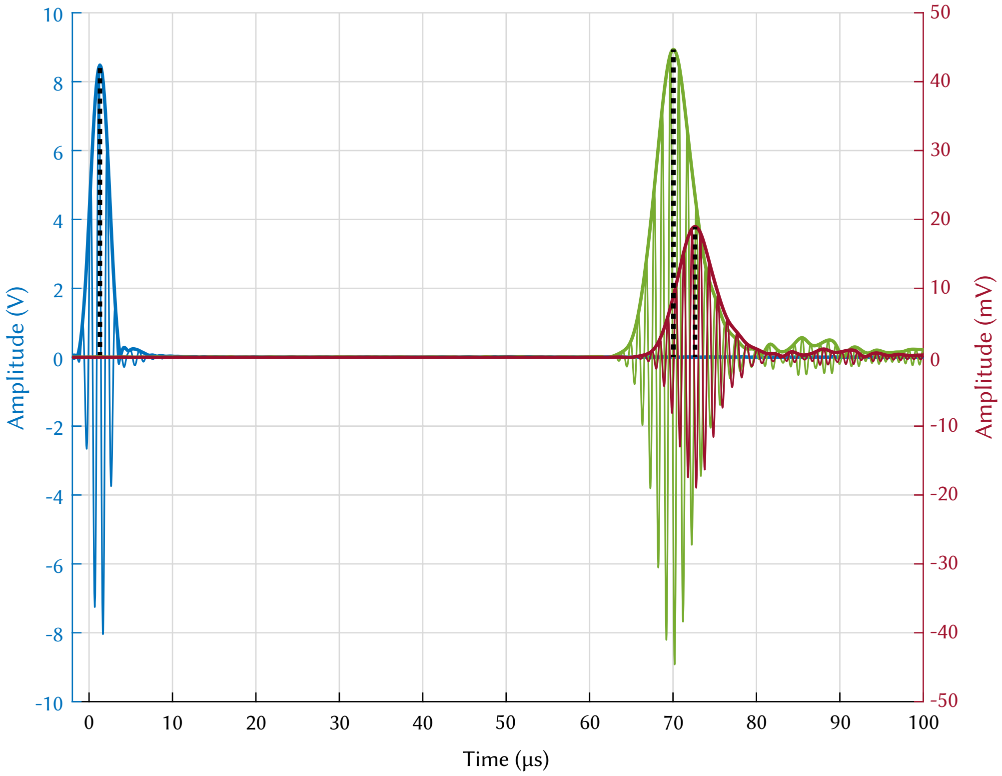

Figure 4.9 – Time of flight (t_F) measurement of A_1 mode using envelope peak method at 20°C (green) and 100°C (red).

4.3.3.1 A_1 mode results

Figure 4.10 shows experimentally measured wave velocity of the A_1 mode plotted against theoretical wave velocity extracted from dispersion curves. Error bars show the standard deviation from the mean. After accounting for the temperature gradient across the transmission path by calculating a temperature average the change in velocity is comparable with predicted velocity extracted from dispersion curves, within 2.43 ± 1.97 $\mathrm{m\,s^{-1}}$ on average. The temperature sensitivity of the system is 1.09–1.17 $\mathrm{m\,s^{-1}\,°C^{-1}}$ over the range 26°C–97°C. The sensitivity is extracted from a second-order polynomial fit of the data (r^2 = 0.9990).

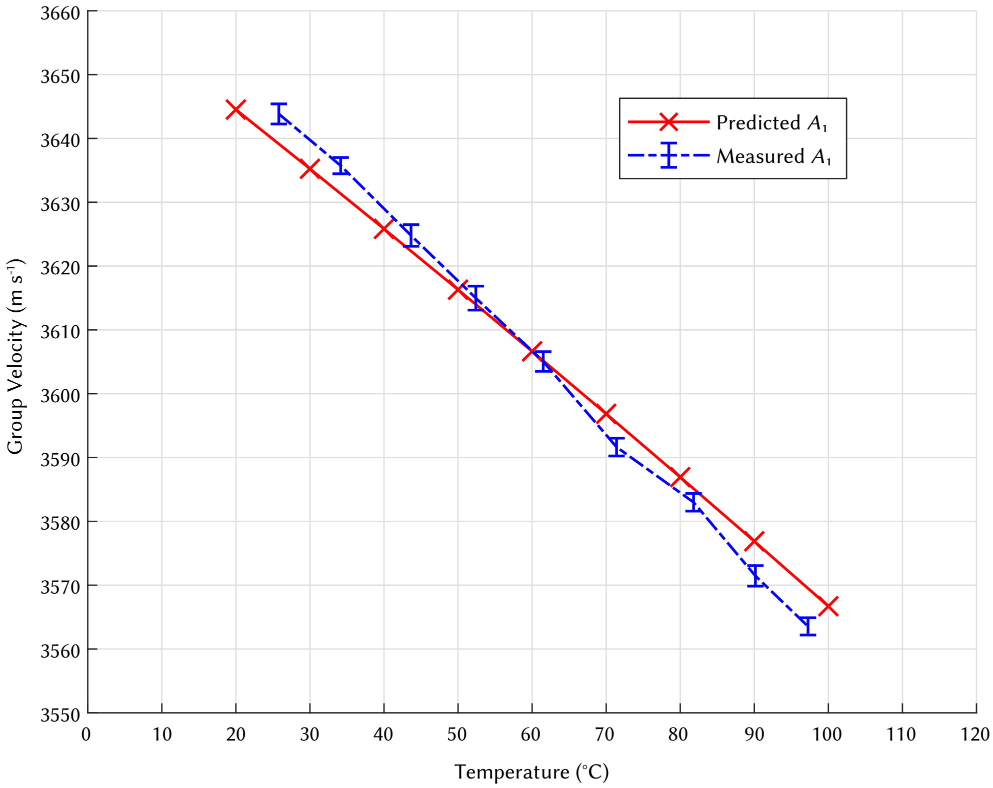

Figure 4.10 – Group velocity change with temperature for the A_1 mode in Aluminium 1050 H14.

4.3.4 S_1 mode (4 MHz-mm)

This region of frequency-thickness product is multi-modal, with both the A_1 and S_1 modes present. Similarities in phase velocity leads to similar excitation angles, which causes both modes to be excited. Using a cross-correlation method for measuring time-of-flight is no longer appropriate, as the received signal differs substantially from the input signal. An envelope peak method is employed instead, whereby analytic envelopes for both the excitation signal and received signal are generated by Hilbert FIR filtering, with a filter length of 2000 samples. This produces a smooth envelope with clearly defined peaks, as seen in Figure 4.11. A peak finding algorithm is used to detect the envelope peaks, as denoted by the dashed lines. The S_1 mode (~4550 m s^{-1}) arrives at the receiver before the A_1 mode (~2550 m s^{-1}) as it has a considerably higher group velocity. At this propagation distance the two modes are clearly separated in the time domain, with the A_1 mode showing considerably more dispersion.

The wedge angle required to excite the S_1 mode is:

$$24.5^\circ = \sin^{-1}\left(\frac{2477}{5971}\right) \tag{4.14}$$

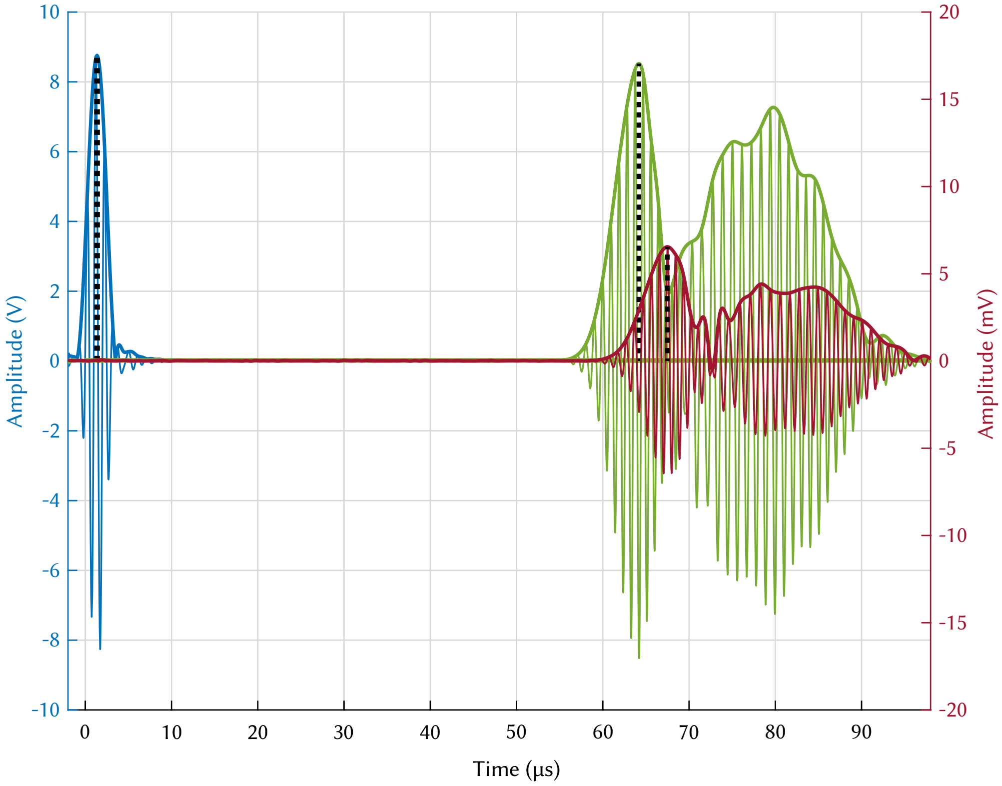

Figure 4.11 – Time of flight (t_F) measurement of S_1 mode using envelope peak method at 20°C (green) and 100°C (red).

4.3.4.1 S_1 mode results

Figure 4.12 shows experimentally measured wave velocity of the S_1 mode plotted against theoretical wave velocity extracted from dispersion curves. Error bars show the standard deviation from the mean. After accounting for the temperature gradient across the transmission path by calculating a temperature average the change in velocity is comparable with predicted velocity extracted from dispersion curves, within 4.44 ± 7.15 $\mathrm{m\,s^{-1}}$ on average. The temperature sensitivity of the system is 1.80 $\mathrm{m\,s^{-1}\,°C^{-1}}$ over the range 25°C–103°C. The sensitivity is extracted from a linear fit of the data (r^2 = 0.9777).

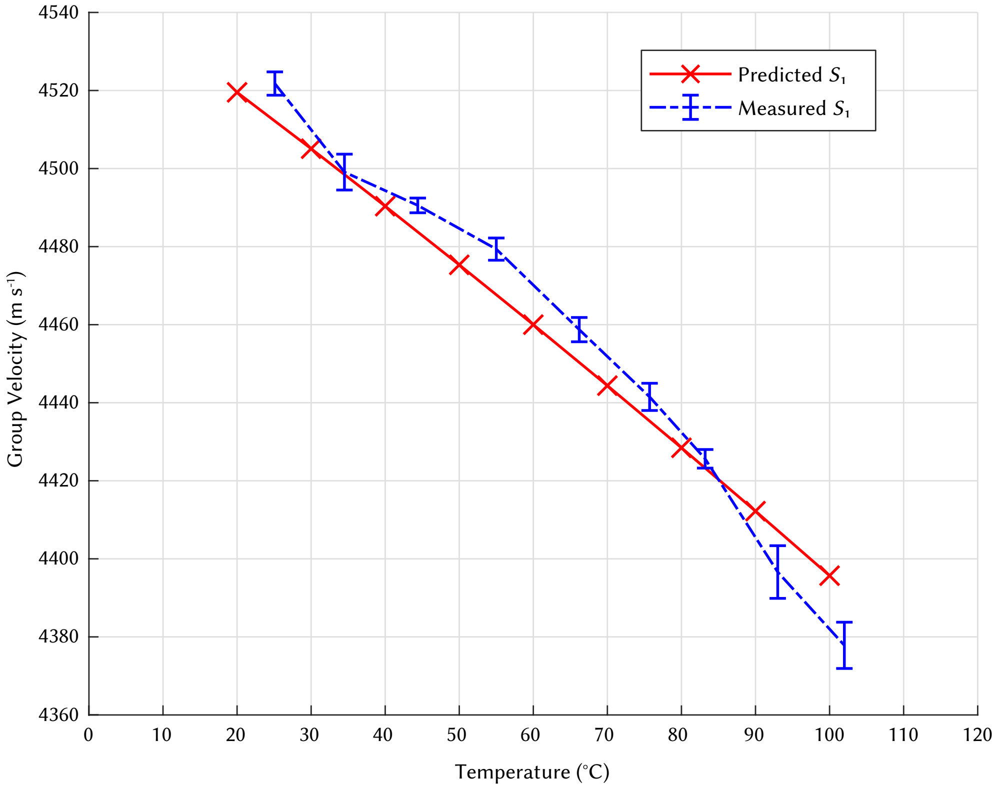

Figure 4.12 – Group velocity change with temperature for the S_1 mode in Aluminium 1050 H14.

4.3.5 Experimental sensitivity analysis

There are a number of experimental error sources to consider. The physical distance between wedges is controlled using 3D printed spacers that keep the wedges aligned at set distances. The movement of the wedges on the surface of the plate increases with temperature as the viscosity of the couplant decreases. Variations in placement cause the calculated velocity to vary by around ± 5 $\mathrm{m\,s^{-1}}$ across multiple (30) wedge re-alignments. The measurement of wedge-to-wedge time to be subtracted from the total t_F is temperature dependant and relies on accurate alignment of the wedge feet, as well as a good connection between them (signal amplitude is highly dependant on couplant). Variation in alignment causes around a ± 10 $\mathrm{m\,s^{-1}}$ velocity change. The wedge foot offset in Equation 4.7 has a large effect on the calculated wave velocity. The exact offset distance is unknown and is assumed to be the point at which the centre line of the transducer aligns with the plate surface. Varying this value raises or lowers the velocity of all results considerably (± 1 mm = ± 35 $\mathrm{m\,s^{-1}}$). The hot plate does not heat the test plate evenly, especially at distances greater than 100 mm between wedges where they overhang the edges of the hot plate. The gradient (the difference in temperature between the centre of the plate and the location of the wedges) increases with temperature. The measured velocity is monitoring the average temperature of the transmission path. The gradient has been measured by placing a number (4) of thermocouples along the transmission path, from the centre of the plate (maximum temperature) to the point at which a wave is transmitted between a wedge foot and the plate. The calculation of aluminium dispersion curves at different temperatures is based on a change in Young's modulus. This is predicted from Hopkin's formula [190] that may not give the correct values for Aluminium 1050 H14, but Aluminium in general.

The largest source of error is the measurement of wedge-to-wedge t_F, as a small error in alignment causes a large change (± 10 $\mathrm{m\,s^{-1}}$) in the wave velocity calculation. This is accounted for through the averaging of multiple (30) measurements, the standard deviation for this range is shown using error bars on Figure 4.8. Variation in wedge foot offset distance dramatically shifts the calculated velocity. This value cannot be directly measured and so the result relies on accurate calculation as discussed in the method.

4.3.6 Discussion of experimental results

The theoretical effect of temperature on various Lamb wave modes in aluminium plates has been investigated by generating dispersion curves based on varying material properties (Figure 4.1). This can be repeated in the future for other materials at higher temperatures (e.g. Inconel 718 up to 1100°C in Figure 3.10). The temperature sensitivities of the S_0, A_1, and S_1 modes at 1 MHz were extracted from these curves (Figure 4.1b) and validated experimentally.

An experimental investigation has been carried out in order to validate theoretical predictions. Wedge transducers in a pitch-catch configuration were used to excite the S_0, A_1, and S_1 modes in 1 mm, 2.5 mm, and 4 mm thick aluminium plates respectively. The time of flight between transducers has been measured and group velocity calculated based on the distance between transducers. This confirms that the S_0 mode has been excited. The change in S_0 wave velocity due to temperature is in line with theoretical predictions over the range 20°C−100°C as shown in Figure 4.8.

It is clear that wedge transducers are not a viable method of transmitting/receiving a wave through a nozzle guide vane at high temperatures. They cannot be permanently mounted to the structure due to the need for a liquid couplant, and their relatively large footprint would make finding a suitable mounting location a challenge. Their operation at high temperatures is limited by the wedge material, which in the case of acrylic melts at around 160°C. The wedge material needs to have a longitudinal wave velocity less than that of the targeted Lamb wave phase velocity, which limits the choice of material severely, mostly to plastics with low melting points. The great benefit of wedge transducers is the ability to selectively target Lamb wave modes, which reduces the complexity of data analysis compared with exciting multiple modes simultaneously. This is difficult to achieve using other transducer configurations but it may instead be possible to excite a higher order region that travels as a single wave packet. The use of PWAS transducers could allow for operation at high temperatures (assuming suitable choice of piezoelectric material) and would be relatively easy to mount to an NGV structure, having a small footprint, although the high temperatures are likely to make bonding difficult. Another option is to couple into the structure using waveguides, distancing the transducers from the high temperature environment. Future research will investigate the temperature sensitivity of higher order modes (such as A_1 and S_1), as operating at higher frequencies can improve resolution (allowing for the detection of smaller phase shifts) and response rates. The ability to monitor wave velocity variations in multi-modal wave packets will also be considered when investigating transducer configurations suitable for higher temperature operation.

4.4 Simulation study (Aluminium)

The multi-physics simulation package COMSOL has been used to replicate the wedge based time of flight measurement system used in the previous experimental study. The model has been validated against experimental results, to be used in subsequent studies involving different materials and surface coatings. The literature covering the use of COMSOL for modelling Lamb wave excitation using wedge transducers is limited, however it has been shown that Lamb waves can be successfully generated using this method [191].

4.4.1 Variable angle wedge simulation

A 2D model has been produced of the experimental test setup described in Section 4.3. This allows for validation of the time of flight measurements, and can be used to separate the effect of temperature on the wedges from the substrate. The effect of temperature on the Lamb wave alone can therefore be analysed.

4.4.1.1 Geometry

The model consists of two variable angle wedges (PMMA), which are based on the geometry of the Olympus variable angle wedges used in the experimental investigation, placed on top of an aluminium plate. The thickness of the plate can be varied to target different Lamb wave modes at different frequency-thickness products. The initial thickness is set to 1 mm to target the S_0 mode at 1 MHz–mm. The transmitting wedge has a simplified piezoelectric transducer (PZT-5H from the COMSOL material library) attached to it's rotating block, to which the excitation signal is applied. The geometry can be seen in Figure 4.13. The received signal is measured at the receiver wedge's rotating block boundary. More realistic transducer configurations are not considered in this study, as the focus is on the effect of temperature on the propagating wave. A boundary area is set underneath the plate to act as the heat source, again mimicking the experimental setup. This is simplified to allow the temperature to be directly set, rather than simulating a hot plate.

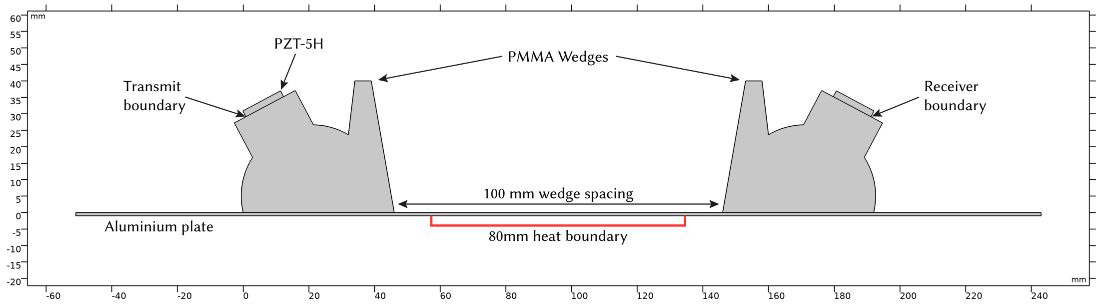

Figure 4.13 – COMSOL geometry diagram.

4.4.1.2 Material properties

The change in Young's Modulus with temperature is included in the material properties for both the wedges and the aluminium using piecewise functions. Unfortunately the specific material properties of the Olympus wedges used in the experimental study are unknown, and the values for PMMA found in literature vary quite dramatically. Figure 4.14 shows five sources of temperature dependant Young's modulus for PMMA, where the shaded green region indicates the temperature range of interest in this study (20–100°C). Polynomial fits were applied to the data sets to allow them to be used in COMSOL (apart from COMSOL's in-built values which are given as a function) and are provided in Table 4.3, where T is the temperature in Kelvin. The Alexandria [192] and Goodyear Aerospace [193] sources were disregarded as the large reduction in E over the temperature range of interest is not considered realistic, based on the use of the Olympus wedges in the experimental study. The Birmingham sources [194] (provided at two different annealing temperatures, 600K and 1000K) differ greatly from the values provided by COMSOL's material library entry for PMMA [195]. Room temperature values of Young's modulus (for which there are many more sources) range from 1.8–5.0 GPa, however they are mostly commonly given at ~3.0 GPa. In order to accurately represent the wedge material used experimentally, the value of Young's modulus has been inferred from measurements of longitudinal wave velocity.

Property	PMMA	Aluminium
Heat capacity at constant pressure (J/(kg·K))	1470	904
Density (kg/m^3)	1190	2700
Thermal conductivity (W/(m·K))	0.18	237
Poisson's ratio	0.35	0.3375

Table 4.2 – COMSOL material properties for PMMA and aluminium.

Source	Function
COMSOL Material Library [195]	$E = 4.3102{\times}10^9 + 6.9344{\times}10^7 \times T^1 - 5.2821{\times}10^5 \times T^2 + 1.5796{\times}10^3 \times T^3 - 1.7421 \times T^4$
Birmingham 600K Annealing [194]	$E = 58.3 \times T^3 + -7.6500{\times}10^4 \times T^2 + 2.1367{\times}10^7 \times T + 2.8500{\times}10^9$
Birmingham 1000K Annealing [194]	$E = -116.7 \times T^3 + 9.3000{\times}10^4 \times T^2 + -2.8333{\times}10^7 \times T + 7.0200{\times}10^9$
Alexandria [192]	$E = -2.6773{\times}10^4 \times T^3 + 2.4371{\times}10^7 \times T^2 + -7.4029{\times}10^9 \times T + 7.5540{\times}10^{11}$
Goodyear Aerospace [193]	$E = -1.5514{\times}10^5 \times T^2 + 6.4090{\times}10^7 \times T + -1.5120{\times}10^9$

Table 4.3 – Functions for PMMA Young's modulus.

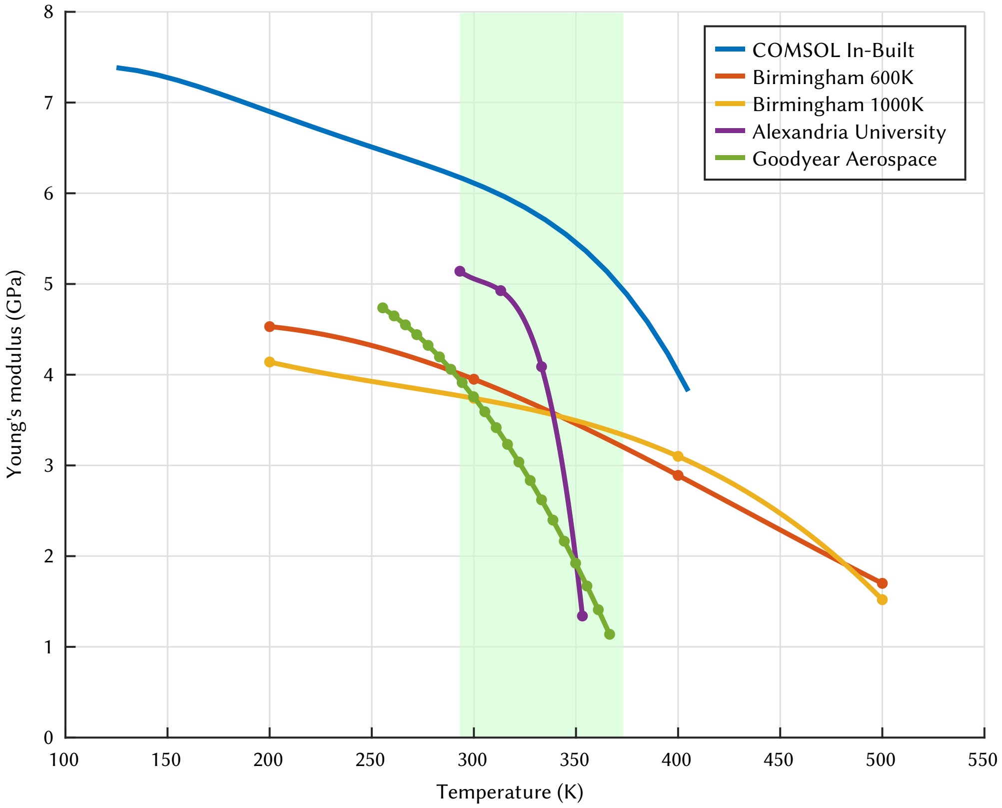

Figure 4.14 – A range of sources for the Young's modulus of PMMA.

4.4.1.3 Determination of Young's modulus from wedge wave velocity

The longitudinal wave velocity of the wedges has been measured experimentally by placing the two wedges together, as shown in Figure 4.15. Time of flight is measured using an envelope peak finding function, where analytic envelopes for both the excitation signal and received signal are generated by Hilbert FIR filtering, with a filter length of 2000 samples. This produces a smooth envelope with clearly defined peaks. Wave velocity calculated using the propagation distance (0.0715 m). The measured velocity of 2477 $\mathrm{m\,s^{-1}}$ differs from that provided by the manufacturer (2720 $\mathrm{m\,s^{-1}}$). Now that the wave velocity is known, the material properties of the model can be adjusted until the simulated wave velocity matches that of the experimental measurements. The model was set to run a parametric sweep of Young's modulus for the wedges, from 3.5×10^9 Pa to 6×10^9 Pa in 0.5×10^9 Pa increments, matching the range of potential values from literature. The wave velocity for each of these steps is calculated, and a polynomial fit of the data is generated in MATLAB. The quadratic equation produced is used to find the value of E closest to the wave velocity measured experimentally. The model was then rerun at smaller increments of E (4.20×10^9 Pa to 4.40×10^9 Pa in increments of 0.05×10^9 Pa) to improve the accuracy of the polynomial fit. The model is then computed using this value of E to verify that the velocity matches the prediction.

In order to determine the temperature dependant Young's modulus for the wedge material, the test setup was placed inside of an oven, and time of flight was measured up to 45°C. Increasing the temperature of the oven above this caused the signal amplitude to decrease dramatically, making time of flight measurement unreliable. The temperature of the oven was allowed time to stabilise, along with time of flight. The velocity calculated at this temperature was then used to find the associated value of E, as described previously. These values were then entered into COMSOL using an interpolation function, extrapolating the value of E for higher and lower temperatures linearly. This method is sufficiently accurate for the small temperature range used in this study, and better represents the real material than using values derived from literature.

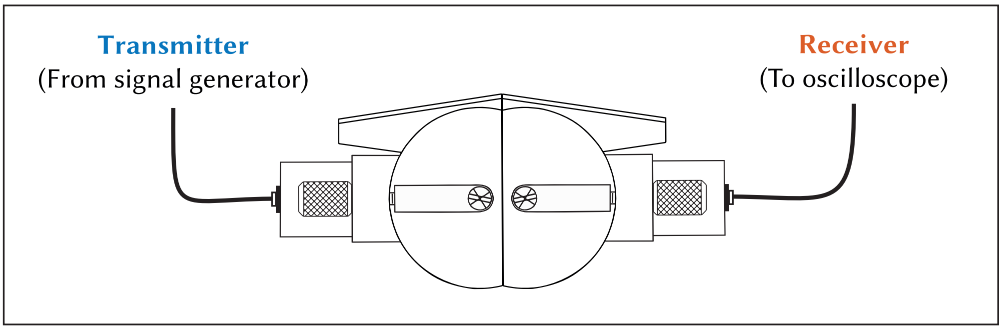

Figure 4.15 – Cross-sectional diagram of on-axis wedge-to-wedge time-of-flight measurement setup.

The experimentally measured longitudinal wave velocity of the wedges is also used to calculate the wedge angle required to excite particular modes, based on Snell's law.

4.4.1.4 Aluminium plate properties

The choice of temperature dependent E for aluminium is more straight forward, as sources for bulk aluminium and aluminium 1050 are provided by the COMSOL material library, and they are very similar to values of bulk aluminium provided by Hopkins [190], as shown in Figure 4.16. The values for 1050 are used in the following simulations. The shaded green region indicates the temperature range of interest in this study (20–100°C). The functions used to generate the curves are given in Table 4.4.

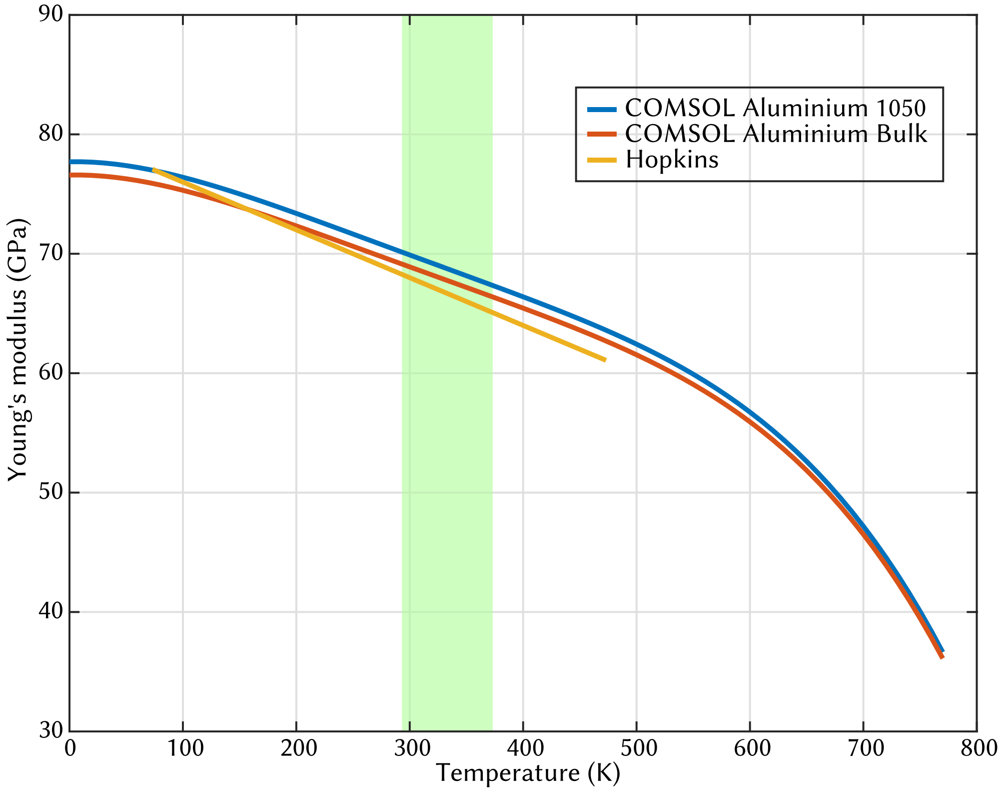

Figure 4.16 – Young's modulus of Aluminium.

Source	Function
COMSOL Aluminium 1050	$7.7703{\times}10^{10} + 2.0365{\times}10^{6} \times T^{1} - 1.8916{\times}10^{5} \times T^{2} + 4.2529{\times}10^{2} \times T^{3} - 3.5457{\times}10^{-1} \times T^{4}$
COMSOL Aluminium Bulk	$7.6593{\times}10^{10} + 2.0074{\times}10^{6} \times T^{1} - 1.8646{\times}10^{5} \times T^{2} + 4.1922{\times}10^{2} \times T^{3} - 3.4951{\times}10^{-1} \times T^{4}$
Hopkins [190]	$-4{\times}10^{7} \times T + 8{\times}10^{10}$

Table 4.4 – Functions for Aluminium Young's modulus.

The change in Poisson's ratio and density is assumed to negligible and is not included in the simulation. Thermal expansion is also considered to have a negligible effect on the propagation distance and is excluded (calculated to have an average reduction in wave velocity of the S_0 mode in aluminium of -1.20 m s^{-1} over the temperature range 20–100°C).

4.4.1.5 Transducer configuration

The simplified ultrasonic transducer used in this study is comprised of an active piezoelectric element and a backing layer. Lead Zirconate Titanate (PZT-5H) from COMSOL's material library is operated at the first through-thickness resonance frequency for 1 MHz, where the ceramic thickness is equal to half a wavelength (2 mm).

$$\text{Piezoelectric material thickness} = \left(\frac{v_p}{2 \times f_0}\right) \qquad [\text{mm}] \qquad (4.15)$$

$$2.05 = \left(\frac{4101}{2 \times 1{\times}10^6}\right) \qquad [\text{mm}] \qquad (4.16)$$

The backing layer is comprised of a highly attenuating material, with an acoustic impedance matching the piezoelectric material as closely as possible. In this case an epoxy resin mixed with Tungsten powder is used [196]. A matching layer is not employed as the signal amplitude is sufficient for this study.

The electrostatics module is set up as follows: A zero charge node is used for the edges of the piezoelectric material, initial values are set to 0 V, a "Charge Conservation, Piezoelectric" node is set for the piezoelectric material, a ground boundary is selected for the wedge side of the material, and a terminal node is set for the opposite boundary. Within the terminal node the type is set to Voltage and the input is set to "V0(t)". The excitation signal is a 1 MHz 5−cycle Hamming windowed sine pulse generated in MATLAB and included in COMSOL using an analytic function (Definitions>Functions>Analytic), given in Equation 3.6 and shown in Figure 3.14. The receiver transducer is setup in the same way, except the terminal node type is set to "charge".

4.4.1.6 Physics & mesh settings

The modules Solid Mechanics, Electrostatics, and Heat Transfer in Solids are used in this simulation, along with a multi-physics node to couple Solid Mechanics with Electrostatics for the piezoelectric effect. Both the wedges and the plate are set to isotropic linear elastic materials, with low reflecting boundaries applied to the wedges.

For the Heat Transfer in Solids module all the domains are set to solid, and initial values are set to 20°C. The boundaries that are exposed to the air are selected in a Heat Flux node, where convective heat flux is selected. A user defined heat transfer coefficient of 7 W/(m^2·K) is used for the plate, and 1 W/(m^2·K) for the wedges. These values were set to produce the temperature gradients measured experimentally in both the plate and the wedges. The external temperature is set to 20°C. The temperature of the boundary underneath the plate is adjusted as required (20°C to 100°C in 20°C increments for this study). An example of the temperature gradients produced from the stationary study step are shown in Figure 4.18, where the temperature boundary underneath the plate is set to 100°C.

As the temperature decreases between the heat area and the end of the plate, the temperature under the wedges is less than temperature applied to the plate. This is important for the wedge-to-wedge study, as the heat boundary between wedges cannot be set to the temperature used for the boundary in the full study. Instead the full model is run first, and temperature probes are used to measure the temperature in the plate underneath the wedges in 5 mm increments from one side to the other. The study is carried out at heat boundary temperatures of 20.0°C, 46.7°C, 73.3°C, and 100.0°C. A mean average of these measurements is calculated and used for the boundary temperature in the wedge-to-wedge study, as shown in Tables 4.5 to 4.7.

	Boundary temperature (°C)			
x (mm)	**20.0**°C	**46.7**°C	**73.3**°C	**100**°C
0	20.0	41.7	63.4	84.4
5	20.0	42.0	64.1	85.4
10	20.0	42.4	64.8	86.6
15	20.0	42.8	65.5	87.7
20	20.0	43.2	66.3	88.9
25	20.0	43.6	67.0	90.2
30	20.0	44.0	67.9	91.5
35	20.0	44.4	68.8	92.9
40	20.0	44.9	69.8	94.5
45	20.0	45.4	70.7	96.0
Average	**20.0**	**43.4**	**66.8**	**89.8**

Table 4.5 – Boundary temperatures for wedge-to-wedge study at S_0.

	Boundary temperature (°C)			
x (mm)	**20.0**°C	**46.7**°C	**73.3**°C	**100**°C
0	20.0	44.3	68.7	93.1
5	20.0	44.5	69.0	93.5
10	20.0	44.7	69.3	94.0
15	20.0	44.8	69.6	94.5
20	20.0	45.0	70.0	95.1
25	20.0	45.2	70.4	95.6
30	20.0	45.4	70.8	96.2
35	20.0	45.6	71.2	96.8
40	20.0	45.8	71.6	97.5
45	20.0	46.1	72.0	98.1
Average	**20.0**	**45.1**	**70.3**	**95.4**

Table 4.6 – Boundary temperatures for wedge-to-wedge study at A_1.

	Boundary temperature (°C)			
x (mm)	**20.0**°C	**46.7**°C	**73.3**°C	**100**°C
0	20.0	45.1	70.2	95.4
5	20.0	45.2	70.4	95.7
10	20.0	45.3	70.6	96.0
15	20.0	45.5	70.8	96.4
20	20.0	45.6	71.1	96.7
25	20.0	45.7	71.3	97.1
30	20.0	45.8	71.6	97.4
35	20.0	45.9	71.9	97.9
40	20.0	46.1	72.1	98.3
45	20.0	46.3	72.4	98.7
Average	**20.0**	**45.7**	**71.2**	**97.0**

Table 4.7 – Boundary temperatures for wedge-to-wedge study at S_1.

The mesh size for each material is determined by excitation frequency. The excitation wavelength for each of the materials is calculated by dividing their longitudinal wave speed by f_0. A free triangular mesh is created for each of the materials, and the maximum element size for each of them is set to LocalWavelength/N. If higher frequency content is expected, the wavelength for each material should be based on the highest frequency expected rather than f_0. In order to accurately resolve a wave, at least 10–12 elements per local wavelength are required [197]. This assumes linear discretization for all modules. Using 12 elements results in an average skewness rating (measure of element quality, 0–1) of 0.9345 over 154728 elements [198]. This is equivalent to a sample rate of 1.2×10^8 Hz.

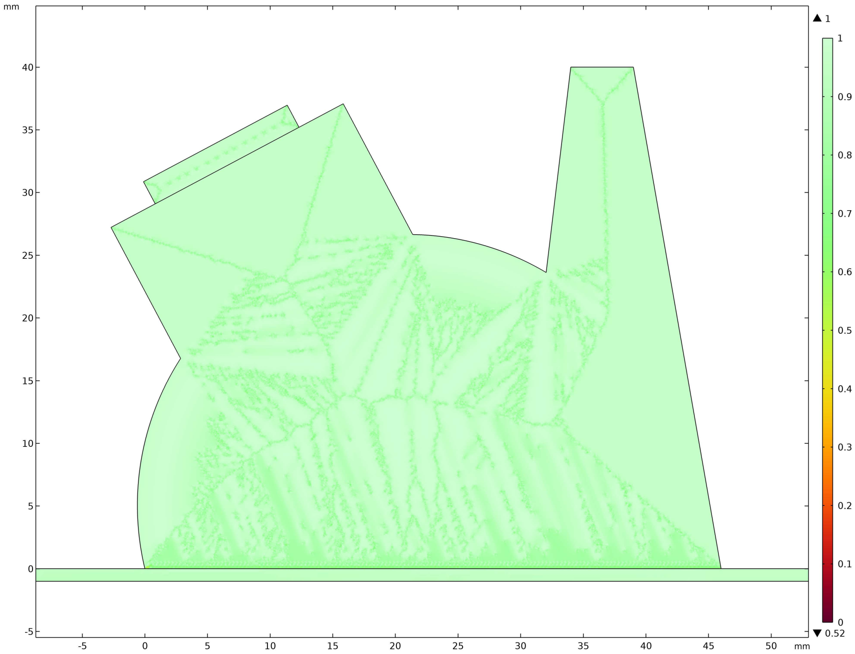

Figure 4.17 – Mesh skewness quality plot. Green elements represent values close to 1.

4.4.1.7 Study settings

This study has two steps, firstly a stationary study to simulate the effect of temperature on the system until an equilibrium is reached, and secondly a time dependant study to simulate wave propagation. The initial conditions of the time dependant study are set by the stationary study. The stationary study solves only for heat transfer and not electrostatics/the piezoelectric effect.

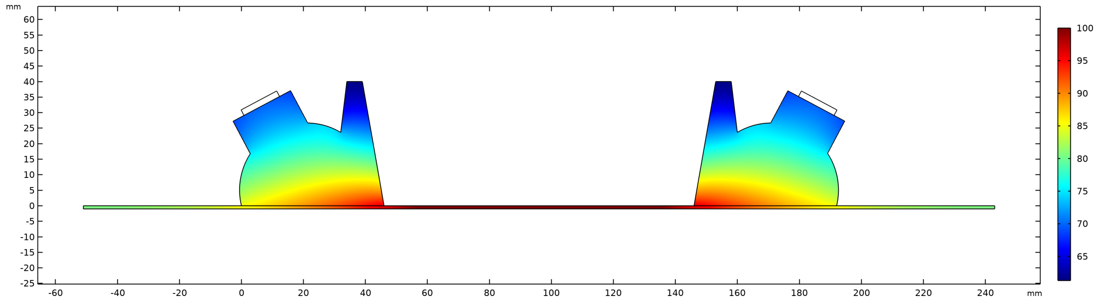

Figure 4.18 – Simulated temperature gradients from stationary study at 100°C. Scale is given in degrees Celsius (°C).

The time dependant study includes electrostatics/the piezoelectric effect to allow for wave generation, but does not include heat transfer. This reduces computation time as it is not necessary to model changing temperature as the time dependant model solves, only to use the fixed values of material properties that were passed on from the stationary study. The time dependant study has its "Output times" set to: range(0,dt,sim_length) where "dt" is a global definition parameter equal to $CFL/(N \times f_0)$. The CFL (Courant Friedrichs Lewy) number is suggested by COMSOL [199] to be less than 0.2, optimally 0.1 (when the default second order, quadratic, mesh elements are used). This value represents the relationship between wave speed, c, maximum mesh size, h, and time step length, Δt: $CFL = c\Delta t/h$. This can be rewritten in terms of frequency as the maximum mesh size h has already been manually defined by N, the number of elements per local wavelength for each material: $CFL = fN\Delta t$. This can then be rearranged to give the time step: $\Delta t = CFL/Nf$.

Under "Values of Dependant Variables" the settings are changed to user controlled, method is changed to Solution, and the study is set to the stationary study. The time step is manually set under Solver Configurations>Solution 1>Time dependant solver>Time stepping. Here the "Steps taken by solver" parameter is changed to "Manual" and the "Time Step" is set to: $CFL/(N \times f_0)$.

To reduce file size only the data at the wedge boundaries is stored by the solver. This can be achieved by adding an "Explicit Selection" node in the Geometry section, and selecting both the transmit and receive wedge boundaries. Within the time dependant study settings select "For selection" under "Store fields in output" and select the boundary group [200]. File size can be further reduced by only storing the field components of interest. Within "Solver Configurations">Solution 1>Dependant Variables 2, the option for storing the displacement field in the output can be deselected, as only the electric potential is necessary.

A parametric sweep node was used to cycle through the temperature boundary values (20.0°C, 46.7°C, 73.3°C, and 100.0°C) and save the output of the time dependant model for each value. This is repeated for the model in the wedge-to-wedge configuration (at temperatures shown in Tables 4.5 to 4.7), mimicking the experimental setup shown in Figure 4.4. The simulations were computed on the University of Southampton's IRIDIS 5 supercomputing platform [201].

4.4.2 Simulation results

A simplified model where PZT is applied directly to the plate shows that both the A_0 and S_0 modes are excited at a frequency of 1 MHz. Figure 4.19 shows exaggerated deformation of pressure in the plate, which makes the presence of the A_0 and S_0 modes clearly visible. A_0 exhibits large out of plane motion, whereas S_0 exhibits large in plane motion. The modes are separated in the time domain after a short distance ($\sim$ 50 mm) due to their differences in group velocity. When wedges are applied to the plate selective mode excitation can be achieved, however it is necessary to use wedges as both transmitters and receivers to most effectively isolate the mode of interest.

To visualise wave propagation and calculate time of flight the pressure at both transmitter and receiver wedge boundaries is exported, and the time of flight is measured using an envelope peak extraction method, to allow direct comparison with experimental results.

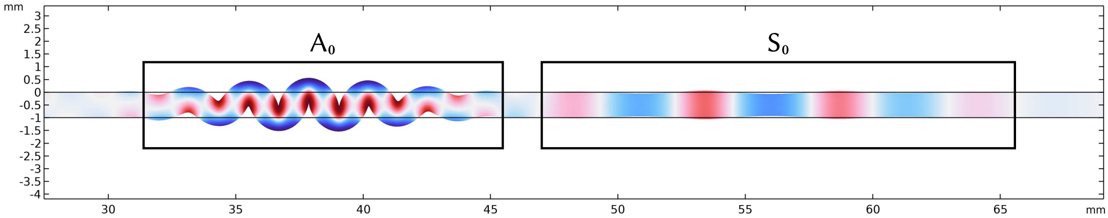

Figure 4.19 – Exaggerated deformation (displacement) showing the presence of the A_0 & S_0 modes. Excitation occurs at the left edge of the plate.

Wedge foot offset (the distance a wave travel under each wedge foot) is calculated in the same way for both the simulation and the experiments, however the value differs, which indicates a difference in geometry between them. Despite this, the difference in calculated velocities is small, as using accurate estimations of wedge foot offset corrects for the difference in total time of flight. Time of flight in the wedge-to-wedge configuration is in line with experimental measurements, which suggests that the geometry and material properties of the wedges are realistic. The material properties of the aluminium plate are the same as those used in the theoretical study, which should (in theory) mean that the velocity in the simulated plate is the same as was extracted from dispersion curves.

	Temperature sensitivity (m s^{-1}°C^{-1})		
Wave mode	**Analytical prediction**	**Numerical prediction**	**Experimental**
S_0	-1.47	-1.47	-1.58
A_1	-0.80	-0.99	-1.13
S_1	-1.33	-1.75	-1.89

Table 4.8 – Average temperature sensitivity of S_0, A_1, and S_1 Lamb wave modes in Aluminium from 20°C to 100°C. Comparing values extracted from dispersion curves (analytical prediction), COMSOL simulations (numerical prediction), and experimental results.

Table 4.8 shows the average temperature sensitivity of S_0, A_1, and S_1 Lamb wave modes in Aluminium from 20°C to 100°C. Predicted, simulated[1], and experimental results are compared. In the following sections the results of the simulations are discussed for each mode.

Time-displacement data is transformed into frequency-wavenumber data using 2D-FFT from spatial B-scan data, using 90 point probes equally spaced 0.8 mm apart. This allows individual modes to be identified, and compared with dispersion curves for verification. Out-of-plane (y-axis) displacement is monitored, to reflect the response detected when using wedge transducers. It should be noted, however, that the displacement response in the plate measured using a point probe will differ from the response received at a second receiver wedge. The use of a second wedge further isolates a particular mode of interest, while the displacement in the plate may still show the presence of other modes.

---

[1] Predictions are carried out by analysing dispersion curves, whereas simulations are carried out using COMSOL.

4.4.2.1 S_0 Mode simulations

Figure 4.20 shows the wave propagation of a pulse exciting the S_0 mode at 20°C and 100°C. The black dotted lines indicate the peak of the envelopes used to calculate time of flight. Figure 4.22 shows the change in velocity with temperature for the S_0 Lamb wave mode in Aluminium, comparing predicted temperature sensitivity extracted from dispersion curves, experimental measurement data (Section 4.3.2), and COMSOL simulations of the experimental setup. Error bars show measurements that fall within one standard deviation of the mean. The experimental result is within $35.93 \pm 3.06\ \mathrm{m\,s^{-1}}$ or $0.71\% \pm 0.06\%$ of the predicted velocity on average. The COMSOL results are within $10.61\ \mathrm{m\,s^{-1}} \pm 0.73\ \mathrm{m\,s^{-1}}$ or $0.21\% \pm 0.01\%$ of the predicted result on average. The standard deviation of group velocity across four wedge spacings (80 mm, 90 mm, 100 mm, 110 mm) at the calculated offset value of 45.3 mm is $0.74\ \mathrm{m\,s^{-1}}$, which indicates that the simulation and time of flight measurement method are producing accurate results.

Figure 4.21 shows the 2D-FFT response of the propagating wave packet. The solid and dashed lines represent the anti-symmetric and symmetric dispersion curves respectively. Almost pure excitation of the S_0 mode is achieved.

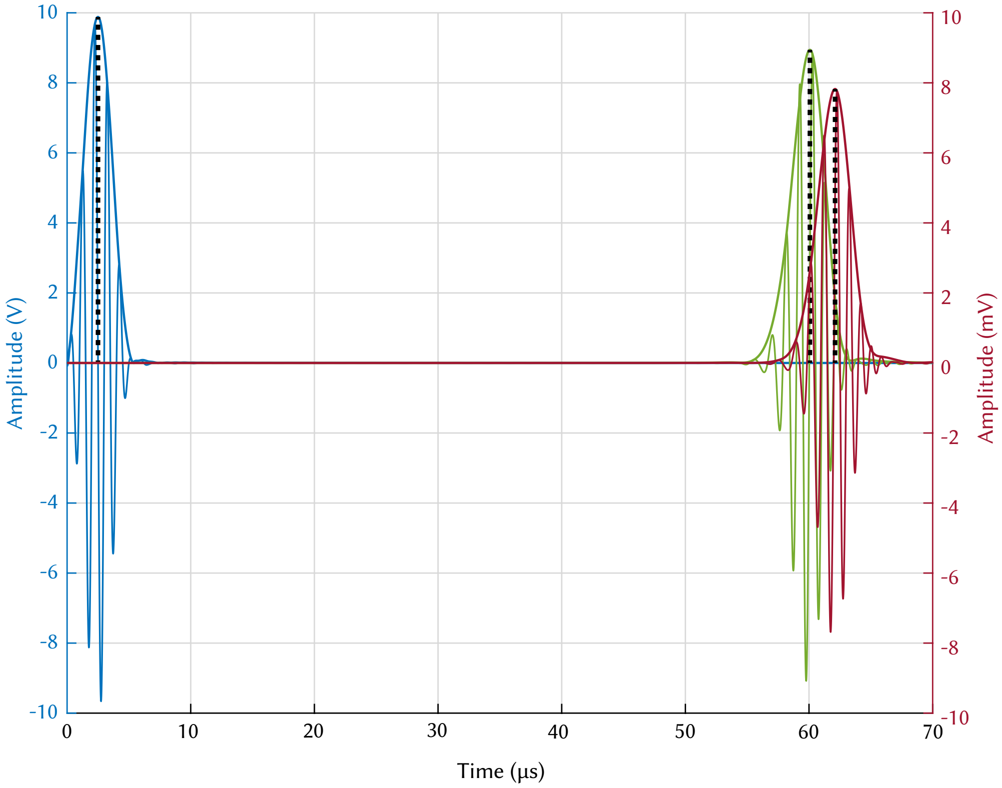

Figure 4.20 – Wave propagation of S_0 Lamb wave mode in Aluminium at 20°C (green) and 100°C (red).

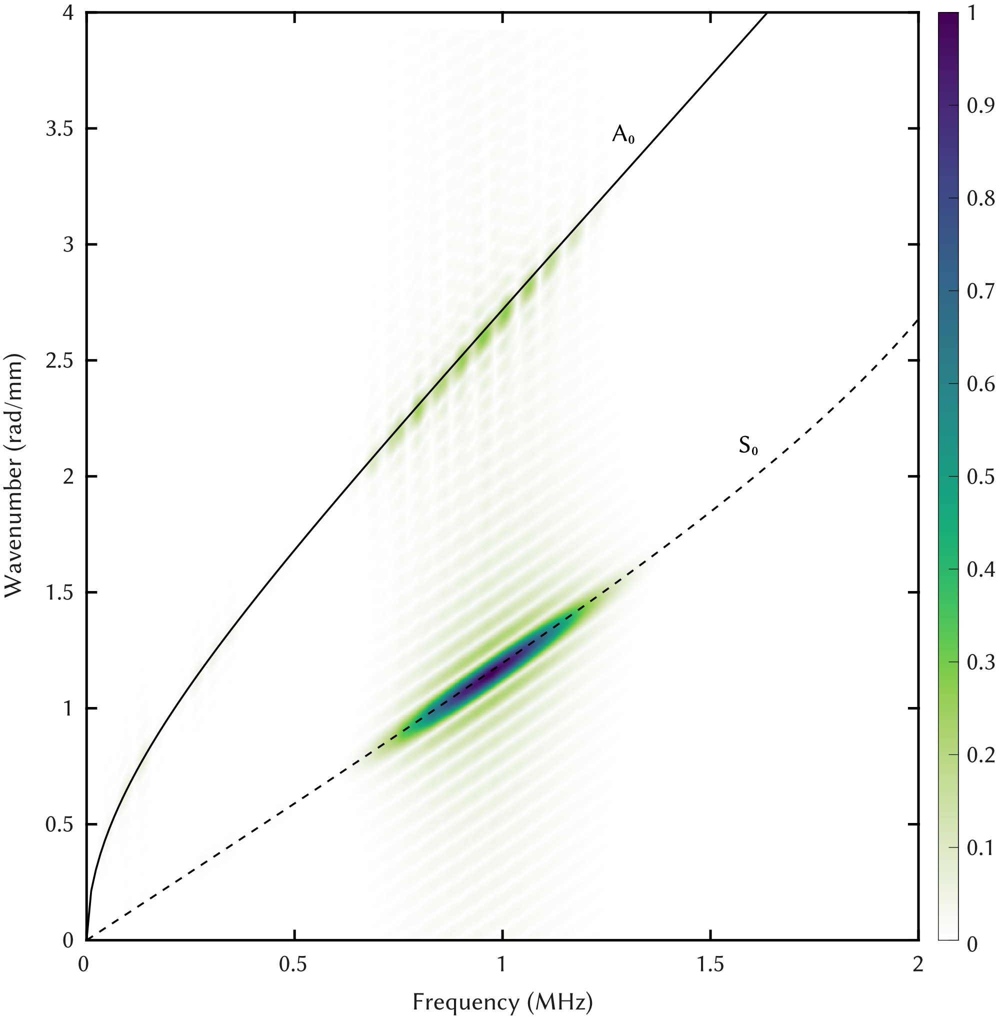

Figure 4.21 – 2D-FFT of S_0 excitation in 1 mm thick Aluminium at 20°C. Solid and dashed lines represent numerically calculated dispersion curves. Areas of high intensity (darker colours) show where modes have been detected.

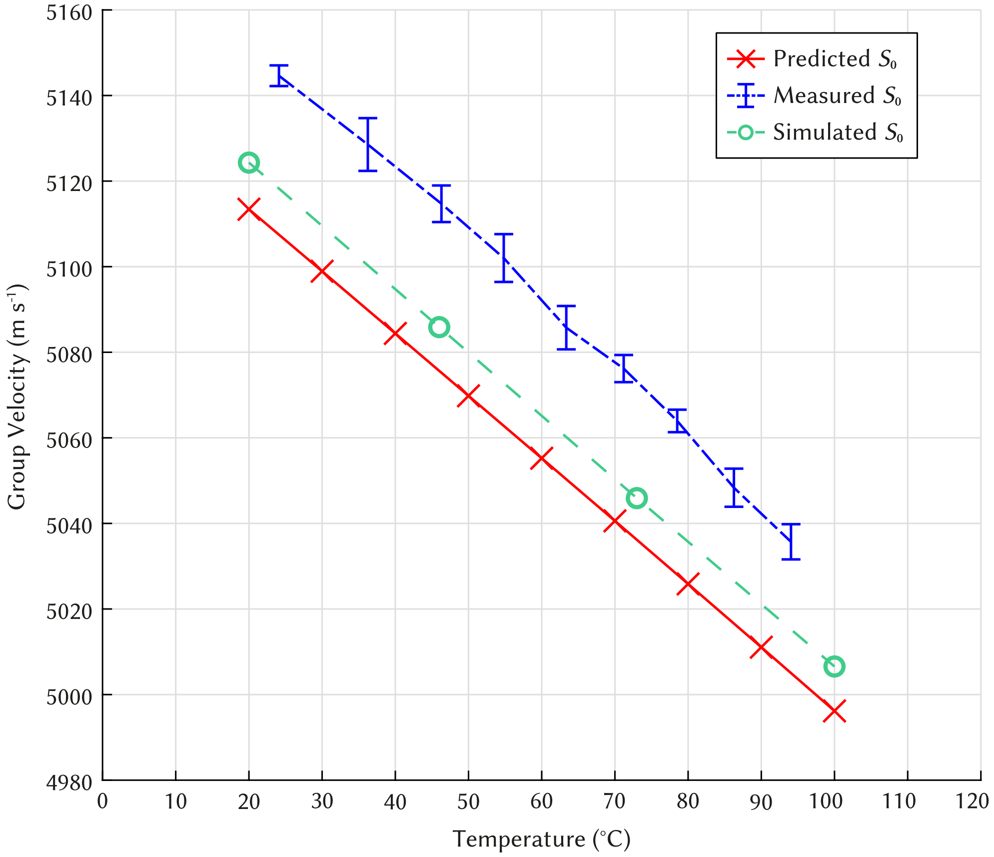

Figure 4.22 – Velocity change with temperature for S_0 Lamb wave mode in Aluminium. Comparison between predicted, experimental, and simulated results. Error bars show measurements that fall within one standard deviation of the mean.

4.4.2.2 A_1 Mode simulations

Figure 4.23 shows the wave propagation of a pulse exciting the A_1 mode at 20°C and 100°C. The black dotted lines indicate the peak of the envelopes used to calculate time of flight. Figure 4.25 shows the change in velocity with temperature for the A_1 Lamb wave mode in Aluminium, comparing predicted temperature sensitivity extracted from dispersion curves, experimental measurement data (Section 4.3.3), and COMSOL simulations of the experimental setup. Error bars show measurements that fall within one standard deviation of the mean. The experimental result is within $49.05 \pm 7.90\ \mathrm{m\,s^{-1}}$ or $1.35\% \pm 0.23\%$ of the predicted velocity on average. The COMSOL results are within $19.22\ \mathrm{m\,s^{-1}} \pm 5.93\ \mathrm{m\,s^{-1}}$ or $0.53\% \pm 0.17\%$ of the predicted result on average. The standard deviation of group velocity across eight wedge spacings (80 mm to 150 mm in 10 mm increments) at the calculated offset value of 46.2 mm is $6.94\ \mathrm{m\,s^{-1}}$, which indicates that the simulation and time of flight measurement method are not producing results as accurately as at S_0.

Figure 4.24 shows the 2D-FFT response of the propagating wave packet. The solid and dashed lines represent the anti-symmetric and symmetric dispersion curves respectively. Almost pure excitation of the A_1 mode is achieved. The presence of the S_0 mode is not evident when analysing the time history shown in Figure 4.23.

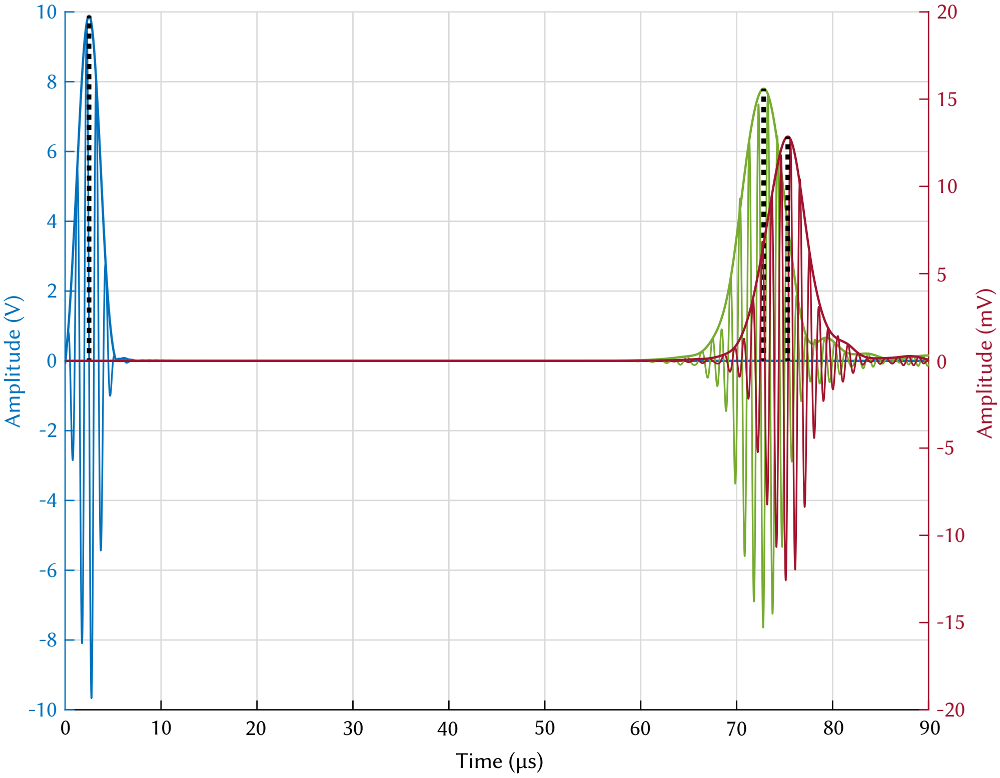

Figure 4.23 – Wave propagation of A_1 Lamb wave mode in Aluminium at 20°C (green) and 100°C (red).

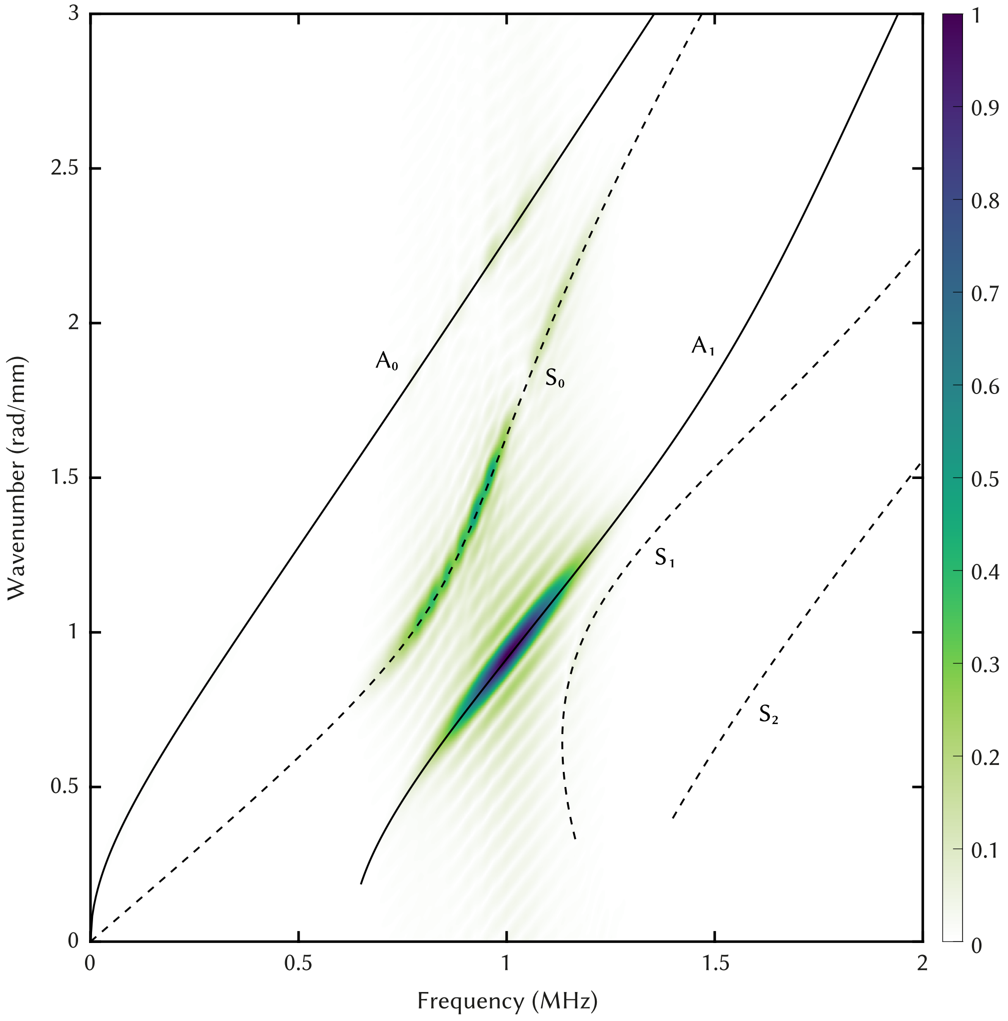

Figure 4.24 – 2D-FFT of A_1 excitation in 2.5 mm thick Aluminium at 20°C. Solid and dashed lines represent numerically calculated dispersion curves. Areas of high intensity (darker colours) show where modes have been detected.

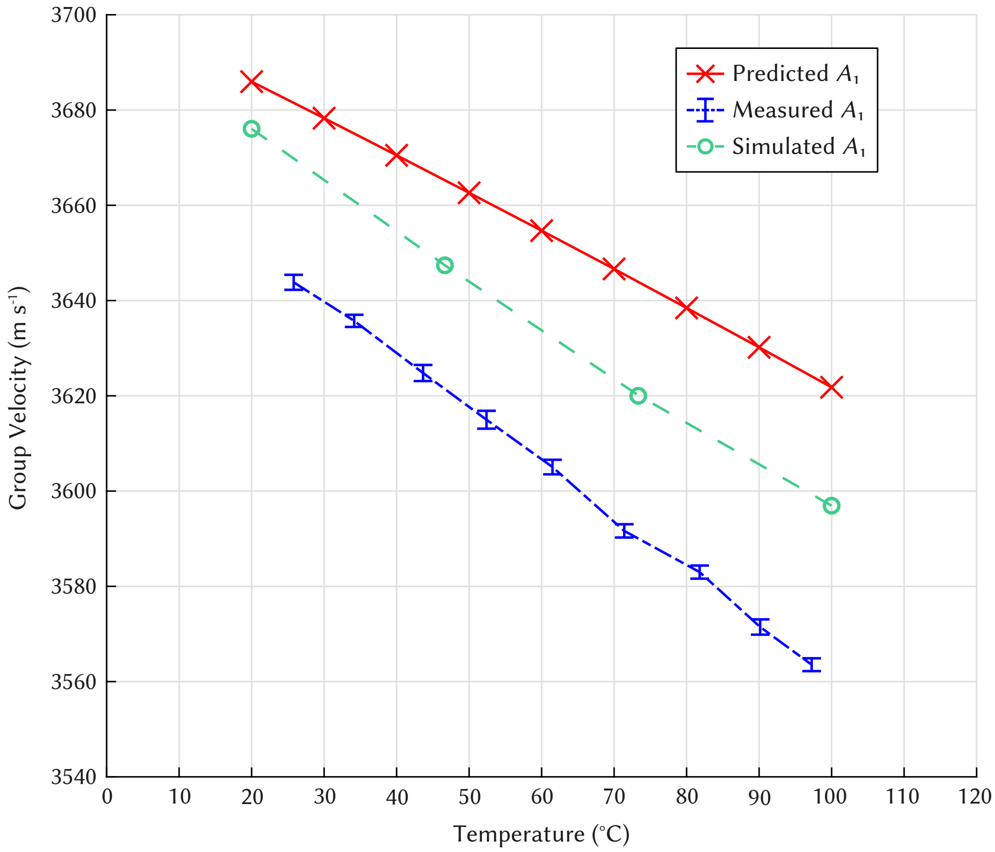

Figure 4.25 – Velocity change with temperature for A_1 Lamb wave mode in Aluminium. Comparison between predicted, experimental, and simulated results. Error bars show measurements that fall within one standard deviation of the mean.

4.4.2.3 S_1 Mode simulations

Figure 4.26 shows the wave propagation of a pulse exciting the S_1 mode at 20°C and 100°C. The black dotted lines indicate the peak of the envelopes used to calculate time of flight. Figure 4.28 shows the change in velocity with temperature for the S_1 Lamb wave mode in Aluminium, comparing predicted temperature sensitivity extracted from dispersion curves, experimental measurement data (Section 4.3.4), and COMSOL simulations of the experimental setup. Error bars show measurements that fall within one standard deviation of the mean. The experimental result is within 60.04 ± 14.00 $\mathrm{m\,s^{-1}}$ or 1.34% ± 0.32% of the predicted velocity on average. The COMSOL results are within 89.83 $\mathrm{m\,s^{-1}}$ ± 13.00 $\mathrm{m\,s^{-1}}$ or 2.01% ± 0.31% of the predicted result on average. The standard deviation of group velocity across six wedge spacings (80 mm to 130 mm in 10 mm increments) at the calculated offset value of 44.69 mm is 7.89 $\mathrm{m\,s^{-1}}$, which indicates that the simulation and time of flight measurement method are not producing results as accurately as at S_0.

Figure 4.24 shows the 2D-FFT response of the propagating wave packet. The solid and dashed lines represent the anti-symmetric and symmetric dispersion curves respectively. The response is dominated by the A_1 mode, which can be seen as the second more dispersive wave packet in Figure 4.26, as it has considerably larger out-of-plane (y-axis) displacement than the S_1 mode. The use of a receiver wedge for the time-of-flight simulations further isolates the S_1 mode, which reduces the amplitude of the A_1 mode to a comparable level to that of S_1.

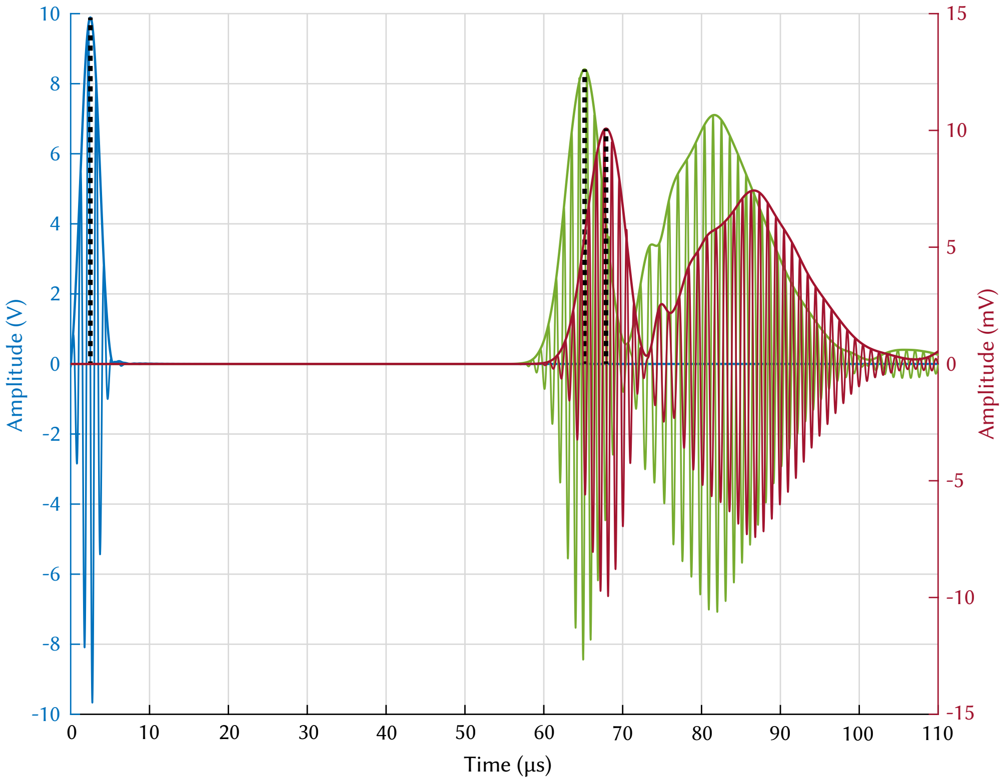

Figure 4.26 – Wave propagation of S_1 Lamb wave mode in Aluminium at 20°C (green) and 100°C (red).

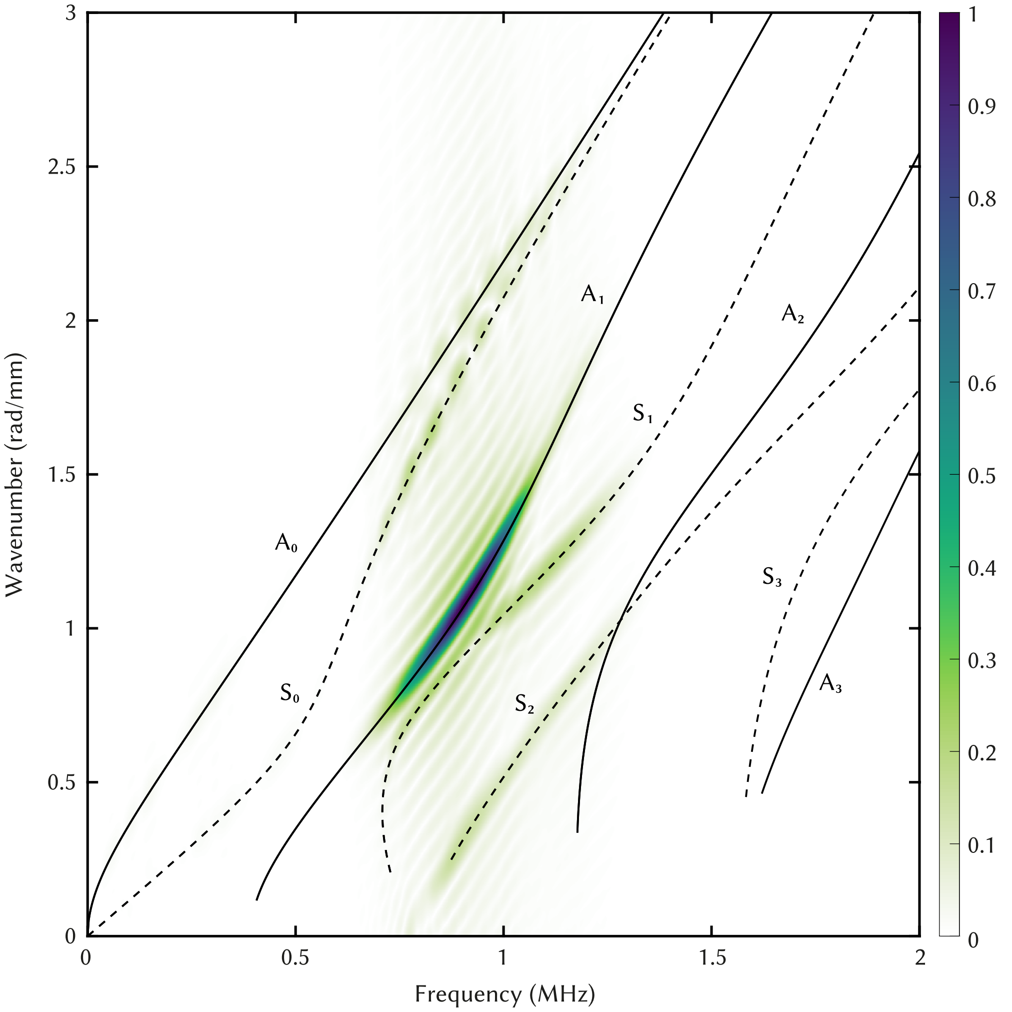

Figure 4.27 – 2D-FFT of S_1 excitation in 4 mm thick Aluminium at 20°C. Solid and dashed lines represent numerically calculated dispersion curves. Areas of high intensity (darker colours) show where modes have been detected.

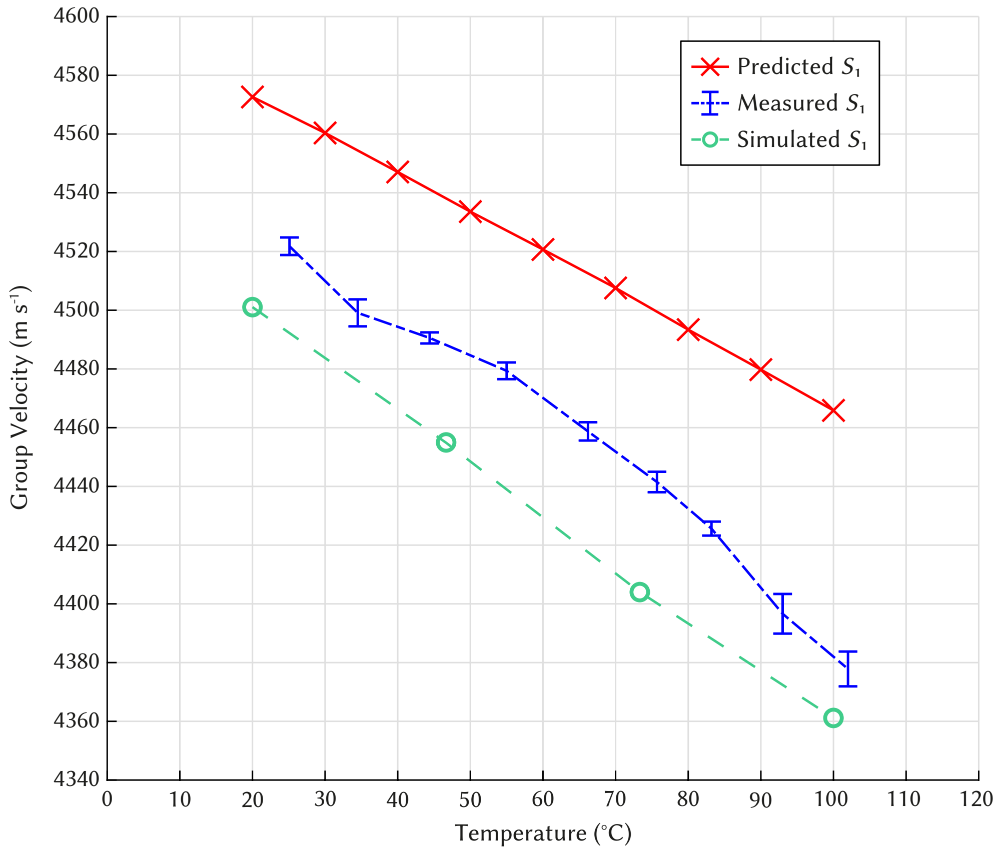

Figure 4.28 – Velocity change with temperature for S_1 Lamb wave mode in Aluminium. Comparison between predicted, experimental, and simulated results. Error bars show measurements that fall within one standard deviation of the mean.

4.5 Inconel 718 simulation study

Applying a guided wave based temperature monitoring system to nozzle guide vanes involves different materials and a higher temperature range than investigated in the previous tests. To test the feasibility of the system (minus an appropriate transducer, complex geometry, and harsh environment) the material of the model has been replaced with Inconel 718, a commonly used superalloy for high temperature aero engine components. The temperature range of the test has been extended to 1027°C. Although the wedges cannot be used in reality for this application, they can still be used in the model for single mode excitation. The heat transfer physics model has been disabled for the wedges, with only the plate affected by a change in temperature. The large temperature range causes a large change to the material properties of the Inconel 718, which in turn causes a large change in wave speed. As the change is so large the wedge angle has to be adjusted to continually target the same area of the frequency-thickness spectrum, as shown in Table 4.9. The longitudinal velocity of the wedge material is 2477 $\mathrm{m\,s^{-1}}$, as measured experimentally.

Temperature (°C)	**Phase velocity** ($\mathrm{m\,s^{-1}}$)	**Wedge angle** (°)
27	5110.74	29.3
227	5020.12	29.9
427	4889.88	30.8
627	4705.97	32.1
827	4450.95	34.2
1027	4090.86	37.7

Table 4.9 – Wedge angle required for S_0 mode excitation in Inconel 718 from 27°C to 1027°C.

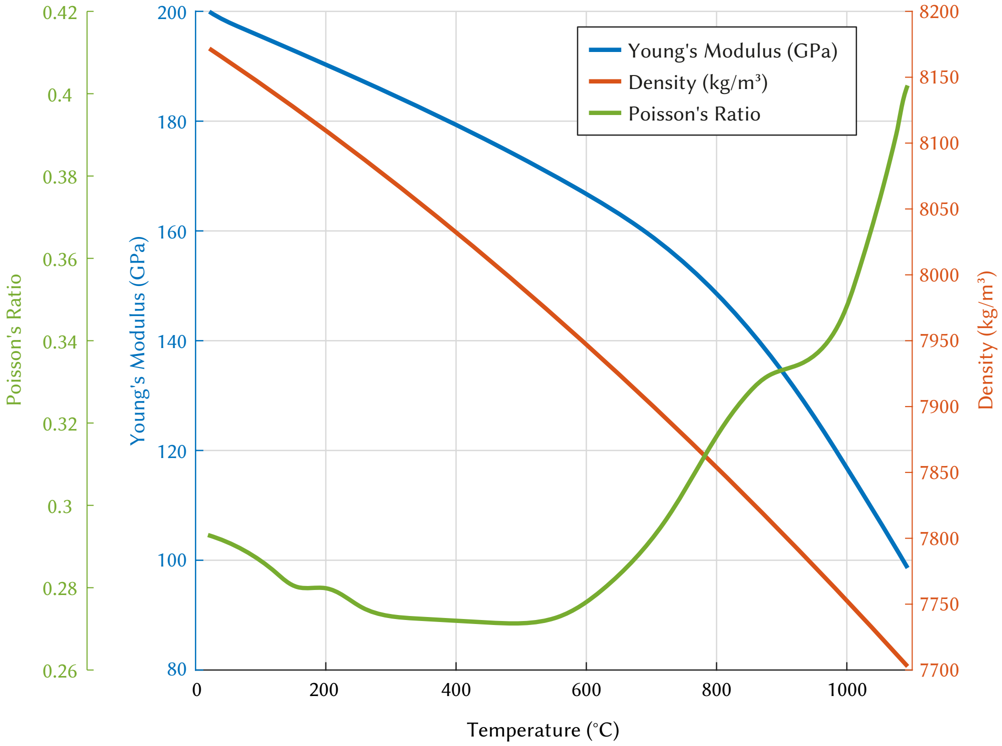

Figure 4.29 – Temperature dependent Young's modulus, density, and calculated Poisson's ratio for Inconel 718 [202, 203].

Figure 4.31 shows the change in group velocity with temperature for the S_0 Lamb wave mode, from 27°C to 1027°C, comparing predicted results extracted from dispersion curves (see Figure 3.10) with simulated results from COMSOL. The average temperature sensitivity for the predicted result is -1.23 $\mathrm{m\,s^{-1}\,{}^{\circ}C^{-1}}$ ± 0.70 $\mathrm{m\,s^{-1}\,{}^{\circ}C^{-1}}$. The average temperature sensitivity for the simulated result is -1.31 $\mathrm{m\,s^{-1}\,{}^{\circ}C^{-1}}$ ± 0.67 $\mathrm{m\,s^{-1}\,{}^{\circ}C^{-1}}$. The temperature sensitivity increases with temperature for both results, from a minimum of -0.37 $\mathrm{m\,s^{-1}\,{}^{\circ}C^{-1}}$ to a maximum of -2.93 $\mathrm{m\,s^{-1}\,{}^{\circ}C^{-1}}$. The simulated group velocity is within 6.78 $\mathrm{m\,s^{-1}}$ ± 27.68 $\mathrm{m\,s^{-1}}$ or 0.10 % ± 0.63% of the predicted group velocity on average.

Table 4.10 shows time of flight data calculated from COMSOL simulations at each temperature step, along with the group velocity calculated using Equation (4.7). Where d_{aligned} is 0.1 m, and d_{offset} is 0.04696 m. The offset value was calculated from simulations of five propagation distances (0.08 to 0.12 m in 0.01 m increments), where the velocity variation at this offset value is 0.012 $\mathrm{m\,s^{-1}}$.

Figure 4.30 shows the wave propagation of a pulse exciting the S_0 mode at 27°C (green) and 1027°C (red). The black dotted lines indicate the peak of the envelopes used to calculate time of flight. As temperature increases the change in material properties causes a dispersion curve shift, and a more dispersive region of the S_0 curve is excited. This can be seen in the response at 1027 °C, where the wave packet is visibly more spread out in comparison to the response at 20 °C.

Temperature (°C)	$t_{\textbf{aligned}}$ (s)	$t_{\textbf{wedge}}$ (s)	**Group velocity** ($\mathrm{m\,s^{-1}}$)
27	5.8906×10^{-5}	2.9615×10^{-5}	5017.13
227	5.9594×10^{-5}	2.9615×10^{-5}	4902.07
427	6.0573×10^{-5}	2.9604×10^{-5}	4745.43
627	6.2063×10^{-5}	2.9604×10^{-5}	4527.65
827	6.4781×10^{-5}	2.9594×10^{-5}	4176.48
1027	6.9208×10^{-5}	2.9552×10^{-5}	3705.85

Table 4.10 – COMSOL simulation data for Inconel 718 model.

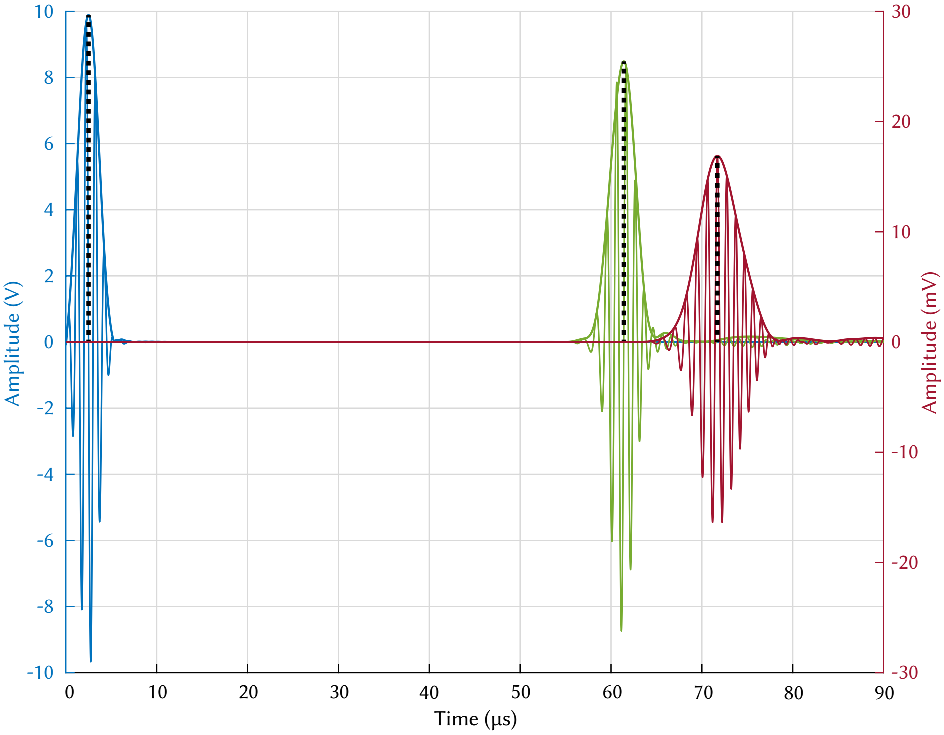

Figure 4.30 – Wave propagation of S_0 Lamb wave mode in Inconel 718 at 27°C and 1027°C.

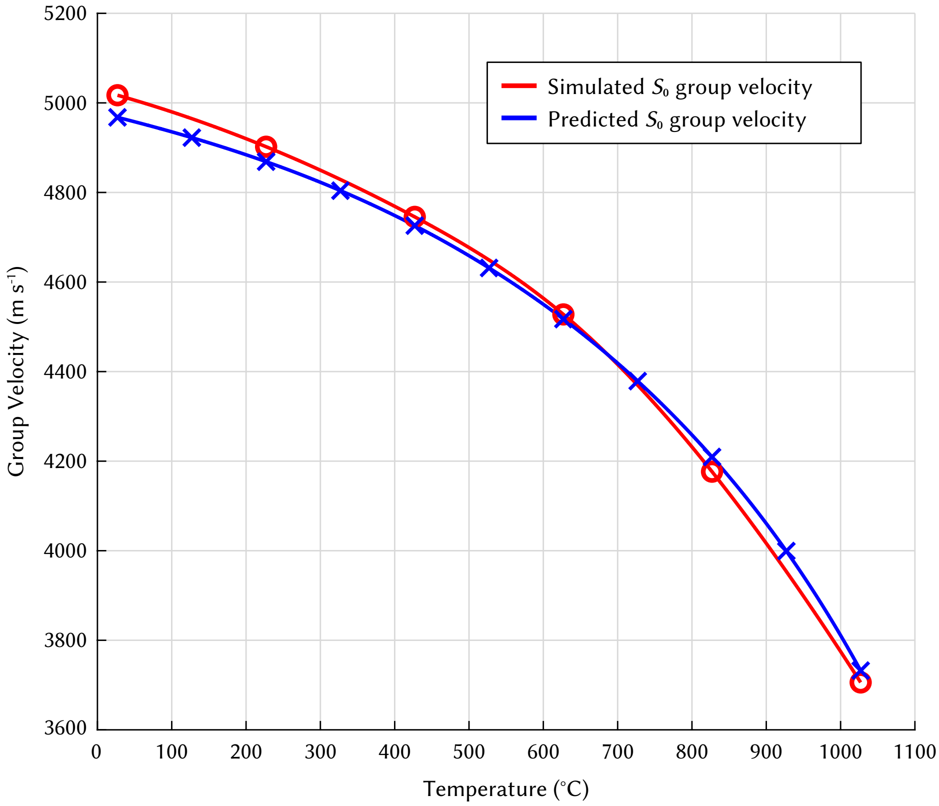

Figure 4.31 – Velocity change with temperature for S_0 Lamb wave mode in Inconel 718.

4.6 Discussion of simulated results

In the previous two sections the effect of temperature on both Aluminium and Inconel 718 has been investigated through COMSOL simulation. Two-dimensional models were used to replicate the experimental system described in Section 4.3, including transmission through a plate to measure overall time of flight, wedge foot offset using a variable wedge spacing, and wedge-to-wedge time by placing wedges directly together.

A range of sources for the material properties of both the wedges (PMMA) and the plate (Aluminium 1050 H14) were considered. A large range of values for the temperature dependant Young's modulus of PMMA were found in literature, which lead to using experimental measurement to deduce more accurate values for this particular system. Longitudinal wave velocity in the wedges was measured, and simulations were carried out at varying values of E until the simulated wave velocity matched that of the experimental measurement. Temperature dependant values were determined by placing the experimental system in an oven and re-measuring wave velocity at elevated temperatures. This provided more accurate values of E than could have been derived from literature. The range of sources for Aluminium were considerably less varied, and so the COMSOL material library was used. The change in wave velocity due to changes in Poisson's ratio or thermal expansion was deemed to be negligible over the temperature range of interest, and were omitted from the simulation. Simple PZT-5H transducers were used to excite the system, operated at their first through-thickness resonant frequency. Heat transfer coefficients for the plate and wedges were determined by comparison to experimental temperature measurements from thermocouples, which were used during the experimental study. Simulations were carried out in two steps to fix the change in material properties due to temperature for the duration of the time-dependant study. The use of 2D-FFT analysis has confirmed the presence of the expected modes, which further verifies the modes excited in the experimental study.

In aluminium the calculated wave velocities closely align with those measured experimentally, as well as those extracted from dispersion curves. All results fall within a 35.93 $\mathrm{m\,s^{-1}}$ range for S_0, a 49.05 $\mathrm{m\,s^{-1}}$ range for A_1, and a 89.60 $\mathrm{m\,s^{-1}}$ range for S_1. The wave packets observed in the time domain closely resemble those measured experimentally. Replicating the geometry of the wedges and plate used in the experimental study, as well as careful selection of material properties, has resulted in an accurate model.

Extending the temperature range of the study up to 1000°C in Inconel 718 also aligns well with predicted velocities extracted from dispersion curves. Both the sensitivity of the mode and the velocity of the mode are in good agreement with prediction. The predicted sensitivity of S_0 is -1.23 $\mathrm{m\,s^{-1}\,{}^{\circ}C^{-1}}$ ± 0.70 $\mathrm{m\,s^{-1}\,{}^{\circ}C^{-1}}$ on average, while the sensitivity calculated from the simulated results is -1.31 $\mathrm{m\,s^{-1}\,{}^{\circ}C^{-1}}$ ± 0.67 $\mathrm{m\,s^{-1}\,{}^{\circ}C^{-1}}$ on average. The simulated group velocity is within 6.78 $\mathrm{m\,s^{-1}}$ ± 27.68 $\mathrm{m\,s^{-1}}$ or 0.10 % ± 0.63% of the predicted group velocity on average. It should be noted however that at higher temperatures dispersion is evident in the signal, which reduces the accuracy of time of flight measurement as there is a less defined central peak to the wave packet.

4.7 Concluding remarks

In this chapter the effect of temperature on ultrasonic guided wave propagation has been investigated through both experimentation and simulation. Experimental work using wedge transducers to target individual modes has measured the group velocity of the S_0, A_1, and S_1 modes in Aluminium plates. Results closely align with values extracted from dispersion curves, even when considering the errors associated with the measurement system. COMSOL simulations replicating the experimental test system were validated against experimental results, and the models have subsequently been used to investigate the effect of temperature up to 1000 °C in Inconel 718 for the S_0 mode. The sensitivity of the S_0 mode is in-line with predicted sensitivity as determined by dispersion curve analysis. Simulations were carried out in two-dimensions to reduce the complexity of the models, which is likely to have an impact on signal attenuation in comparison to the experimental measurements, however changes in amplitude with temperature were not considered in this study. Although the use of wedge transducers is not suitable for permanent installation on nozzle guide vanes (as discussed in Section 4.3.6), the isolation of single modes has allowed their temperature sensitivity to be measured, and the properties of each mode to be evaluated independently.

In the following chapters the effect of cooling hole structures and thermal barrier coatings on wave propagation are investigated through simulation, using models adapted from those developed in this study.

CHAPTER 5

The effect of cooling holes on wave propagation

In this chapter the effect of cooling holes on wave propagation is investigated through experimentation and COMSOL simulation.

As the operating temperature of gas turbines has increased, cooling systems have been employed to allow components to operate above the thermal limits of their materials. This is particularly important for the operation of NGVs, which are exposed to the highest gas path temperatures of the turbine section. A commonly used method of cooling the external surface of turbine blades or NGVs is through film cooling. Air is directed from the engine's compressor through the internal structure of the blade/vane and expelled through an array of holes. This creates a thin layer of relatively cool gas that protects the surface from combustion gases [204].

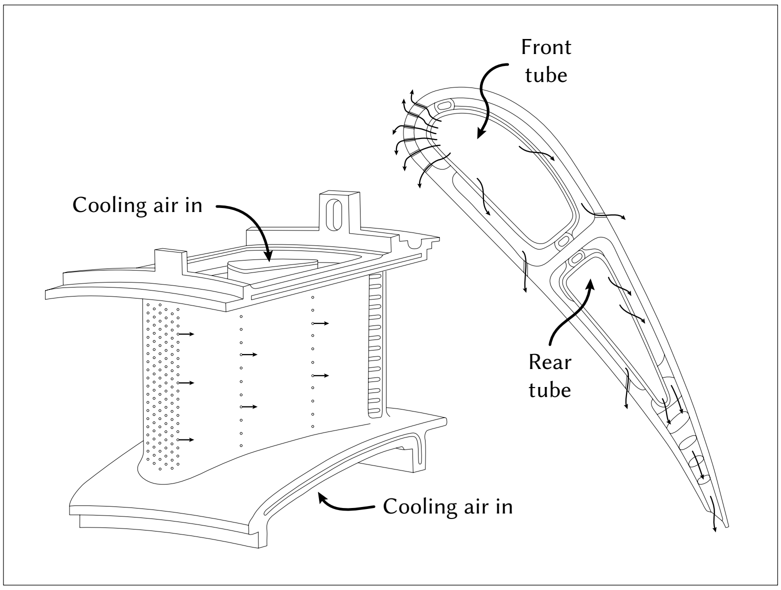

Figure 5.1 – Cross section of typical NGV using film cooling. Arrows indicate direction of cooling airflow.

The holes can vary in diameter from the inside surface to the outside surface, and can be angled to optimally direct gas flow [205]. As the leading edge of the NGV is exposed to the highest temperatures, holes are often more numerous and larger in this area. The diameter of the holes can vary from 0.3–1.5 mm [206, 207], with a spacing between holes ranging from 1× the diameter, to around 7× the diameter [22]. A detailed analysis of film cooling techniques is provided by Irvine *et al.* [208]. The cooling holes found on nozzle guide vanes are often arranged in rows, aligned from the inside edge to the outside edge of the vane. The proximity of the rows to one another often increases towards the leading edge. Each row can have ~30 holes, and there can be ~5 rows in close proximity to the leading edge. The rows can be arranged in-line with one another, or staggered [209]. An example of an NGV from a Rolls Royce RB211-24C engine with cooling holes present can be seen in Figure 5.2.

Figure 5.2 – Photograph of a V2500 high-pressure nozzle guide vane [210]. Used under CC BY-SA 3.0 license.

The scattering of guided waves from defects, flaws, cracks, notches, and holes, has been investigated by a number of authors [211, 212, 213, 214, 215]. In these studies the scattering from a single feature is investigated, however the range of literature concerning hole arrays is much less comprehensive. Acoustic metamaterials, in particular phononic crystals, utilise periodic structures (such as holes) to control wave propagation [216]. Band gaps can be created that limit wave propagation over a particular frequency range. A selection of phononic crystal devices for guided waves are described by Jin *et al.* [217]. These systems are often used as filters, waveguides [218], and for aircraft sound absorption [219].

In the next section the the effect of hole size on reflection amplitude is investigated experimentally. A pseudo-pulse-echo transducer configuration is introduced. This is followed by an investigation into how arrays of cooling holes will affect wave propagation through COMSOL simulation. A number of models are used to replicate the dense array of holes typically found at the leading edge of a vane, as well as the towards the trailing edge of the vane, where a reduced number of holes are present. Both pulse-echo and pitch-catch configurations are considered. The ability to detect temperature hotspots is investigated for both regions.

5.1 The effect of hole size on reflection amplitude

The change in reflected signal amplitude with respect to hole size is investigated in this section. A simplified case is considered, using aluminium plates. Two wedge transducers are arranged in a pulse-echo configuration, whereby the wedges are placed close to one another, one acting as the transmitter and one as the receiver. A single transducer setup was considered however the difference in amplitude between the excitation signal (10 V) and reflected signal (~50 mV) makes digitisation difficult, without either losing the reflected signal in noise or overloading the excitation input. By using two transducers the sensitivity of each channel can be adjusted to match the signal amplitude accordingly. A 3D printed spacer has been designed to allow transducers to be accurately and repeatably aimed at a hole. The angle of incidence/reflection can easily be adjusted. In this configuration a reflection is received from the hole, followed by a stronger reflection from the edge of the plate. The angle between transducers is kept at a minimum to most closely mimic a pulse-echo configuration using only one transducer.

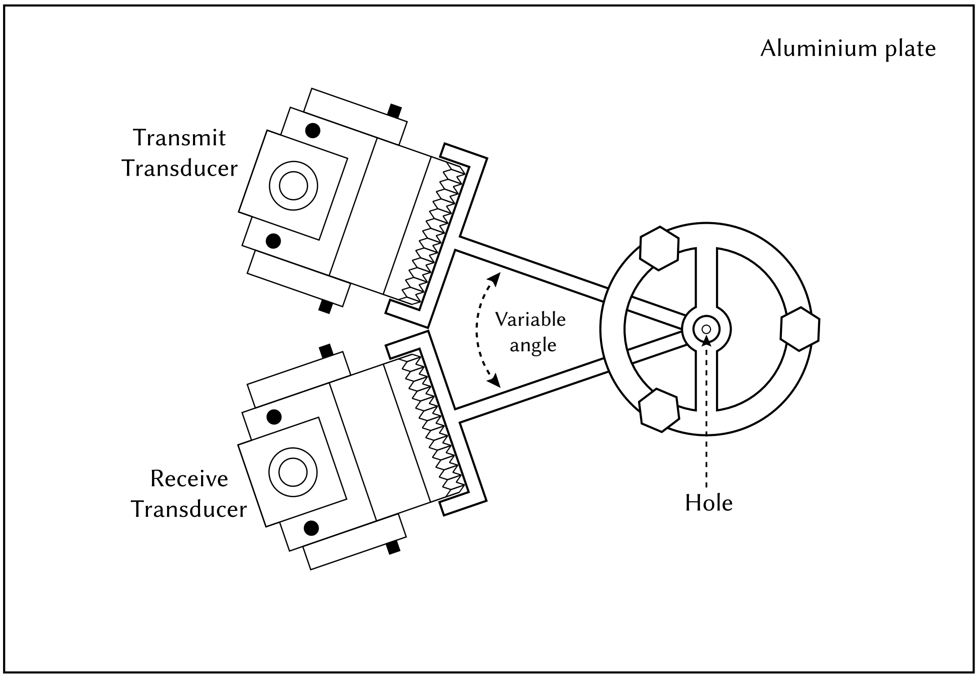

Figure 5.3 – Diagram of single hole reflection measurement setup, showing wedge transducers and 3D-printed spacer to control reflection angle.

5.1.1 Determination of transmission distance

As the calculation of group velocity is dependant on accurate knowledge of the distance between transducers, an initial test is carried out to determine the distance from transmitter to receiver via hole reflection. Firstly, the transducers are aligned on axis with no hole present, spaced apart by 100 mm (as in previous experiments) and time of flight is measured (t_{aligned}). The wedge-to-wedge time (t_{wedge}) and offset distance (d_{offset}) are also measured, as described in Section 4.3. The group velocity (v) can now be calculated using Equation 5.1. Next, the time of flight from a reflection is measured ($t_{\text{reflected}}$), as shown in Figure 5.3. Now the distance travelled in the plate between transducer faces ($d_{\text{reflected}}$) can be calculated (Equation 5.3) by multiplying the velocity (v) by the reflected time of flight ($t_{\text{reflected}}$) minus the wedge-to-wedge time of flight (t_{wedge}), minus the offset distance (d_{offset}). Calculation of this distance allows a change in velocity with temperature to be measured using time of flight methods.

$$v = \left(\frac{d_{\text{aligned}} + d_{\text{offset}}}{t_{\text{aligned}} - t_{\text{wedge}}}\right) \qquad [\mathrm{m\,s^{-1}}] \qquad (5.1)$$

$$5099.18 = \left(\frac{0.1 + 0.04587}{5.812{\times}10^{-5} - 2.951{\times}10^{-5}}\right) \qquad [\mathrm{m\,s^{-1}}] \qquad (5.2)$$

$$d_{\text{reflected}} = v \times \left(t_{\text{reflected}} - t_{\text{wedge}}\right) - d_{\text{offset}} \qquad [\mathrm{m}] \qquad (5.3)$$

$$0.178 = 5099.18 \times \left(7.335{\times}10^{-5} - 2.951{\times}10^{-5}\right) - 0.04587 \qquad [\mathrm{m}] \qquad (5.4)$$

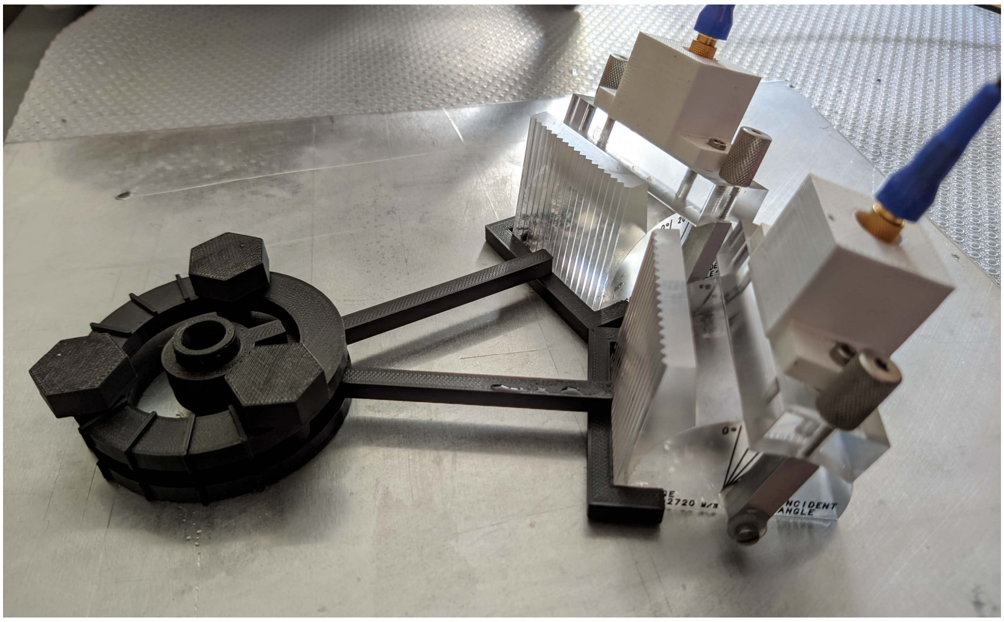

Figure 5.4 – Photo of single hole reflection measurement setup, showing wedge transducers and 3D-printed spacer to control reflection angle. The spacer is centred on a hole in the aluminium plate.

5.1.2 The effect of hole size on signal amplitude

The setup shown in Figure 5.3 is used to compare the difference in reflection amplitude between different hole sizes. The tests are carried out on three different plate thicknesses (1 mm, 2.5 mm, and 4 mm), targeting three different Lamb wave modes (S_0, A_1, and S_1 respectively). The signal amplitude is highly dependant on the coupling between wedges and plate, so fresh couplant is applied for every test, and an average amplitude is calculated after multiple removals and replacements of the wedges. The reflection angle (36°) and distance (0.178 m) between transducers is kept consistent across all measurements. A 60 dB voltage amplifier is applied to the receiver transducer. Reflection amplitude is measured at hole sizes of 1.5 mm, 2 mm, 2.5 mm, 3 mm, 3.2 mm, 3.5 mm, and 4 mm. Absolute peak amplitude is measured using MATLAB. The wedges were removed from the plate and the couplant was reapplied five times for each hole size, taking ten measurements per reapplication, for a total of fifty measurements per hole size. The edges of the holes were deburred on both sides of the plate after every new hole was drilled.

5.1.2.1 S_0 Result

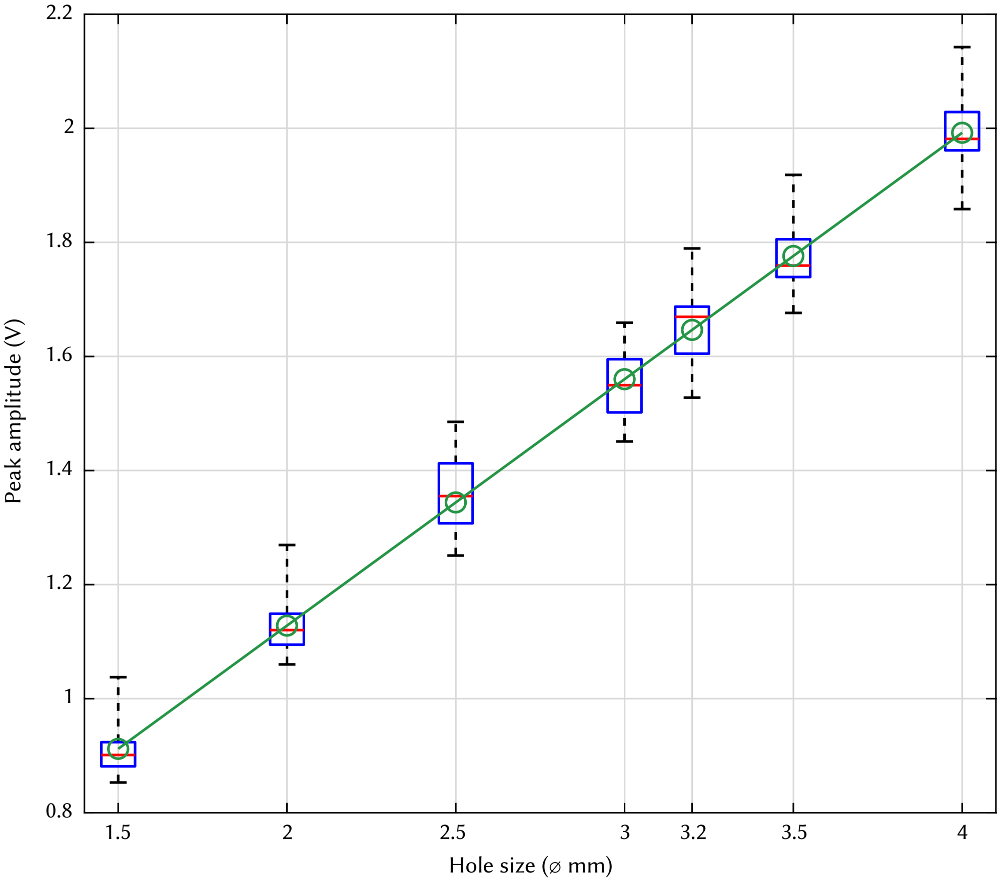

Figure 5.5 – Boxplot showing change in reflection signal amplitude with hole size for the S_0 mode at 1 MHz-mm. Reflection angle of 36°. The green trace shows linear regression.

Results for the S_0 mode are shown in Figure 5.5. There is a linear relationship ($R^2 = 0.9994$) between increasing hole size and increasing amplitude, as shown by the green trace. The average increase in amplitude for a ⌀ 0.5 mm change in hole size is 0.216 V ± 0.014 V.

5.1.2.2 A_1 Result

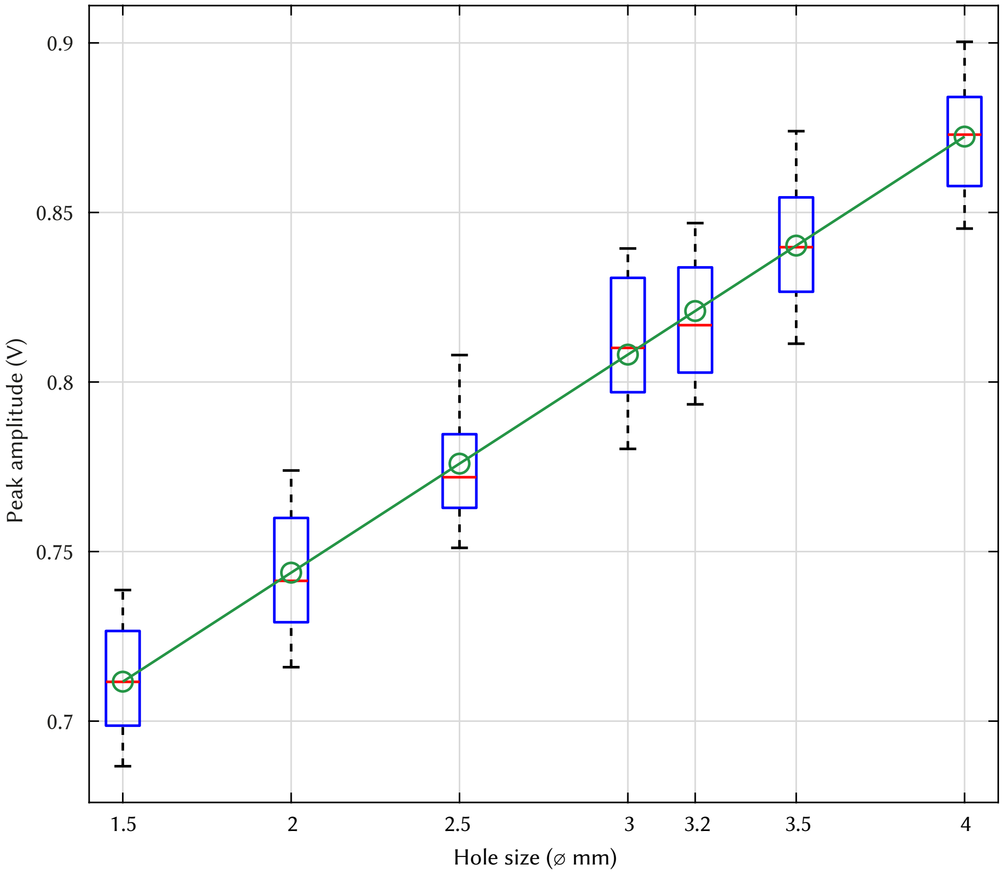

Figure 5.6 – Boxplot showing change in reflection signal amplitude with hole size for the A_1 mode at 2.5 MHz-mm. Reflection angle of 36°. The green trace shows linear regression.

Results for the A_1 mode are shown in Figure 5.6. There is a linear relationship ($R^2 = 0.9981$) between increasing hole size and increasing amplitude, as shown by the green trace. The average increase in amplitude for a ⌀ 0.5 mm change in hole size is 0.034 V ± 0.05 V.

5.1.2.3 S_1 Result

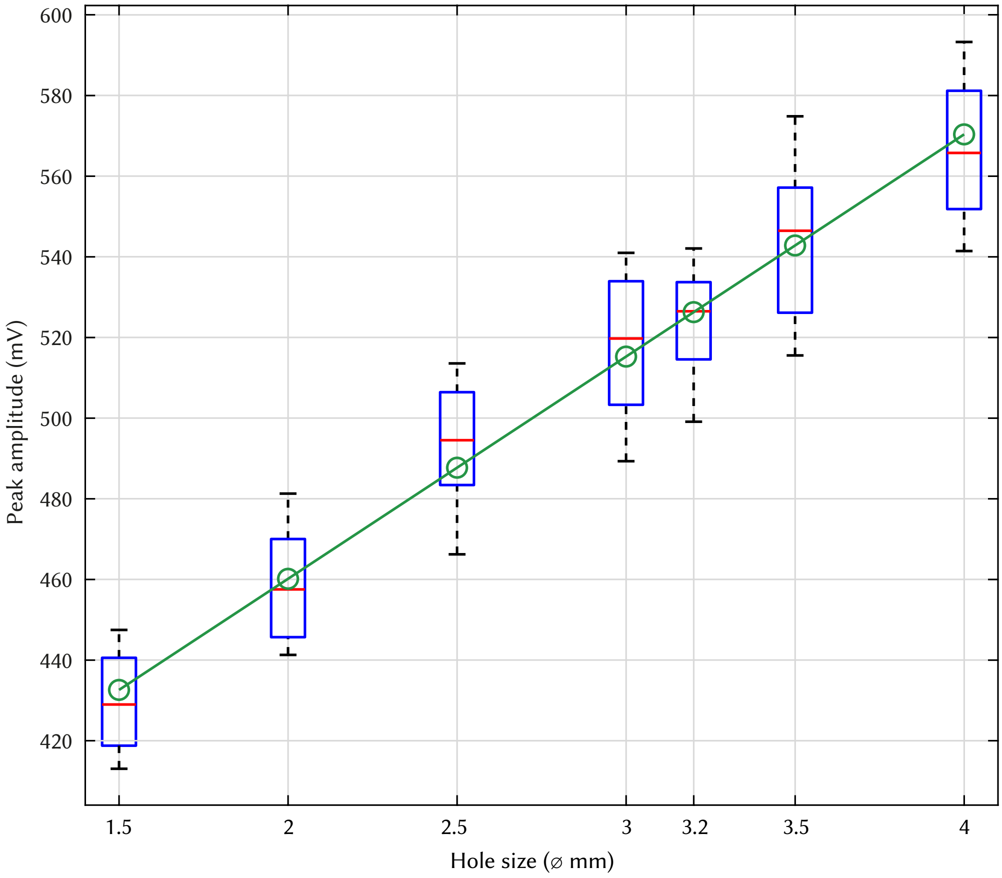

Figure 5.7 – Boxplot showing change in reflection signal amplitude with hole size for the S_1 mode at 4 MHz-mm. Reflection angle of 36°. The green trace shows linear regression.

Results for the S_1 mode are shown in Figure 5.7. There is a linear relationship (R^2 = 0.9909) between increasing hole size and increasing amplitude, as shown by the green trace. The average increase in amplitude for a ⌀ 0.5 mm change in hole size is 0.027 V ± 0.03 V.

5.1.3 Discussion of experimental results

The S_0 mode is significantly more sensitive to changes in hole size than the A_1 or S_1 modes. The large in-plane displacement of the S_0 mode (Figure 4.2a) is very sensitive to defects at any depth (such as holes), whereas the A_1 and S_1 modes (Figures 4.2b and 4.2c respectively) exhibit a lower sensitivity due to their middle thickness nodes. Results are in line with those reported by Jeong *et al.* [220]. The increased sensitivity of the S_0 mode may be advantageous in differentiating between different hole sizes on an NGV, where the holes along the leading edge of the vane may use a different geometry than the rest of the holes. Overall the results suggest that signals reflected from holes with diameters comparable with those found on NGVs, and at wavelengths comparable with hole sizes, would be detectable in a pulse-echo configuration.

5.2 Wave propagation across the leading edge

A 3-dimensional COMSOL model has been developed to investigate the effect of cooling holes on wave propagation. The general effect on wave propagation with multiple holes present is investigated. The plausibility of monitoring temperature changes at multiple locations is also investigated. Additional simulations are carried out at higher temperatures.

When considering the appropriate excitation frequency for this application, careful attention should be paid to the wavelength in relation to the size of holes and the spacing between them [221]. Another element to consider is the length of the excitation signal in relation to the first received reflection, as using a higher frequency signal with a shorter wavelength means transducers can be placed closer to the first hole. Figure 5.8 shows the relationship between wavelength and frequency for the first four symmetric/antisymmetric modes in a 1 mm thick Inconel 718. It can be seen that S_0 below the cut-off frequency of A_1 (1.6 MHz) has a substantially longer wavelength than that of A_0. At a frequency of 1 MHz the wavelength of S_0 is 5.12 mm in comparison to 2.28 mm for A_0. Although this appears to make A_0 more suitable, the temperature sensitivity of the mode is considerably less than that of S_0, which should also be taken into account.

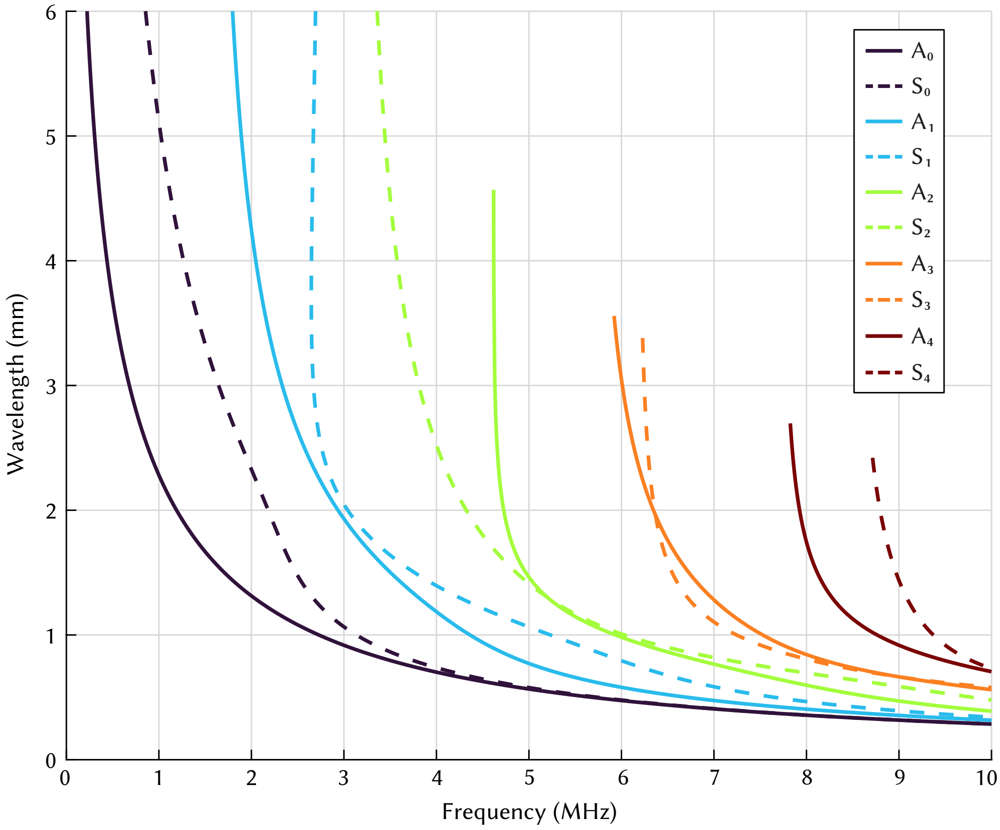

Figure 5.8 – Wavelength in relation to frequency for modes propagating in 1 mm thick Inconel 718. Solid lines represent antisymmetric modes, dashed lines represent symmetric modes.

Two scenarios are considered in the following sections. Firstly, wave propagation along the leading edge of the vane. This area is exposed to the highest temperatures which results in the densest array of cooling holes. This is likely to have a considerable impact on wave propagation. The ability to detect a temperature hotspot along the leading edge is also explored using the same model. Secondly, the area towards the trailing edge of the vane is considered. This area is generally less geometrically complex, which may allow distinct acoustic reflections from the cooling holes to be detected. The plausibility of using these reflections for temperature monitoring at different locations is discussed.

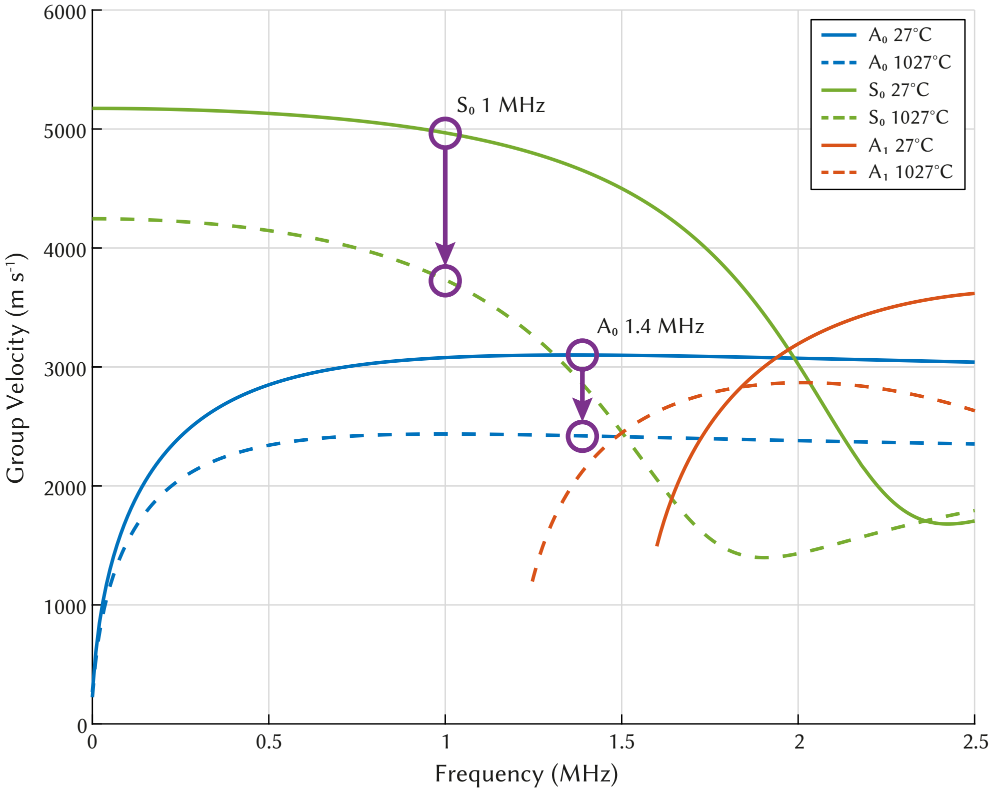

Figure 5.9 – Group velocity dispersion curves for Inconel 718 at 27°C (solid lines) and 1027°C (dashed lines). Purple regions indicate areas of the spectrum targeted.

Figure 5.9 shows group velocity dispersion curves for Inconel 718 at 27°C and 1027°C, where purple regions indicate areas of the spectrum targeted in this study. The average temperature sensitivity of the A_0 mode at 1.4 MHz is 0.68 $\mathrm{m\,s^{-1}\,{}^{\circ}C^{-1}}$ ± 0.34 $\mathrm{m\,s^{-1}\,{}^{\circ}C^{-1}}$, where the sensitivity increases from 0.26 $\mathrm{m\,s^{-1}\,{}^{\circ}C^{-1}}$ at 27°C, rising to 1.42 $\mathrm{m\,s^{-1}\,{}^{\circ}C^{-1}}$ at 1027 °C. The S_0 mode at 1 MHz has almost double the sensitivity on average, 1.24 $\mathrm{m\,s^{-1}\,{}^{\circ}C^{-1}}$ ± 0.67 $\mathrm{m\,s^{-1}\,{}^{\circ}C^{-1}}$, where the sensitivity increases from 0.52 $\mathrm{m\,s^{-1}\,{}^{\circ}C^{-1}}$ at 27°C, rising to 2.77 $\mathrm{m\,s^{-1}\,{}^{\circ}C^{-1}}$ at 1027°C.

The first model to be evaluated consists of a 1 mm thick Inconel 718 plate, with 3 rows of 20 cooling holes, imitating the configuration commonly found along the leading edge of an NGV. Each hole has a diameter of 1 mm, and are spaced 2 mm apart. Each row is offset from the adjacent row by 1 mm in the x-axis. As the most probable location for the attachment of transducers is on either the inside or outside edge of the vane, excitation is set to occur at the end of a row of cooling holes, at the edge of the plate. A number of probes are placed on the opposite edge of the plate, staggered along the y-axis, to act as receivers in a pitch-catch configuration. The simulations are repeated staggering the excitation point along the y-axis. Both the the A_0 at 1.4 MHz and S_0 at 1 MHz are targeted using two-sided excitation. This allows the response of the A_0 mode at a considerably shorter wavelength to be compared with S_0, as discussed previously. Below is a list of models used in the simulations, where the geometry of each model is shown in Figure 5.11:

- 1×1 - Single hole. Middle row position.
- 3×1 - Three holes along y-axis, middle row offset by +1 mm along x-axis.
- 3×2 - Additional three holes along x-axis.
- 3×5 - Three rows of five holes along x-axis.
- 3×10 - Three rows of 10 holes along x-axis.
- 3×20 - Three rows of 20 holes along x-axis.

A swept mesh is used for the bulk of the plate, which dramatically reduces the number of domain elements in comparison to using a tetrahedral mesh. Ten elements per wavelength are used throughout the model. The area around each hole is meshed using tetrahedral elements (in a box measuring 2× the diameter of the hole), to ensure that the geometry of the hole is represented accurately, and the edges of the holes are meshed using 10 fixed elements. With one hole present the average element quality is 0.991. The mesh elements of the 3×20 model are shown in Figure 5.10.

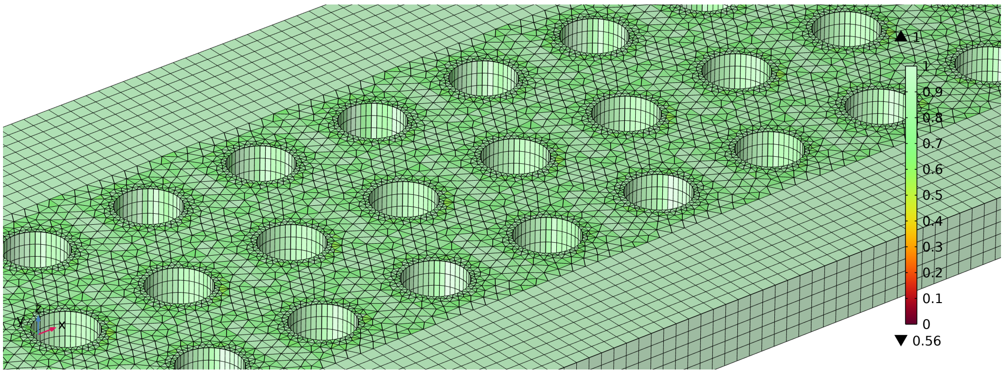

Figure 5.10 – Mesh elements of 3×20 model. Green indicates skewness quality close to 1.

To reduce the complexity of the model, and therefore computation time, transducers are omitted from the model. Using a prescribed displacement node as both a transmitter and a receiver is not normally possible, as the displacement is clamped at zero after the excitation, acting like a fixed and rigid boundary. There are two methods of avoiding this. One is to use a boundary/point load to apply a force in the z-axis, which allows the boundary/point to freely deform after excitation. Another option is to split the study in to two steps, where the first step only covers the time required for excitation, and the second step covers the rest of the simulation. As no excitation occurs in the second step, the point/boundary is able to freely deform and act as a receiver. For this study point loads are used.

Point probes are placed on the far edge of the plate, to act as receivers. This allows both pulse-echo and pitch-catch configurations to be analysed. Displacement in the z-axis is measured in all cases. Low reflecting boundaries are applied to all four edges to dissipate edge reflections, which ensures that only reflections from the holes are present. The amplitude of the input signal in all cases is 1×10^{-3} nm. 2D-FFT analysis has been carried out by extending the length of the plate past the array of holes to accommodate 60 point probes spaced 0.4 mm apart. This spacing allows for a maximum wavenumber of 8 rad/mm, which ensures that the lowest order modes are captured. y-axis displacement is measured for all probes.

Section 5.2.1 considers the reflected response from the array of cooling holes, when the excitation point is operated in a pulse-echo configuration. Section 5.2.2 considers the transmitted response from the excitation point to the receiver point when operated in a pitch-catch configuration.

5.2.1 Reflected response at excitation point

The response measured at the central excitation point for models with varying numbers of holes is shown in Figure 5.12 for S_0, and Figure 5.13 for A_0. The first 10 µs of the signal where the excitation signal is present has been removed, leaving only the reflected signals. The S_0 wave packet is received considerably faster than A_0, due to the difference in group velocity of ~2000 m s^{-1} (see Figure 5.9). The reflection amplitude of A_0 is significantly larger than that of S_0, and is substantially larger with three holes (3×1) over one (1×1). In both cases the first reflection is received faster when three holes are introduced over one, as the outer rows of holes are shifted towards the excitation point by 1 mm. The introduction of a second row (3×1 > 3×2) produces a distinct second wave packet, which is of larger amplitude than the first. The addition of more rows past the first two rows does not have a significant impact on the reflected signal for either mode, which suggests that the signal is not propagating further than the first few rows of holes. This limits the use of a pulse-echo system operated in an area of dense holes such as the leading edge, unless the temperature at the edges of the vane are of interest.

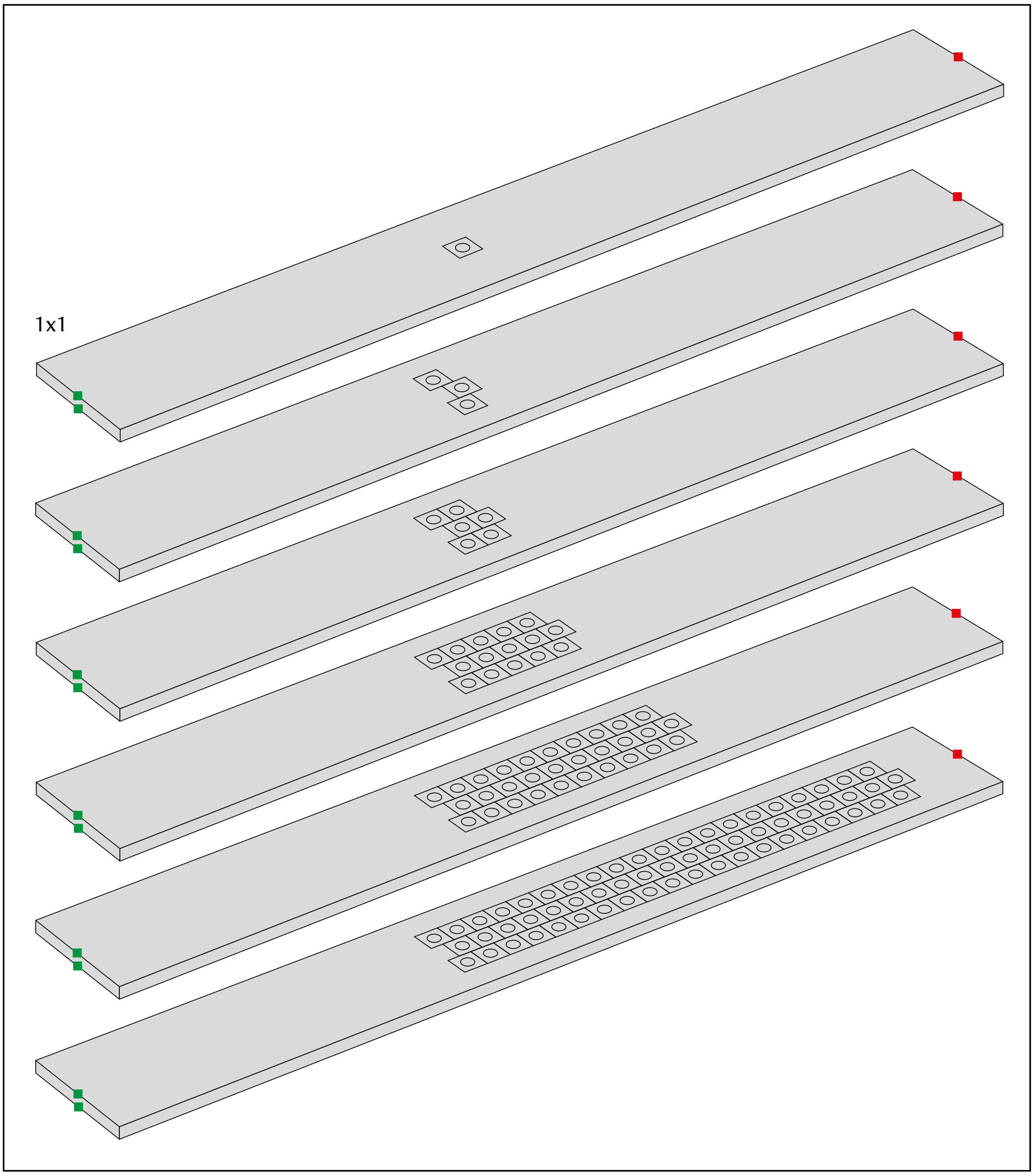

Figure 5.11 – Geometry of COMSOL models with an increasing number of holes. The green squares indicate the excitation points, while the red squares indicate the receiver points. Each model is named based on the hole arrangement (e.g. 1×1, 3×1, etc.)

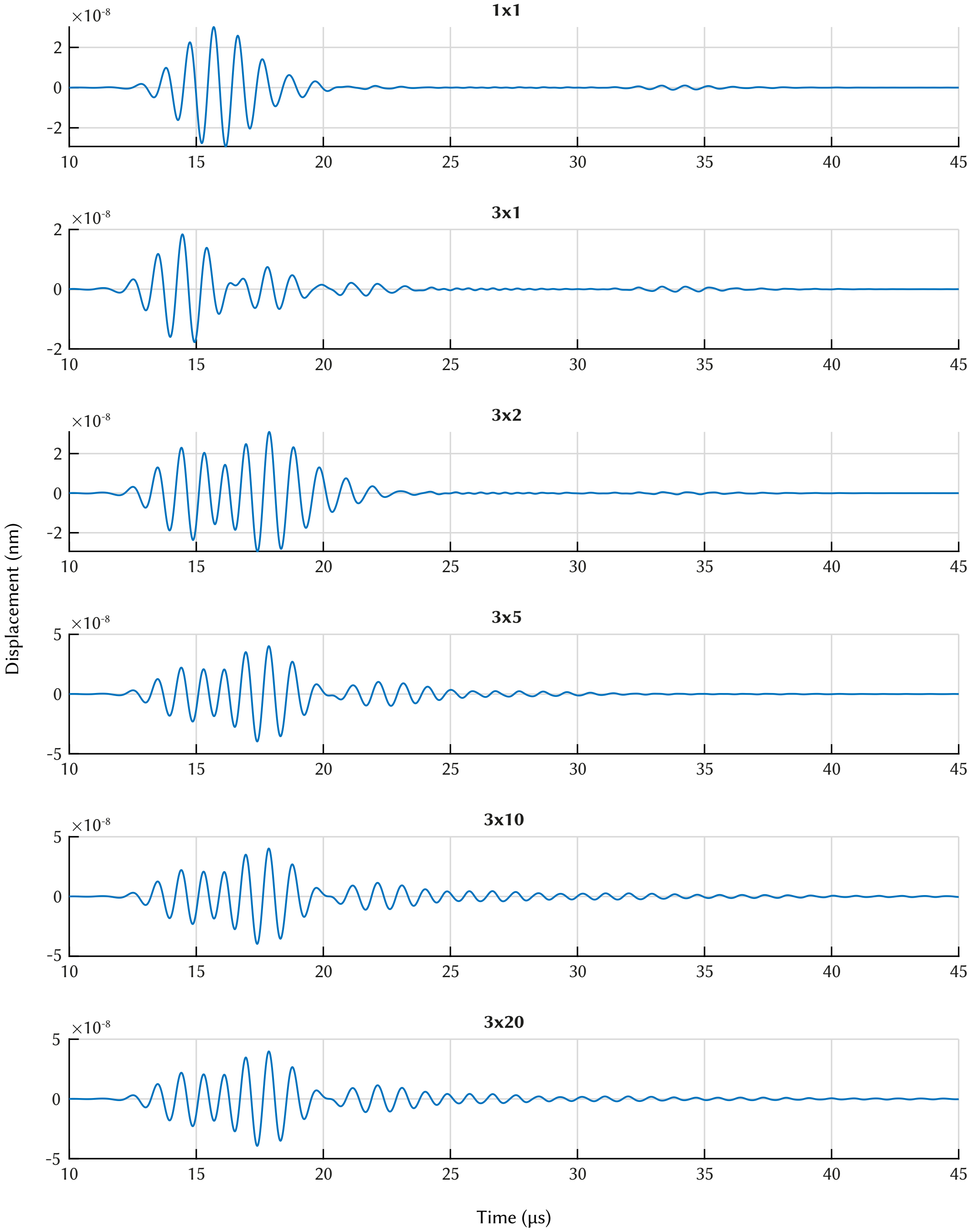

Figure 5.12 – Reflected response of S_0 at 1 MHz with a varying number of holes at 20°C.

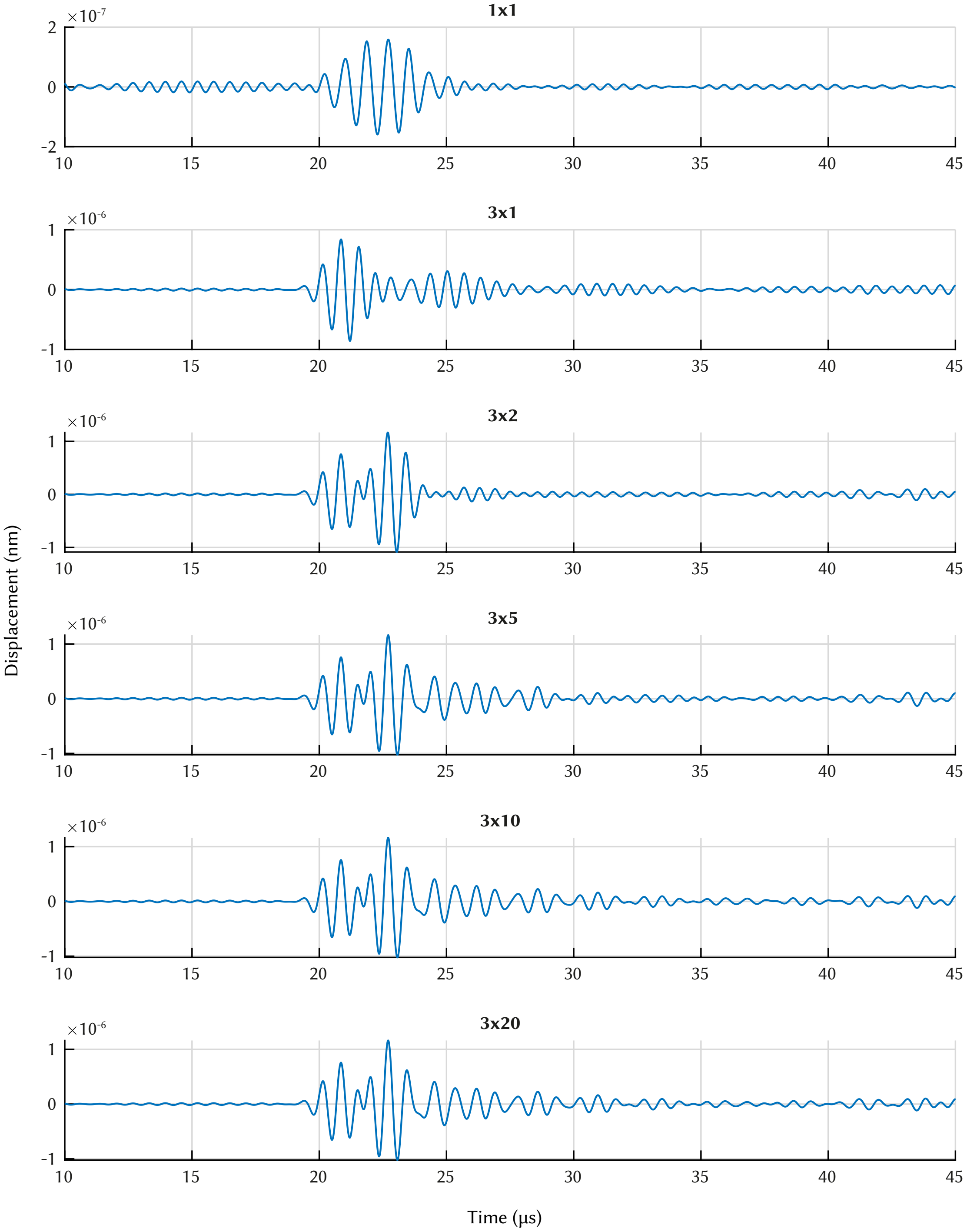

Figure 5.13 – Reflected response of A_0 at 1.4 MHz with a varying number of holes at 20°C.

5.2.2 Output point transmitted response

The response measured at the central receiver point for models with varying numbers of holes is shown in Figure 5.14 for S_0, and Figure 5.15 for A_0. The S_0 wave packet is received considerably faster than A_0, due to the difference in group velocity of ~2000 $\mathrm{m\,s^{-1}}$ (see Figure 5.9). The amplitude of A_0 is substantially higher than that of S_0. In both cases the amplitude reduces with an increasing number of holes. The addition of more rows has a substantial impact on the propagation of S_0, causing a severely dispersive wave packet with no defined peak as the number of holes increased past 3×2. This suggests that a time of flight based monitoring system would not be applicable in this case, as the accuracy of such a system would be severely diminished by such a wide peak. The response of A_0 is substantially less affected, and the signal closely resembles the input signal, followed by a number of reflections. This suggests that A_0 at 1.4 MHz is more applicable for use in a pitch-catch configuration that S_0 at 1 MHz.

The plausibility of using the A_0 mode at 1.4 MHz for monitoring temperature across the leading edge is investigated in the next section, followed by an investigation into the ability to detect temperature hotspots with the system.

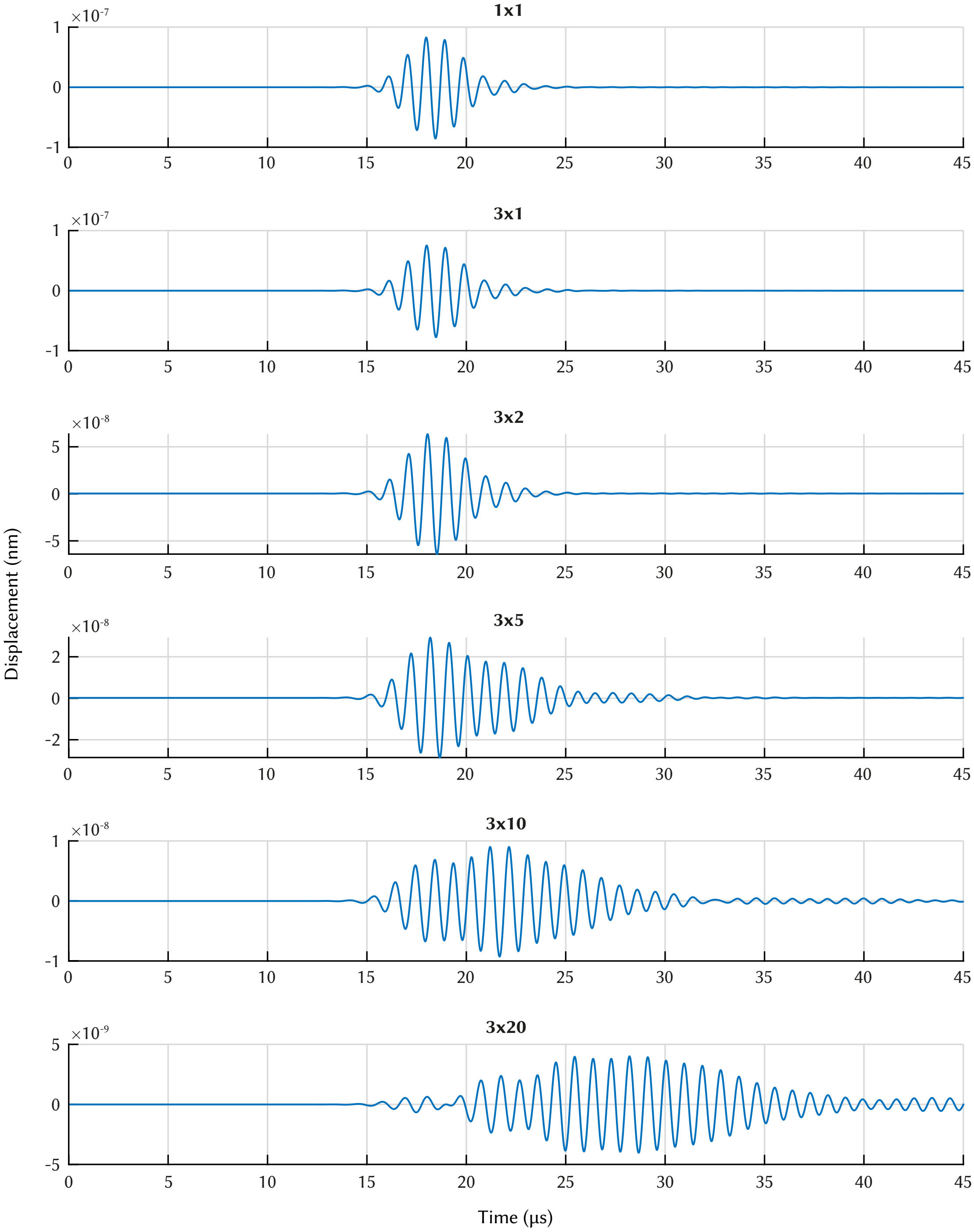

Figure 5.14 – Transmitted response of S_0 at 1 MHz with a varying number of holes at 20°C.

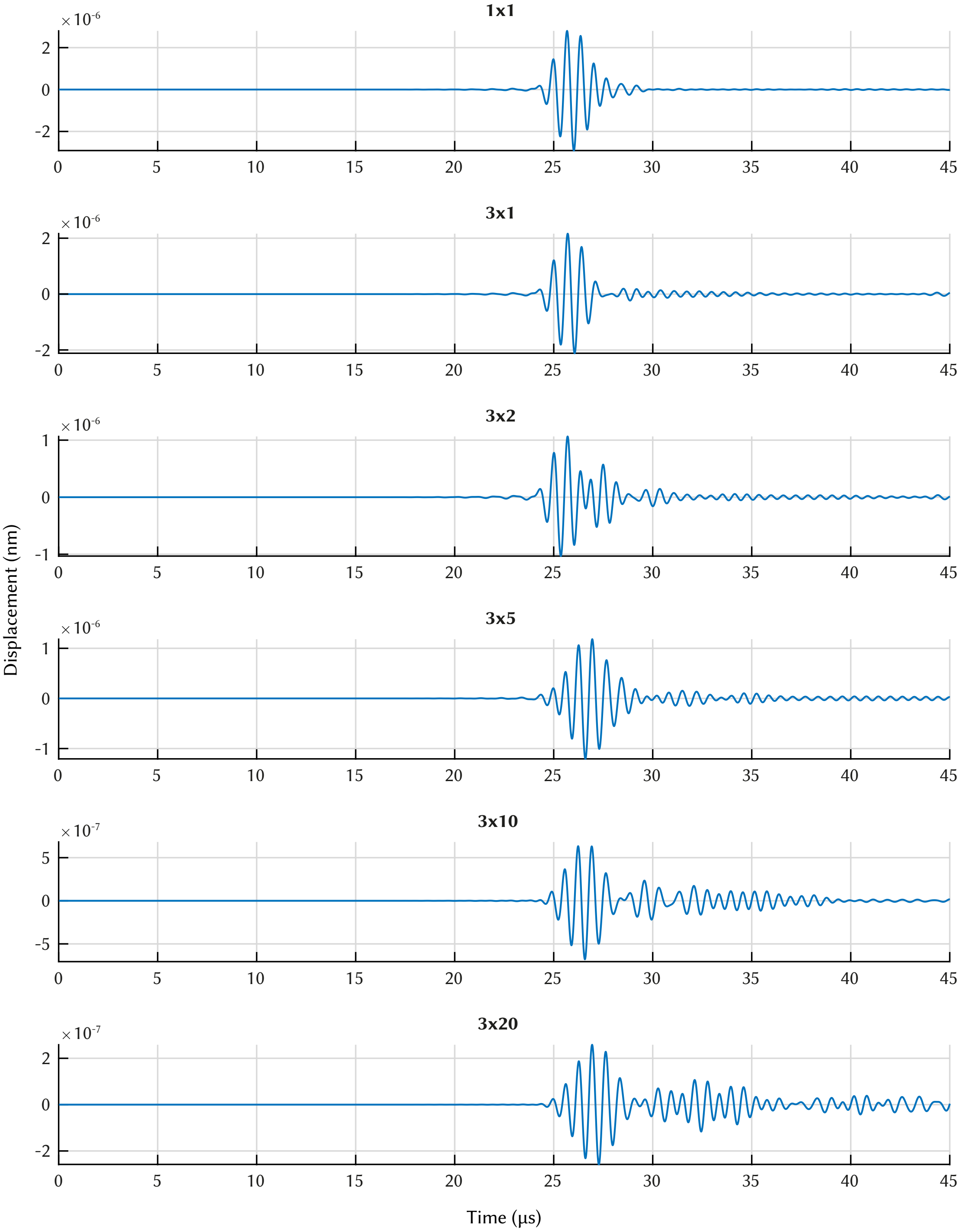

Figure 5.15 – Transmitted response of A_0 at 1.4 MHz with a varying number of holes at 20°C.

5.2.3 Temperature monitoring using the A_0 mode

The 3x20 model used previously has been used to investigate the effect of temperature on wave velocity, through repeated simulations at temperatures ranging from 27°C up to 1027°C. Wave velocities calculated from time of flight measurements are compared to predicted wave velocities extracted from dispersion curves.

Figure 5.17 shows the change in group velocity with temperature for A_0 at 1.4 MHz from 27°C to 1027°C, comparing predicted and simulated results. Results show the predicted relationship between wave velocity and temperature, however the overall result is on average ~130 $\mathrm{m\,s^{-1}}$ slower than the values extracted from dispersion curves. If no holes are present the response is within 20 $\mathrm{m\,s^{-1}}$ of the prediction. The addition of holes to the material can be thought of as increasing the porosity, which reduces stiffness, and subsequently the wave velocity. This is equivalent to a reduction in Young's modulus of around 15 GPa in this case. The average temperature sensitivity from the COMSOL model is 0.57 $\mathrm{m\,s^{-1}\,{}^{\circ}C^{-1}} \pm 0.19\ \mathrm{m\,s^{-1}\,{}^{\circ}C^{-1}}$, where the sensitivity increases from 0.30 $\mathrm{m\,s^{-1}\,{}^{\circ}C^{-1}}$ at 27°C, rising to 0.80 $\mathrm{m\,s^{-1}\,{}^{\circ}C^{-1}}$ at 1027°C. Above ~500°C the sensitivity of the COMSOL model does not increase at the same rate as the prediction, likely due to a combination of dispersion and reflections, which can be clearly seen in the results at 827°C and 1027°C (Figure 5.18). The additional reflections seen as temperature increases are likely a result of the reduction in wavelength with temperature, which becomes more comparable with the diameter of the cooling holes. The wavelength of A_0 reduces from 1.76 mm at 27°C to 1.46 mm at 1027°C. The A_1 mode also begins to propagate as cut-off frequency reduces at higher temperatures (see Figure 5.9), which can be seen in 2D-FFT analysis (Figure 5.19) of the signal propagating past the array of cooling holes at 1027°C. To carry out 2D-FFT analysis the length of the plate was extended to 100 mm, and 90 point probes equally spaced 0.8 mm apart were placed past the array of cooling holes (see Figure 5.16). Out-of-plane (y-axis) displacement was monitored.

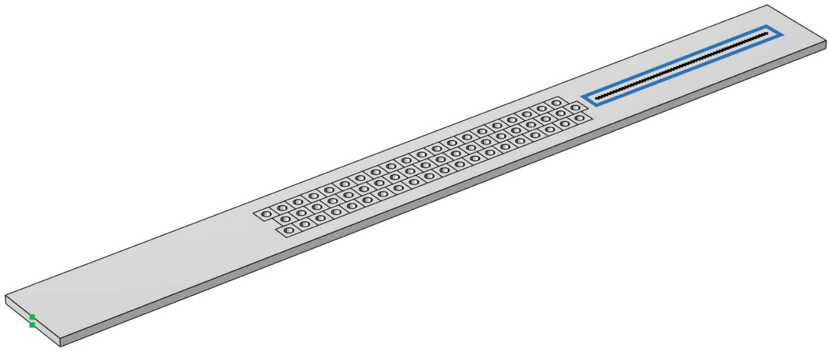

Figure 5.16 – Diagram showing model used for 2D-FFT analysis. The green squares indicate the excitation points, while the blue region contains the 90 point probes equally spaced 0.8 mm apart used to monitor out-of-plane (y-axis) displacement.

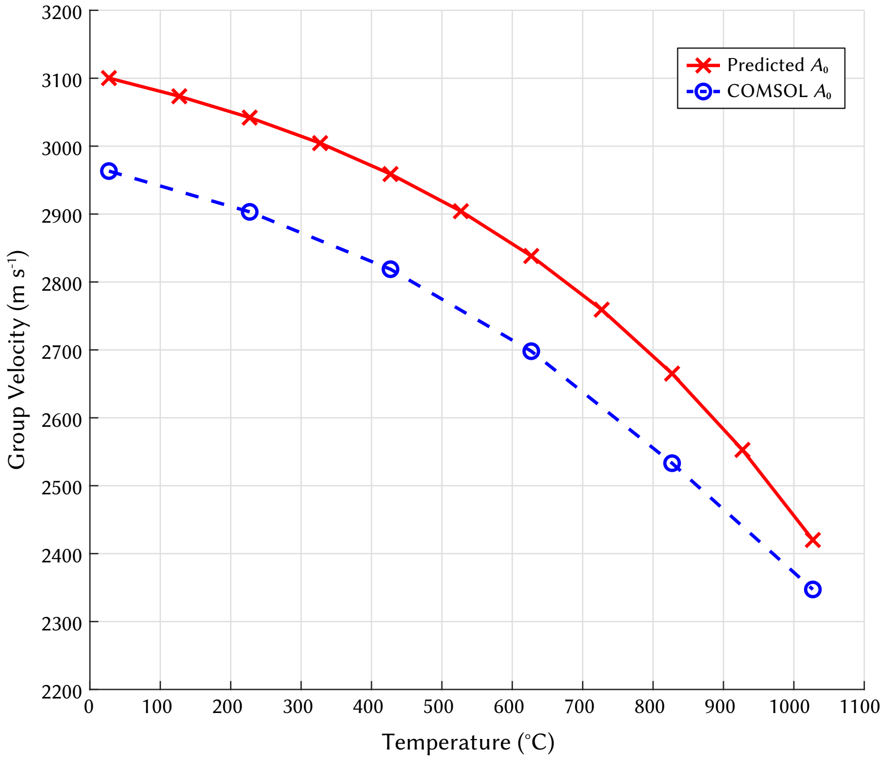

Figure 5.17 – Change in group velocity with temperature for A_0 at 1.4 MHz from 27°C to 1027°C. Comparison between predicted and simulated results.

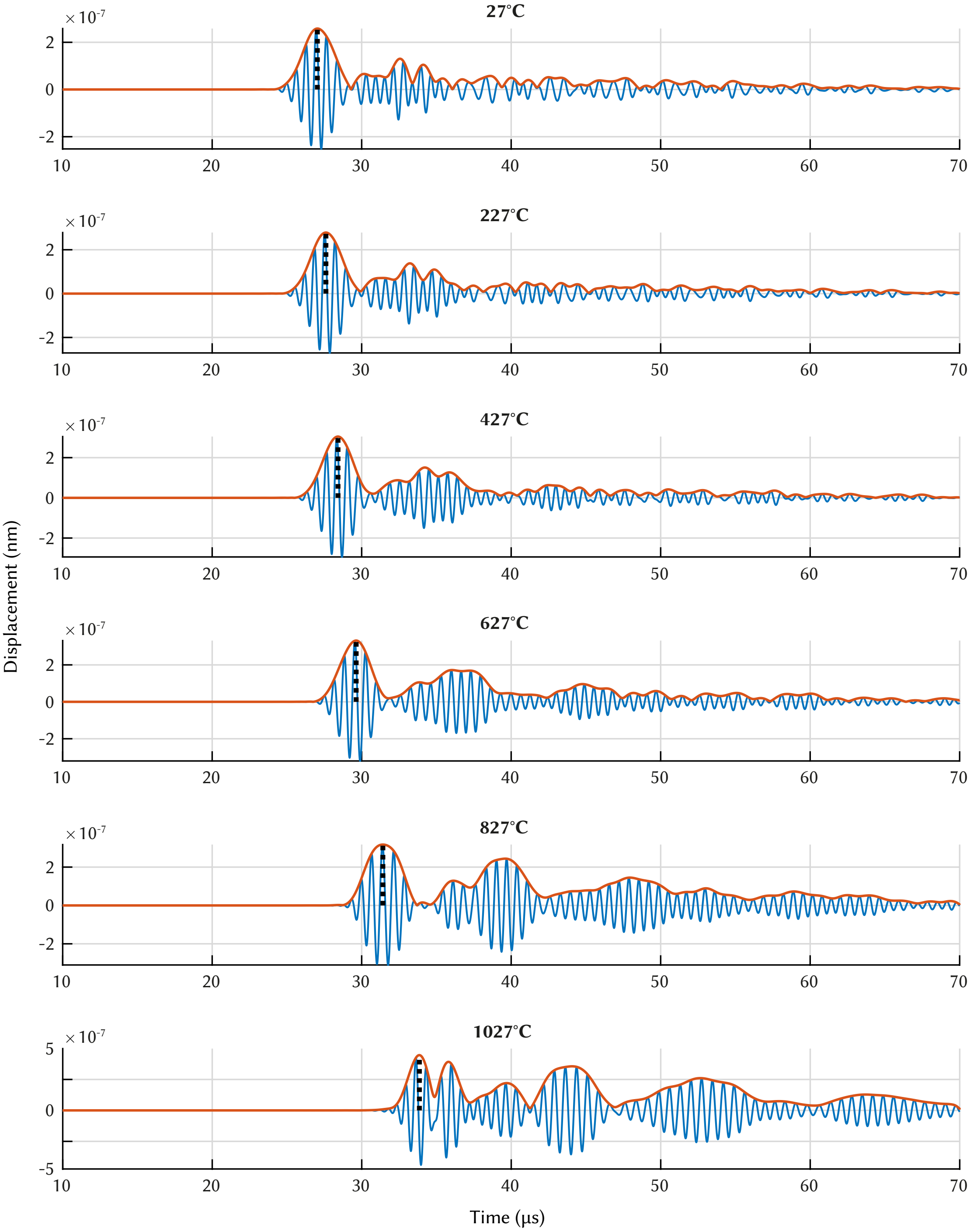

Figure 5.18 – Transmitted response of A_0 at 1.4 MHz at 27°C, 227°C, 427°C, 627°C, 827°C, and 1027°C. The orange line shows the envelope of the signal, while the black dotted line shows the peak of the envelope from which time of flight is measured.

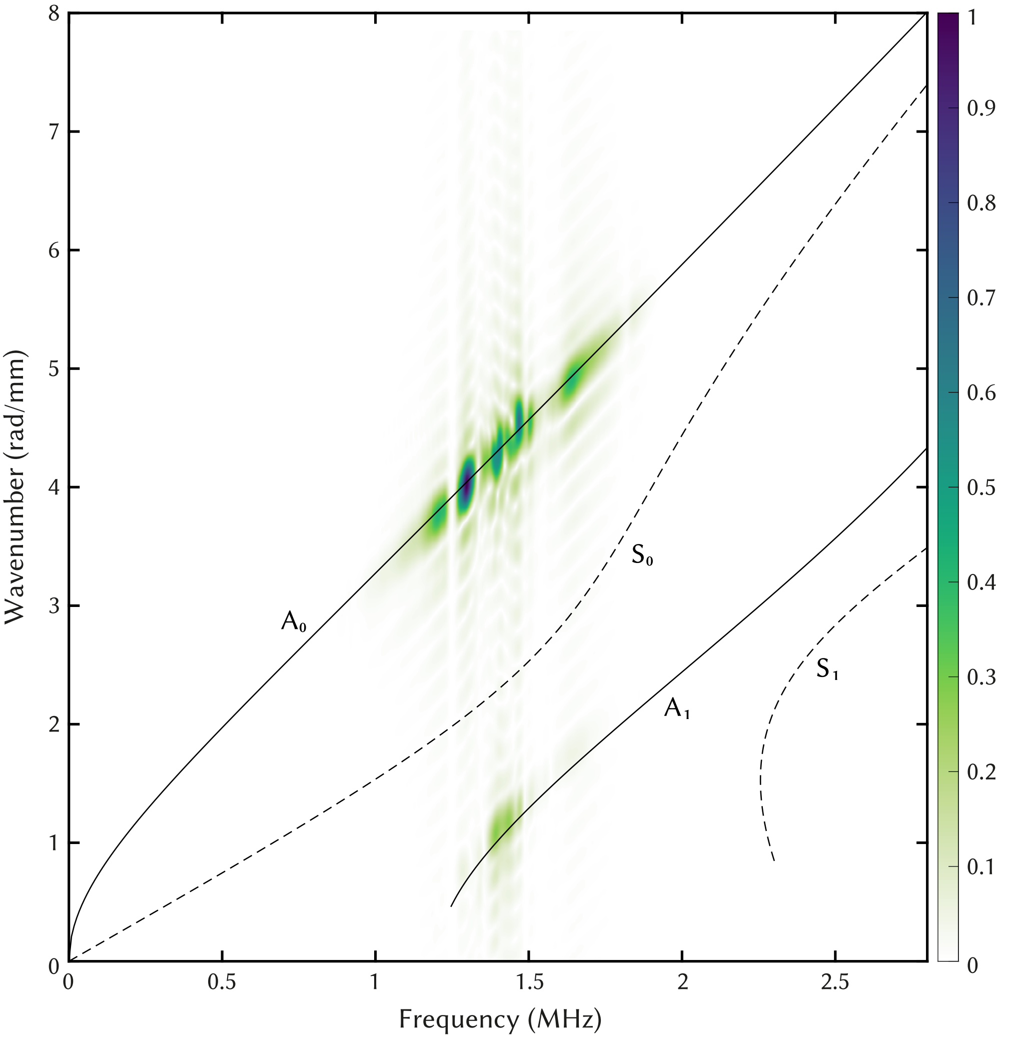

Figure 5.19 – 2D-FFT of wave propagation at 1027°C. Solid and dashed lines represent numerically calculated dispersion curves. Areas of high intensity (darker colours) show where modes have been detected.

5.2.4 Hotspot detection

The following study considers the effect of a temperature hotspot on wave propagation. If a temperature hotspot can be detected it can indicate damage or abnormal operation, which can be as important as absolute temperature monitoring. A model with a temperature of 500°C across the entire surface is compared to a model with a 700°C hotspot at one of the central cooling holes. The heat transfer coefficient of the plate is adjusted until there is a large temperature gradient between the hotspot and the ambient temperature (500°C). Figure 5.20 shows the surface temperature of the hotspot model. The A_0 mode is excited at 1.4 MHz using two-sided excitation, as used previously. y-axis displacement is recorded using a point probe at the far edge of the plate, in-line with the central row of cooling holes. The full array of holes (3×20) from the previous study are used.

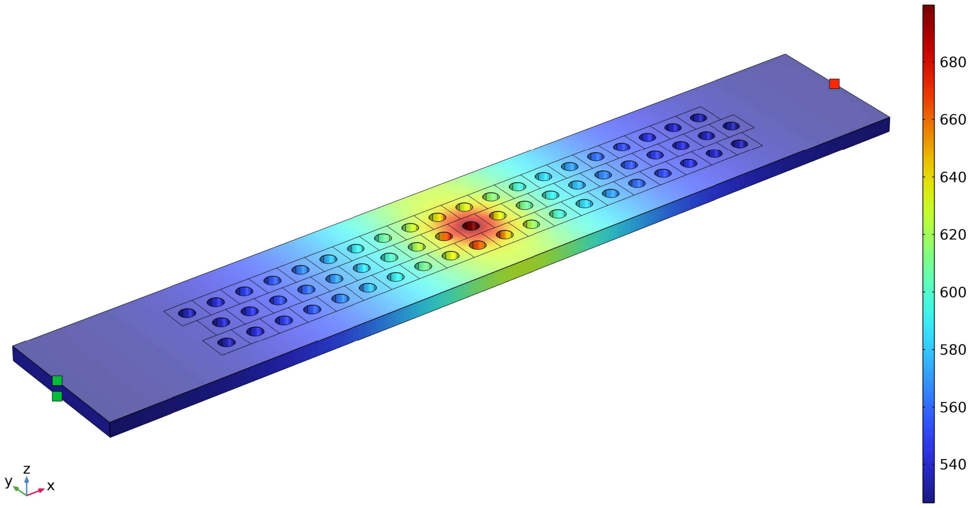

Figure 5.20 – Surface temperature of leading edge model with a 700°C hotspot, and an ambient temperature of 500°C. The temperature scale is given in degrees Celsius (°C). The green squares indicate the excitation points, while the red square indicates the receiver point.

Figure 5.21 shows the wave propagation across the cooling hole structure at 500°C (green), and 500°C with a 700°C hotspot (red). An overall shift in time of flight with the hotspot present is indicated by the shift in the peak of the initial wave packet. This could not be distinguished from an overall temperature change of the whole plate, which suggests that a time of flight based system would not be able to identify a hotspot in this case. Past the first two wave packets there are substantial differences in the signals, however these cannot necessarily be attributed to the hotspot directly, as overall changes in temperature also cause considerable variation in this region, as seen in Figure 5.18.

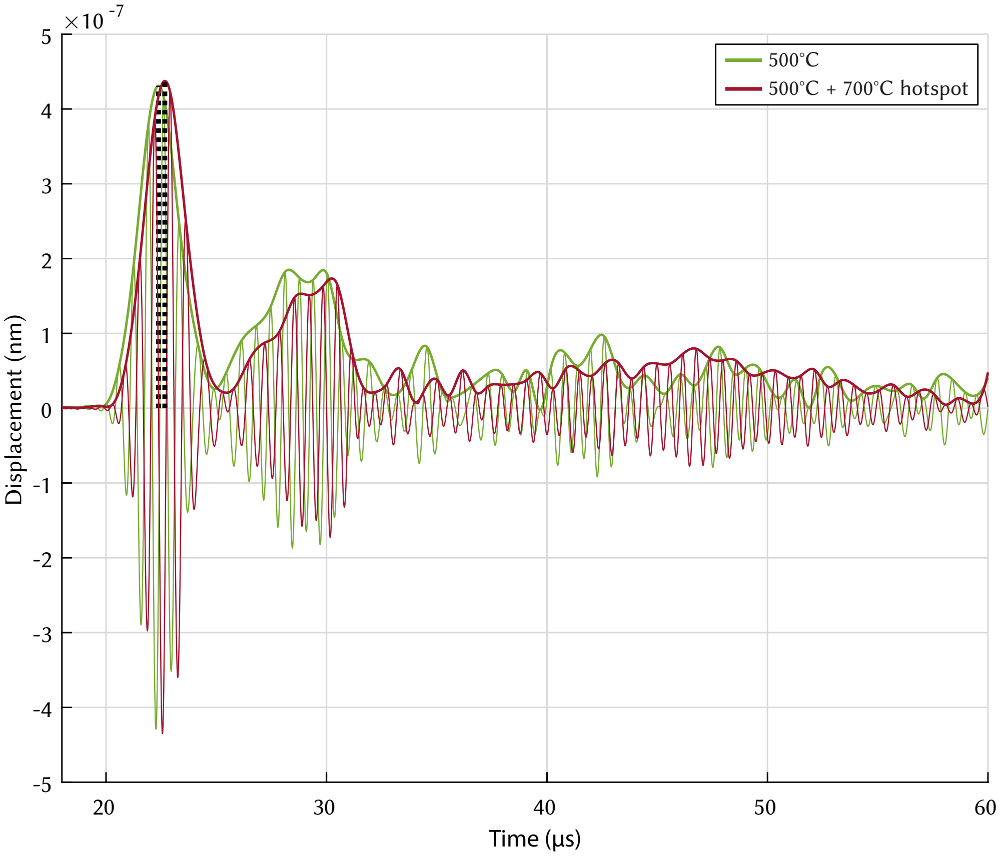

Figure 5.21 – Wave propagation across leading edge model at 500°C, and 500°C with a 700°C hotspot.

5.3 Wave propagation in the region towards the trailing edge

In this region of the vane, cooling holes are often arranged in single rows, with each row spaced considerably further apart than in the leading edge region. In some cases the number of holes per row is also reduced, which increases the hole spacing within each row.

A model has been developed with a single row of cooling holes, using excitation/receiver points offset from the holes. A row of holes has been added spaced 10× further apart (1 mm > 10 mm) than in the leading edge model, and the diameter of the holes has been increased to 2 mm. On the example NGV shown in Figure 5.2 the spacing between rows increases to around 5× the spacing at the leading edge towards the trailing edge, up to a maximum of 10× the distance. The number of excitation cycles has been reduced from five to three in comparison to previous simulations, to increase the time separation between wave packets.

Figure 5.22 shows the temperature gradient across the surface of the trailing edge model when the internal surfaces of the central cooling hole are set to 700°C. The heat transfer coefficient of the plate is set to match the previous hotspot simulation on the leading edge model. As seen in Figure 5.24, a second wave packet is received after the direct signal, which is believed to be reflected from the central hole. When z-axis displacement is animated on the upper surface of the plate, a reflection is present from this hole. By introducing a temperature hotspot at this location (as in the previous section) the effect on the reflected signal can be investigated.

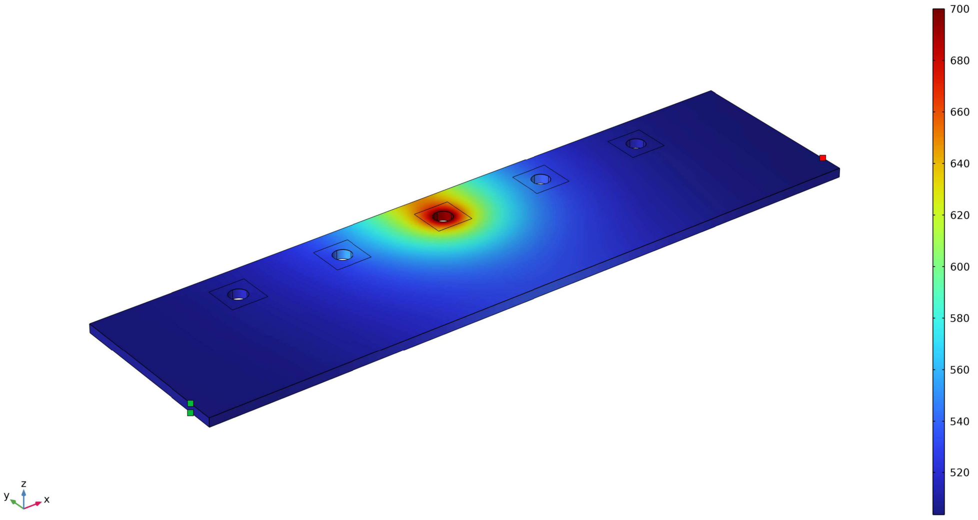

Figure 5.22 – Surface temperature of trailing edge model with a 700°C hotspot, and an ambient temperature of 500°C. The temperature scale is given in degrees Celsius (°C). The green squares indicate the excitation points, while the red square indicates the receiver point.

5.3.1 Transmitted response (pitch-catch)

When the time of flight between the first set of wave packets and the second set of wave packets is compared, a clear difference is detected. The first wave packet is the direct path from transmitter to receiver, which is marginally affected by the introduction of the hotspot. The temperature along this path is 515.70°C on average with the hotspot present. The second wave packet is a reflection (or series of reflections) from the cooling holes, which is more greatly affected by the temperature hotspot, as the transmission path has a considerably higher temperature gradient across it in comparison to the direct path. The temperature along this path is 535.98°C on average.

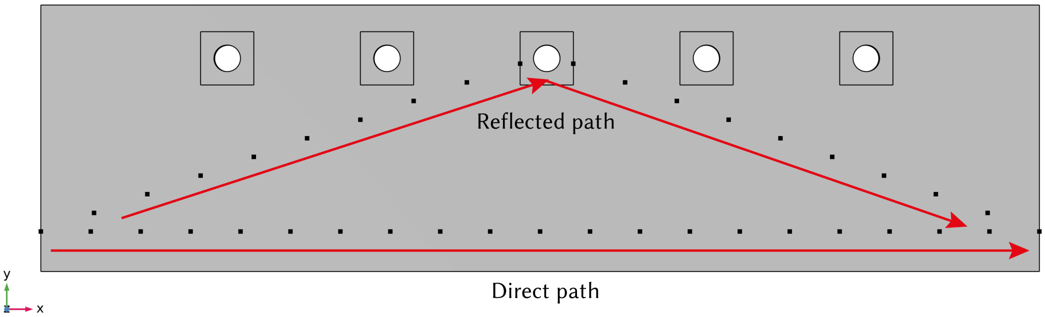

Figure 5.23 – Geometry of COMSOL model showing temperature point probes along transmission paths.

If the difference in time between the first set of wave packets is attributed to an increase in temperature of 15.70°C, the temperature change between the second set of wave packets can be extrapolated from the time difference between them. A least squares method is used to calculate the linear trend of the change in time with temperature, and the resulting equation is rearranged to solve for temperature. This results in a temperature of 542.61°C. Although the temperature along the reflected path has been overestimated (+6.64°C) based on the average temperature, a temperature hotspot has been successfully detected using this method.

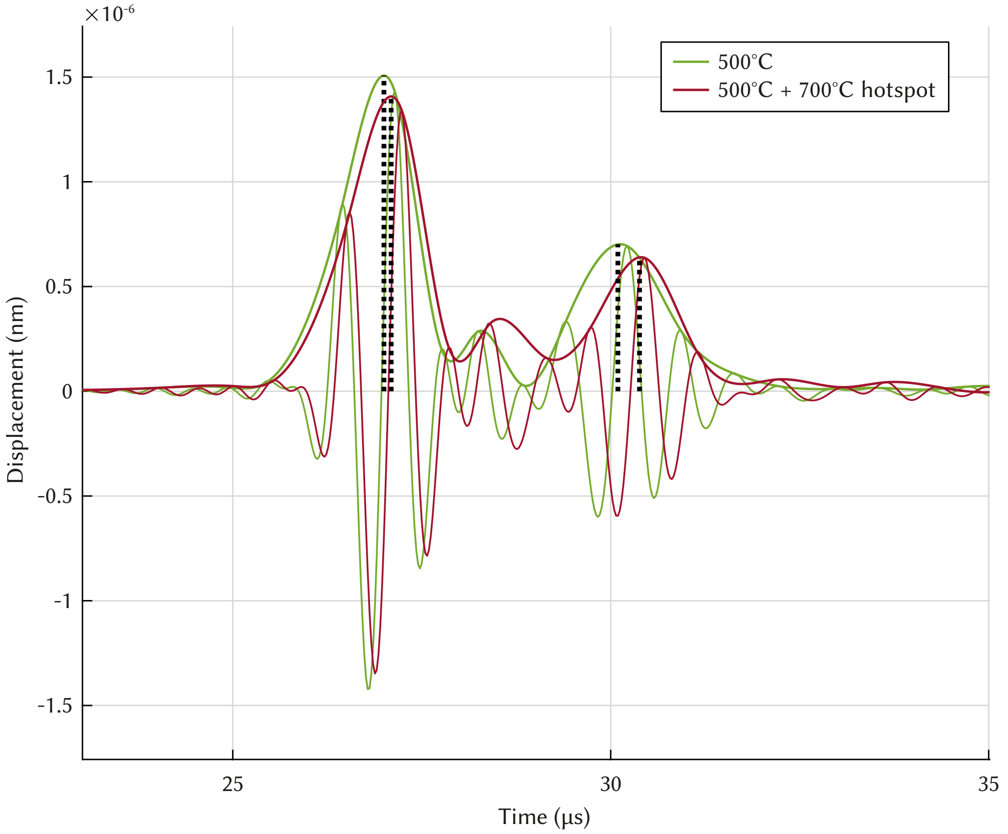

Figure 5.24 – Transmitted response of trailing edge model at 500°C (green), and 500°C with a 700°C hotspot (red).

5.3.2 Reflected response (pulse-echo)

Figure 5.25 shows the response measured at the input point, with the excitation signal removed (<10 µs). The reflections from each hole are denoted (a)-(e), and the reflection from the far edge of the plate is denoted (f). The responses begin to differ at reflection (c), where the temperature hotspot is present. The amplitude of the reflections diminishes substantially past the third reflection (c), which limits the ability to detect a hotspot past this point.

Figure 5.26 shows the wave (in terms of z-axis displacement) propagating across the plate in $0.5{\times}10^{-5}$ s increments. In Figure 5.26b a reflection from the first cooling hole can clearly be seen, followed by the second hole in Figure 5.26c. Figure 5.26d shows both the reflections back towards the excitation point from holes three and four, as well as strong reflection from hole three propagating towards the receiver point at the far side of the plate. In Figure 5.26e reflections from holes three, four, and five can be seen propagating back towards the excitation point, while the strong reflection from the third hole is due to arrive at the receiver point shortly after the direct wave, as seen in Figure 5.24.

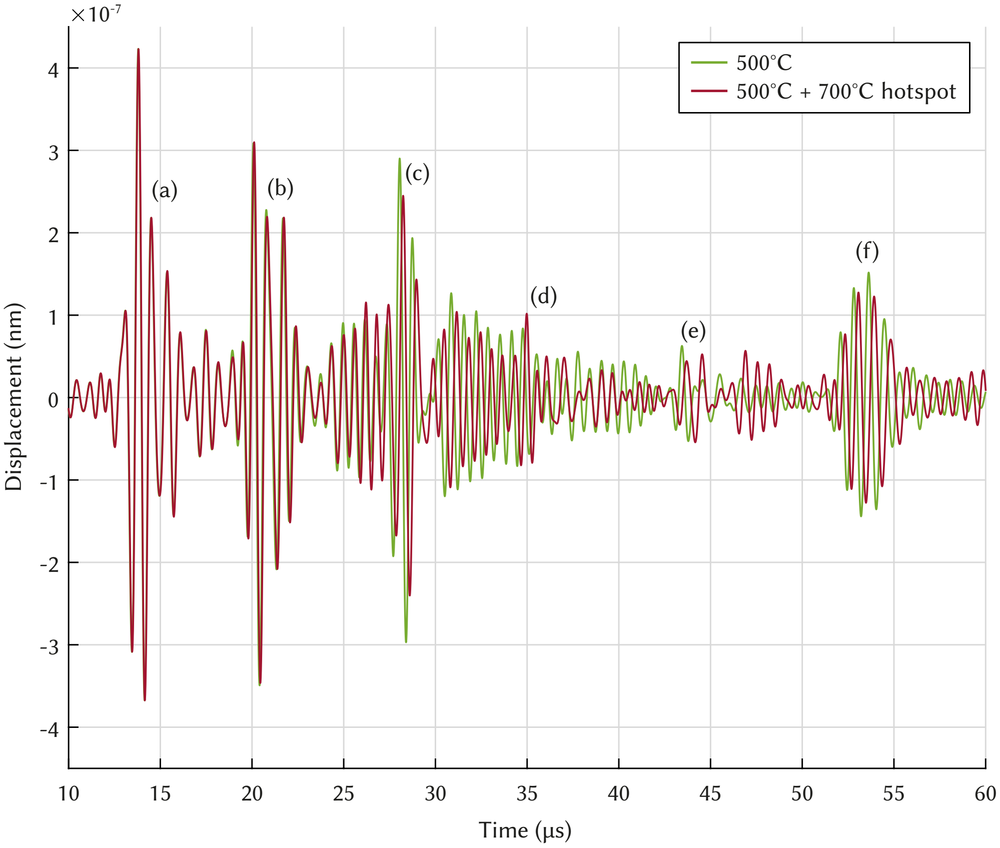

Figure 5.25 – Reflected response of trailing edge model at 500°C (green), and 500°C with a 700°C hotspot (red).

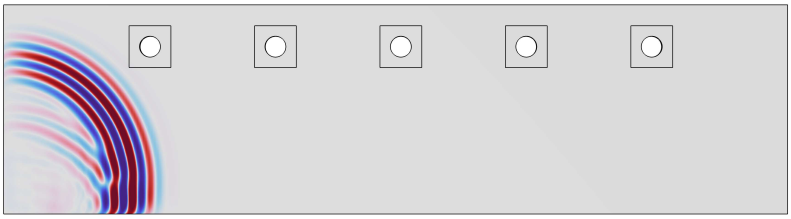

(a) 0.5×10^{-5} s

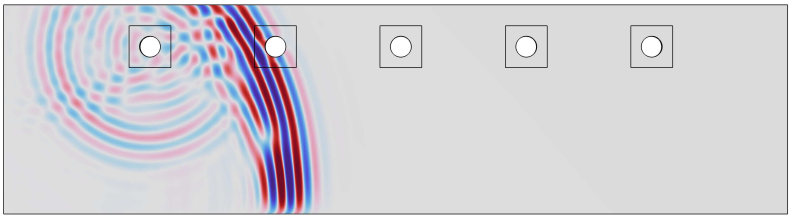

(b) 1.0×10^{-5} s

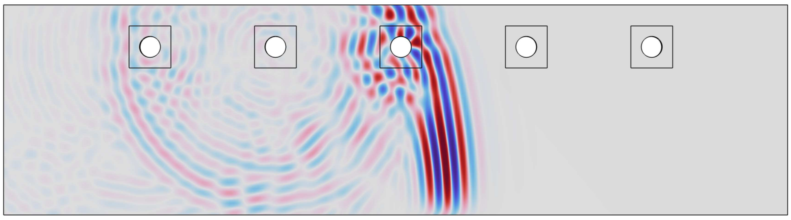

(c) 1.5×10^{-5} s

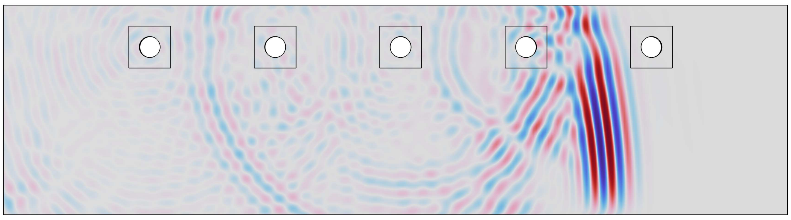

(d) 2.0×10^{-5} s

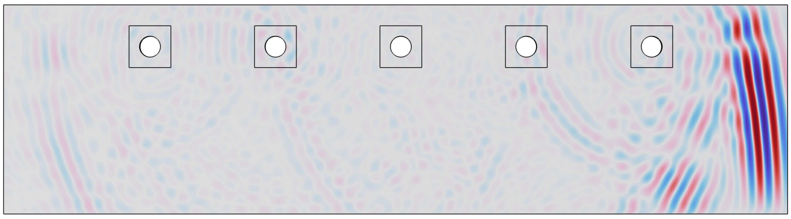

(e) 2.5×10^{-5} s

Figure 5.26 – z-axis displacement in 0.5×10^{-5} s increments.

5.4 Concluding remarks

In this chapter the effect of cooling hole structures on wave propagation has been investigated through experimentation and simulation. Experimental work has shown that in a pseudo-pulse-echo (pitch-catch at an acute angle) configuration, reflection amplitude increases linearly with hole diameter for a number of modes (S_0 at 1 MHz-mm, A_1 at 2.5 MHz-mm, and S_1 at 4 MHz-mm), where S_0 exhibits a considerably larger change in amplitude than the other modes. Results are in line with work carried out by Jeong [220].

The effect of cooling hole structures on wave propagation at the leading edge and trailing edge of a vane have been investigated through simulation. Both pitch-catch and pulse-echo configurations have been considered. At the leading edge of a vane where there is likely to be a dense array of cooling holes neither A_0 or S_0 produce reflections past the few rows of holes, which limits the use of a pulse-echo system in this instance. When considering the full array of holes in this study, the transmitted S_0 wave packet is severely distorted in comparison to A_0. A time of flight based temperature monitoring system would only be applicable to A_0 in this case, and further simulations confirm that velocity reduces in line with predictions, assuming that the reduction in stiffness from the introduction of holes is accounted for. When considering the trailing edge of the vane, the number of cooling holes has been reduced (20>5) and the spacing between them increased (1 mm > 2 mm) in comparison to the leading edge. When operated in a pitch-catch configuration an additional reflected wave packet is received along with the direct signal. The presence of a temperature hotspot at the third cooling hole can be detected by comparing the signals to a baseline, where the time difference between the reflected signals is larger than between the direct signals. This system is reliant on the presence of clear additional reflections, which even in this simplified case only produces one clear reflection. A hotspot present at one of the other cooling holes may not be possible to detect using this method. When operated in a pulse-echo mode a number of reflections are detected, which can be attributed to each of the cooling holes. In this case the third reflection in the signal shows a clear shift in time in comparison to the baseline signal. The response from the fourth and fifth holes is less clearly defined, which makes the detection of changes more challenging. Operating sensors at both ends of the vane in pulse-echo configurations could allow the whole vane to be effectively monitored. Excitation should be staggered to avoid interference between signals.

It should be made clear that these observations may only be applicable to the models in this study, as different configurations of hole sizes, shapes, and spacings are likely to produce different results. The interference patterns and complex interactions of hole reflections will differ greatly for each circumstance. The simplified simulations used in this study do not consider the additional reflections that are likely to be produced from other elements of the geometry (e.g. internal flanges, the trailing edge, or the side-wall boundary), which may be useful in monitoring temperature from different locations, but may also complicate the signal packet. With that being said, there are a number of general recommendations that can be made. Modes with larger in-plane motion (symmetric) are likely to be greatly affected by through-thickness features such as holes. When arranged in arrays the propagation of these modes is more greatly affected in comparison to antisymmetric modes. Careful attention should be paid to the excitation frequency to ensure that at the highest temperature monitored additional modes are not excited, as this is likely to complicate signal analysis. This is particularly important if attempting to operating below the cut-off frequency of A_1, as both A_0 and A_1 propagate with similar group velocities, which causes interference between the modes as A_1 begins to propagate.

If using two-sided excitation, S_0 can be excited at a higher frequency than A_1 before the next mode (S_1) is excited, however this region is highly dispersive. Although time of flight based monitoring may not be applicable in all cases, there is likely to be a measurable effect of temperature on wave propagation by other means. Machine learning algorithms could be used to identify differences from baseline signals. Outlier detection methods are already used for defect detection systems using guided waves, such as for detecting sealant delamination in integrated circuit (IC) packages [222], defects in composite plates [223], or cracks in the trusses of highway signs [224]. A comprehensive summary of outlier detection methods for time series data is given by Ane Blázquez-García and Angel Conde [225].

CHAPTER 6

The effect of thermal barrier coatings on wave propagation

Thermal barrier coatings are made up of multiple layers, a bond coat, a thermally grown oxide layer (TGO), and a top coat (see Figure 2.1). Both the composition of TBC materials as well as their application technique has an effect on the material properties, which in turn changes how guided waves propagate. Differences in air plasma spray (APS) application methods cause variances in porosity as well as bonding efficiency [226]. Electron-beam physical vapor deposition (EB-PVD) produces elongated intercolumnar pores perpendicular to the thickness, whereas air plasma spray methods exhibit inter-splat pores parallel to the TBC surface [227]. Both APS and EB-PVD produce orientation specific Young's modulus, where the cross-sectional E is larger than the plan-section E. In general EB-PVD results in higher values of Young's modulus (20–120 GPa [228, 229]) for YSZ top coats than APS (8.7–54.6 GPa [230]). The Young's modulus of YSZ coatings shows a significant dependence on porosity and microstructure, where Young's modulus decreases with increasing porosity. The E of ZrO_2-4 mol% Y_2O_3 applied by EB-PVD has been shown to decrease from around 200 GPa at 8% porosity, to 80 GPa at 28% porosity [231]. A number of studies [232, 233] have shown that the Young's modulus of TBC materials increases after thermal ageing, as fine microcracks and porosities are sealed. The increase is in the region of 30 GPa. Exposure to higher temperatures during the ageing process causes a larger increase in E. In a non-symmetric laminate such as this the wave modes do not have a clear symmetric or antisymmetric character, especially when the different layers have substantially different material properties, and therefore wave speeds. The modes are therefore denoted using B (as proposed by The Dispersion Calculator [152]), rather than categorising them as either symmetric, S, or antisymmetric, A.

An initial study has been carried out that considers a typical TBC configuration at room temperature, with a relatively high value (48 GPa) of Young's modulus for the YSZ top coat. Dispersion curves and through thickness displacement profiles have been generated to demonstrate the effect on wave propagation. A second study has been carried out using temperature dependant material properties for both the superalloy substrate (Inconel 718) and the TBC materials. In this study the values of Young's modulus for the YSZ top coat are lower (17.5 GPA at 20°C reducing to 11.7 GPA at 1020°C) than in the room temperature study, which is likely to cause an even larger shift in displacement for the top coat layer. A COMSOL model has been used to simulate wave propagation at increasing temperatures, to investigate the suitability of using the B_1 mode for temperature monitoring.

6.1 Fixed temperature study

A typical configuration is considered in Table 6.1, where the values for Young's modulus and Poisson's ratio are provided by Li [234]. Table 6.2 shows the longitudinal and shear wave velocities of each TBC material used in this study, as calculated by COMSOL from the material properties used in Table 6.1.

The energy and phase velocity dispersion curves shown in Figures 6.2a and 6.2b respectively differ substantially from those of only Inconel 718. Figure 6.1 shows a comparison between the energy velocity curves of Inconel 718 with a TBC applied (solid lines) to that of pure Inconel 718 (dashed lines) at the same thickness (1.31 mm). It can be seen that B_0 is closely related to S_0, whereas B_1 does not converge towards the Rayleigh wave speed at high frequency-thickness products, as A_0 does. The B_1 mode propagates ~1000 $\mathrm{m\,s^{-1}}$ faster than the B_0 mode. After the TBC is applied the prominent peaks of the A_1 (becoming B_2) and S_1 (becoming B_3) modes are substantially diminished, and neither mode will be easily distinguishable in the time domain.

Figure 6.3 shows the through-thickness displacement profiles for five different modes, at frequency-thickness values that correspond to points of energy velocity maxima for the associated modes. At low frequency-thickness products (below the cut-off frequency of third mode, B_2) the modes respond in a similar manner to A_0 and S_0 in a single material (see Figure 4.2), as the first mode (B_0) exhibits large out-of-plane motion (Figure 6.3a), while the second mode (B_1) exhibits large in-plane motion (Figure 6.3b). Above B_1, however, the YSZ top coat exhibits a large through-thickness displacement in comparison to the rest of the materials, which is especially apparent for B_2 (Figure 6.3c). This is due to YSZ having a considerably lower Young's modulus than the other materials that make up a TBC. This will make these modes substantially more sensitive to defects in the TBC surface. This effect will be partially reduced as the value of E increases after thermal ageing. Modes B_5, B_7, and B_9 have energy velocity maxima distinctly separate from other modes, which is advantageous for the excitation/identification of single modes, however these higher order modes exhibit relatively less displacement than lower order modes (Figure 6.3e), which limits their sensitivity to holes, and results in lower amplitude signals.

Layer type	**Material**	**Young's Modulus** (GPa)	**Poisson's ratio**	**Density** (kg/m^3)	**Thickness** (µm)
Top coat	ZrO_2-8 wt% Y_2O_3 (8YSZ)	48	0.1	5770 [235]	200
TGO	α-Al_2O_3	400	0.23	3987 [236]	10
Bond coat	NiCrAlY	200	0.3	7500 [237]	100
Substrate	Inconel 718 [238]	202	0.29	8226	1000

Table 6.1 – Material properties of thermal barrier coatings.

Layer type	**Material**	**Longitudinal velocity** ($\mathrm{m\,s^{-1}}$)	**Shear velocity** ($\mathrm{m\,s^{-1}}$)
Top coat	ZrO_2-8 wt% Y_2O_3 (8YSZ)	2916.84	1944.56
TGO	α-Al_2O_3	10784.57	6386.15
Bond coat	NiCrAlY	5991.45	3202.56
Substrate	Inconel 718	5672.72	3085.12

Table 6.2 – Wave velocities of thermal barrier coatings.

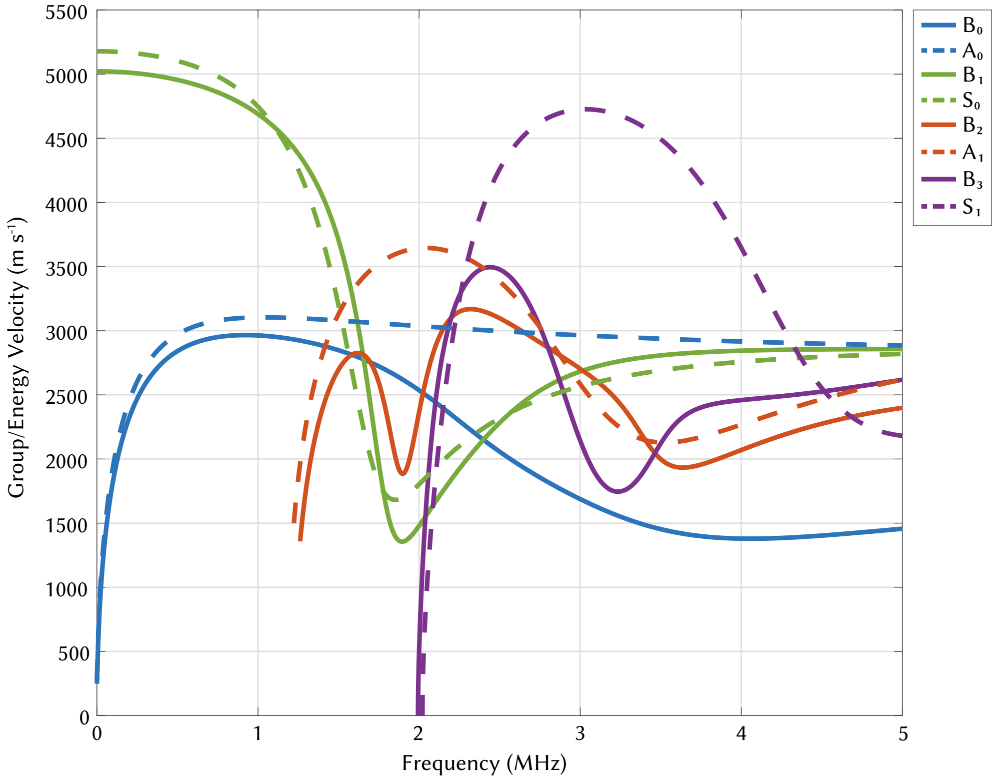

Figure 6.1 – Comparison of group/energy velocity dispersion curves for Inconel 718 with and without a TBC applied. Solid lines represent the curves with TBC applied, dashed lines represent pure Inconel 718 at the same thickness.

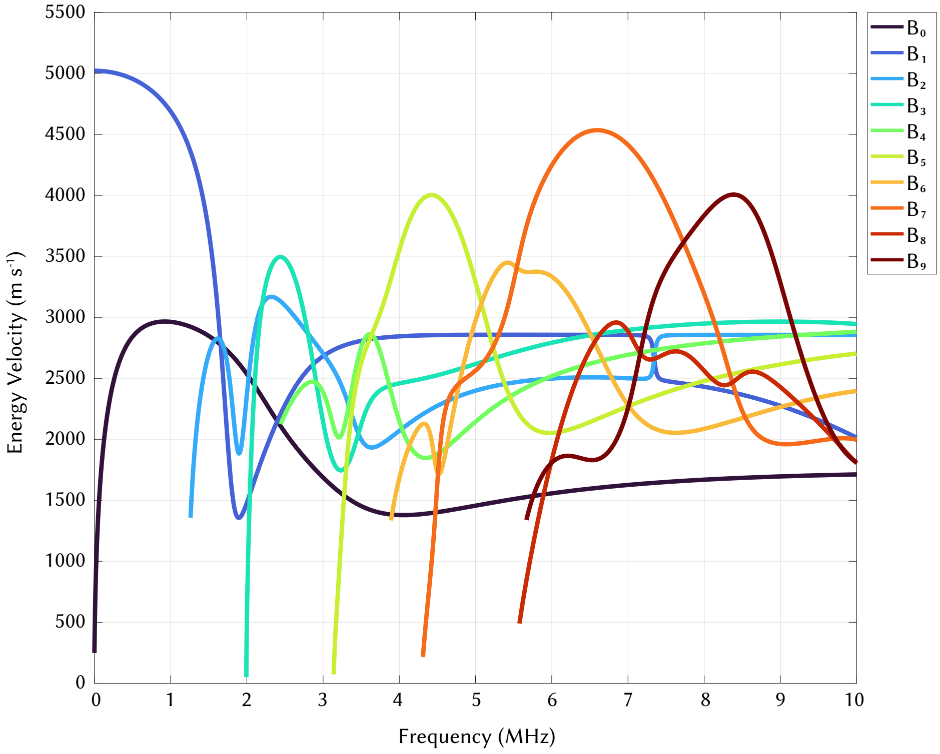

(a) Energy velocity.

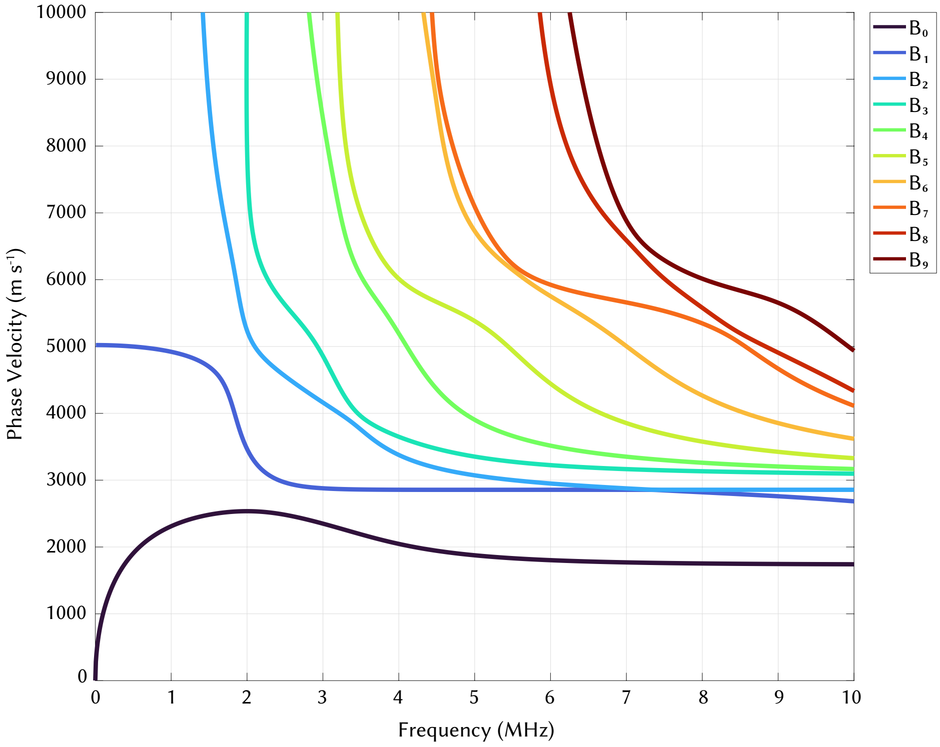

(b) Phase velocity.

Figure 6.2 – Dispersion curves for Inconel 718 with TBC applied (Table 6.1).

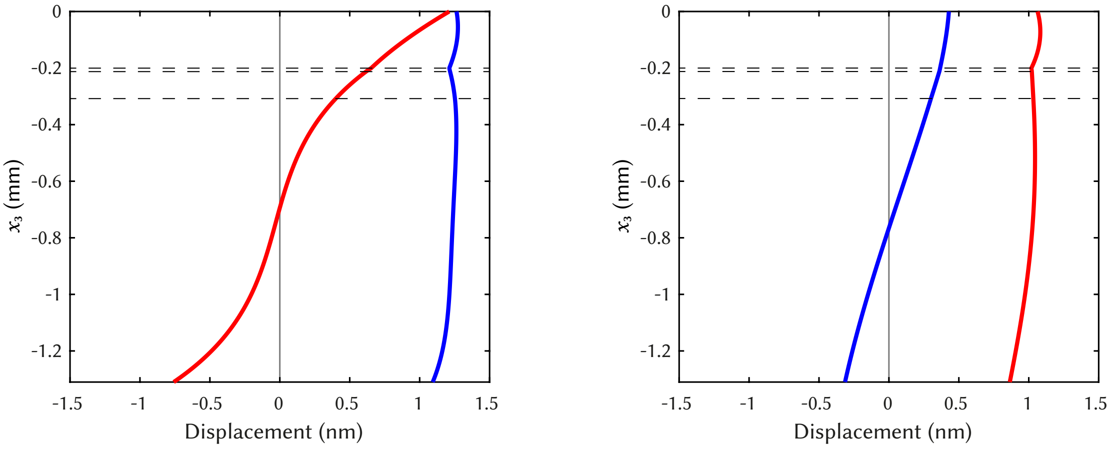

(a) B_0 Displacement – 1 MHz. **(b)** B_1 Displacement – 1 MHz.

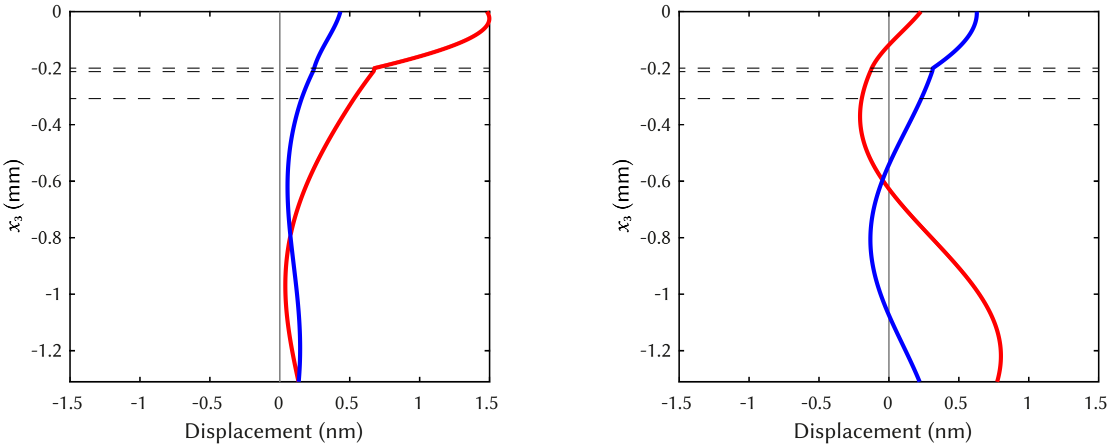

(c) B_2 Displacement – 2.4 MHz. **(d)** B_3 Displacement – 2.4 MHz.

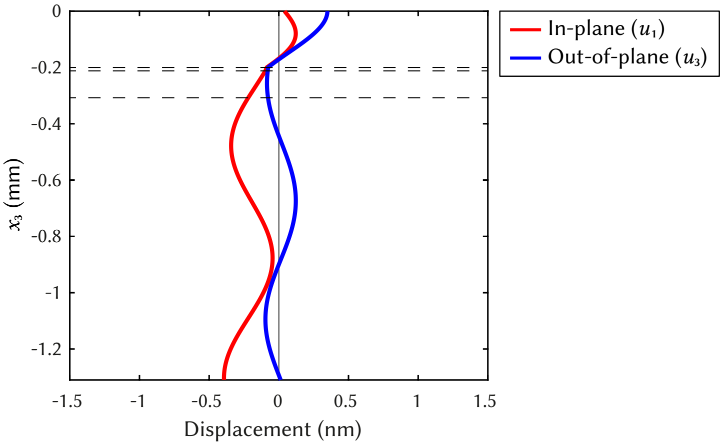

(e) B_5 Displacement – 4.4 MHz.

Figure 6.3 – Through thickness displacement profiles for Inconel 718 with TBC applied. Dashed lines indicate the boundaries between layers.

6.2 Temperature dependant study

Temperature dependant Young's moduli for TBC materials are provided in Table 6.1, and shown in Figure 6.4. All three sources of values for the top coat (YSZ) show linear reductions in E with temperature, while there is a significantly larger reduction in E for the bond coat (MCrAlY) with increasing temperature. Saucedo-Mora *et al.* [239] suggest that the data provided by Beghini *et al.* [226] shows a significant decrease in E due to microcracking. The elevated initial values of E in comparison to the other sources suggests that the tested material has undergone thermal ageing [232, 233]. The change in Young's modulus with temperature for the TGO is ignored, as the effect is considered insignificant due to the thickness of the layer. Temperature dependant material properties for Inconel 718 are shown in Figure 4.29. The Poisson's ratio of the TBC materials is considered to be temperature independent for this study, 0.33 for the bond coat, and 0.2 for the top coat. Changes in density due to thermal expansion in the TBC are not considered in this study, as the effect on wave propagation is small in comparison to changes in Young's modulus, as discussed in Section 3.3.2.

As temperature increases there is a large shift in the shape of the dispersion curves (from Figure 6.10a to Figure 6.10b), which makes it difficult to select a suitable mode/frequency to target. The lowest two modes, B_0 & B_1, are the only two modes that show relatively stable areas of low dispersion, in the regions of 0.4–0.8 MHz, however the effect of dispersion still increases with temperature, especially for B_1. B_5 is the only other mode that exhibits an energy velocity peak that would allow the single mode to be identified across the temperature range of interest, however there is only a very small frequency window (~3.1 MHz) in which dispersion is relatively stable.

Source	**Material**	$E_{20^{\circ}\mathrm{C}}$	$E_{220^{\circ}\mathrm{C}}$	$E_{420^{\circ}\mathrm{C}}$	$E_{620^{\circ}\mathrm{C}}$	$E_{820^{\circ}\mathrm{C}}$	$E_{1020^{\circ}\mathrm{C}}$
Bednarz *et al.*[240]	Top Coat	17.50	16.34	15.18	14.02	12.86	11.70
Beghini *et al.*[226]	Top Coat	46.50	41.75	37.00	32.25	27.50	22.75
Gregori *et al.*[241]	Top Coat	22.00	21.05	20.14	19.26	18.43	17.62
Bednarz *et al.*[240]	Bond Coat	151.85	150.75	145.25	132.33	108.92	71.89
COMSOL	Inconel 718	201.86	193.23	181.86	166.89	147.46	122.72

Table 6.3 – Temperature dependant Young's modulus of substrate and TBC materials.

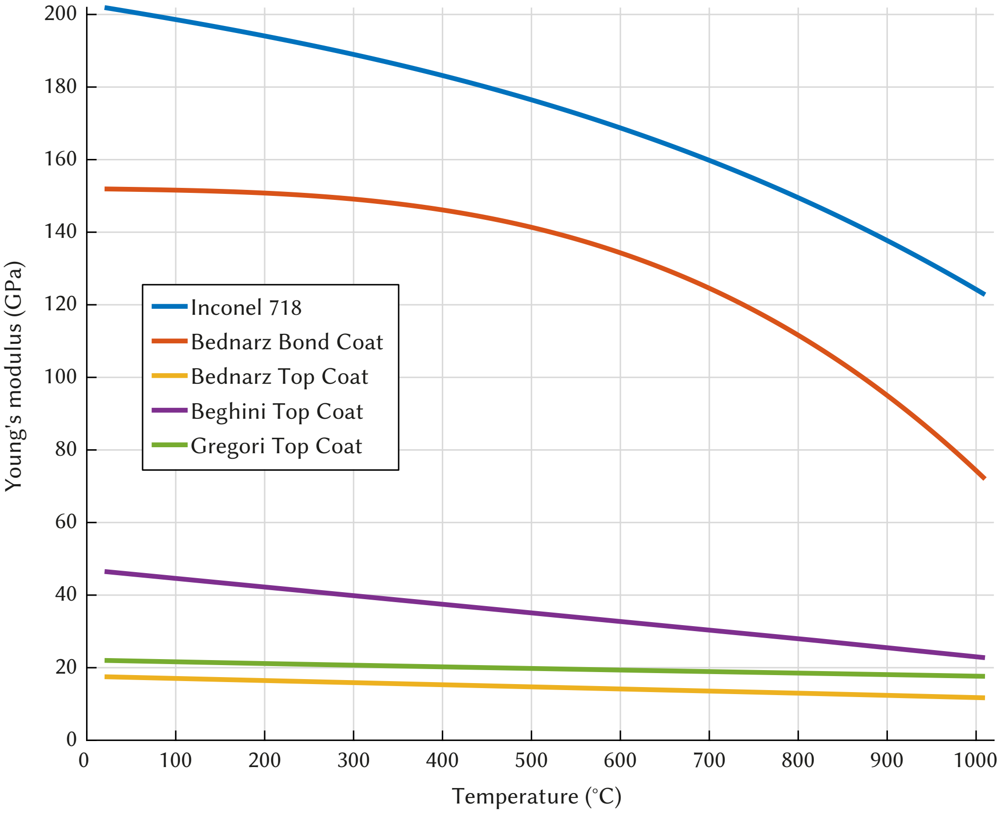

Figure 6.4 – Values of Young's modulus for TBC materials.

6.2.1 COMSOL Simulations

A smaller wedge model is used in comparison to the simulations carried out in Section 4.4 to reduce computation time, however the same process of subtracting wedge-to-wedge time from the total time of flight, as well as calculating the wedge foot offset is used. The geometry of the model is shown in Figure 6.5. Twelve elements per wavelength are used throughout the model, recalculated for each material. Mesh quality for the Inconel 718 plate with TBC applied is shown in Figure 6.6, where green regions indicate skewness quality close to 1. A mapped mesh is used for the Inconel 718, bond coat, and TGO layers, as well as the piezoelectric material. Triangular mesh elements are used for the top coat and wedges. This ensures a smooth transition between layers, keeping the element quality high. At least two elements are used in narrow regions for each layer, except for the TGO layer, to avoid unnecessarily small mesh elements. This is not expected to have a significant impact on wave propagation as the thickness of the TGO layer in comparison to excitation wavelength is small. Average element quality based on skewness is 0.93. The mesh consists of 73255 domain elements and 5921 boundary elements. The spacing between wedges was set to 80 mm. The sampling rate used in the simulation is 6.72×10^7 Hz, which provides a maximum theoretical velocity resolution of ± 2.97 m s^{-1}. Simulations are carried out at six temperatures, 20°C, 220°C, 420°C, 620°C, 820°C, and 1020°C.

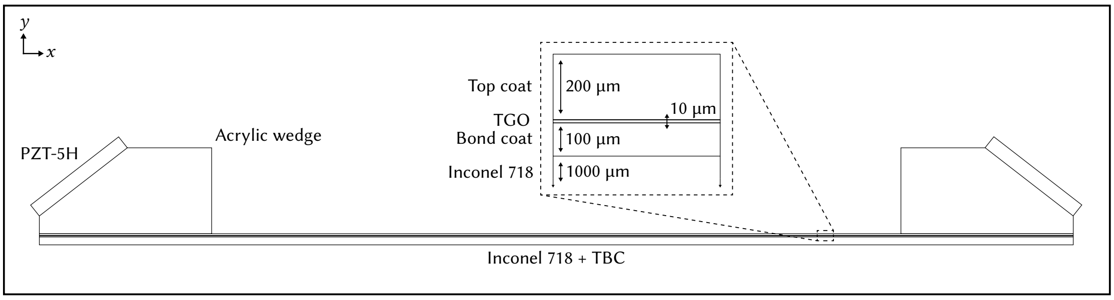

Figure 6.5 – Diagram of COMSOL geometry.

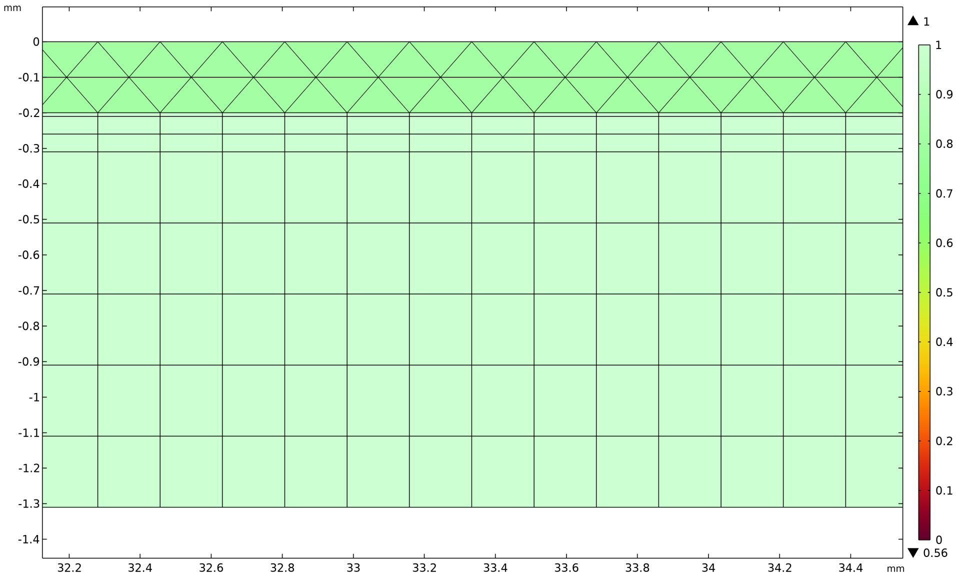

Figure 6.6 – Mesh quality of Inconel 718 with TBC applied. Green indicates skewness quality close to 1.

6.2.1.1 Targeting the B_1 mode

Through analysis of energy velocity dispersion curves (Figures 6.10a and 6.10b) the B_1 mode below the cut-off of B_2 has been identified as the most suitable mode for temperature monitoring. The large difference in energy velocity from B_0 means that it should be distinguishable in the time domain, even without single mode excitation. The dispersive nature of the mode (steep slope) from around 0.5 MHz to 1.2 MHz is advantageous for temperature monitoring as it ensures a high temperature sensitivity, although dispersion of the wave packet will affect time of flight measurement accuracy. To determine excitation frequency, dispersion curves at the highest temperature of interest (1020°C) are consulted. As seen in Figure 6.10b, the B_1 mode intersects B_0 at around 1 MHz, so excitation frequency should be lower than this to ensure that the B_1 mode is still distinguishable at high temperatures. An excitation frequency of 0.8 MHz is used in this study.

The heat transfer physics model has been disabled for the wedges, with only the plate affected by a change in temperature. The large temperature range causes a large change to the material properties of the Inconel 718 and TBC, which in turn causes a large change in wave speed. As the change is so large the wedge angle is adjusted continually to target the same area of the frequency spectrum, as shown in Table 6.4. Wedge offset is also recomputed for each temperature, as the change in wedge angle changes the location at which the wave enters the plate from the wedge. The longitudinal velocity of the wedge material is 2477 $\mathrm{m\,s^{-1}}$, as measured experimentally.

Temperature (°C)	**Phase velocity ($\mathrm{m\,s^{-1}}$)**	**Wedge angle (°)**
20	4781.21	31.2
220	4698.85	31.8
420	4570.67	32.8
620	4382.39	34.4
820	4125.72	36.9
1020	3751.43	41.3

Table 6.4 – Wedge angle required for B_1 mode excitation in Inconel 718 with TBC from 20°C to 1020°C.

Figure 6.7 shows a 2D-FFT of the predicted response in the excited B_1 mode. Time-displacement data is transformed into frequency-wavenumber data using 2D-FFT from spatial B-scan data, using 90 point probes equally spaced 0.8 mm apart. This allows individual modes to be identified, and plotted against dispersion curves for verification. Out-of-plane (y) displacement is monitored. It should be noted that the displacement response in the plate measured using a point probe will differ from the response received at a second receiver wedge. The use of a second wedge further isolates a particular mode of interest, while the displacement in the plate may still show the presence of other modes.

Figure 6.8 shows the time of flight shift of the B_1 mode from 20°C to 1020°C. The response at 20°C is shown in green, while the response at 1020°C is shown in red. The black dashed lines indicate the peaks of each envelope, which are used in the calculation of time of flight. As temperature increases the effect of dispersion becomes more apparent, and there is less of a defined central peak to the wave packet.

Figure 6.9 shows predicted and simulated energy velocity of the B_1 mode (0.8 MHz) from 20°C to 1020°C in Inconel 718 with TBC applied. The simulated results are within ±29.24 $\mathrm{m\,s^{-1}}$ or 0.79% of the predicted velocities on average.

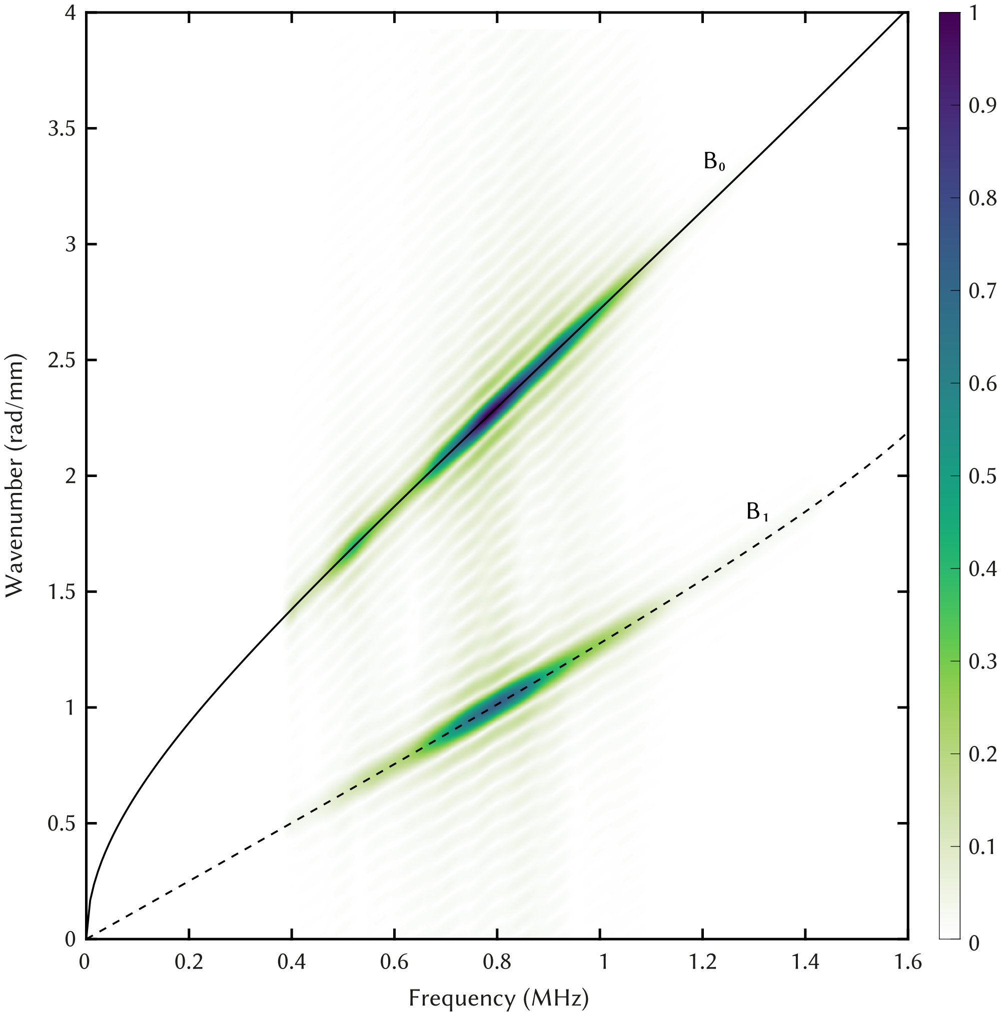

Figure 6.7 – 2D-FFT of B_1 excitation in Inconel 718 with TBC applied at 20°C. Solid and dashed lines represent numerically calculated dispersion curves. Areas of high intensity (darker colours) show where modes have been detected.

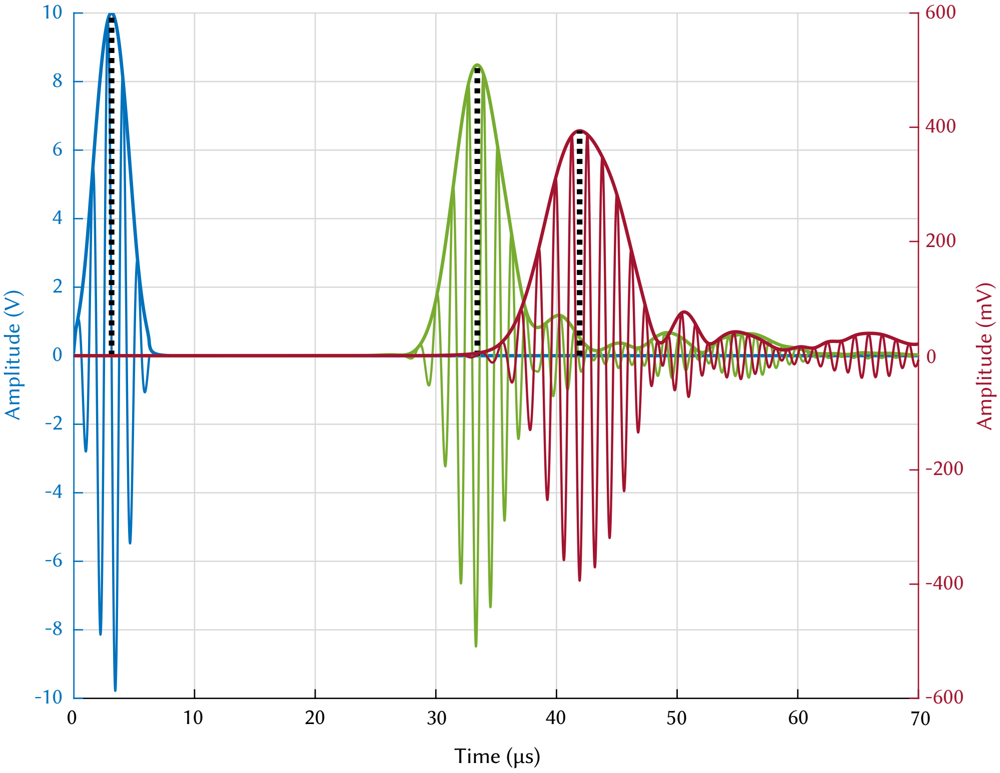

Figure 6.8 – Wave propagation of B_1 mode (0.8 MHz) at 20°C (green) and 1020°C (red) in Inconel 718 with TBC applied.

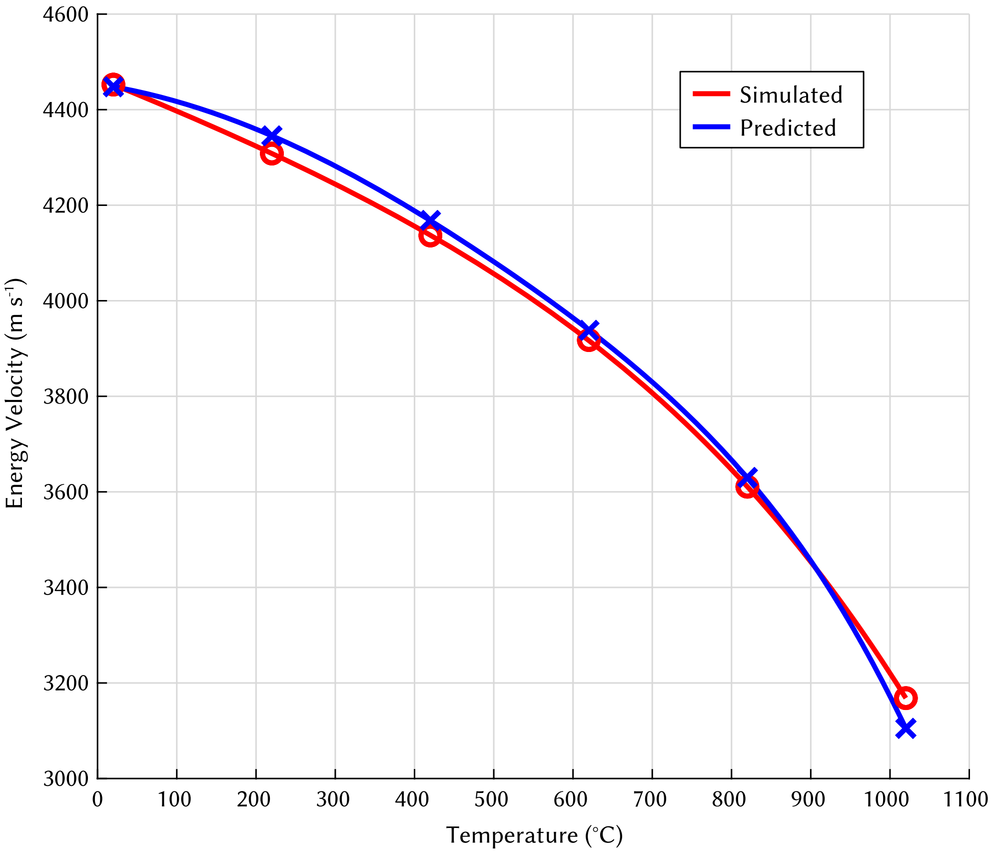

Figure 6.9 – Predicted and simulated energy velocity of B_1 mode (0.8 MHz) from 20°C to 1020°C in Inconel 718 with TBC applied.

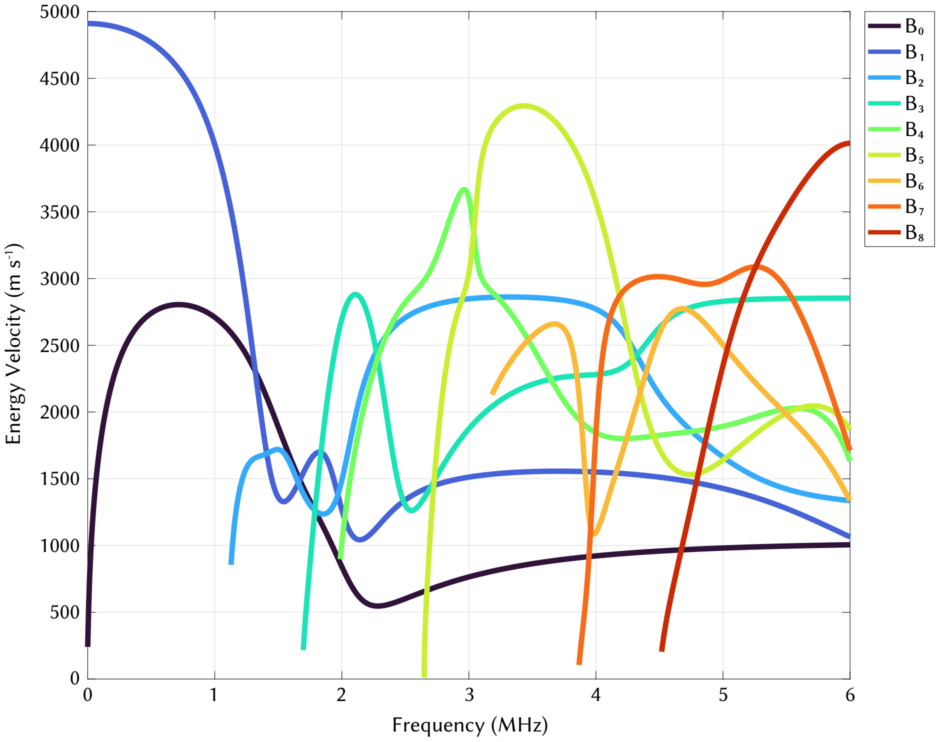

(a) 20°C

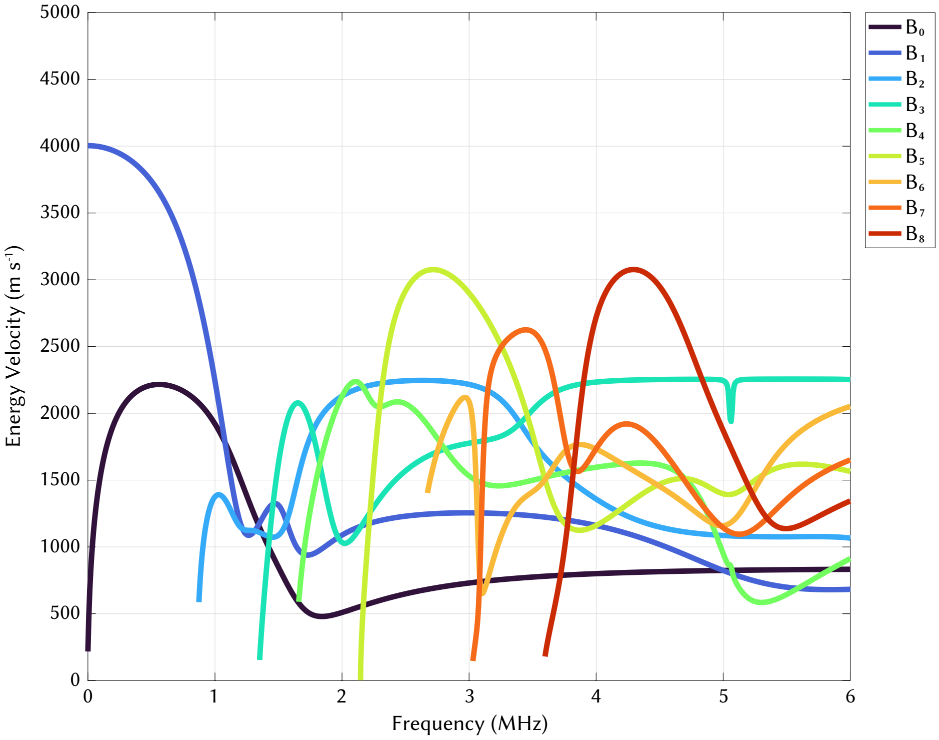

(b) 1020°C

Figure 6.10 – Energy velocity dispersion curves for Inconel 718 with TBC applied at 20°C (a) and 1020°C (b).

6.2.1.2 Targeting the B_5 mode

As seen in Figures 6.10a and 6.10b the B_5 mode shows a distinct energy velocity peak, which looks promising for identification in the time domain. Unfortunately the large shift in the mode (reducing in frequency) from low to high temperature, and the relatively small bandwidth of the peak, makes it difficult to select a suitable excitation frequency that does not fall within a dispersive region. Excitation must occur at, or higher in frequency, than the maximum energy velocity of the mode (~3.3 MHz), to ensure that velocity reduces with increasing temperature. This further reduces the available bandwidth, to the point that at higher temperatures (above around 500°C) the mode is no longer distinguishable in the time domain. Analysis of phase velocity dispersion curves shows that the B_5 mode is closely related to the B_4 mode, which further limits the ability to excite a single mode in this region. This becomes more problematic at higher temperatures when the difference in energy velocity between the two modes is reduced.

6.3 Concluding remarks

In this chapter the effect of thermal barrier coatings on wave propagation has been investigated through the generation of dispersion curves, through-thickness displacement profiles, and COMSOL simulations.

As the construction, application, and material properties of TBCs can vary dramatically, the specific effect on wave propagation for every case cannot be quantified. There are a number of generalisations that can be made, however. The top coat, typically made of YSZ, exhibits a substantially lower Young's modulus than the other materials, which has a large impact on wave propagation. Through analysis of through-thickness displacement profiles it can be seen that in some cases substantially larger displacement is observed in this layer. This is likely to make some modes more sensitive to defects or holes. Increased sensitivity is likely to be more prominent if APS application techniques are used, as opposed to EB-PVD, as the former results in lower values of Young's modulus. In general it can be seen from energy velocity dispersion curves that, in comparison to single materials, the dispersion curves are quite complex, and there are less areas in which single mode excitation is possible. Having said that, the TBC considered in the temperature dependant study does exhibit a mode (B_5) that has a distinct energy velocity peak, although the bandwidth of the peak is too narrow to be preferentially excited across the whole temperature range of the TBC in this case. It should be noted that the multi-layered structure of a NGV with a TBC applied is likely to have a considerable through-thickness temperature gradient, which will be difficult to detect using the proposed monitoring method. As temperature increases the effect of dispersion on wave propagation becomes more apparent, as the target frequency shifts into a more dispersive region. This begins to have an effect on the calculation of time of flight as there is a less defined central peak to the wave packet, which can be seen in the result at 1020°C. In this case a larger reduction in velocity than expected is measured.

CHAPTER 7

Conclusions and future research

7.1 Conclusions

7.1.1 Research summary

A literature review has been undertaken to identify the currently used temperature monitoring methods for nozzle guide vanes. Both offline and online monitoring systems were evaluated. Within the online monitoring sector there is scope for the development of a new sensor that can operate without influencing component or system operation. An ultrasonic guided wave based system was identified as a potential alternative, and further investigations were undertaken to consider the viability of using such a system. The feasibility of using ultrasonic guided waves for temperature monitoring has been investigated by evaluating other applications of the technology, analysing potential sensor options, considering the range of piezoelectric materials suitable for high temperature operation, how temperature affects material properties, and determining the most appropriate mode for the application. The effect of cooling hole arrays and thermal barrier coatings on wave propagation have been investigated through a range of COMSOL simulations. The temperature influence study consisted of experimental work to measure the temperature sensitivity of three Lamb wave modes (S_0, A_1, and S_1) in aluminium plates using wedge transducers to selectively target each mode of interest. Results are in good agreement with predicted values extracted from dispersion curves, despite the range of errors identified. It has been shown that prior knowledge of material properties can enable changes in wave velocity with temperature to be accurately predicted. Using a sampling rate of 5×10^8 Hz the accuracy of the system based on temporal resolution alone is $\pm0.27\mathrm{m\,s^{-1}}$, which is equivalent to a temperature resolution of 0.18°C for the S_0 mode, 0.24°C for the A_1 mode, and 0.15°C for the S_1 mode.

The results of the experimental work were used to validate a two-dimensional finite element model of the test system, produced in COMSOL. The range of material properties available in literature for both the plate (aluminium) and wedges (PMMA) were evaluated. The properties of Aluminium were chosen to match that of the properties used to generate dispersion curves, while the Young's modulus of PMMA was determined by experimental measurement of temperature dependant longitudinal wave velocity. This ensured that the change in wave velocity with temperature in the wedges closely matched that of reality. Wave velocity was calculated in the same manner as in the experimental study, measuring total time of flight, wedge-to-wedge time of flight, and calculating wedge foot offset distance. 2D-FFT analysis confirms the presence of the modes targeted, and results are in excellent agreement with dispersion curves. The wave velocity results from the simulations align closely with both the experimental and predicted results, all falling within a 2% range. The model was then used as a feasibility study for extending the temperature range up to 1000°C for an Inconel 718 plate, which is a Nickel-based super alloy typically used for jet engine components. Results continue to align with predictions at high temperatures.

The cooling hole study consisted of a number of elements. Firstly, an experimental study of reflection amplitude from different sized holes, repeated for three Lamb wave modes (S_0, A_1, and S_1) in a pulse-echo configuration. This study showed the comparatively higher sensitivity to hole size for the S_0 mode in comparison to the A_1 and S_1 modes, which may be advantageous in discriminating between reflections from different areas of nozzle guide vanes. Sufficient reflection amplitude for any of these modes can be expected, assuming wavelength comparable with hole diameter.

A three dimensional finite element model has been developed to investigate more complex cooling hole configurations at higher temperatures than the experimental equivalent. Two areas of a nozzle guide vane are considered, the trailing edge and the leading edge. The leading edge generally has a higher density of cooling holes as this area is exposed to the highest gas temperatures. Using a pulse-echo configuration is not viable at the leading edge as the signal does not propagate past the first few rows of cooling holes. Transmission in a pitch-catch configuration is more suitable for the A_0 mode than S_0, as a wave packet with a defined peak is received even with a full array (3x20) of cooling holes. Simulations at increased temperatures indicate that the addition of holes to the structure causes a reduction in stiffness, which results in a slower wave velocity than expected based on dispersion curves. The introduction of a temperature hotspot to the model could not easily be distinguished from an overall change in temperature using time of flight based methods, however machine learning models may be be able to detect otherwise indistinguishable changes to wave propagation. This monitoring method would rely on large amounts of training data to work effectively.

At the trailing edge of the vane where there are usually fewer holes and a greater spacing between them, the plausibility of monitoring temperature at different locations using acoustic reflections has been explored. Both pulse-echo and pitch-catch configurations have been considered. When operated in a pulse-echo mode, strong reflections are received from a number of cooling holes, and a hotspot can be successfully identified. Sensors may need to be operated from both sides of the vane to effectively cover the whole array. When operated in a pitch-catch configuration a secondary reflected wave packet is received, which can be seen to be from the third cooling hole. A hotspot at this location can be detected using this method, by comparing a change in time of flight with a baseline signal, however there are not a clear number of other reflections that would allow a hotspot to be detected at other locations. Even under the favourable conditions of these models (with limited additional reflections, environmental noise, etc.) identifying changes in temperature at multiple locations is challenging, and the extent to which reflections from cooling holes can be used for this application is highly dependant on the specific geometry of the vane.

The thermal barrier coating study has considered the range of materials, make up, and application methods typically used, and evaluated the effect of temperature on their structure. Dispersion curves generated for the multi-layered composite show how the higher order modes increase in complexity in comparison with the response in a single material. Through-thickness displacement varies across the thickness as material properties vary, with the top coat often exhibiting considerably larger displacement than then other layers. Although the work carried out looking at a single material (Aluminium or Inconel 718) looked to have promising advantages to working at higher order modes (above S_0), the application of TBCs complicates signal propagation, causing there to be less suitable areas of the spectrum (based on dispersion curve analysis) available for use. That is not to say that specific combinations of material properties and layer thicknesses cannot produce more desirable areas to target, however. Operating below the cut-off frequency of B_2 is likely to be the most effective method of targeting/identifying single modes.

7.1.2 General recommendations

Considering the wide range of superalloy materials used for NGVs, the range of thermal barrier coating composites, and cooling hole configurations, there is not a frequency or mode applicable to all cases, however there are a number of general recommendations that can be made.

When considering the physical properties of a material it has been shown that changes in temperature have the largest impact on Young's modulus, in comparison to Poisson's ratio and density (thermal expansion). This is true even for large temperature ranges (assuming no phase changes occur), although the effect on Poisson's ratio becomes more influential at temperatures closer to the thermal limits of materials. The materials used for NGVs exhibit considerable changes in Young's modulus over the temperature ranges of interest, which has a measurable effect on wave velocity.

There are a number of factors that determine the most suitable operating mode and frequency. Firstly, the ability to identify a single mode in a multi-modal wave packet is critical to time of flight measurement. This can be achieved by attempting to separate the mode of interest in the time domain, by exciting a mode that is substantially faster or slower than other modes at the same frequency, or by selecting a mode that is likely to have a substantially larger amplitude than neighbouring modes. The mode of interest should be targeted at it's group velocity maxima to ensure time domain separation, however the bandwidth of the peak should also be considered, as high temperatures will cause the peak to shift, potentially into a more dispersive region with other modes present.

The lowest two modes, A_0 and S_0, propagate with the largest amplitude in comparison to higher order modes, which can be seen by analysing through thickness displacement profiles, as well as considering that the antisymmetric modes exhibit larger out of plane motion in comparison to symmetric modes, which is more easily detected by piezoelectric transducers. The symmetric modes are less affected by surface defects, and less scattering occurs from features such as holes.

The next factor to consider is wavelength in relation to cooling hole diameter and spacing. The A_0 mode has a substantially shorter wavelength than S_0 at the same frequency, which produces more easily detectable reflections. Operating higher in frequency is advisable, however the low frequency regions of each higher order mode (closer to their cut-off frequency) still exhibit relatively long wavelengths. The likelihood of mode conversion is also determined by wavelength in relation to hole diameter and spacing.

Temperature sensitivity is determined by both mode, and the dispersiveness of the curve at the excitation frequency. A_0 is the least sensitive mode to temperature because of its relatively low dispersion, however this can be advantageous in ensuring a clearly detectable peak even at high temperatures. S_0 on the other hand can provide a considerably higher temperature sensitivity in steep regions of its group velocity dispersion curve, while only exhibiting small amounts of dispersion to a wave packet propagating over a short distance.

Careful dispersion curve analysis is critical to identifying a suitable mode, based on the parameters described previously. This is reliant on accurate knowledge of the material properties in question, as well as of the composite structure of a system with a thermal barrier coating applied, for example.

Temperature monitoring using guided waves can be thought of as providing an average of the through thickness temperature, considering that waves are guided by both surfaces. Lower frequency modes exhibit changes in displacement throughout their thickness, whereas higher order modes have greater displacement towards either surface. This implies that lower order modes provide a better average, whereas the higher order modes are more affected by surface temperatures.

Response time is limited by excitation frequency, pulse width, and received wave packet length. If a long pulse width is used, or a large number of modes are excited, then a longer time between pulses is required to ensure that energy has dissipated before repeating a pulse. Operating in dispersive areas of the spectrum will cause elongated wave packets to be received. That being said, working in the MHz range is likely to provide adequate response times regardless of specific frequency.

Temperature resolution is limited by a combination of mode sensitivity, sampling rate, signal to noise ratio, and pulse width (frequency, and number of cycles). Assuming an adequate sampling rate then uncertainty is caused by the difficulty in detecting the true peak of a wave packet, which is determined by frequency, and signal to noise ratio. A short pulse width (e.g. <5 cycles) reduces the amplitude of the signal, which is likely to make the effect of noise more evident. An increased bandwidth from a short pulse will cause more modes to be excited than intended. Mode sensitivity can change with temperature as the excitation frequency falls on a more or less dispersive region.

The extent to which reflections from cooling holes or other features of the vane can be used for temperature monitoring at different locations is highly dependant on the specific geometry of that vane. The use of dispersion curves and simulations can aide in the identification of appropriate modes, based on wavelength. Pulse-echo operation is likely to provide the response (highest number of reflections) assuming that the signal path is clear. Operating sensors at both ends of a vane would likely provide the most coverage. In areas of high cooling hole density it is unlikely that distinct reflections can be identified, however operating in a pitch-catch configuration can still allow for average temperature monitoring, as well as the possibility of identifying temperature hotspots.

Thermal barrier coatings mostly complicate the higher order mode regions, making it unlikely that a higher order mode can be identified over the whole temperature range of interest. It may still be possible to pick out B_0 or B_1 at higher frequencies however, in areas where the other modes are particularly dispersive and therefore don't exhibit strong peaks or large amplitudes. The lowest order modes exhibit through thickness displacement profiles comparable with A_0 and S_0. When analysing the material properties of TBCs for the generation of dispersion curves, careful consideration should be made for the application method, as it has a significant impact on the Young's modulus, particularly for the top coat.

7.2 Recommendations for future work

There is great scope for further research in this field:

- The development and testing of an appropriate sensor system.
- Evaluating additional signal processing methods.
- Investigating the effect of complex geometry (curved surfaces) on wave propagation in NGVs.
- Applying a test system to an NGV.
- The application of this technology to other systems.

One of the biggest challenges to overcome for the implementation of such as system is in sensor configuration. The limited space, access points for a vane, power constraints, as well as the high temperatures, severely limit the available options. Ideally the transducer configuration developed for this application should be able to achieve single mode excitation, however this is unlikely considering that wedge transducers are unsuitable for permanent installation, and EMATS have a large power consumption. Two-sided excitation is the next best alternative, as it reduces the number of modes excited by half, although this may not be possible in an asymmetric composite such as a NGV with TBC applied to the outer surface. Operation at high temperatures is challenging for piezoelectric transducers, however a number of materials have been identified that can used in these conditions, or the sensors could be distanced from the harsh conditions of the gas path by the use of waveguides. This may have the added benefit of allowing adequate time/distance between excitation and the first reflection from a cooling hole. The range of potential options have been considered in Chapter 3.

This study has focussed on the use of time of flight based temperature monitoring, where changes in wave velocity are linked to changes in temperature. However, this is not the only method of guided wave based temperature monitoring that should be considered. The use of machine learning algorithms should be investigated as a method of hotspot detection, as small changes in wave propagation can indicate changes to the thermal profile that would otherwise be very difficult to detect. Outlier detection methods are already used for a range of defect detection systems using guided waves [222, 224, 225], which highlights the potential of such a system.

The effect of complex curved surfaces on wave propagation is yet to be investigated, however the 3D model developed for the cooling hole study (Chapter 5) could be further adapted for this task. Degradation such as pitting and surface microcracking should also be considered, as changes in surface characteristics can significantly alter the attenuation of guided waves, and cracks/defects are likely to cause additional reflections to occur. Complex geometry is also likely to have a significant impact on the mounting of sensors.

An ultrasonic guided wave based temperature monitoring system has the potential for many other applications (see Section 3.6), especially if the installation of traditional sensors is impractical, or if it would be advantageous to monitor the temperature of an internal structure, as opposed to ambient or surface temperature.

List of references

[1] Lawrence Yule et al. ‘Temperature monitoring of Nozzle Guide Vanes (NGVs) using ultrasonic guided waves’. In: *ASME Turbo Expo 2020*. The American Society of Mechanical Engineers, 2020. URL: http://eprints.soton.ac.uk/id/eprint/445982.

[2] Lawrence Yule et al. ‘Surface temperature condition monitoring methods for aerospace turbomachinery: exploring the use of ultrasonic guided waves’. In: *Meas. Sci. Technol.* 32.5.052002 (May 2021). ISSN: 0957-0233. DOI: 10.1088/1361-6501/abda96. URL: https://iopscience.iop.org/article/10.1088/1361-6501/abda96.

[3] Lawrence M. Yule et al. ‘Towards in-flight temperature monitoring for nozzle guide vanes using ultrasonic guided waves’. In: *AIAA Propuls. Energy 2021 Forum*. Reston, Virginia: American Institute of Aeronautics and Astronautics, Aug. 2021. ISBN: 978-1-62410-611-8. DOI: 10.2514/6.2021-3475. URL: https://arc.aiaa.org/doi/10.2514/6.2021-3475.

[4] Lawrence Yule et al. ‘Modelling and Validation of a Guided Acoustic Wave Temperature Monitoring System’. In: *Sensors* 21.21.7390 (Nov. 2021). ISSN: 1424-8220. DOI: 10.3390/s21217390. URL: https://www.mdpi.com/1424-8220/21/21/7390.

[5] Jeff Dahl. *Diagram of jet engine cross section*. 2008. URL: https://commons.wikimedia.org/wiki/File:Jet_engine_numbered.svg (visited on 15/09/2022).

[6] Federal Aviation Administration. *Aviation emissions, impacts and mitigation: A primer*. 2015. URL: https://www.faa.gov/regulations_policies/policy_guidance/envir_policy/media/primer_jan2015.pdf (visited on 31/08/2022).

[7] Xiaole Zhang, Xi Chen and Jing Wang. ‘A number-based inventory of size-resolved black carbon particle emissions by global civil aviation’. In: *Nat. Commun.* 10.1.534 (Dec. 2019). ISSN: 2041-1723. DOI: 10.1038/s41467-019-08491-9. URL: http://dx.doi.org/10.1038/s41467-019-08491-9.

[8] Bahareh Zaghari et al. ‘High-Temperature Self-Powered Sensing System for a Smart Bearing in an Aircraft Jet Engine’. In: *IEEE Trans. Instrum. Meas.* 69.9 (Sept. 2020), pp. 6165–6174. ISSN: 0018-9456. DOI: 10.1109/TIM.2020.2971288. URL: https://ieeexplore.ieee.org/document/8979443/.

[9] Bahareh Zaghari et al. ‘Integrated smart bearings for next generation aero-engines. Part II: Energy harvesting and wireless communication Development’. In: *WCCM 2017 - 1st World Congr. Cond. Monit. 2017* (2017).

[10] Clive Kerr and Paul Ivey. ‘An overview of the measurement errors associated with gas turbine aeroengine pyrometer systems’. In: *Meas. Sci. Technol.* 13.6 (2002), pp. 873–881. ISSN: 09570233. DOI: 10.1088/0957-0233/13/6/307.

[11] William J. Becker et al. ‘Dynamic turbine blade temperature measurements’. In: *J. Propuls. Power* 10.1 (1994), pp. 69–78. ISSN: 07484658. DOI: 10.2514/3.23713.

[12] Wenwu Zhou. ‘Novel cooling strategies for improved protection of gas turbine blades’. In: *Grad. Theses Diss.* (2016). URL: https://lib.dr.iastate.edu/etd/15167.

[13] S. L. Dixon and C. A. Hall. *Fluid mechanics and thermodynamics of turbomachinery, 7th edition.* Elsevier, 2013, pp. 1–537. ISBN: 9780124159549. DOI: 10.1016/C2011-0-05059-7.

[14] A. L. Heyes, H Sieverding and JF Brouckaert. ‘Thermographic Phosphor thermometry for gas turbines’. In: *Adv. Meas. Tech. aeroengines Station. gas turbines. Von Karmen Inst. fluid Dyn.* (2004).

[15] Jayant Gopal Thakare et al. ‘Thermal Barrier Coatings—A State of the Art Review’. In: *Met. Mater. Int.* 27.7 (July 2021), pp. 1947–1968. ISSN: 1598-9623. DOI: 10.1007/s12540-020-00705-w. URL: https://doi.org/10.1007/s12540-020-00705-w.

[16] P. G. Lashmi et al. ‘Present status and future prospects of plasma sprayed multilayered thermal barrier coating systems’. In: *J. Eur. Ceram. Soc.* 40.8 (2020), pp. 2731–2745. ISSN: 1873619X. DOI: 10.1016/j.jeurceramsoc.2020.03.016. URL: https://doi.org/10.1016/j.jeurceramsoc.2020.03.016.

[17] J. P. Feist. ‘Development of phosphor thermometry for gas turbines’. PhD thesis. University of London, 2001.

[18] Fahed Abou Nada et al. ‘Remote temperature sensing on and beneath atmospheric plasma sprayed thermal barrier coatings using thermographic phosphors’. In: *Surf. Coatings Technol.* 302 (2016), pp. 359–367. ISSN: 02578972. DOI: 10.1016/j.surfcoat.2016.06.038. URL: http://dx.doi.org/10.1016/j.surfcoat.2016.06.038.

[19] Ahmed M. Abdelrhman et al. ‘Condition Monitoring of Blade in Turbomachinery: A Review’. In: *Adv. Mech. Eng.* 6.210717 (Jan. 2014). ISSN: 1687-8140. DOI: 10.1155/2014/210717. URL: http://journals.sagepub.com/doi/10.1155/2014/210717.

[20] Frank Mevissen and Michele Meo. ‘A Review of NDT/Structural Health Monitoring Techniques for Hot Gas Components in Gas Turbines’. In: *Sensors* 19.3 (Feb. 2019). ISSN: 1424-8220. DOI: 10.3390/s19030711. URL: http://www.mdpi.com/1424-8220/19/3/711.

[21] Hengbei Zhao, Carlos G. Levi and Haydn N.G. Wadley. ‘Molten silicate interactions with thermal barrier coatings’. In: *Surf. Coatings Technol.* 251 (2014), pp. 74–86. ISSN: 02578972. DOI: 10.1016/j.surfcoat.2014.04.007. URL: http://dx.doi.org/10.1016/j.surfcoat.2014.04.007.

[22] Peng Guan, Yan-Ting Ai and Cheng-Wei Fei. ‘An Enhanced Flow-Thermo-Structural Modeling and Validation for the Integrated Analysis of a Film Cooling Nozzle Guide Vane’. In: *Energies* 12.14.2775 (July 2019). ISSN: 1996-1073. DOI: 10.3390/en12142775. URL: https://www.mdpi.com/1996-1073/12/14/2775.

[23] E. Findeisen et al. ‘Evaluation of Numerical Methods to Predict Temperature Distributions of an Experimentally Investigated Convection-Cooled Gas-Turbine Blade’. In: *Vol. 5B Heat Transf.* Vol. 5B-2017. American Society of Mechanical Engineers, June 2017, pp. 1–13. ISBN: 978-0-7918-5088-6. DOI: 10.1115/GT2017-64205. URL: https://asmedigitalcollection.asme.org/GT/proceedings-abstract/GT2017/50886/V05BT22A012/241886.

[24] David Peral et al. 'Reliable Temperature Measurement With Thermal History Paints: An Uncertainty Estimation Model'. In: *Vol. 6 Ceram. Control. Diagnostics, Instrumentation; Educ. Manuf. Mater. Metall.* Vol. 6. American Society of Mechanical Engineers, June 2019, p. 10. ISBN: 978-0-7918-5867-7. DOI: 10.1115/GT2019-92087. URL: https://asmedigitalcollection.asme.org/GT/proceedings/GT2019/58677/Phoenix,%20Arizona,%20USA/1067013.

[25] COMSOL. *Thermal Stress Analysis of a Turbine Stator Blade.* 2022. URL: https://www.comsol.com/model/thermal-stress-analysis-of-a-turbine-stator-blade-10476 (visited on 06/08/2022).

[26] Ali Nikparto and Meinhard T. Schobeiri. 'Combined numerical and experimental investigations of heat transfer of a highly loaded low-pressure turbine blade under periodic inlet flow condition'. In: *Proc. Inst. Mech. Eng. Part A J. Power Energy* 232.7 (Nov. 2018), pp. 769–784. ISSN: 0957-6509. DOI: 10.1177/0957650918758158. URL: http://journals.sagepub.com/doi/10.1177/0957650918758158.

[27] Igor Shevchenko et al. 'Verification of Thermal Models of Internally Cooled Gas Turbine Blades'. In: *Int. J. Rotating Mach.* 2018.6780137 (2018), pp. 1–10. ISSN: 1023-621X. DOI: 10.1155/2018/6780137. URL: https://www.hindawi.com/journals/ijrm/2018/6780137/.

[28] Peng Guan et al. 'Thermal Fatigue Life Prediction of Thermal Barrier Coat on Nozzle Guide Vane via Master–Slave Model'. In: *Appl. Sci.* 9.20.4357 (Oct. 2019). ISSN: 2076-3417. DOI: 10.3390/app9204357. URL: https://www.mdpi.com/2076-3417/9/20/4357.

[29] Thamasha Samarasinghe, Chamil Abeykoon and Ali Turan. 'Modelling of heat transfer and fluid flow in the hot section of gas turbines used in power generation: A comprehensive survey'. In: *Int. J. Energy Res.* 43.5.er.4296 (Dec. 2018). ISSN: 0363-907X. DOI: 10.1002/er.4296. URL: https://onlinelibrary.wiley.com/doi/10.1002/er.4296.

[30] Li Yang and Li Zhi-min. 'The Research of Temperature Indicating Paints and its Application in Aero-engine Temperature Measurement'. In: *Procedia Eng.* 99 (2015), pp. 1152–1157. ISSN: 18777058. DOI: 10.1016/j.proeng.2014.12.697. URL: http://dx.doi.org/10.1016/j.proeng.2014.12.697.

[31] Andrew Neely and Philip Tracy. 'Transient Response of Thermal Paints for Use on Short-Duration Hypersonic Flight Tests'. In: *14th AIAA/AHI Sp. Planes Hypersonic Syst. Technol. Conf.* Reston, Virigina: American Institute of Aeronautics and Astronautics, Nov. 2006, pp. 1–15. ISBN: 978-1-62410-050-5. DOI: 10.2514/6.2006-8000. URL: https://arc.aiaa.org/doi/10.2514/6.2006-8000.

[32] C. Lempereur, R. Andral and J. Y. Prudhomme. 'Surface temperature measurement on engine components by means of irreversible thermal coatings'. In: *Meas. Sci. Technol.* 19.10.105501 (Oct. 2008). ISSN: 0957-0233. DOI: 10.1088/0957-0233/19/10/105501. URL: https://iopscience.iop.org/article/10.1088/0957-0233/19/10/105501.

[33] J. Coleto et al. 'Phase Change Materials and Thermosensitive Painting: Application on Smart Thermal Protection Systems'. In: *57th Int. Astronaut. Congr.* Vol. 8. Reston, Virigina: American Institute of Aeronautics and Astronautics, Oct. 2006, pp. 5276–5287. ISBN: 978-1-62410-042-0. DOI: 10.2514/6.IAC-06-C2.5.03. URL: https://arc.aiaa.org/doi/10.2514/6.IAC-06-C2.5.03.

[34] Andrew J Neely. 'Permanent-Change Thermal Paints for Hypersonic Flight-Test'. PhD thesis. University of New South Wales, 2010.

[35] C Bird et al. 'Surface temperature measurements in turbines'. In: *AGARD Conf. Proc. 598*. 1998. URL: https://www.semanticscholar.org/paper/Surface-temperature-measurement-in-turbines-Bird-Mutton/15949a3e8d8e8d40bbae0326ffcdd44bc24fd198.

[36] European Parliament. *Regulation (EC) No 1907/2006 - Registration, Evaluation, Authorisation and Restriction of Chemicals (REACH) - Safety and health at work - EU-OSHA*. 2006. URL: https://osha.europa.eu/en/legislation/directives/regulation-ec-no-1907-2006-of-the-european-parliament-and-of-the-council (visited on 07/05/2020).

[37] Jorg Feist, J. R. Nicholls and A. L. Heyes. *Monitoring thermal history of components*. 2007.

[38] S.K. Biswas et al. 'Thermal history paints - principles and progress'. In: *IET ISA 60th Int. Instrum. Symp. 2014*. Institution of Engineering and Technology, 2014. ISBN: 978-1-84919-858-5. DOI: 10.1049/cp.2014.0538. URL: https://digital-library.theiet.org/content/conferences/10.1049/cp.2014.0538.

[39] Silvia Araguás Rodríguez et al. 'Accelerated thermal profiling of gas turbine components using luminescent thermal history paints'. In: *J. Glob. Power Propuls. Soc.* 2 (2018), S3KTGK. DOI: 10.22261/jgpps.s3ktgk.

[40] Christopher Pilgrim et al. 'Surface Temperature Measurements in an Industrial Gas Turbine Using Thermal History Paints'. In: *12th Eur. Conf. Turbomach. Fluid Dyn. Thermodyn. ETC 2017*. 2017. DOI: 10.29008/ETC2017-303. URL: http://www.euroturbo.eu/publications/proceedings-papers/ETC2017-303/.

[41] A. Rabhiou et al. 'Phosphorescent thermal history sensors'. In: *Sensors Actuators A Phys.* 169.1 (Sept. 2011), pp. 18–26. ISSN: 09244247. DOI: 10.1016/j.sna.2011.04.022. URL: http://dx.doi.org/10.1016/j.sna.2011.04.022.

[42] Stéphane Amiel et al. 'On the thermal sensitivity and resolution of a YSZ:Er3+/YSZ:Eu3+ fluorescent thermal history sensor'. In: *Sensors Actuators A Phys.* 272 (Apr. 2018), pp. 42–52. ISSN: 09244247. DOI: 10.1016/j.sna.2018.01.040. URL: http://dx.doi.org/10.1016/j.sna.2018.01.040.

[43] A. L. Heyes et al. 'Phosphor Based Temperature Indicating Paints'. In: *Vol. 1 Aircr. Engine; Ceram. Coal, Biomass Altern. Fuels; Control. Diagnostics Instrum.* Vol. 1. American Society of Mechanical Engineers, June 2012, pp. 927–933. ISBN: 978-0-7918-4467-0. DOI: 10.1115/GT2012-69811. URL: https://asmedigitalcollection.asme.org/GT/proceedings/GT2012/44670/927/289192.

[44] M Annerfeldt et al. 'GTX100 Turbine section measurement using a temperature sensitive crystal technique. A comparison with 3D thermal and aerodynamic analysis'. In: *PowerGen Eur.* (2004). URL: https://www.energy.siemens.com/br/pool/hq/energy-topics/pdfs/en/gas-turbines-power-plants/1_GTX_100_Turbine.pdf.

[45] Geoff E. Fair, Ronald J. Kerans and Triplicane A. Parthasarathy. 'Thermal history sensor based on glass-ceramics'. In: *Sensors Actuators A Phys.* 141.2 (Feb. 2008), pp. 245–255. ISSN: 09244247. DOI: 10.1016/j.sna.2007.08.031. URL: https://linkinghub.elsevier.com/retrieve/pii/S0924424707006656.

[46] Kin-Ho Lo, Chan-Hung Shek and Joseph Lai. 'Metallurgical Temperature Sensors'. In: *Recent Patents Mech. Eng.* 1.3 (Nov. 2008), pp. 225–232. ISSN: 22127976. DOI: 10.2174/2212797610801030225. URL: http://www.eurekaselect.com/openurl/content.php?genre=article&issn=2212-7976&volume=1&issue=3&spage=225.

[47] Daniel P. Madison et al. ‘Comparison of Piston Temperature Measurement Methods: Templugs Versus Wireless Telemetry With Thermocouples’. In: *J. Eng. Gas Turbines Power* 135.6 (June 2013). ISSN: 0742-4795. DOI: 10.1115/1.4023493. URL: https://asmedigitalcollection.asme.org/gasturbinespower/article/doi/10.1115/1.4023493/373421/Comparison-of-Piston-Temperature-Measurement.

[48] Franklin Li Duan et al. ‘Robust Thin-Film Temperature Sensors Embedded on Nozzle Guide Vane Surface’. In: *AIAA J.* 58.4 (Apr. 2020), pp. 1441–1445. ISSN: 0001-1452. DOI: 10.2514/1.J058854. URL: https://arc.aiaa.org/doi/10.2514/1.J058854.

[49] Kenneth G. Kreider. ‘Sputtered high temperature thin film thermocouples’. In: *J. Vac. Sci. Technol. A Vacuum, Surfaces, Film.* 11.4 (July 1993), pp. 1401–1405. ISSN: 0734-2101. DOI: 10.1116/1.578561. URL: http://avs.scitation.org/doi/10.1116/1.578561.

[50] Dongfang Yang et al. ‘Laser deposited high temperature thin film sensors for gas turbines’. In: *Aircr. Eng. Aerosp. Technol.* 92.1 (Jan. 2020), pp. 2–7. ISSN: 1748-8842. DOI: 10.1108/AEAT-11-2018-0292. URL: https://www.emerald.com/insight/content/doi/10.1108/AEAT-11-2018-0292/full/html.

[51] Yantao Liu et al. ‘A Highly Thermostable In2O3/ITO Thin Film Thermocouple Prepared via Screen Printing for High Temperature Measurements’. In: *Sensors* 18.4.958 (Mar. 2018). ISSN: 1424-8220. DOI: 10.3390/s18040958. URL: http://www.mdpi.com/1424-8220/18/4/958.

[52] Yanli Zhang et al. ‘Laser Cladding of Embedded Sensors for Thermal Barrier Coating Applications’. In: *Coatings* 8.5.176 (May 2018). ISSN: 2079-6412. DOI: 10.3390/coatings8050176. URL: http://www.mdpi.com/2079-6412/8/5/176.

[53] Junchao Gao et al. ‘Electrical insulation of ceramic thin film on metallic aero-engine blade for high temperature sensor applications’. In: *Ceram. Int.* 42.16 (Dec. 2016), pp. 19269–19275. ISSN: 02728842. DOI: 10.1016/j.ceramint.2016.09.093. URL: http://dx.doi.org/10.1016/j.ceramint.2016.09.093.

[54] T. N. Satish et al. ‘Functional Validation of K-Type (NiCr-NiMn) Thin Film Thermocouple on Low Pressure Turbine Nozzle Guide Vane (LPT NGV) of Gas Turbine Engine’. In: *Exp. Tech.* 41.2 (Apr. 2017), pp. 131–138. ISSN: 0732-8818. DOI: 10.1007/s40799-016-0162-1. URL: http://link.springer.com/10.1007/s40799-016-0162-1.

[55] Zhonglin Ji et al. ‘Temperature Distribution Measurements on Turbine Blade Surface by the Aid of Simple Dotted Pt/PtRh Thermal Couple Test Array’. In: *AIAA Propuls. Energy 2019 Forum.* Vol. 1. August. Reston, Virginia: American Institute of Aeronautics and Astronautics, Aug. 2019. ISBN: 978-1-62410-590-6. DOI: 10.2514/6.2019-4084. URL: https://arc.aiaa.org/doi/10.2514/6.2019-4084.

[56] Jih-Fen Lei, Lisa C. Martin and Herbert A. Will. ‘Advances in Thin Film Sensor Technologies for Engine Applications’. In: *Vol. 4 Manuf. Mater. Metall. Ceram. Struct. Dyn. Control. Diagnostics Instrumentation; Educ. IGTI Sch. Award.* Vol. 4. American Society of Mechanical Engineers, June 1997. ISBN: 978-0-7918-7871-2. DOI: 10.1115/97-GT-458. URL: https://asmedigitalcollection.asme.org/GT/proceedings/GT1997/78712/Orlando,%20Florida,%20USA/249043.

[57] Erdogan Guk et al. ‘Performance and Durability of Thin Film Thermocouple Array on a Porous Electrode’. In: *Sensors* 16.9.1329 (Aug. 2016). ISSN: 1424-8220. DOI: 10.3390/s16091329. URL: http://www.mdpi.com/1424-8220/16/9/1329.

[58] Clive Kerr and Paul Ivey. 'Optical pyrometry for gas turbine aeroengines'. In: *Sens. Rev.* 24.4 (Dec. 2004), pp. 378–386. ISSN: 0260-2288. DOI: 10.1108/02602280410558412. URL: https://www.emerald.com/insight/content/doi/10.1108/02602280410558412/full/html.

[59] Dong Li et al. 'Turbine blade temperature error as measured with an optical pyrometer under different wavelengths and blade TBC thickness'. In: *Appl. Opt.* 58.7.1626 (Mar. 2019). ISSN: 1559-128X. DOI: 10.1364/AO.58.001626. URL: https://opg.optica.org/abstract.cfm?URI=ao-58-7-1626.

[60] Y. B. Yu and W. K. Chow. 'Review on an Advanced High-Temperature Measurement Technology: The Optical Fiber Thermometry'. In: *J. Thermodyn.* 2009.823482 (Jan. 2009). ISSN: 1687-9244. DOI: 10.1155/2009/823482. URL: https://www.hindawi.com/journals/jther/2009/823482/.

[61] Dong Li et al. 'Effect of pyrometer type and wavelength selection on temperature measurement errors for turbine blades'. In: *Infrared Phys. Technol.* 94.July (Nov. 2018), pp. 255–262. ISSN: 13504495. DOI: 10.1016/j.infrared.2018.09.004. URL: https://doi.org/10.1016/j.infrared.2018.09.004.

[62] António Araújo. 'Multi-spectral pyrometry—a review'. In: *Meas. Sci. Technol.* 28.8.082002 (Aug. 2017). ISSN: 0957-0233. DOI: 10.1088/1361-6501/aa7b4b. URL: https://iopscience.iop.org/article/10.1088/1361-6501/aa7b4b.

[63] Molly M. Gentleman et al. 'Noncontact Methods for Measuring Thermal Barrier Coating Temperatures'. In: *Int. J. Appl. Ceram. Technol.* 3.2 (Mar. 2006), pp. 105–112. ISSN: 1546-542X. DOI: 10.1111/j.1744-7402.2006.02069.x. URL: https://onlinelibrary.wiley.com/doi/10.1111/j.1744-7402.2006.02069.x.

[64] Stefan L. F. Frank et al. 'Application of a High Resolution Turbine Pyrometer to Heavy Duty Gas Turbines'. In: *Vol. 4 Manuf. Mater. Metall. Ceram. Struct. Dyn. Control. Diagnostics Instrumentation; Educ. IGTI Sch. Award.* Vol. 4. American Society of Mechanical Engineers, June 2001. ISBN: 978-0-7918-7853-8. DOI: 10.1115/2001-GT-0577. URL: https://asmedigitalcollection.asme.org/GT/proceedings/GT2001/78538/New%20Orleans,%20Louisiana,%20USA/249728.

[65] Guanghua Wang et al. 'Real-Time Burst Signal Removal Using Multicolor Pyrometry Based Filter for Improved Jet Engine Control'. In: *J. Turbomach.* 137.8.081008-1 (Aug. 2015). ISSN: 0889-504X. DOI: 10.1115/1.4029615. URL: https://asmedigitalcollection.asme.org/turbomachinery/article/doi/10.1115/1.4029615/378589/RealTime-Burst-Signal-Removal-Using-Multicolor.

[66] Tomoki Taniguchi et al. 'Temperature Measurement of High Speed Rotating Turbine Blades Using a Pyrometer'. In: *Vol. 2 Aircr. Engine; Ceram. Coal, Biomass Altern. Fuels; Control. Diagnostics Instrumentation; Environ. Regul. Aff.* Vol. 2. ASMEDC, Jan. 2006, pp. 521–529. ISBN: 0-7918-4237-1. DOI: 10.1115/GT2006-90247. URL: https://asmedigitalcollection.asme.org/GT/proceedings/GT2006/42371/521/314598.

[67] Anders Hellberg. *The siemens SGT-750 gas turbine: Developed for the oil and gas industry.* Tech. rep. 1. 2018. URL: https://www.semanticscholar.org/paper/THE-SIEMENS-SGT-750-GAS-TURBINE-:-DEVELOPED-FOR-THE-Hellberg/42184387d70614ac0c66fc8442d95de11d20f285?sort=relevance&citationIntent=methodology.

[68] C. Falsetti, M. Sisti and P.F. Beard. 'Infrared thermography and calibration techniques for gas turbine applications: A review'. In: *Infrared Phys. Technol.* 113.103574.May 2020 (Mar. 2021). ISSN: 13504495. DOI: 10.1016/j.infrared.2020.103574. URL: https://doi.org/10.1016/j.infrared.2020.103574.

[69] T Liu and J.P. Sullivan. *Pressure and Temperature Sensitive Paints*. Experimental Fluid Mechanics. Berlin/Heidelberg: Springer-Verlag, 2005. ISBN: 3-540-22241-3. DOI: 10.1007/b137841. URL: http://link.springer.com/10.1007/b137841.

[70] Mayur D Patel and Mark A Ricklick. 'In-house fabrication of temperature sensitive paint for turbine cooling research'. In: *Beyond Undergrad. Res. J.* 1.January (2016). URL: https://commons.erau.edu/beyond/vol1/iss1/5.

[71] Ashiq Khalid and Konstantinos Kontis. 'Thermographic Phosphors for High Temperature Measurements: Principles, Current State of the Art and Recent Applications'. In: *Sensors* 8.9 (Sept. 2008), pp. 5673–5744. ISSN: 1424-8220. DOI: 10.3390/s8095673. URL: http://www.mdpi.com/1424-8220/8/9/5673.

[72] S. W. Allison and G. T. Gillies. 'Remote thermometry with thermographic phosphors: Instrumentation and applications'. In: *Rev. Sci. Instrum.* 68.7 (1997), pp. 2615–2650. ISSN: 00346748. DOI: 10.1063/1.1148174.

[73] A. H. Khalid, K. Kontis and H. Z. Behtash. 'Phosphor thermometry in gas turbines: Consideration factors'. In: *Proc. Inst. Mech. Eng. Part G J. Aerosp. Eng.* 224.7 (2010), pp. 745–755. ISSN: 09544100. DOI: 10.1243/09544100JAERO560.

[74] Jan Brübach et al. 'On surface temperature measurements with thermographic phosphors: A review'. In: *Prog. Energy Combust. Sci.* 39.1 (Feb. 2013), pp. 37–60. ISSN: 03601285. DOI: 10.1016/j.pecs.2012.06.001. URL: https://linkinghub.elsevier.com/retrieve/pii/S0360128512000433.

[75] X. Chen et al. 'Industrial Sensor TBCs: Studies on Temperature Detection and Durability'. In: *Int. J. Appl. Ceram. Technol.* 2.5 (Sept. 2005), pp. 414–421. ISSN: 1546-542X. DOI: 10.1111/j.1744-7402.2005.02042.x. URL: https://onlinelibrary.wiley.com/doi/10.1111/j.1744-7402.2005.02042.x.

[76] J. P. Feist et al. 'Application of an Industrial Sensor Coating System on a Rolls-Royce Jet Engine for Temperature Detection'. In: *J. Eng. Gas Turbines Power* 135.1.012101-1 (Jan. 2013). ISSN: 0742-4795. DOI: 10.1115/1.4007370. URL: https://doi.org/10.1115/1.4007370.

[77] A. Yañez Gonzalez et al. 'On-Line Temperature Measurement Inside a Thermal Barrier Sensor Coating During Engine Operation'. In: *J. Turbomach.* 137.10.101004-1 (Oct. 2015). ISSN: 0889-504X. DOI: 10.1115/1.4030260. URL: https://asmedigitalcollection.asme.org/turbomachinery/article/doi/10.1115/1.4030260/378219/OnLine-Temperature-Measurement-Inside-a-Thermal.

[78] Thomas P Jenkins et al. 'Measurements of turbine blade temperature in an operating aero engine using thermographic phosphors'. In: *Meas. Sci. Technol.* 31.4.044003 (Apr. 2020). ISSN: 0957-0233. DOI: 10.1088/1361-6501/ab4c20. URL: https://iopscience.iop.org/article/10.1088/1361-6501/ab4c20.

[79] Jeffrey I. Eldridge. 'Luminescence decay-based Y2O3:Er phosphor thermometry: Temperature sensitivity governed by multiphonon emission with an effective phonon energy transition'. In: *J. Lumin.* 214.116535 (Oct. 2019). ISSN: 00222313. DOI: 10.1016/j.jlumin.2019.116535. URL: https://linkinghub.elsevier.com/retrieve/pii/S002223131930674X.

[80] Patrick Nau et al. 'Wall Temperature Measurements in Gas Turbine Combustors With Thermographic Phosphors'. In: *J. Eng. Gas Turbines Power* 141.4 (Apr. 2019). ISSN: 0742-4795. DOI: 10.1115/1.4040716. URL: https://asmedigitalcollection.asme.org/gasturbinespower/article/doi/10.1115/1.4040716/367158/Wall-Temperature-Measurements-in-Gas-Turbine.

[81] Franklin Li Duan et al. 'Development of robust high temperature mems sensor on aero-engine turbine blade surface'. In: *2018 Jt. Propuls. Conf.* (2018), pp. 1–7. DOI: 10.2514/6.2018-4622.

[82] Bahareh Zaghari, Alex Weddell and Neil White. 'Opportunities and challenges for energy harvesting sensor systems for harsh environments'. In: *ENSsys 2017 - Proc. 5th Int. Work. Energy Harvest. Energy-Neutral Sens. Syst. Part SenSys 2017.* New York, New York, USA: Association for Computing Machinery, Inc, Nov. 2017, pp. 40–42. ISBN: 9781450354776. DOI: 10.1145/3142992.3143001. URL: http://dl.acm.org/citation.cfm?doid=3142992.3143001.

[83] Mira Mitra and S. Gopalakrishnan. 'Guided wave based structural health monitoring: A review'. In: *Smart Mater. Struct.* 25.5.053001 (May 2016). ISSN: 0964-1726. DOI: 10.1088/0964-1726/25/5/053001. URL: https://iopscience.iop.org/article/10.1088/0964-1726/25/5/053001.

[84] M Fatemi. 'Ultrasonic B-scan imaging: Theory of image formation and a technique for restoration'. In: *Ultrason. Imaging* 2.1 (Jan. 1980). ISSN: 01617346. DOI: 10.1016/0161-7346(80)90201-1. URL: https://linkinghub.elsevier.com/retrieve/pii/0161734680902011.

[85] Roman Růžek, Radek Lohonka and Josef Jironč. 'Ultrasonic C-Scan and shearography NDI techniques evaluation of impact defects identification'. In: *NDT E Int.* 39.2 (Mar. 2006), pp. 132–142. ISSN: 09638695. DOI: 10.1016/j.ndteint.2005.07.012. URL: https://linkinghub.elsevier.com/retrieve/pii/S096386950500112X.

[86] K. Imielińska et al. 'Air-coupled ultrasonic C-scan technique in impact response testing of carbon fibre and hybrid: glass, carbon and Kevlar/epoxy composites'. In: *J. Mater. Process. Technol.* 157-158.SPEC. ISS. (Dec. 2004), pp. 513–522. ISSN: 09240136. DOI: 10.1016/j.jmatprotec.2004.07.143. URL: https://linkinghub.elsevier.com/retrieve/pii/S0924013604011355.

[87] Ichiro Komura et al. 'Crack detection and sizing technique by ultrasonic and electromagnetic methods'. In: *Nucl. Eng. Des.* 206.2-3 (June 2001), pp. 351–362. ISSN: 00295493. DOI: 10.1016/S0029-5493(00)00421-0. URL: http://link.springer.com/10.1007/s11003-011-9382-9.

[88] Bahareh Zaghari, Victor Humphrey and Mohamed Moshrefi-Torbati. 'Dispersion behavior of torsional guided waves in a small diameter steel gas pipe'. In: *ICAC 2013 - Proc. 19th Int. Conf. Autom. Comput. Futur. Energy Autom.* 1.September (2013), pp. 37–42.

[89] Hongmei Shi et al. 'An Ultrasonic Guided Wave Mode Selection and Excitation Method in Rail Defect Detection'. In: *Appl. Sci.* 9.6.1170 (Mar. 2019). ISSN: 2076-3417. DOI: 10.3390/app9061170. URL: https://www.mdpi.com/2076-3417/9/6/1170.

[90] Yu Wang et al. 'A stretchable and large-scale guided wave sensor network for aircraft smart skin of structural health monitoring'. In: *Struct. Heal. Monit.* 20.3 (May 2021), pp. 861–876. ISSN: 1475-9217. DOI: 10.1177/1475921719850641. URL: http://journals.sagepub.com/doi/10.1177/1475921719850641.

[91] K. Dransfeld and E. Salzmann. 'Excitation, Detection, and Attenuation of High-Frequency Elastic Surface Waves'. In: *Phys. Acoust.* Vol. 7. 1. ACADEMIC PRESS, INC., 1970, pp. 219–272. DOI: 10.1016/B978-0-12-395667-5.50010-6. URL: http://dx.doi.org/10.1016/B978-0-12-395667-5.50010-6.

[92] A. Gajdacsi et al. 'Reconstruction of Temperature Distribution in a Steel Block Using an Ultrasonic Sensor Array'. In: *J. Nondestruct. Eval.* 33.3 (Sept. 2014), pp. 458–470. ISSN: 0195-9298. DOI: 10.1007/s10921-014-0241-0. URL: http://link.springer.com/10.1007/s10921-014-0241-0.

[93] A.J Croxford et al. ‘Strategies for guided-wave structural health monitoring’. In: *Proc. R. Soc. A Math. Phys. Eng. Sci.* 463.2087 (Nov. 2007), pp. 2961–2981. ISSN: 1364-5021. DOI: 10.1098/rspa.2007.0048. URL: https://royalsocietypublishing.org/doi/10.1098/rspa.2007.0048.

[94] J. B. Harley and J. M. F. Moura. ‘Scale transform signal processing for optimal ultrasonic temperature compensation’. In: *IEEE Trans. Ultrason. Ferroelectr. Freq. Control* 59.10 (Oct. 2012), pp. 2226–2236. ISSN: 0885-3010. DOI: 10.1109/TUFFC.2012.2448. URL: http://ieeexplore.ieee.org/document/6327494/.

[95] G. Konstantinidis, B. W. Drinkwater and P. D. Wilcox. ‘The temperature stability of guided wave structural health monitoring systems’. In: *Smart Mater. Struct.* 15.4 (Aug. 2006), pp. 967–976. ISSN: 0964-1726. DOI: 10.1088/0964-1726/15/4/010. URL: https://iopscience.iop.org/article/10.1088/0964-1726/15/4/010.

[96] T. Clarke, F. Simonetti and P. Cawley. ‘Guided wave health monitoring of complex structures by sparse array systems: Influence of temperature changes on performance’. In: *J. Sound Vib.* 329.12 (June 2010), pp. 2306–2322. ISSN: 0022460X. DOI: 10.1016/j.jsv.2009.01.052. URL: http://dx.doi.org/10.1016/j.jsv.2009.01.052.

[97] Anthony J. Croxford et al. ‘Efficient temperature compensation strategies for guided wave structural health monitoring’. In: *Ultrasonics* 50.4-5 (Apr. 2010), pp. 517–528. ISSN: 0041624X. DOI: 10.1016/j.ultras.2009.11.002. URL: http://dx.doi.org/10.1016/j.ultras.2009.11.002%20https://linkinghub.elsevier.com/retrieve/pii/S0041624X09001826.

[98] Yishou Wang et al. ‘An adaptive filter–based temperature compensation technique for structural health monitoring’. In: *J. Intell. Mater. Syst. Struct.* 25.17 (Nov. 2014), pp. 2187–2198. ISSN: 1045-389X. DOI: 10.1177/1045389X13519001. URL: http://journals.sagepub.com/doi/10.1177/1045389X13519001.

[99] Dan Li et al. ‘A New Approach to Guided Wave Ray Tomography for Temperature-Robust Damage Detection Using Piezoelectric Sensors’. In: *Sensors* 18.10.3518 (Oct. 2018). ISSN: 1424-8220. DOI: 10.3390/s18103518. URL: http://www.mdpi.com/1424-8220/18/10/3518.

[100] Guoqiang Liu et al. ‘Baseline Signal Reconstruction for Temperature Compensation in Lamb Wave-Based Damage Detection’. In: *Sensors* 16.8.1273 (Aug. 2016). ISSN: 1424-8220. DOI: 10.3390/s16081273. URL: http://www.mdpi.com/1424-8220/16/8/1273.

[101] Stefano Mariani, Sebastian Heinlein and Peter Cawley. ‘Compensation for temperature-dependent phase and velocity of guided wave signals in baseline subtraction for structural health monitoring’. In: *Struct. Heal. Monit.* 19.1 (Jan. 2020). ISSN: 1475-9217. DOI: 10.1177/1475921719835155. URL: http://journals.sagepub.com/doi/10.1177/1475921719835155.

[102] Balint Herdovics and Frederic Cegla. ‘Compensation of phase response changes in ultrasonic transducers caused by temperature variations’. In: *Struct. Heal. Monit.* 18.2 (Mar. 2019). ISSN: 1475-9217. DOI: 10.1177/1475921718759272. URL: http://journals.sagepub.com/doi/10.1177/1475921718759272.

[103] Joel B. Harley et al. ‘Application of Mellin transform features for robust ultrasonic guided wave structural health monitoring’. In: *AIP Conf. Proc.* Vol. 1430. 31. 2012, pp. 1551–1558. ISBN: 9780735410138. DOI: 10.1063/1.4716399. URL: http://aip.scitation.org/doi/abs/10.1063/1.4716399.

[104] Nathan Ida. *Sensors, Actuators, and their Interfaces: A Multidisciplinary Introduction.* Edison, NJ: Institution of Engineering and Technology, Dec. 2013. ISBN: 9781613530061. DOI: 10.1049/SBCS502E. URL: https://digital-library.theiet.org/content/books/cs/sbcs502e.

[105] Mauricio Pereira da Cunha et al. 'Recent advances in harsh environment acoustic wave sensors for contemporary applications'. In: *2011 IEEE SENSORS Proc.* IEEE, Oct. 2011. ISBN: 978-1-4244-9289-3. DOI: 10.1109/ICSENS.2011.6126948. URL: http://ieeexplore.ieee.org/document/6126948/.

[106] Wenxiu Dong et al. 'Sensitivity enhanced temperature sensor: one-port 2D surface phononic crystal resonator based on AlN/sapphire'. In: *Semicond. Sci. Technol.* 34.5.055005 (May 2019). ISSN: 0268-1242. DOI: 10.1088/1361-6641/ab0a82. URL: https://iopscience.iop.org/article/10.1088/1361-6641/ab0a82.

[107] Shuzeng Zhang, Xiongbing Li and Hyunjo Jeong. 'Measurement of Rayleigh Wave Beams Using Angle Beam Wedge Transducers as the Transmitter and Receiver with Consideration of Beam Spreading'. In: *Sensors* 17.6.1449 (June 2017). ISSN: 1424-8220. DOI: 10.3390/s17061449. URL: http://www.mdpi.com/1424-8220/17/6/1449.

[108] Pouyan Khalili and Peter Cawley. 'Excitation of Single-Mode Lamb Waves at High-Frequency-Thickness Products'. In: *IEEE Trans. Ultrason. Ferroelectr. Freq. Control* 63.2 (Feb. 2016), pp. 303–312. ISSN: 0885-3010. DOI: 10.1109/TUFFC.2015.2507443. URL: http://ieeexplore.ieee.org/document/7352350/.

[109] Hanfei Mei et al. 'Recent Advances in Piezoelectric Wafer Active Sensors for Structural Health Monitoring Applications'. In: *Sensors* 19.2.383 (Jan. 2019). ISSN: 1424-8220. DOI: 10.3390/s19020383. URL: http://www.mdpi.com/1424-8220/19/2/383.

[110] Victor Giurgiutiu. 'Lamb wave generation with piezoelectric wafer active sensors for structural health monitoring'. In: *Smart Struct. Mater. 2003 Smart Struct. Integr. Syst.* Ed. by Amr M. Baz. Vol. 5056. August 2003. Aug. 2003, pp. 111–122. DOI: 10.1117/12.483492. URL: http://proceedings.spiedigitallibrary.org/proceeding.aspx?doi=10.1117/12.483492.

[111] Baiyang Ren and Cliff J. Lissenden. 'A fully coupled model for actuation of higher order modes of Lamb waves'. In: *AIP Conf. Proc.* Vol. 1806.03000. February 2017. 2017. ISBN: 9780735414747. DOI: 10.1063/1.4974577. URL: http://aip.scitation.org/doi/abs/10.1063/1.4974577.

[112] David A. Parks, Shujun Zhang and B. R. Tittmann. 'High-temperature (>500 /spl deg C) ultrasonic transducers: an experimental comparison among three candidate piezoelectric materials'. In: *IEEE Trans. Ultrason. Ferroelectr. Freq. Control* 60.5 (May 2013), pp. 1010–1015. ISSN: 0885-3010. DOI: 10.1109/TUFFC.2013.2659. URL: http://ieeexplore.ieee.org/document/6512839/.

[113] Frederic B. Cegla et al. 'High-temperature (>500°c) wall thickness monitoring using dry-coupled ultrasonic waveguide transducers'. In: *IEEE Trans. Ultrason. Ferroelectr. Freq. Control* 58.1 (Jan. 2011), pp. 156–167. ISSN: 0885-3010. DOI: 10.1109/TUFFC.2011.1782. URL: http://ieeexplore.ieee.org/document/5688409/.

[114] F.L. Degertakin and B. Khuri-Yakub. 'Lamb wave excitation by Hertzian contacts with applications in NDE'. In: *IEEE Trans. Ultrason. Ferroelectr. Freq. Control* 44.4 (July 1997), pp. 769–779. ISSN: 0885-3010. DOI: 10.1109/58.655191. URL: http://ieeexplore.ieee.org/document/655191/.

[115] Raimond Grimberg et al. 'Determination of elastic properties of CFRP using lamb waves resonant spectroscopy'. In: *NDT Aerosp.* 1 (2010). URL: http://www.2010.ndt-aerospace.com/Portals/aerospace2010/BB/we5b1.pdf.

[116] M. Willsch, T. Bosselmann and N.M. Theune. 'New approaches for the monitoring of gas turbine blades and vanes'. In: *Proc. IEEE Sensors, 2004.* Vol. 1. IEEE, 2004, pp. 20–23. ISBN: 0-7803-8692-2. DOI: 10.1109/ICSENS.2004.1426089. URL: http://ieeexplore.ieee.org/document/1426089/.

[117] Pouyan Khalili and Peter Cawley. 'The choice of ultrasonic inspection method for the detection of corrosion at inaccessible locations'. In: *NDT E Int.* 99.March 2017 (2018), pp. 80–92. ISSN: 09638695. DOI: 10.1016/j.ndteint.2018.06.003. URL: https://doi.org/10.1016/j.ndteint.2018.06.003.

[118] Taeyang Kim et al. 'Narrow band photoacoustic lamb wave generation for nondestructive testing using candle soot nanoparticle patches'. In: *Appl. Phys. Lett.* 115.10.102902 (Sept. 2019). ISSN: 0003-6951. DOI: 10.1063/1.5100292. URL: http://aip.scitation.org/doi/10.1063/1.5100292.

[119] Xiaoning Jiang et al. 'High-Temperature Piezoelectric Sensing'. In: *Sensors* 14.1 (Dec. 2013), pp. 144–169. ISSN: 1424-8220. DOI: 10.3390/s140100144. URL: http://www.mdpi.com/1424-8220/14/1/144.

[120] R. Fachberger et al. 'Properties of radio frequency rayleigh waves on langasite at elevated temperatures'. In: *IEEE Ultrason. Symp. 2004.* Vol. 2. c. IEEE, 2004, pp. 1223–1226. ISBN: 0-7803-8412-1. DOI: 10.1109/ULTSYM.2004.1418008. URL: http://ieeexplore.ieee.org/document/1418008/.

[121] Adam M Hurst et al. 'Real-time, advanced electrical filtering for pressure transducer frequency response correction'. In: *Proc. ASME Turbo Expo.* Vol. 6. American Society of Mechanical Engineers, June 2015. ISBN: 9780791856758. DOI: 10.1115/GT2015-42895. URL: https://asmedigitalcollection.asme.org/GT/proceedings/GT2015/56758/Montreal,%20Quebec,%20Canada/237608.

[122] Sungwon Ha et al. 'Adhesive Layer Effects on PZT-induced Lamb Waves at Elevated Temperatures'. In: *Struct. Heal. Monit.* 9.3 (May 2010), pp. 247–256. ISSN: 1475-9217. DOI: 10.1177/1475921710365267. URL: http://journals.sagepub.com/doi/10.1177/1475921710365267.

[123] R.C. Turner et al. 'Materials for high temperature acoustic and vibration sensors: A review'. In: *Appl. Acoust.* 41.4 (1994), pp. 299–324. ISSN: 0003682X. DOI: 10.1016/0003-682X(94)90091-4. URL: https://linkinghub.elsevier.com/retrieve/pii/0003682X94900914.

[124] James F. Tressler, Sedat Alkoy and Robert E. Newnham. 'Piezoelectric sensors and sensor materials'. In: *J. Electroceramics* 2.4 (1998), pp. 257–272. ISSN: 13853449. DOI: 10.1023/A:1009926623551. URL: https://link.springer.com/article/10.1023/A:1009926623551.

[125] Bernhard R Tittmann, David A Parks and Shujun O Zhang. 'High temperature piezoelectrics - A comparison'. In: *13th Int. Symp. Nondestruct. Characterisation Mater.* Vol. 1. May. 2013. URL: https://www.ndt.net/article/ndcm2013/content/papers/43_Tittmann.pdf.

[126] Mark J Schulz et al. 'Piezoelectric Materials at Elevated Temperature'. In: *J. Intell. Mater. Syst. Struct.* 14.11 (Nov. 2003), pp. 693–705. ISSN: 1045-389X. DOI: 10.1177/1045389X03038577. URL: http://journals.sagepub.com/doi/10.1177/1045389X03038577.

[127] Shujun Zhang and Fapeng Yu. 'Piezoelectric Materials for High Temperature Sensors'. In: *J. Am. Ceram. Soc.* 94.10 (Oct. 2011). Ed. by D. J. Green, pp. 3153–3170. ISSN: 0002-7820. DOI: 10.1111/j.1551-2916.2011.04792.x. URL: https://onlinelibrary.wiley.com/doi/10.1111/j.1551-2916.2011.04792.x.

[128] Shujun Zhang et al. 'Recent Developments in Piezoelectric Crystals'. In: *J. Korean Ceram. Soc.* 55.5 (Sept. 2018), pp. 419–439. ISSN: 1229-7801. DOI: 10.4191/kcers.2018.55.5.12. URL: http://jkcs.or.kr/journal/view.php?doi=10.4191/kcers.2018.55.5.12.

[129] T. Stevenson et al. ‘Piezoelectric materials for high temperature transducers and actuators’. In: *J. Mater. Sci. Mater. Electron.* 26.12 (Dec. 2015), pp. 9256–9267. ISSN: 0957-4522. DOI: 10.1007/s10854-015-3629-4. URL: http://link.springer.com/10.1007/s10854-015-3629-4.

[130] Hongfei Zu, Huiyan Wu and Qing-Ming Wang. ‘High-Temperature Piezoelectric Crystals for Acoustic Wave Sensor Applications’. In: *IEEE Trans. Ultrason. Ferroelectr. Freq. Control* 63.3 (Mar. 2016). ISSN: 0885-3010. DOI: 10.1109/TUFFC.2016.2527599. URL: http://ieeexplore.ieee.org/document/7404038/.

[131] Shujun Zhang et al. ‘Characterization of piezoelectric single crystal YCa4O(BO3)3 for high temperature applications’. In: *Appl. Phys. Lett.* 92.20.202905 (May 2008). ISSN: 0003-6951. DOI: 10.1063/1.2936276. URL: http://aip.scitation.org/doi/10.1063/1.2936276.

[132] Taeyang Kim et al. ‘High-temperature electromechanical characterization of AlN single crystals’. In: *IEEE Trans. Ultrason. Ferroelectr. Freq. Control* 62.10 (Oct. 2015), pp. 1880–1887. ISSN: 0885-3010. DOI: 10.1109/TUFFC.2015.007252. URL: http://ieeexplore.ieee.org/document/7296776/.

[133] Taeyang Kim, Jinwook Kim and Xiaoning Jiang. ‘AlN Ultrasound Sensor for Photoacoustic Lamb Wave Detection in a High-Temperature Environment’. In: *IEEE Trans. Ultrason. Ferroelectr. Freq. Control* 65.8 (Aug. 2018), pp. 1444–1451. ISSN: 0885-3010. DOI: 10.1109/TUFFC.2018.2839034. URL: https://ieeexplore.ieee.org/document/8361498/.

[134] Lawrence C. Lynnworth and Emmanuel P. Papadakis. ‘Ultrasonic Measurements for Process Control: Theory, Techniques , Applications’. In: *J. Acoust. Soc. Am.* 88.1 (July 1990), p. 589. ISSN: 0001-4966. DOI: 10.1121/1.399906. URL: http://asa.scitation.org/doi/10.1121/1.399906.

[135] Cleon E. Davis et al. ‘In Situ Acoustic Temperature Measurement During Variable-Frequency Microwave Curing’. In: *IEEE Trans. Electron. Packag. Manuf.* 31.4 (Oct. 2008), pp. 273–284. ISSN: 1521-334X. DOI: 10.1109/TEPM.2008.2004570. URL: http://ieeexplore.ieee.org/document/4634592/.

[136] Manabu Takahashi and Ikuo Ihara. ‘Ultrasonic determination of temperature distribution in thick plates during single sided heating’. In: *Mod. Phys. Lett. B* 22.11 (May 2008), pp. 971–976. ISSN: 0217-9849. DOI: 10.1142/S0217984908015693. URL: https://www.worldscientific.com/doi/abs/10.1142/S0217984908015693.

[137] Yunlu Jia and Mikhail Skliar. ‘Noninvasive Ultrasound Measurements of Temperature Distribution and Heat Fluxes in Solids’. In: *Energy & Fuels* 30.5 (May 2016), pp. 4363–4371. ISSN: 0887-0624. DOI: 10.1021/acs.energyfuels.6b00054. URL: https://pubs.acs.org/doi/10.1021/acs.energyfuels.6b00054.

[138] Mikhail Skliar. *In-situ acoustic measurements of temperature profile in extreme environments.* Tech. rep. University of Utah: Department of Energy National Energy Technology Laboratory, 2015.

[139] Yunlu Jia and Mikhail Skliar. ‘Ultrasonic Measurements of Temperature Distribution and Heat Fluxes Across Containments of Extreme Environments’. In: *2019 IEEE Int. Ultrason. Symp.* Vol. 2019-Octob. IEEE, Oct. 2019, pp. 940–943. ISBN: 978-1-7281-4596-9. DOI: 10.1109/ULTSYM.2019.8925643. URL: https://ieeexplore.ieee.org/document/8925643/.

[140] Yifeng Zhang, Frederic Cegla and Joseph Corcoran. ‘Ultrasonic monitoring of pipe wall interior surface temperature’. In: *Struct. Heal. Monit.* (Sept. 2020). ISSN: 1475-9217. DOI: 10.1177/1475921720957592. URL: http://journals.sagepub.com/doi/10.1177/1475921720957592.

[141] Yifeng Zhang and Frederic Cegla. ‘Co-located dual-wave ultrasonics for component thickness and temperature distribution monitoring’. In: *Struct. Heal. Monit.* 0.0 (May 2022), p. 147592172211044. ISSN: 1475-9217. DOI: 10.1177/14759217221104463. URL: http://journals.sagepub.com/doi/10.1177/14759217221104463.

[142] Taylor Jeffrey, David Jack and David Moore. ‘Listening to temperature: Ultrasonic non-destructive identification of material phase and temperature’. In: *AIP Conf. Proc.* Vol. 2102.02001. May. 2019. ISBN: 9780735418325. DOI: 10.1063/1.5099721. URL: http://aip.scitation.org/doi/abs/10.1063/1.5099721.

[143] Krishnan Balasubramaniam et al. ‘High temperature ultrasonic sensor for the simultaneous measurement of viscosity and temperature of melts’. In: *Rev. Sci. Instrum.* 70.12 (Dec. 1999), pp. 4618–4623. ISSN: 0034-6748. DOI: 10.1063/1.1150123. URL: http://aip.scitation.org/doi/10.1063/1.1150123.

[144] A. Hashmi et al. *Intelligent Systems in Cybernetics and Automation Theory.* Ed. by Radek Silhavy et al. Vol. 348. Advances in Intelligent Systems and Computing. Cham: Springer International Publishing, 2015, pp. 139–150. ISBN: 978-3-319-18502-6. DOI: 10.1007/978-3-319-18503-3. URL: http://link.springer.com/10.1007/978-3-319-18503-3.

[145] Anas Hashmi and Alexander N. Kalashnikov. ‘Sensor data fusion for responsive high resolution ultrasonic temperature measurement using piezoelectric transducers’. In: *Ultrasonics* 99.105969.July (Nov. 2019). ISSN: 0041624X. DOI: 10.1016/j.ultras.2019.105969. URL: https://doi.org/10.1016/j.ultras.2019.105969.

[146] Said Alzebda and Alexander N. Kalashnikov. ‘Ultrasonic sensing of temperature of liquids using inexpensive narrowband piezoelectric transducers’. In: *IEEE Trans. Ultrason. Ferroelectr. Freq. Control* 57.12 (Dec. 2010), pp. 2704–2711. ISSN: 0885-3010. DOI: 10.1109/TUFFC.2010.1744. URL: http://ieeexplore.ieee.org/document/5610556/.

[147] Yong Jin Lee, B.T. Khuri-Yakub and K. Saraswat. ‘Temperature measurement in rapid thermal processing using the acoustic temperature sensor’. In: *IEEE Trans. Semicond. Manuf.* 9.1 (Feb. 1996), pp. 115–121. ISSN: 08946507. DOI: 10.1109/66.484291. URL: http://ieeexplore.ieee.org/document/484291/.

[148] Dan Klimek et al. ‘Laser Ultrasonic Instrumentation for Accurate Temperature Measurement of Silicon Wafers in Rapid Thermal Processing Systems’. In: *MRS Proc.* 525 (Feb. 1998), pp. 135–140. ISSN: 0272-9172. DOI: 10.1557/PROC-525-135. URL: http://link.springer.com/10.1557/PROC-525-135.

[149] Joseph L. Rose. *Ultrasonic Guided Waves in Solid Media.* Vol. 9781107048. Cambridge University Press, Aug. 2014, pp. 1–512. ISBN: 9781107048959. DOI: 10.1017/CBO9781107273610. URL: https://www.cambridge.org/core/product/identifier/9781107273610/type/book.

[150] Zhongqing Su and Lin Ye. *Identification of Damage Using Lamb Waves.* Vol. 48. Lecture Notes in Applied and Computational Mechanics. London: Springer London, 2009. ISBN: 978-1-84882-783-7. DOI: 10.1007/978-1-84882-784-4. URL: http://link.springer.com/10.1007/978-1-84882-784-4.

[151] J. David N. Cheeke. *Fundamentals and Applications of Ultrasonic Waves.* Ed. by J. David and N. Cheeke. 1st. CRC Press, Dec. 2017. ISBN: 9781315217307. DOI: 10.1201/b12260. URL: https://www.taylorfrancis.com/books/9781439854983.

[152] Armin Huber. *The Dispersion Calculator.* 2020. URL: https://www.dlr.de/zlp/en/desktopdefault.aspx/tabid-14332/24874_read-61142/%7B%5C#%7D/gallery/33485 (visited on 20/06/2020).

[153] C.Anand Badrish et al. 'Study of Anisotropic Material Behavior for Inconel 625 Alloy at Elevated Temperatures'. In: *Mater. Today Proc.* 18 (2019), pp. 2760–2766. ISSN: 22147853. DOI: 10.1016/j.matpr.2019.07.140. URL: https://doi.org/10.1016/j.matpr.2019.07.140.

[154] Luis Espinosa et al. 'Accuracy on the Time-of-Flight Estimation for Ultrasonic Waves Applied to Non-Destructive Evaluation of Standing Trees: A Comparative Experimental Study'. In: *Acta Acust. united with Acust.* 104.3 (May 2018), pp. 429–439. ISSN: 1610-1928. DOI: 10.3813/AAA.919186. URL: http://www.ingentaconnect.com/content/10.3813/AAA.919186.

[155] Linas Svilainis. 'Review of high resolution time of flight estimation techniques for ultrasonic signals'. In: *52nd Annu. Conf. Br. Inst. Non-Destructive Test. 2013, NDT 2013.* Vol. 1. September 2013. 2013. ISBN: 9781629939933. URL: https://www.researchgate.net/profile/Linas-Svilainis/publication/260264798_Review_of_high_resolution_time_of_flight_estimation_techniques_for_ultrasonic_signals/links/02e7e530621214eda3000000/Review-of-high-resolution-time-of-flight-estimation-techniques-.

[156] Lecheng Jia et al. 'A High-Resolution Ultrasonic Ranging System Using Laser Sensing and a Cross-Correlation Method'. In: *Appl. Sci.* 9.7.1483 (Apr. 2019). ISSN: 2076-3417. DOI: 10.3390/app9071483. URL: https://www.mdpi.com/2076-3417/9/7/1483.

[157] Md Omar Khyam et al. 'Highly Accurate Time-of-Flight Measurement Technique Based on Phase-Correlation for Ultrasonic Ranging'. In: *IEEE Sens. J.* 17.2 (Jan. 2017), pp. 434–443. ISSN: 1530-437X. DOI: 10.1109/JSEN.2016.2631244. URL: http://ieeexplore.ieee.org/document/7750545/.

[158] José F.S. Costa-Júnior et al. 'Measuring uncertainty of ultrasonic longitudinal phase velocity estimation using different time-delay estimation methods based on cross-correlation: Computational simulation and experiments'. In: *Measurement* 122.May 2017 (July 2018), pp. 45–56. ISSN: 02632241. DOI: 10.1016/j.measurement.2018.01.073. URL: https://doi.org/10.1016/j.measurement.2018.01.073.

[159] P. Wilcox. 'Modeling the Excitation of Lamb and SH Waves by Point and Line Sources'. In: *AIP Conf. Proc.* Vol. 700. April 2004. AIP, 2004, pp. 206–213. ISBN: 073540173X. DOI: 10.1063/1.1711626. URL: http://aip.scitation.org/doi/abs/10.1063/1.1711626.

[160] P.D. Wilcox. 'A rapid signal processing technique to remove the effect of dispersion from guided wave signals'. In: *IEEE Trans. Ultrason. Ferroelectr. Freq. Control* 50.4 (Apr. 2003), pp. 419–427. ISSN: 0885-3010. DOI: 10.1109/TUFFC.2003.1197965. URL: http://ieeexplore.ieee.org/document/1197965/.

[161] Chandrasekaran Jayaraman et al. 'Higher Order Modes Cluster (Homc) Guided Waves—A New Technique For NDT Inspection'. In: *AIP Conf. Proc.* Vol. 121. 2009. AIP, 2009, pp. 121–128. DOI: 10.1063/1.3114094. URL: http://aip.scitation.org/doi/abs/10.1063/1.3114094.

[162] A A Swaminathan et al. 'Higher Order Mode Cluster (HOMC) guided wave testing of corrosion under pipe supports (CUPS)'. In: *Proc. Natl. Semin. Exhib. Non-Destructive Eval.* (2011), pp. 224–227. URL: https://www.ndt.net/article/nde-india2011/pdf/2-18D-4.pdf.

[163] Jayaraman Chandrasekaran et al. 'Axial Higher Order Modes Cluster (A-HOMC) Guided Wave For Pipe Inspection'. In: *AIP Conf. Proc.* Vol. 1211.161. 2010. 2010, pp. 161–168. ISBN: 9780735407480. DOI: 10.1063/1.3362262. URL: http://aip.scitation.org/doi/abs/10.1063/1.3362262.

[164] Krishnan Balasubramaniam et al. 'Imaging Hidden Corrosion Using Ultrasonic Non-Dispersive Higher Order Guided Wave Modes'. In: *AIP Conf. Proc.* Vol. 975. 215. AIP, 2008, pp. 215–222. DOI: 10.1063/1.2902661. URL: http://aip.scitation.org/doi/abs/10.1063/1.2902661.

[165] Bhupesh Verma, Swaminathan Annamalai and Prabhu Rajagopal. 'The effect of curvature on the scattering of circumferential higher order mode cluster (C-HOMC) from changes in cross-section'. In: *Proc. Natl. Semin. Exhib. Non-Destructive Eval.* 2011. URL: https://www.ndt.net/article/nde-india2011/pdf/ext-pdf/4-Bhupesh.pdf.

[166] Sri Harsha Reddy K. et al. 'Interaction of Higher Order Modes Cluster (HOMC) guided waves with notch-like defects in plates'. In: *AIP Conf. Proc.* Vol. 1806.03001. February. 2017. ISBN: 9780735414747. DOI: 10.1063/1.4974583. URL: http://aip.scitation.org/doi/abs/10.1063/1.4974583.

[167] J.C. Dodson and D.J. Inman. 'Thermal sensitivity of Lamb waves for structural health monitoring applications'. In: *Ultrasonics* 53.3 (Mar. 2013), pp. 677–685. ISSN: 0041624X. DOI: 10.1016/j.ultras.2012.10.007. URL: http://dx.doi.org/10.1016/j.ultras.2012.10.007.

[168] Alessandro Marzani and Salvatore Salamone. 'Numerical prediction and experimental verification of temperature effect on plate waves generated and received by piezoceramic sensors'. In: *Mech. Syst. Signal Process.* 30 (July 2012), pp. 204–217. ISSN: 08883270. DOI: 10.1016/j.ymssp.2011.11.003. URL: http://dx.doi.org/10.1016/j.ymssp.2011.11.003.

[169] Saqlain Abbas et al. 'Optimization of ultrasonic guided wave inspection in structural health monitoring based on thermal sensitivity evaluation'. In: *J. Low Freq. Noise, Vib. Act. Control* 40.1 (Mar. 2021), pp. 601–622. ISSN: 1461-3484. DOI: 10.1177/1461348419886189. URL: http://journals.sagepub.com/doi/10.1177/1461348419886189.

[170] Jochen Moll et al. 'Temperature affected guided wave propagation in a composite plate complementing the Open Guided Waves Platform'. In: *Sci. Data* 6.1 (Dec. 2019). ISSN: 2052-4463. DOI: 10.1038/s41597-019-0208-1. URL: http://www.nature.com/articles/s41597-019-0208-1.

[171] Yifeng Zhang et al. 'Ultrasonic guided wave monitoring of dendrite formation at electrode–electrolyte interface in aqueous zinc ion batteries'. In: *J. Power Sources* 542.231730 (Sept. 2022). ISSN: 03787753. DOI: 10.1016/j.jpowsour.2022.231730. URL: https://linkinghub.elsevier.com/retrieve/pii/S037877532200725X.

[172] Ming Huang et al. 'Quantitative characterisation of the layered structure within lithium-ion batteries using ultrasonic resonance'. In: *J. Energy Storage* 50.104585 (June 2022). ISSN: 2352152X. DOI: 10.1016/j.est.2022.104585. URL: https://linkinghub.elsevier.com/retrieve/pii/S2352152X22006016.

[173] Ben Kasemsadeh, Aaron Heng and Amit Ashara. *Temperature sensors: PCB guidelines for surface mount devices.* Tech. rep. Texas Instruments, 2019. URL: https://www.ti.com/lit/an/snoa967a/snoa967a.pdf.

[174] David Vaseliou and Emmy Denton. *Optimizing Remote Temperature Sensor Design.* Tech. rep. Texas Instruments, 2017. URL: https://www.ti.com/lit/an/sboa173a/sboa173a.pdf?ts=1663496868261.

[175] S. Bagavathiappan et al. 'Infrared thermography for condition monitoring – A review'. In: *Infrared Physics & Technology* 60 (24th Mar. 2013), pp. 35–55. DOI: 10.1016/j.infrared.2013.03.006.

[176] Akshay Sarawade and Nadir Charniya. 'Detection of Faulty Integrated Circuits in PCB With Thermal Image Processing'. In: *2019 International Conference on Nascent Technologies in Engineering (ICNTE 2019)*. IEEE, 2019. URL: https://ieeexplore.ieee.org/abstract/document/8946061.

[177] Institute for Interconnecting and Packaging Electronic Circuits. *IPC-6012E: Qualification and Performance Specification for Rigid Printed Boards*. Tech. rep. 2020. 76 pp. ISRN: 978-1-951577-09-4. URL: https://shop.ipc.org/automotive-general-electronics-medical-space-and-defense/standards/6012-0-e-english.

[178] He Liu et al. 'Digital Twin-Driven Machine Condition Monitoring: A Literature Review'. In: *Journal of Sensors* 2022 (30th July 2022). Ed. by Xueliang Xiao, pp. 1–13. DOI: 10.1155/2022/6129995.

[179] André Canal Marques, José-María Cabrera and Célia de Fraga Malfatti. 'Printed circuit boards: A review on the perspective of sustainability'. In: *Journal of Environmental Management* 131 (Dec. 2013), pp. 298–306. DOI: 10.1016/j.jenvman.2013.10.003.

[180] F. C. Nix and D. MacNair. 'The Thermal Expansion of Pure Metals: Copper, Gold, Aluminum, Nickel, and Iron'. In: *Phys. Rev.* 60.8 (Oct. 1941), pp. 597–605. ISSN: 0031-899X. DOI: 10.1103/PhysRev.60.597. URL: https://link.aps.org/doi/10.1103/PhysRev.60.597.

[181] R. Feder and A. S. Nowick. 'Use of Thermal Expansion Measurements to Detect Lattice Vacancies near the Melting Point of Pure Lead and Aluminum'. In: *Phys. Rev.* 109.6 (Mar. 1958), pp. 1959–1963. ISSN: 0031-899X. DOI: 10.1103/PhysRev.109.1959. URL: https://link.aps.org/doi/10.1103/PhysRev.109.1959.

[182] D. F. Gibbons. 'Thermal Expansion of Some Crystals with the Diamond Structure'. In: *Phys. Rev.* 112.1 (Oct. 1958), pp. 136–140. ISSN: 0031-899X. DOI: 10.1103/PhysRev.112.136. URL: https://link.aps.org/doi/10.1103/PhysRev.112.136.

[183] M. Lalpoor, D.G. Eskin and L. Katgerman. 'Cold-Cracking Assessment in AA7050 Billets during Direct-Chill Casting by Thermomechanical Simulation of Residual Thermal Stresses and Application of Fracture Mechanics'. In: *Metall. Mater. Trans. A* 40A.13 (Dec. 2009), pp. 3304–3313. ISSN: 1073-5623. DOI: 10.1007/s11661-009-0031-y. URL: http://link.springer.com/10.1007/s11661-009-0031-y.

[184] K. Sakai, A. Matsumuro and M. Senoo. 'Elastic moduli of Al-Li alloys treated at a high pressure of 5.4 GPa'. In: *J. Mater. Sci.* 31.12 (June 1996), pp. 3309–3313. ISSN: 0022-2461. DOI: 10.1007/BF00354683. URL: http://link.springer.com/10.1007/BF00354683.

[185] Rex B. McLellan and Tomaz Ishikawa. 'The elastic properties of aluminum at high temperatures'. In: *J. Phys. Chem. Solids* 48.7 (Jan. 1987), pp. 603–606. ISSN: 00223697. DOI: 10.1016/0022-3697(87)90147-8. URL: https://linkinghub.elsevier.com/retrieve/pii/0022369787901478.

[186] H. J. Stokes. 'Apparatus for the measurement of Young's modulus, between -200 and 700 C by tranverse vibration in vacuum'. In: *J. Sci. Instrum.* 37.7 (July 1960), pp. 117–120. ISSN: 0950-7671. DOI: 10.1088/0950-7671/37/7/116. URL: https://iopscience.iop.org/article/10.1088/0950-7671/37/7/116.

[187] E. R. Naimon, H. M. Ledbetter and W. F. Weston. 'Low-temperature elastic properties of four wrought and annealed aluminium alloys'. In: *J. Mater. Sci.* 10.8 (Aug. 1975), pp. 1309–1316. ISSN: 0022-2461. DOI: 10.1007/BF00540820. URL: http://link.springer.com/10.1007/BF00540820.

[188] David N. Alleyne and Peter Cawley. 'Optimization of lamb wave inspection techniques'. In: *NDT E Int.* 25.1 (Jan. 1992), pp. 11–22. ISSN: 09638695. DOI: 10.1016/0963-8695(92)90003-Y. URL: https://linkinghub.elsevier.com/retrieve/pii/096386959290003Y.

[189] Manton John Guers. 'In-Situ Monitoring of Remote Specimens Using Ultrasonic Guided Waves'. PhD Thesis. Pennsylvania State University, 2011.

[190] Douglas C. Hopkins et al. 'Extreme Thermal Transient Stress Analysis with Pre-Stress in a Metal Matrix Composite Power Package'. In: *Addit. Conf. (Device Packag. HiTEC, HiTEN, CICMT)* 2012.HITEC (Jan. 2012). ISSN: 2380-4491. DOI: 10.4071/HITEC-2012-THA25. URL: http://meridian.allenpress.com/imaps-conferences/article/2012/HITEC/000361/25402/Extreme-Thermal-Transient-Stress-Analysis-with.

[191] Viktor A. Nikolaevtsev et al. 'Efficiency of Lamb wave excitation by wedge-shaped ultrasonic transducer'. In: *2016 13th Int. Sci. Conf. Actual Probl. Electron. Instrum. Eng.* Vol. 1. IEEE, Oct. 2016, pp. 42–47. ISBN: 978-1-5090-4069-8. DOI: 10.1109/APEIE.2016.7802286. URL: http://ieeexplore.ieee.org/document/7802286/.

[192] Adel A. Abdel-Wahab, Sabbah Ataya and Vadim V. Silberschmidt. 'Temperature-dependent mechanical behaviour of PMMA: Experimental analysis and modelling'. In: *Polym. Test.* 58 (Apr. 2017), pp. 86–95. ISSN: 01429418. DOI: 10.1016/j.polymertesting.2016.12.016. URL: http://dx.doi.org/10.1016/j.polymertesting.2016.12.016.

[193] Richard S Hassard. *Plastics for aerospace vehicles: Part II transparent glazing materials.* Tech. rep. January. Litchfield Park, Arizona: Goodyear Aerospace Corporation, 1973. URL: https://www.abbottaerospace.com/downloads/mil-hdbk-17a-p2-plastics-for-aerospace-vehicles-part-ii-transparent-glazing-materials/.

[194] Iwan H. Sahputra, Alessio Alexiadis and Michael J. Adams. 'Temperature and configurational effects on the Young's modulus of poly (methyl methacrylate): a molecular dynamics study comparing the DREIDING, AMBER and OPLS force fields'. In: *Mol. Simul.* 44.9 (June 2018). ISSN: 0892-7022. DOI: 10.1080/08927022.2018.1450983. URL: https://www.tandfonline.com/doi/full/10.1080/08927022.2018.1450983.

[195] Mikio Fukuhara and Asao Sampei. 'Low-temperature elastic moduli and internal dilational and shear friction of polymethyl methacrylate'. In: *J. Polym. Sci. Part B Polym. Phys.* 33.12 (Sept. 1995), pp. 1847–1850. ISSN: 08876266. DOI: 10.1002/polb.1995.090331214. URL: https://onlinelibrary.wiley.com/doi/10.1002/polb.1995.090331214.

[196] Vivek T. Rathod. 'A Review of Acoustic Impedance Matching Techniques for Piezoelectric Sensors and Transducers'. In: *Sensors* 20.14.4051 (July 2020). ISSN: 1424-8220. DOI: 10.3390/s20144051. URL: https://www.mdpi.com/1424-8220/20/14/4051.

[197] COMSOL. *Mesh Refinement for Wave Problems.* 2013. URL: https://uk.comsol.com/blogs/mesh-refinement-for-wave-problems/ (visited on 09/09/2021).

[198] COMSOL. *How to Inspect Your Mesh in COMSOL Multiphysics.* 2017. URL: https://uk.comsol.com/blogs/how-to-inspect-your-mesh-in-comsol-multiphysics/ (visited on 09/09/2021).

[199] COMSOL. *Resolving time dependant waves.* 2021. URL: https://uk.comsol.com/support/knowledgebase/1118 (visited on 03/09/2021).

[200] COMSOL. *Reducing the amount of solution data stored in a model.* 2021. URL: https://www.comsol.ch/support/knowledgebase/1255 (visited on 09/09/2021).

[201] University of Southampton. *IRIDIS 5*. 2021. URL: https://www.southampton.ac.uk/isolutions/staff/iridis.page (visited on 03/09/2021).

[202] P.E. Aba-Perea et al. ‘Determination of the high temperature elastic properties and diffraction elastic constants of Ni-base superalloys’. In: *Mater. Des.* 89 (Jan. 2016), pp. 856–863. ISSN: 02641275. DOI: 10.1016/j.matdes.2015.09.152. URL: http://dx.doi.org/10.1016/j.matdes.2015.09.152.

[203] R. N. Abdullaev et al. ‘Density and volumetric expansion of the Inconel 718 alloy in solid and liquid states’. In: *Thermophys. Aeromechanics* 26.5 (Sept. 2019), pp. 785–788. ISSN: 0869-8643. DOI: 10.1134/S0869864319050160. URL: http://link.springer.com/10.1134/S0869864319050160.

[204] Je-Chin Han and Srinath Ekkad. ‘Recent Development in Turbine Blade Film Cooling’. In: *Int. J. Rotating Mach.* 7.1 (2001), pp. 21–40. ISSN: 1023-621X. DOI: 10.1155/S1023621X01000033. URL: http://www.hindawi.com/journals/ijrm/2001/860837/abs/.

[205] Firat Kiyici, Tekin Aksu and Sitki Uslu. ‘Design of a High Pressure Turbine Nozzle Guide Vane with Effective Film Cooling System on Leading Edge’. In: *54th AIAA Aerosp. Sci. Meet.* Vol. 1. April 2017. Reston, Virginia: American Institute of Aeronautics and Astronautics, Jan. 2016. ISBN: 978-1-62410-393-3. DOI: 10.2514/6.2016-0654. URL: https://arc.aiaa.org/doi/10.2514/6.2016-0654.

[206] C. Clum et al. ‘Particle Deposition in Internal Cooling Cavities of a Nozzle Guide Vane: Part I — Experimental Investigation’. In: *Vol. 5A Heat Transf.* Vol. 5A. 1. American Society of Mechanical Engineers, June 2014. ISBN: 978-0-7918-4571-4. DOI: 10.1115/GT2014-27150. URL: https://asmedigitalcollection.asme.org/GT/proceedings/GT2014/45714/D%7B%5C%22%7Bu%7D%7Dsseldorf,%20Germany/235328.

[207] Paul Headland. ‘Sealing arrangement for a nozzle guide vane and gas turbine’. In: US9617920B (2017).

[208] Thomas Irvine and James Hartnett. *Advances in heat transfer: Volume 7*. Volume 7. Academic Press, 1971. ISBN: 9780080575612. URL: https://www.sciencedirect.com/bookseries/advances-in-heat-transfer.

[209] Long Meng et al. ‘Film cooling performance on pressure side of turbine blade with different number of hole rows under rotating state’. In: *Aerosp. Sci. Technol.* 126.107569 (July 2022). ISSN: 12709638. DOI: 10.1016/j.ast.2022.107569. URL: https://doi.org/10.1016/j.ast.2022.107569.

[210] Olivier Cleynen. *Photo of V2500 high-pressure turbine guide vane*. 2013. URL: https://commons.wikimedia.org/wiki/File:Repair_process_for_a_V2500_high-pressure_turbine_guide_vane_(10).jpg (visited on 15/09/2022).

[211] O. Diligent et al. ‘The low-frequency reflection and scattering of the S0 Lamb mode from a circular through-thickness hole in a plate: Finite Element, analytical and experimental studies’. In: *J. Acoust. Soc. Am.* 112.6 (Dec. 2002), pp. 2589–2601. ISSN: 0001-4966. DOI: 10.1121/1.1512292. URL: http://asa.scitation.org/doi/10.1121/1.1512292.

[212] Tomas Grahn. ‘Lamb wave scattering from a circular partly through-thickness hole in a plate’. In: *Wave Motion* 37.1 (Jan. 2003), pp. 63–80. ISSN: 01652125. DOI: 10.1016/S0165-2125(02)00051-3. URL: https://linkinghub.elsevier.com/retrieve/pii/S0165212502000513.

[213] J.C.P. McKeon and M.K. Hinders. ‘Lamb wave scattering from a through hole’. In: *J. Sound Vib.* 224.5 (July 1999), pp. 843–862. ISSN: 0022460X. DOI: 10.1006/jsvi.1999.2164. URL: https://linkinghub.elsevier.com/retrieve/pii/S0022460X99921648.

[214] F.B. Cegla, A. Rohde and M. Veidt. ‘Analytical prediction and experimental measurement for mode conversion and scattering of plate waves at non-symmetric circular blind holes in isotropic plates’. In: *Wave Motion* 45.3 (Jan. 2008), pp. 162–177. ISSN: 01652125. DOI: 10.1016/j.wavemoti.2007.05.005. URL: https://linkinghub.elsevier.com/retrieve/pii/S0165212507000650.

[215] Zensheu Chang and Ajit Mal. ‘Scattering of Lamb waves from a rivet hole with edge cracks’. In: *Mech. Mater.* 31.3 (Mar. 1999), pp. 197–204. ISSN: 01676636. DOI: 10.1016/S0167-6636(98)00060-X. URL: https://linkinghub.elsevier.com/retrieve/pii/S016766369800060X.

[216] A.-C. Hladky-Hennion. ‘Phononic crystal (PC) applications of ATILA’. In: *Appl. ATILA FEM Softw. to Smart Mater.* Elsevier, 2013, pp. 190–203. ISBN: 9780857090652. DOI: 10.1533/9780857096319.2.190. URL: https://linkinghub.elsevier.com/retrieve/pii/B9780857090652500096.

[217] Yabin Jin, Bahram Djafari-Rouhani and Daniel Torrent. ‘Gradient index phononic crystals and metamaterials’. In: *Nanophotonics* 8.5 (Feb. 2019), pp. 685–701. ISSN: 2192-8614. DOI: 10.1515/nanoph-2018-0227. URL: https://www.degruyter.com/document/doi/10.1515/nanoph-2018-0227/html.

[218] Feng-Chia Hsu et al. ‘Acoustic band gaps in phononic crystal strip waveguides’. In: *Appl. Phys. Lett.* 96.5 (Feb. 2010), p. 051902. ISSN: 0003-6951. DOI: 10.1063/1.3298643. URL: http://aip.scitation.org/doi/10.1063/1.3298643.

[219] Giorgio Palma et al. ‘Acoustic metamaterials in aeronautics’. In: *Appl. Sci.* 8.6 (2018), pp. 1–18. ISSN: 20763417. DOI: 10.3390/app8060971.

[220] Hee Don Jeong, Hyeon Jae Shin and Joseph L Rose. ‘Detection of defects in a thin steel plate using ultrasonic guided wave’. In: *15th World Conf. Non-Destructive Test.* Rome, 2000. URL: https://www.ndt.net/article/wcndt00/papers/idn020/idn020.htm.

[221] Ning Hu et al. ‘Damage Identification of Metallic Structures Using A0 Mode of Lamb Waves’. In: *Struct. Heal. Monit.* 7.3 (Sept. 2008), pp. 271–285. ISSN: 1475-9217. DOI: 10.1177/1475921708090566. URL: http://journals.sagepub.com/doi/10.1177/1475921708090566.

[222] Hyunseong Lee et al. ‘Damage detection technique using ultrasonic guided waves and outlier detection: Application to interface delamination diagnosis of integrated circuit package’. In: *Mech. Syst. Signal Process.* 160.107884 (Nov. 2021). ISSN: 08883270. DOI: 10.1016/j.ymssp.2021.107884. URL: https://doi.org/10.1016/j.ymssp.2021.107884%20https://linkinghub.elsevier.com/retrieve/pii/S088832702100279X.

[223] Jagadeeshwar L. Tabjula et al. ‘Outlier analysis for defect detection using sparse sampling in guided wave structural health monitoring’. In: *Struct. Control Heal. Monit.* 28.3 (Mar. 2021), pp. 1–13. ISSN: 1545-2255. DOI: 10.1002/stc.2690. URL: https://onlinelibrary.wiley.com/doi/10.1002/stc.2690.

[224] Xuan ‘Peter’ Zhu et al. ‘Ultrasonic guided waves for nondestructive evaluation/structural health monitoring of trusses’. In: *Meas. Sci. Technol.* 21.045701.4 (Apr. 2010). ISSN: 0957-0233. DOI: 10.1088/0957-0233/21/4/045701. URL: https://iopscience.iop.org/article/10.1088/0957-0233/21/4/045701.

[225] Ane Blázquez-García et al. ‘A Review on Outlier/Anomaly Detection in Time Series Data’. In: *ACM Comput. Surv.* 54.3 (Apr. 2022), pp. 1–33. ISSN: 0360-0300. DOI: 10.1145/3444690. arXiv: 2002.04236. URL: https://dl.acm.org/doi/10.1145/3444690.

[226] M. Beghini et al. 'Measurement of coatings' elastic properties by mechanical methods: Part 2. Application to thermal barrier coatings'. In: *Exp. Mech.* 41.4 (Dec. 2001), pp. 305–311. ISSN: 0014-4851. DOI: 10.1007/BF02323923. URL: http://link.springer.com/10.1007/BF02323923.

[227] Stephen Akwaboa and Patrick F. Mensah. 'A Comparison Study of Heat Transfer Through Electron Beam Physical Vapor Deposition (EBPVD) and Air Plasma Sprayed (APS) Coated Gas Turbine Blades'. In: *2010 14th Int. Heat Transf. Conf. Vol. 5.* Vol. 5. ASMEDC, Jan. 2010, pp. 249–255. ISBN: 978-0-7918-4940-8. DOI: 10.1115/IHTC14-22961. URL: https://asmedigitalcollection.asme.org/IHTC/proceedings/IHTC14/49408/249/350755.

[228] E. Lugscheider et al. 'Mechanical properties of EB-PVD-thermal barrier coatings by nanoindentation'. In: *Surf. Coatings Technol.* 138.1 (Apr. 2001), pp. 9–13. ISSN: 02578972. DOI: 10.1016/S0257-8972(00)01147-6. URL: https://linkinghub.elsevier.com/retrieve/pii/S0257897200011476.

[229] Shuqi Guo and Yutaka Kagawa. 'Effect of thermal exposure on hardness and Young's modulus of EB-PVD yttria-partially-stabilized zirconia thermal barrier coatings'. In: *Ceram. Int.* 32.3 (Jan. 2006), pp. 263–270. ISSN: 02728842. DOI: 10.1016/j.ceramint.2005.01.018. URL: https://linkinghub.elsevier.com/retrieve/pii/S0272884205000684.

[230] Kai Duan and Rolf W. Steinbrech. 'Influence of sample deformation and porosity on mechanical properties by instrumented microindentation technique'. In: *J. Eur. Ceram. Soc.* 18.2 (Jan. 1998), pp. 87–93. ISSN: 09552219. DOI: 10.1016/S0955-2219(97)00088-5. URL: https://linkinghub.elsevier.com/retrieve/pii/S0955221997000885.

[231] Byung-Koog Jang and Hideaki Matsubara. 'Influence of porosity on hardness and Young's modulus of nanoporous EB-PVD TBCs by nanoindentation'. In: *Mater. Lett.* 59.27 (Nov. 2005), pp. 3462–3466. ISSN: 0167577X. DOI: 10.1016/j.matlet.2005.06.014. URL: https://linkinghub.elsevier.com/retrieve/pii/S0167577X05005938.

[232] Yasuhiro Yamazaki et al. 'Deformation and Fracture Behaviors in the Freestanding APS-TBC - Effects of Process Parameters and Thermal Exposure'. In: *Key Eng. Mater.* 353-358.December (Sept. 2007), pp. 1935–1938. ISSN: 1662-9795. DOI: 10.4028/www.scientific.net/KEM.353-358.1935. URL: https://www.scientific.net/KEM.353-358.1935.

[233] Subhasisa Nath, Indranil Manna and Jyotsna Dutta Majumdar. 'Nanomechanical behavior of yttria stabilized zirconia (YSZ) based thermal barrier coating'. In: *Ceram. Int.* 41.4 (May 2015), pp. 5247–5256. ISSN: 02728842. DOI: 10.1016/j.ceramint.2014.11.039. URL: http://dx.doi.org/10.1016/j.ceramint.2014.11.039.

[234] Biao Li et al. 'Design of Thermal Barrier Coatings Thickness for Gas Turbine Blade Based on Finite Element Analysis'. In: *Math. Probl. Eng.* 2017 (2017). ISSN: 1024-123X. DOI: 10.1155/2017/2147830. URL: https://www.hindawi.com/journals/mpe/2017/2147830/.

[235] Yanli Zhang et al. 'Influence of Gd2O3 and Yb2O3 Co-doping on Phase Stability, Thermophysical Properties and Sintering of 8YSZ'. In: *Chinese J. Aeronaut.* 25.6 (Dec. 2012), pp. 948–953. ISSN: 10009361. DOI: 10.1016/S1000-9361(11)60466-4. URL: http://dx.doi.org/10.1016/S1000-9361(11)60466-4.

[236] Katarína Bodišová et al. 'Alumina ceramics prepared by pressure filtration of alumina powder dispersed in boehmite sol'. In: *Ceram. - Silikaty* 50.4 (2006), pp. 239–244. ISSN: 08625468. URL: https://www.ceramics-silikaty.cz/2006/pdf/2006_04_239.pdf.

[237] Saint-Gobain Coating Solutions. *NiCrAlY Technical Bulletin.* Tech. rep. 2017. URL: https://www.coatingsolutions.saint-gobain.com/sites/imdf.coatingsolutions.com/files/thermal-spray-flexicord-nicraly-tds.pdf.

[238] Special Metals. *IN718 Datasheet.* Tech. rep. 2007, pp. 1–28. URL: https://www.specialmetals.com/assets/smc/documents/inconel_alloy_718.pdf.

[239] L. Saucedo-Mora et al. 'Multi-scale modeling of damage development in a thermal barrier coating'. In: *Surf. Coatings Technol.* 276.June (Aug. 2015), pp. 399–407. ISSN: 02578972. DOI: 10.1016/j.surfcoat.2015.06.038. URL: https://linkinghub.elsevier.com/retrieve/pii/S0257897215300761.

[240] P Bednarz et al. 'Stress Distribution in APS-TBCs Under Thermal Cycling Loading Conditions'. In: *Adv. Ceram. Coatings Ceram. Syst.* Ed. by Dongming Zhu and Kevin Plucknett. Cocoa Beach, Florida: The American Ceramic Society, 2005, pp. 73–80. ISBN: 6147945890. DOI: 10.1002/9780470291238.ch9. URL: https://onlinelibrary.wiley.com/doi/10.1002/9780470291238.ch9.

[241] Giuliano Gregori et al. 'Vibration damping of superalloys and thermal barrier coatings at high-temperatures'. In: *Mater. Sci. Eng. A* 466.1-2 (Sept. 2007), pp. 256–264. ISSN: 09215093. DOI: 10.1016/j.msea.2007.02.047. URL: https://linkinghub.elsevier.com/retrieve/pii/S0921509307003723.